INFORMATION TO USERS

This manuscript has been reproduced from the microfilm master. UMI films the text directly from the original or copy submitted. Thus, some thesis and dissertation copies are in typewriter face, while others may be from any type of computer printer.

The quality of this reproduction is dependent upon the quality of the copy submitted. Broken or indistinct print, colored or poor quality illustrations and photographs, print bleedthrough, substandard margins, and improper alignment can adversely affect reproduction.

In the unlikely event that the author did not send UMI a complete manuscript and there are missing pages, these will be noted. Also, if unauthorized copyright material had to be removed, a note will indicate the deletion.

Oversize materials (e.g., maps, drawings, charts) are reproduced by sectioning the original, beginning at the upper left-hand corner and continuing from left to right in equal sections with small overlaps. Each original is also photographed in one exposure and is included in reduced form at the back of the book.

Photographs included in the original manuscript have been reproduced xerographically in this copy. Higher quality 6" x 9" black and white photographic prints are available for any photographs or illustrations appearing in this copy for an additional charge. Contact UMI directly to order.

UMI

A Bell & Howell Information Company
300 North Zeeb Road, Ann Arbor MI 48106-1346 USA
313/761-4700 800/521-0600

TRANSIENT COMBUSTION IN HYBRID ROCKETS

A DISSERTATION
SUBMITTED TO THE DEPARTMENT OF
AERONAUTICS AND ASTRONAUTICS
AND THE COMMITTEE ON GRADUATE STUDIES
OF STANFORD UNIVERSITY
IN PARTIAL FULFILLMENT OF THE REQUIREMENTS
FOR THE DEGREE OF
DOCTOR OF PHILOSOPHY

By
Mustafa A. Karabeyoglu
August 1998

I certify that I have read this dissertation and that in my opinion it is fully adequate, in scope and quality, as a dissertation for the degree of Doctor of Philosophy.

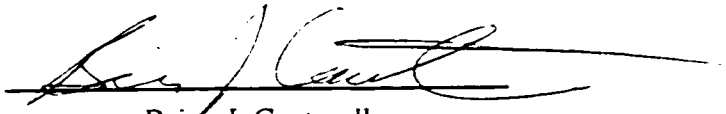

Brian J. Cantwell
(Principal Adviser)

I certify that I have read this dissertation and that in my opinion it is fully adequate, in scope and quality, as a dissertation for the degree of Doctor of Philosophy.

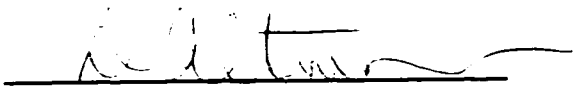

David Altman

I certify that I have read this dissertation and that in my opinion it is fully adequate, in scope and quality, as a dissertation for the degree of Doctor of Philosophy.

Sanjiva Lele

I certify that I have read this dissertation and that in my opinion it is fully adequate, in scope and quality, as a dissertation for the degree of Doctor of Philosophy.

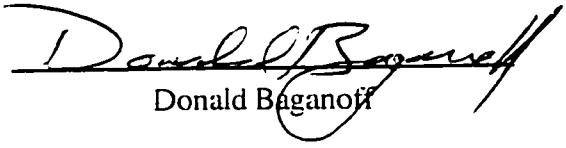

Donald Baganoff

Approved for the University Committee on Graduate Studies:

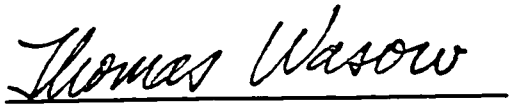

To my parents

Enver and Nadire Karabeyoglu

Abstract

Hybrid rockets regained interest recently as an alternative chemical propulsion system due to their advantages over the solid and liquid systems that are currently in use. Development efforts on hybrids revealed two important problem areas: 1) low frequency instabilities and 2) slow transient response. Both of these are closely related to the transient behavior which is a poorly understood aspect of hybrid operation. This thesis is mainly involved with a theoretical study of transient combustion in hybrid rockets. We follow the methodology of identifying and modeling the subsystems of the motor such as the thermal lags in the solid, boundary layer combustion and chamber gasdynamics from a dynamic point of view. We begin with the thermal lag in the solid which yield the regression rate for any given wall heat flux variation. Interesting phenomena such as overshooting during throttling and the amplification and phase lead regions in the frequency domain are discovered. Later we develop a quasi-steady transient hybrid combustion model supported with time delays for the boundary layer processes. This is integrated with the thermal lag system to obtain the thermal combustion (TC) coupled response. The TC coupled system with positive delays generated low frequency instabilities. The scaling of the instabilities are in good agreement with actual motor test data. Finally, we formulate a gasdynamic model for the hybrid chamber which successfully resolves the filling/emptying and longitudinal acoustic behavior of the motor. The TC coupled system is later integrated to the gasdynamic model to obtain the overall response (TCG coupled system) of gaseous oxidizer motors with stiff feed systems. Low frequency instabilities were also encountered for the TCG coupled system.

Apart from the transient investigations, the regression rate behavior of liquefying hybrid propellants such as solid cryogenic materials are also studied. The theory is based on the possibility of enhancement of regression rate by the entrainment mass transfer from a liquid layer formed on the fuel surface. The predicted regression rates are in good agreement with the cryogenic experimental findings obtained recently at Edwards Airforce Base with a frozen pentane and gaseous oxygen system.

Acknowledgments

Completion of this thesis and my Ph.D. degree would have been extremely difficult if not impossible without the support and guidance of many valuable individuals. Here, I will try to acknowledge a few of them. I would like start with expressing my most sincere gratitude to the late Professor Daniel Bershader who first introduced me the concept of hybrid rockets. My memories with this insightful physicist and true gentleman will be fresh in my mind for the rest of my life.

I am also very grateful to my advisor Professor Brian J. Cantwell who accepted me in his research group after Professor Bershader's demise and guided me with his great knowledge and fairness for the last three years of my work. It has truly been a pleasure, as well as a privilege to be member of his research team.

The person who inspired and guided me most for the creation of this work is most definitely Dr. David Altman. My interaction with this rocket scientist with incredible experience and knowledge have educated me in both academic and also practical issues of the field of propulsion. Our discussions on various aspects of rockets were among my most joyful moments during my stay at Stanford. I also would like thank Professor Paul Green of the Biology department who gave me the joy of working on an extremely interesting problem, phyllotaxis. Paul's great personality and enthusiasm was my sole guidance during my work in a discipline quite remote from my background.

I would like to acknowledge the other two members of my reading committee Professors Sanjiva Lele and Donald Baganoff who also provided significant advice for the development of this work. I also would recognize the help of Karl von Ellenreider, John Pye and the rest of my research group. I am indebted to graduate students Hideki Moriai, Robert St. Clair and Kaveh Hosseni for their precious help with the simulation of gasdynamic system, scaling of entrainment rate and the Labview program developed for the experimental set up. I also would like to acknowledge all of my Turkish friends for making my life at Stanford enjoyable.

Most of all I would like to thank to my family: my late parents Enver and Nadire Karabeyoglu who have always inspired and guided me to do better, my sisters and brothers in law Yasemin-Ali Dermanci and Ayse-Halim Anisoglu for their precious help and understanding during all those years that I was away from home.

This work is supported in part by TUBITAK of Turkey, by UTC/CSD under grants PZ04 and NCC8-30-TRP and by Joint Institute for Aeronautics and Acoustics under NASA grant NCC 2-55.

Finally, I would like express my gratitude to my beloved fiancée Banu Bilsel for her great support and patience.

Table of Contents

List of Tables

List of Figures

Nomenclature

A:	Pre-exponential coefficient
A_p, A_n:	Port and nozzle throat areas
a:	Absorption coefficient
a_{ent}:	Entrainment coefficient
B:	Blowing parameter
B_a B_t:	Aerodynamic and thermochemical blowing parameters
B_g:	Gas phase blowing parameter
C:	Specific heat
c':	Boundary layer delay time coefficient
C_f C_H:	Skin friction coefficient and Stanton number
c^*_{exp}, c^*_{theo}:	Measured and calculated characteristic velocities
c^-:	Mass flow corrected characteristic velocity
c_d:	Discharge coefficient
D:	Port diameter
E_a:	Activation energy
E_L, E_h, E_{E_s}:	Energy Parameters
G_o, G_t:	Oxidizer and total mass fluxes
h:	Melt layer thickness
h_v:	Effective heat of gasification
Δh:	Enthalpy difference between the flame and the surface
k:	Blowing parameter exponent
I:	Laplace transform of oxidizer mass flux
L:	Length of the fuel port
L_m, L_v:	Latent heat of melting and vaporization
M_f:	Total fuel mass

$\dot{m}$:	Total mass flow rate
$\dot{m}_f$, $\dot{m}_{ox}$:	Fuel and oxidizer mass flow rates
n:	Mass flux exponent
O/F:	Oxidizer to fuel ratio
P_c:	Chamber pressure
P_d:	Dynamic pressure in the port
$\dot{Q}_r$, $\dot{Q}_c$:	Radiative and convective heat transfer at the surface
$\dot{q}_r$:	Radiative energy flux
R:	Ratio of thermal to radiative thickness
$\dot{r}$ R:	Dimensional and nondimensional regression rate
R_{ent}:	Nondimensional entrainment parameter
R_h:	Ratio of heat of gasifications
R_g:	Specific gas constant
S_w:	Burning area
s:	Laplace transform variable
T_a:	Initial fuel temperature
T_m, T_v:	Melting and vaporization temperatures
t_b:	Burn out time
u, v:	Axial and normal velocities
V_p, V_m:	Port and motor volumes
y, z:	Coordinate normal to the surface and axial distance along the port
α, β:	Dynamic pressure and thickness exponents
δ:	Thermal thickness
η_c:	Combustion efficiency
Φ:	Regression rate nondimensionalized with respect to the classical value
κ, λ:	Thermal diffusivity and conductivity
μ:	Viscosity
ρ:	Density
τ_{bl} τ_{tl}:	Boundary layer response time and thermal lag time
σ:	Surface tension
σ_1,σ_2:	Gas phase response coefficients
ω, f:	Angular frequency and frequency

Subscripts:

1:	First perturbation variable
2:	Second perturbation value
b:	Flame value
e:	Free stream value
cl:	Classical
ent:	Entrainment
f:	Fuel
g:	Gaseous state
o:	Oxidizer
l:	Liquid
s:	Solid, surface
v:	Vaporization
ref :	Reference quantities

Superscripts:

-	Nondimensional variable
qs:	Quasi-steady

Chapter 1

Introduction

A hybrid rocket is a chemical rocket with one propellant stored in the solid phase while the other one is stored in the liquid phase. In most applications the solid propellant is the fuel and the liquid propellant is the oxidizer. Even though reverse hybrids with fuel in liquid phase and oxidizer in the solid phase are also feasible, the number of tests performed with the reverse scheme is very limited. Although a large variety of fuels including trash and wood has been considered for hybrid rockets, the most commonly used fuel materials in practice are the polymers such as Plexiglas, PE, HTPB etc. It is worth noting that cryogenic fuels such as frozen pentane and acetylene have been tried as hybrid fuels. The typical oxidizers that are frequently used are liquid and gaseous oxygen, flourine and hydrogen peroxide.

The introduction of the concept of a hybrid rocket dates back to the late 1930's [1, 2]. The earliest significant effort was in the mid 1940's and was performed by the Pacific Rocket Society. Hybrid motors built by the Pacific Rocket Society powered sounding rockets and used wood (Douglas fir) as the fuel and liquid oxygen as the oxidizer. Also the in mid 1940's GE initiated investigations on hybrids. However, the most intense research on hybrids started in the 1960's at various institutions such as UTC/CSD, Locheed Propulsion Company, Stanford Research Institute and ONERA (France). Most of the understanding of the fundamental phenomena occurring in the motor was developed during these years. Due to the lack of interest in the 1970's and 1980's the intensity of research on hybrids decreased significantly. Eventually in the 1990's hybrids, which possess several advantages over other chemical rockets currently in use, have regained interest as a consequence of increased commercial demand for a reliable and low cost launch vehicle. The most important advantage which makes hybrids a strong candidate for the propulsion system of future vehicles is their inherently safe nature both in the operation mode and also in the hold down mode. A private company, AMROC built and tested (on

the ground) one of the largest hybrid motors, DM-01 with a nominal thrust level of 250,000 lbf in 1994. Unfortunately the company went bankrupt in 1995 due to the lack of funds required for further development. The government and industry have recently started a joint program (Hybrid Propulsion Demonstration Program) to demonstrate the feasibility of hybrid technology. Currently, a new 250,000 lbf thrust motor is under development within the HPDP program [3]. Moreover, many universities, private and government organizations are individually running research programs on many aspects of hybrid propulsion.

The overall schematic of a typical single port hybrid rocket is shown figure 1.1. In the hybrid combustion scheme the oxidizer in the liquid or gaseous phase is injected into the motor chamber at the front end. The injected oxidizer, as it flows through the port, forms a boundary layer over the fuel grain. It is reported by many investigators in the past that, in the standard hybrid operating regimes, the hybrid boundary layer is turbulent in nature over a large portion of the fuel grain length. In this turbulent boundary layer there exists a turbulent diffusion flame filling the entire fuel grain length with a thickness, in general, very small compared to the boundary layer thickness. The heat generated in the flame, which is located approximately 20-30% of the boundary layer thickness from the wall, is transferred to the wall mainly by convection. The wall heat flux evaporates the solid fuel which later is transferred to the flame to react with the oxidizer which is transported from the free stream by turbulent diffusion mechanisms. The diffusion flame combustion products, the unburned fuel that travels beneath the flame and the unburned oxidizer, mix and further react in the post combustion chamber to the level quantified by the combustion efficiency for a specific motor. The hot gases then expand through a convergent divergent nozzle to deliver the required thrust for the mission.

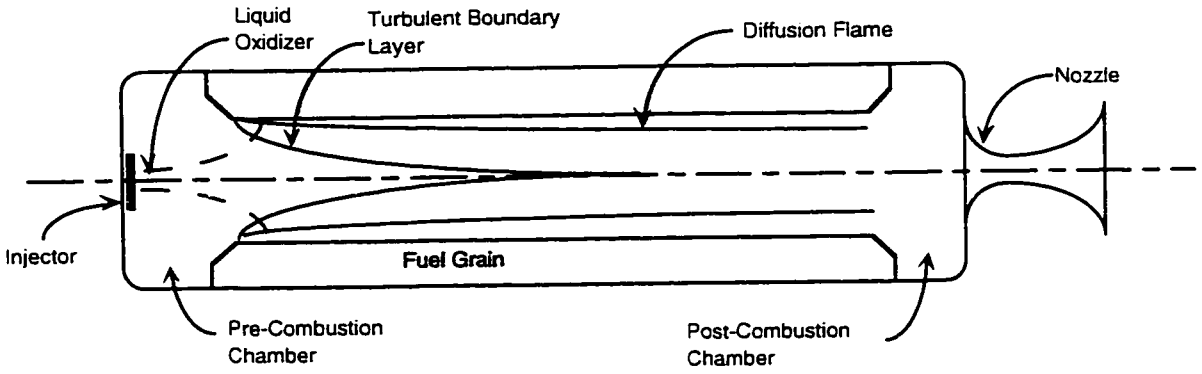

Figure 1.1. Schematic of a single port hybrid rocket motor.

It is important to note that even though the geometry of a hybrid motor is similar to a solid motor, the combustion scheme is vastly different. In a solid rocket, the oxidizer and fuel are both stored in the solid phase next to each other (if not homogeneously mixed). Consequently, the solid combustion takes place in a deflegration (premixed) flame that is closer to the surface compared to the hybrid diffusion flame [4]. Also in solids there exists some heterogeneous reactions at the surface. Later in this study it will be argued that these differences in the combustion scheme of an hybrid motor, significantly alter the transient operation characteristics, especially the generation mechanisms of the instabilities.

As mentioned previously, hybrids have various advantages over solid and liquid rockets. Some of those advantages over the solid-propellant rockets are 1) thrust termination, restart and throttling capabilities, 2) higher specific impulse (although lower thrust density), 3) safe manufacturing, transportation and operation (fundamentally non explosive), 4) lower development costs for new systems and possibly lower operational costs, 5) less environmental impact. The significant advantages over the liquid-propellant rockets can be listed as, 1) lower development and operating costs (life cycle costs), 2) lower fire and explosion hazards. The major disadvantages of hybrid rockets are their lack of technological maturity and their low thrust densities as a result of slow regression rates. A detailed summary of the comparison of the three types of chemical rockets is shown in table 1.1.

In the last decade, the emerging commercial market has made the economic aspects of transferring payload to earth orbit more dominant. The price for the service that the customers of the market observe, reflects the contributions of 1) cost of launching charged by the launching company and 2) insurance costs (or risk of failure) [5]. Thus for a competitive operability in this increasing returns to scale market, a launch company needs to optimize the combination of reducing the average costs per launch and improving the overall reliability of the system (to reduce risk of failure). The safety, reliability, life cycle cost and performance advantages of hybrid rockets makes them an excellent candidate for a solution for this optimization problem and thus for the next generation boosters.

The high thrust density requirements of launching applications requires the usage of the multiport configuration for the fuel grain. Figure 1.2 shows the schematic of the AMROC H1800 motor which is a multiport hybrid rocket with a pressurized oxidizer feed system. The schemetic of the Aquila hybrid launch vehicle which uses a total of four H-1800 motors for the first two stages is shown in figure 1.3. Other possible applications

for hybrids are launch vehicle upper stages, space engines, gas generators, target drone tactical missile propulsion and sounding rockets [2].

Chemical Rockets	**Liquid**	**Solid**	**Hybrid**
Safety/Reliability: (Uncontrolled Deflagration/Detonation)			
Preflight (TNT equivalency)	yes	yes	no
Onflight	yes	yes	no
Control Capabilities:	2-D	0-D	1-D
Thrust:	yes	no	yes
Specific Impulse:	yes	no	no
Performance:			
Specific Impulse (sec):	340-460	max 320	340
Thrust Density (F/V):	low	high	low
Combustion Efficiency:	0.99	0.98	0.96
Unburned Residues:	low	low	high
Contribution to Vehicle Efficiency	high	low	high
Technology Maturity:	high	high	low
Ecological Impact: (Al-Cl-NOX emission)	low	high	low
Operability:			
Pre-Launch Operations:	complex	complex	simple
Hold-Down Mode:	yes	no	yes
Economics:			
Life Cycle Costs	high	high	low

Table 1.1. Comparison of the chemical rockets.

The lack of development of hybrids at large scales is their major disadvantage. The goal of most of the research programs is to scale up the available hybrid motors towards the levels imposed by mission requirements. In the scaling of hybrid motor to larger sizes, several problems areas have been identified. Foremost among them are: 1) motor instability (especially non-acoustic low frequency modes), 2) delayed transients in ignition, throttling and shut-down and 3) grain integrity during operation for multiport

grains. Since, the hybrid operates by establishing a macroscopic diffusion flame filling the entire grain length, the combustion and motor operating characteristics are intimately related not only to the grain configuration but also to the internal flow. A theory that predicts the burning rate for steady-state operation as a function of the geometry and thermochemistry of the propellants is available [6, 7, 8]. But the literature treating the transient operation of hybrid rockets is deficient. Furthermore, the effective and efficient usage of throttling capabilities of hybrids to fly thrust-tailored optimized trajectories requires a significant amount of understanding of transient combustion. We further believe that an understanding of transient phenomena in the motor is essential to explain the low frequency pressure oscillations observed in practice.

The major objective of this thesis is to study the transient characteristics of hybrid combustion as it relates to the first two problem areas mentioned above. Apart from the transients we will also study the steady-state regression rate behavior of cryogenic hybrid rockets [9] which have their solid propellant in a frozen state at a temperature below ambient.

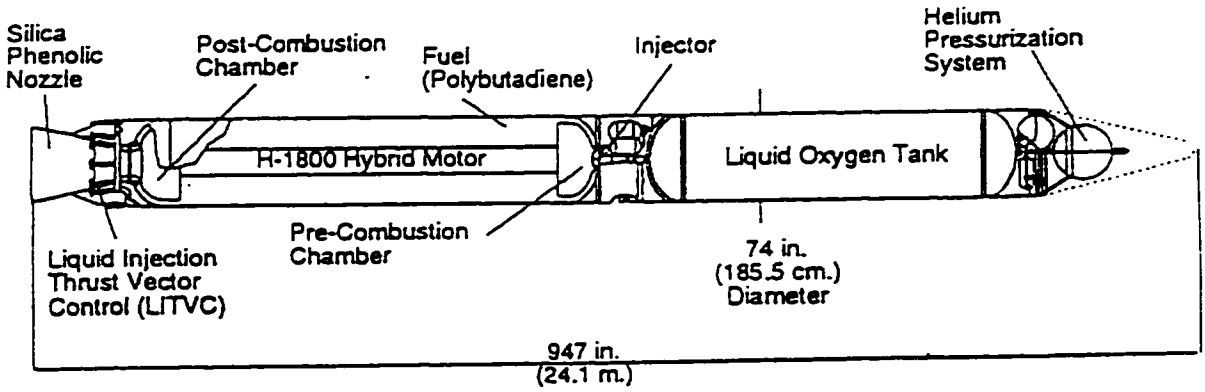

Figure 1.2. Schematic of the AMROC H-1800 multiport hybrid motor.

For a full description of the transients one has to consider the dynamic phenomena due to 1) dynamics of the feed system (i.e. liquid flow in the hydraulic lines), 2) vaporization of the liquid oxidizer droplets, 3) diffusion/transport dynamic processes in the boundary layer, 4) combustion mechanisms in the flame zone, 5) chamber gasdynamics and 6) thermal profile changes in the solid grain. Since our goal is to develop an understanding for the most fundamental phenomena occurring in the motor, in a significant portion this study, we will not consider the feed system dynamics and the liquid droplet

evaporation time lags. For that reason our treatment will be restricted to the gaseous oxidizer systems. However, the results of this study can easily be combined with a feed system model and an evaporation model to extend the application field to liquid oxidizer motors.

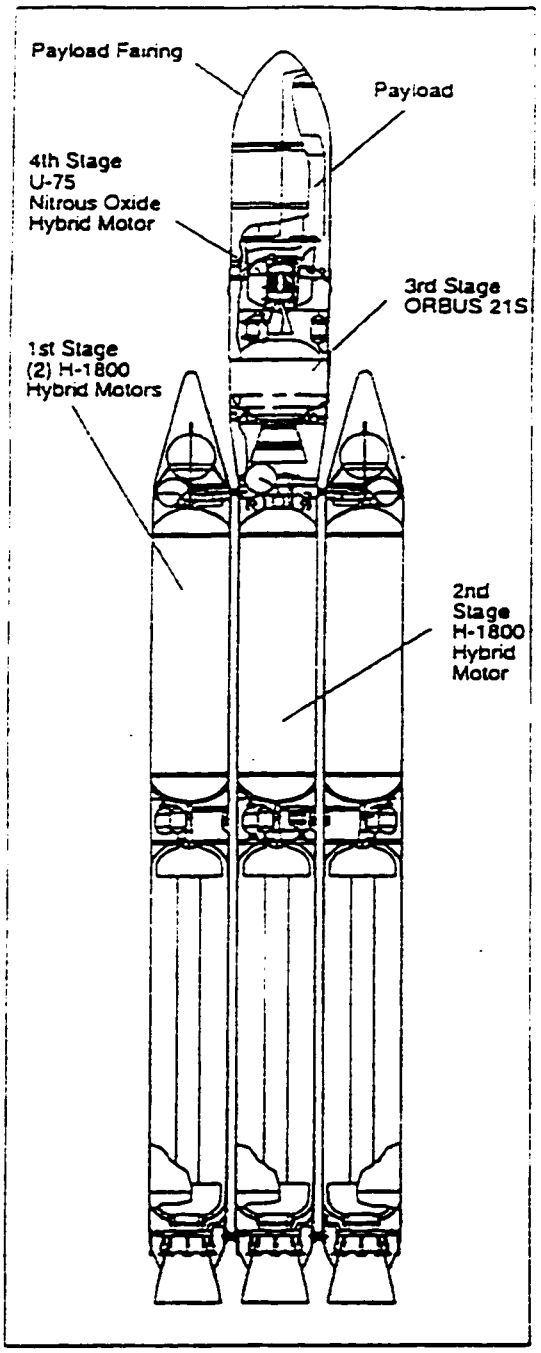

Figure 1.3. Schematic of AMROC's Aquila launch vehicle is shown.

Chapter 2 of this thesis is devoted to the description of the steady-state operation of hybrids, since it is essential for the understanding of transients. The derivation of the classical diffusion limited regression rate law will be summarized. Specifically, the treatment for the blocking factor will be reconsidered and some unrealistic assumptions made by Marxman for the derivation of an analytical expression will be relaxed. The chapter will be closed by a brief argument on the scaling issues of hybrid rockets.

In chapter 3 we give a discussion of the transients in hybrids such as ignition, throttling, instabilities and thrust termination. The transient events will be classified and briefly explained. The characteristics of the low frequency oscillations observed in hybrid tests along with various previous theories for the generation mechanisms of these instabilities will be discussed and criticized in detail.

In chapters 4, 5 and 6 we develop our transient hybrid model. In Chapter 4 we investigate the dynamic response of the fuel grain temperature profile to the changes in wall heat flux. We introduce the thermal lag model and develop numerical and analytical solutions techniques for the mathematical formulation of the model. In Chapter 5 we consider the dynamic response of the reacting boundary layer of the hybrid motor. We start with a quasi-steady argument and later introduce the concept of boundary layer delay in our model. Also in this chapter the thermal lag model and the combustion model are coupled to obtain the TC coupled system. The characteristics of the TC coupled system, such as the stability are investigated.

Finally in chapter 6 we develop an isothermal gasdynamic model that considers the port as a quasi-1D pipe and the pre and post-combustion chambers as zero dimensional volume elements. We conclude the transient modeling aspect of the thesis by integrating the gasdynamic model with the TC coupled system to find the overall response of a gaseous oxidizer hybrid motor with a stiff feed system.

Eventually we perform an investigation of the steady-state regression rate behavior of hybrid rockets that possess significantly thick melt layers on the fuel grain (in chapter 7). The primary application of theory is the cryogenic hybrid rockets that have been recently tested at the Edwards Airforce Base [9]. These experiments showed very high regression rates for the cryogenic motors compared to the classical hybrids. At these elevated regression rate levels the cryogenic motors possess thrust densities comparable with the

solid rocket motors. Thus one of the most important shortcoming of hybrids is eliminated with the cryogenic hybrid alternative.

We extend the classical hybrid theory for the possibility of entrainment mass transfer from the liquid film into the gas stream. We finally note that the liquid layer hybrid combustion theory developed in this study captures the classical hybrid operation as a limiting case.

Chapter 2

Steady-State Hybrid Combustion Theory

The understanding of the steady-state operation of hybrid rockets is essential for the development of any transient model for the motor. For that reason, in this chapter we will give a brief discussion of the existing steady-state theory of hybrid combustion. We will follow the classical approach which was developed in 1960's by Marxman and his colleagues. This classical hybrid theory is still the only widely accepted description of hybrid combustion in the hybrid rocket community.

In this chapter, other than the review of the classical theory, we will make a conceptual correction to the blocking factor expression derived by Marxman. This factor accounts for the reduction of the convective heat flux to the fuel surface due to injection of gasified fuel from the wall. We will conclude the chapter with the derivation of some scaling rules for hybrids which will later be used in the interpretation of hybrid motor instability test data.

2.1 Diffusion Limited Model

As indicated in the previous chapter most of the hybrid combustion reactions takes place in a relatively thin diffusion flame that covers the entire surface of the fuel grain. A detailed schematic of the hybrid reacting boundary layer with some feasible velocity, temperature and concentration profiles is shown in figure 2.1. This conceptual configuration of the hybrid boundary layer is confirmed by Schlieren pictures of a boundary layer developed by the oxygen flow over a burning slab of plexiglass [10]. The issue of practical importance is the determination of the mass flow generation rate (i.e. regression rate) in terms of the known properties of the system such as the chamber

pressure, external flow mass flux and thermochemical properties of the propellants. Note that during the steady-state operation the regression rate is, in some sense, the flame propagation speed in the laboratory coordinates. Thus, from that point of view, we are interested in finding the flame speed.

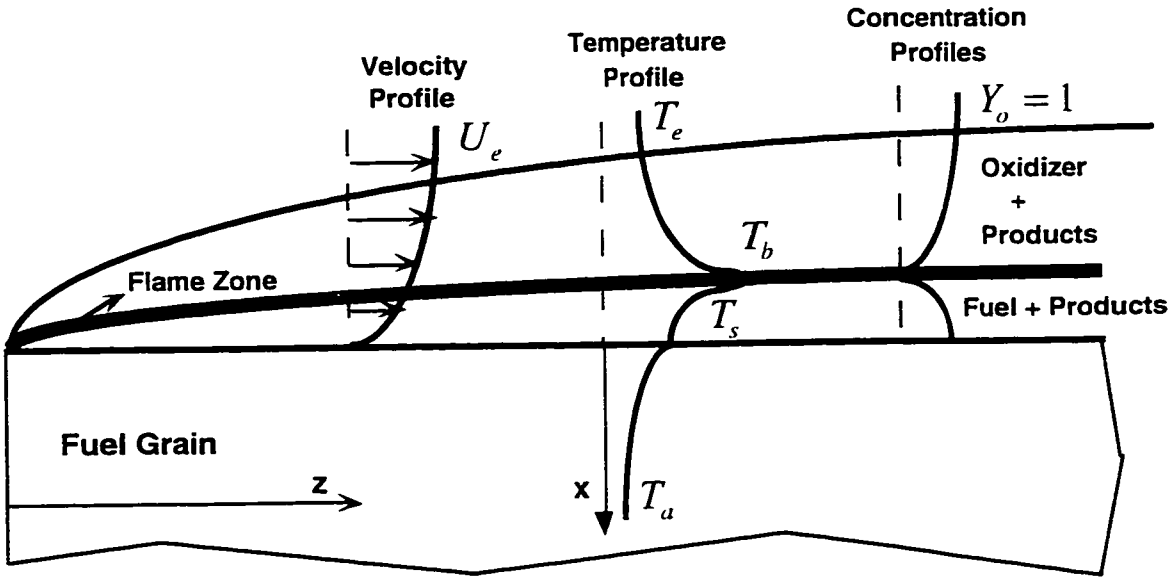

Figure 2.1. The schematic of the hybrid boundary layer.

The most successful theory for determination of the regression rate law for hybrids was developed by Marxman *et al* [6, 7, 8, 11] in the early 1960's. This theory which is also called the 'Diffusion Limited Model' is based on the following assumptions.

1) All of the physical and chemical processes are steady-state.

2) The fuel grain geometry is represented as a flat plate.

3) No exothermic reactions in the solid grain or at the surface are allowed. This a good assumption for hybrids which posses a fuel rich diffusion flame. It is conceivable that all the oxidizer will be depleted at the flame. As a consequence no oxidizer is expected to exist beneath the flame to attack the fuel surface.

4) Oxidizer enters the port as a uniform gas. Its assumed that all the liquid oxidizer is evaporated in the pre-combustion chamber.

5) Both Lewis and Prandtl numbers are assumed to be unity. This assumption can be relaxed to give explicit results that are now also dependent on the Lewis and Prandtl numbers [12].

6) No heat transfer to the ambient air through the walls of the rocket is allowed. Since the size of the thermal layer thickness in the hybrid fuel grain is very small compared to the web thickness, this is an excellent assumption.

7) All kinetic effects are neglected compared to the transport processes. In other words the characteristic times associated with all chemical reactions (combustion reactions in the gas phase or pyrolysis reactions in the solid) are very small compared to the characteristic times for the diffusion/transport processes in the boundary layer. It is this assumption that gives its name to this classical theory.

8) As a consequence of the previous assumption the flame zone can be assumed to be infinitely thin compared to the boundary layer thickness.

9) The boundary layer is turbulent all over the length of the fuel grain. It is shown experimentally that this is a good assumption for typical hybrid operating regimes. This fact is easy to believe, since the strong blowing of the fuel from the surface destabilizes the boundary layer, decreasing the critical Reynolds number significantly.

10) The properties of the gas across the boundary layer is assumed to be constant. This strong assumption can be relaxed with the application of the reference enthalpy technique [8, 12]. It is known that the variation of the properties across the boundary layer does not change the qualitative nature of the solution.

Under the light of the preceding assumptions, the burning law for the hybrids can be developed. We start with the energy balance at the surface which can be expressed as

$$\dot{Q}_w = \dot{m}_f h_v = \rho_f \dot{r} h_v = (\rho v)_w h_v . \tag{2.1}$$

Here $\dot{Q}_w$ is the total heat flux to the wall and h_v is the effective heat of gasification. The effective heat of gasification is the energy required per unit mass to obtain the gas state

at the wall from the solid state of the fuel at the ambient temperature. In general it involves the energy required for the heating of the solid fuel, the heat of melting and evaporation and the heat of the endothermic reactions associated with the degradation of the polymer (if the fuel is in the polymeric form).

As a further simplification we will consider a purely convective system for which the wall heat flux has only the convective term. This assumption will later be relaxed to study the influence of radiation on the regression rate. For the purely convective case the heat flux can be written in terms of the temperature gradient at the surface.

$$\dot{Q}_w = \dot{Q}_c = -\left(\frac{k}{c_p}\frac{\partial h}{\partial y}\right)_w \tag{2.2}$$

At this stage it is useful to define a Stanton number as $C_H = \dot{Q}_c/\rho_b u_b \Delta h$ where $\Delta h = h_b - h_w$ is the enthalpy difference between the surface and the flame. Here ρ_b and u_b are the density and velocity at the flame, respectively. After combining this definition with the energy balance at the surface one can obtain

$$\rho_f \dot{r} = \frac{\dot{Q}_c}{h_v} = C_H \rho_b u_b \frac{\Delta h}{h_v}. \tag{2.3}$$

This expression for the regression rate involves the Stanton number, a parameter which is extremely difficult to measure in a hybrid boundary layer. For that reason, it is better to express the Stanton number in terms of the skin friction coefficient with use of the concept of Reynolds analogy. It is reported in the literature that for wall turbulent flows the Reynolds analogy holds to a very good degree due to the existence of similar transport mechanisms for momentum and energy in the log region where most of the variations occur [13]. Boundary layers encountered in hybrid motor configurations are significantly different from the classical incompressible turbulent boundary layers over a flat plate which have been extensively investigated. As mentioned previously this is mainly due to the presence of gas phase chemical reactions and strong blowing generated by the gasification of the solid fuel. Despite these complications we assume that, as many early researchers [7, 14], the Reynolds analogy is applicable also to the turbulent hybrid boundary layer. With the use of the analogy, the wall heat flux can be related to the skin friction as

$$\frac{\dot{Q}_w}{\Delta h} = \frac{\tau_w}{u_b}. \tag{2.4}$$

After the use of the definition of the skin friction coefficient (equation 2.5), one can obtain the formula (equation 2.6) for the Stanton number in terms of the skin friction coefficient.

$$\tau_w = 0.5 C_f \rho_e u_e^2 \tag{2.5}$$

$$C_H = 0.5 C_f \frac{\rho_e u_e^2}{\rho_b u_b^2} \tag{2.6}$$

Since we are mainly interested in the modification of the heat transfer coefficient by blowing, it is convenient to rearrange equation 2.1 in the form of ratios as in equation 2.2 in which C_{f_o} and C_{H_o} are the coefficients for a boundary layer with no blowing.

$$F_B \equiv \frac{C_H}{C_{H_o}} = \frac{C_f}{C_{f_o}} \tag{2.7}$$

Substitution of this equation in the previous regression rate expression yields

$$\dot{r} = \frac{C_{f_o} \rho_e u_e B}{2\rho_f} \frac{C_f}{C_{f_o}}. \tag{2.8}$$

where B is the "Blowing parameter" defined as

$$B \equiv \frac{u_e}{u_b} \frac{\Delta h}{h_v} = \frac{2(\rho v)_w}{\rho_e u_e C_f} \tag{2.9}$$

Several semi-empirical relations for the skin friction coefficient for standard turbulent boundary layers with no blowing or reactions are reported extensively in the literature. The form that is commonly used for hybrid boundary layers is [15]

$$C_{f0} = 0.06\,\mathrm{Re}_z^{-0.2} \qquad \text{where} \qquad \mathrm{Re}_z = \frac{\rho_e u_e z}{\mu_e}. \tag{2.10}$$

This empirical formula can be substituted in equation 2.8 to obtain the regression rate

$$\dot{r} = 0.03\frac{\rho_e}{\rho_f} u_e\,\mathrm{Re}_z^{-0.2}\left(\frac{C_f}{C_{f0}}\right)B. \tag{2.11}$$

This form of the regression rate expression involves the ratio C_f/C_{f0} which is a correction for blowing (blocking effect) that has to be determined in terms of the blowing parameter. This will be studied in detail in the next section.

2.2 Blowing Correction

Many researchers in the past, using various simplifying approximations, made estimations for the blowing factor defined by equation 2.2 [7, 14, 16]. One of the early treatments is Marxman's work, which is the most widely accepted theory in the field. An other formulation is introduced by Legelle who criticized some of Marxman's assumptions on eddy diffusivity and developed his own formulation. However, as we will show later in this section, both treatments have inconsistencies with the experimental resuits. In this section, we will derive the blowing factor expression with first Marxman's and then Legelle's assumptions. Later, we will investigate another case with a different assumption on the eddy diffusivity that yields more reasonable results.

In any case, our primary goal is to drive an explicit relation for the blowing factor in terms of the known properties of the problem, such as the blowing parameter, B, which is defined by equation 2.9. We start with the assumptions that u and $\partial u/\partial z$ are small, which probably hold only in some small region next to the wall [14]. As a result of this approximation the continuity equation reduces to $\rho v = (\rho v)_w$, whereas the momentum equation becomes

$$\tau = (\mu + \rho\varepsilon)\frac{du}{dz} = \tau_w + (\rho v)_w u \tag{2.12}$$

Here ε is the turbulent momentum diffusivity which, in general, is a function of local flow properties. With use of the definitions for the blowing parameter and skin friction coefficient, the momentum equation can be expressed as

$$\tau = (\mu + \rho\varepsilon)\frac{du}{dy} = \tau_w\left(1 + B\frac{u}{u_e}\right). \tag{2.13}$$

Note that we used the standard definitions for the blowing parameter and the skin friction coefficient, defined by equations 2.9 and 2.5, respectively.

Eventually in terms of non-dimensional velocity, $\phi = u/u_e$ and traverse distance $\eta = y/\delta$, we obtain the non-dimensional form of the momentum equation.

$$\frac{d\phi}{d\eta} = \frac{1}{2}C_f \,\mathrm{Re}_\delta \frac{(1 + B\phi)}{(1 + \varepsilon\rho/\mu)} \tag{2.14}$$

Note that Reynolds number is with respect to the boundary layer thickness and it is defined in the standard form as

$$\mathrm{Re}_\delta = \frac{\rho u_e \delta}{\mu}. \tag{2.15}$$

We use equation 2.14 to determine the velocity profile shape which will later be needed in the estimation of the blowing factor. We start with the assumption on the velocity gradient first introduced by Marxman [7]

$$\frac{d\phi}{d\eta} = f(\eta, B)(1 + B\phi). \tag{2.16}$$

In the limit $B \to 0$, the velocity profile has to approach one of the standard forms for turbulent boundary layers with no blowing. For the Reynolds number range of practical hybrid motors ($10^5 < \mathrm{Re}_x < 10^7$) an acceptable approximation is a power law profile [15] such as

$$\phi|_{B=0} = \eta^n \tag{2.17}$$

Thus the velocity gradient is $d\phi/d\eta|_{B=0} = n\eta^{n-1}$. We further follow Marxman and assume that

$$\frac{d\phi}{d\eta} = n\eta^{n-1}A(B)(1+B\phi). \tag{2.18}$$

Although equation 2.18 should apply only in a small region next to the wall, following Marxman and Lee, we will integrate it from the wall to the boundary layer edge. The justification for this approach comes from the fact that, the velocity profile of a turbulent boundary layer, even with blowing, is very steep close to the wall. Thus the contribution of this region near the wall to the integral is dominant. In the integration process Marxman further assumed $B\phi = B\eta^n$ and obtained the velocity profile

$$\phi = \frac{\eta^n(1+B\eta^n/2)}{1+B/2} \tag{2.19}$$

Marxman's last assumption is a crude one for strong blowing and more over it is not necessary to obtain an analytical expression for the velocity profile. Without any further assumptions, Equation 2.18 can be integrated simply by separation of variables. After the application of the boundary conditions $\phi(0) = 0$ and $\phi(1) = 1$, one can determine $A(B)$ and obtain the following explicit formula for the velocity profile.

$$\phi = \frac{1}{B}\left[(1+B)^{\eta^n} - 1\right] \tag{2.20}$$

Note that in the limit as B tends to zero this formula gives the correct no blowing profile η^n, as expected. Legelle [14] suggested the following relation as a good approximation to the exact velocity profile given by 2.20.

$$\phi = \eta^{\alpha} \qquad \text{where} \qquad \alpha = n(1+B)\log(1+B)/B \tag{2.21}$$

The non-dimensional velocity profiles calculated with equations 2.17, 2.19, 2.20 and 2.21 are plotted in figure 2.2 for n=1/7 and four values of the blowing parameter, 1, 10, 50 and 100. Note that B=10 is a typical value for hybrid rocket applications. As shown in the figure Marxman's result is appreciably different from the exact profile whereas Legelle's profile is in good agreement with the exact form.

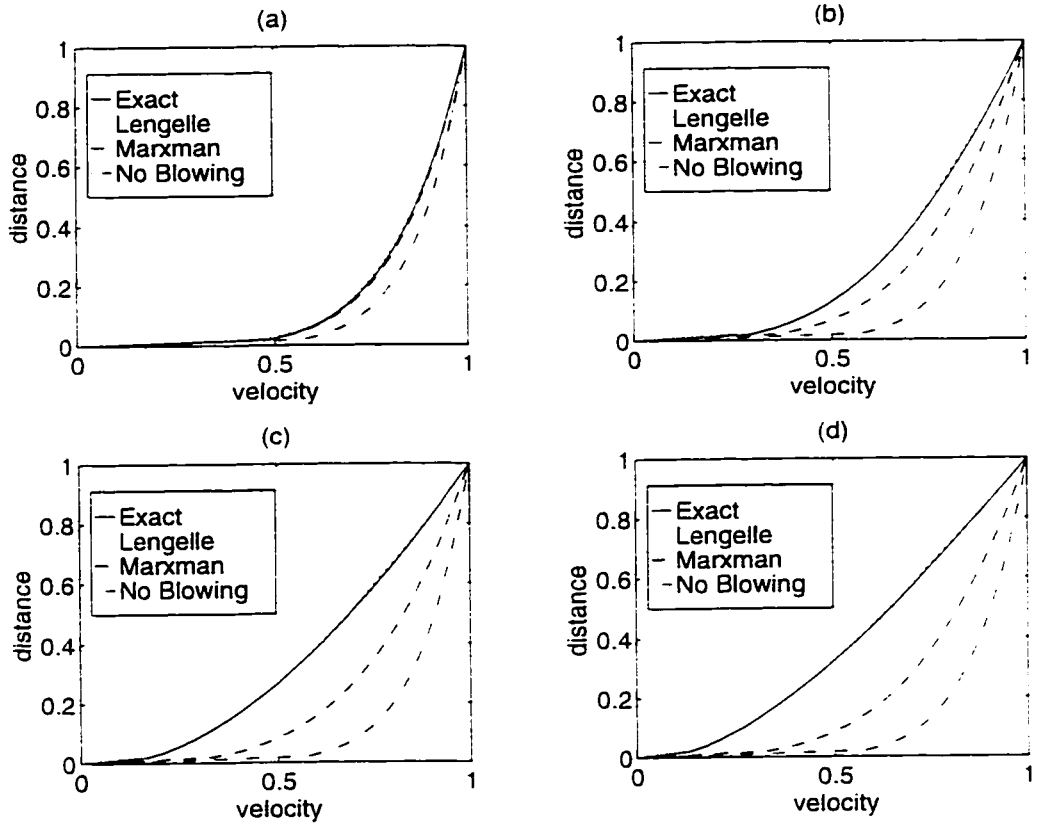

Figure 2.2. Effect of blowing on the non-dimensional velocity profiles for various models. (a) B=1, (b) B=10, (c) B=50, (d) B=100.

After the determination of boundary layer velocity profiles under various assumptions, we intend to investigate the effect of blowing on the skin friction coefficient. A reasonable start is the integration of the non-dimensional momentum equation (equation 2.6) to obtain the skin friction coefficient in terms of the blowing parameter and the thickness of the boundary layer. First we have to assume a functional form for the dependency of the turbulent diffusivity on the mean properties of the flow. In turbulent boundary layers with sufficiently high Reynolds numbers and without blowing, a classical model for the turbulent diffusivity is the Prandtl's mixing length hypothesis which relates the diffusivity to the local velocity gradient as in equation 2.22.

$$\varepsilon\rho/\mu = c'\,\mathrm{Re}_\delta\,\eta^2\frac{d\phi}{d\eta} \tag{2.22}$$

At this point, we assume that the mixing length hypothesis is also valid for boundary layers with blowing. Initially, we follow Marxman's treatment. In his derivation, Marxman assumed that 1) the boundary layer velocity profile with blowing is not far different from the profile with no blowing, namely $\phi \approx \eta^n$, 2) since the exponent n in a turbulent boundary layer is a small number compared to unity, the eddy viscosity can be approximated to vary linearly with the position, namely $\varepsilon \propto \eta^2\, d\phi/d\eta = n\eta^{1-n} \approx n\eta$ or $\varepsilon = c''\eta$ where $c'' = nc'$ is constant.

After the substitution of this eddy viscosity approximation in equation 2.14, we obtain the differential equation

$$\frac{d\phi}{1+B\phi} = \frac{C_f}{2}\mathrm{Re}_\delta\frac{d\eta}{1+\mathrm{Re}_\delta c''\eta} \tag{2.23}$$

Equation 2.23 can now be integrated from the wall to the boundary layer edge with the boundary conditions, $\phi(0) = 0$ and $\phi(1) = 1$.

$$\frac{C_f}{2} = \frac{c''}{\ln(1+\mathrm{Re}_\delta c'')}\frac{\ln(1+B)}{B} = g(\mathrm{Re}_\delta)\frac{\ln(1+B)}{B} \tag{2.24}$$

Next, Marxman argues that in this expression $g(\mathrm{Re}_\delta)$ represents the effect of boundary layer thickness on the skin friction coefficient and if there is no blowing $g(\mathrm{Re}_\delta) = C_{f_o}/2$. Whereas for the skin friction coefficient without blowing, a standard form such as the one suggested by Schlichting [15], can be used.

$$\frac{C_f}{2} = 0.0225\,\mathrm{Re}_\delta^{-0.25}\left[\frac{\ln(1+B)}{B}\right] \tag{2.25}$$

One would expect that Marman's expression for the skin friction (equation 2.25) would converge to $C_{f_o}/2$ in the limit of zero blowing. To check on the consistency of Marxman's analysis we plot the result of the analysis $g(\mathrm{Re}_\delta)$ and the empirical expression

$0.0225\,\mathrm{Re}_\delta^{-0.25}$ as a function of Re_τ in figure 2.3. One can immediately see from the figure that Marxman's result is off by almost a factor of two in all the Re_τ range of interest. We believe that is due to his second assumption on the form of the eddy diffusivity. This result shows that the skin friction coefficient is very sensitive to the exponent in the eddy diffusivity expression.

Legelle pointed out that Marxman's first assumption on the eddy diffusivity is not a valid one for large blowing parameters such as the range observed in hybrids [14]. This fact can be easily seen from figure 2.2 which shows that the blowing significantly alters both the velocity profile and its derivative. The velocity profile form suggested by Legelle represents the exact form fairly good even for large blowing parameters. Also the exponent of the Legelle's profile is quite different from n for strong blowing and it is, in general, not very small compared to unity. Thus Marxman's second approximation is also not likely to be valid for hybrid applications.

Next, we redrive the blowing correction with use of the Legelle's profile. We first combine equations 2.21 and 2.22 and obtain

$$\varepsilon\rho/\mu = c'\alpha\,\mathrm{Re}_\delta\,\eta^{1+\alpha}. \tag{2.26}$$

We can substitute this eddy diffusivity expression in equation 2.14 to get the differential form of momentum equation

$$\frac{d\phi}{1+B\phi} = \frac{C_f}{2}\mathrm{Re}_\delta\frac{d\eta}{1+\mathrm{Re}_\delta c'\alpha\eta^{1+\alpha}} \tag{2.27}$$

Upon the transformation $z = \eta^{1+\alpha}$, this can easily be integrated by separation of variables.

$$\frac{C_f}{2} = c'\alpha(\alpha+1)\left[\frac{B-\ln(1+B)}{B^2}\right]\frac{1}{\ln\left(1+\mathrm{Re}_\delta c'\alpha\right)} \tag{2.28}$$

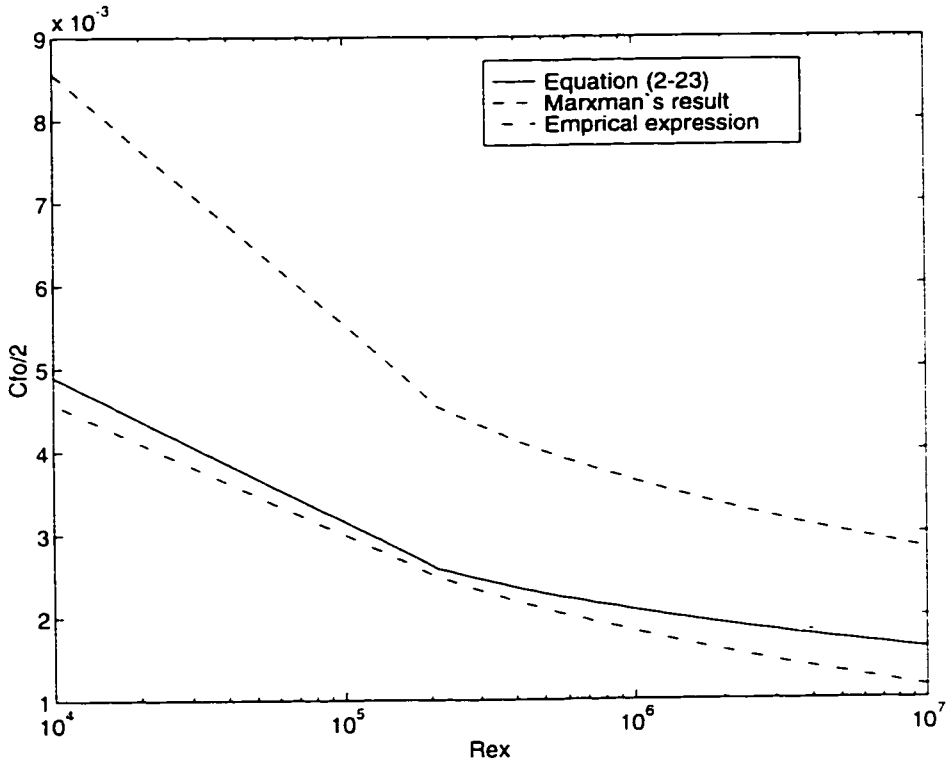

Figure 2.3. Variation of no blowing skin friction coefficient with the length Reynolds number.

After the substitution of the definition of α, we obtain equation 2.29 for the skin friction.

$$\frac{C_f}{2} = c'\alpha(\alpha+1)\bar{f}(B)\frac{1}{\ln(1+\mathrm{Re}_\delta c'n)+h(B)} \tag{2.29}$$

where the blowing functions are defined as

$$\bar{f}(B) = \frac{B-\ln(1+B)}{B^2} \qquad \text{and} \qquad h(B) = \frac{(1+B)\ln(1+B)}{B}. \tag{2.30}$$

In the zero blowing limit equation 2.29 yields

$$\frac{C_{f_o}}{2} = \frac{c'n(n+1)}{2\ln(1+\mathrm{Re}_\delta c'n)} \tag{2.31}$$

Equation 2.31 can be used to express equation 2.29 in a more convenient form.

$$\frac{C_f}{2} = \bar{f}(B)\frac{1}{\frac{n(n+1)}{2}\frac{2}{C_{f_o}} + \frac{h(B)}{c'}} = \bar{f}(B)\frac{1}{\frac{n(n+1)}{2}\frac{\mathrm{Re}_\delta^{0.25}}{0.0225} + \frac{h(B)}{c'}} \tag{2.32}$$

Figure 2.3 also shows the behavior of the skin friction coefficient without blowing according to equation 2.23. Unlike Marxman's expression, equation 2.32 yields consistent results with the empirical formula. This indicates that, at least for the no blowing case, Marxman's assumptions are too restrictive to estimate the absolute value of the skin friction coefficient.

In the preceding paragraphs we derived expressions for the skin friction coefficients in terms of the blowing parameter and the boundary layer thickness for two different assumed forms of eddy diffusivity. For relatively large blowing rates, blowing increases the boundary layer thickness significantly. Thus, the determination of the blowing factor as a function of blowing parameter alone requires an estimate for the boundary layer thickness. Whereas the thickness can be related to the skin friction through the integral momentum equation (see appendix A for the derivation).

$$\frac{d\delta}{dz} = \frac{(1+B)}{I}\frac{C_f}{2} \qquad \text{where} \qquad I = \int_0^1 \phi(\phi - 1)d\eta. \tag{2.33}$$

We integrate equation 2.33 for δ for two cases of interest: 1) with Marxman's expression of the skin friction coefficient (equation 2.24), 2) C_f expression derived based on the Legelle's profile (equation 2.32). The performation of the integration for case 1 yields the following dependency of the thickness on the blowing as first derived by Marxman.

$$\frac{\delta}{z} = \mathrm{Re}_z^{-0.2}\left[\frac{(1+B)\ln(1+B)}{B}\right]^{0.8}\left[\frac{0.02813}{I}\right]^{0.8} \tag{2.34}$$

Equation 2.34 can be coupled with equation 2.25 to obtain Marxman's final result for the blowing factor.

$$\frac{C_f}{C_{f_o}} = \left[\frac{\ln(1+B)}{B}\right]^{0.8}\left[\frac{I/I_o}{(1+B)}\right]^{0.2} \tag{2.35}$$

The integration of equation 2.33 for case 2 (Legelle) yields the following relation for the thickness.

$$\frac{\delta}{z} = \frac{(1+B)\bar{f}(B)}{I}\frac{1}{\frac{n(n+1)\mathrm{Re}_\delta^{0.25}}{0.0563} + \frac{h(B)}{c'}} \tag{2.36}$$

Although the boundary layer thickness can not be solved explicitly from this equation, it can be calculated numerically fairly easily. For a given Re_z and after the selection of n and c', equations 2.32 and 2.36 can be used to determine the blowing factor.

Figure 2.4 shows the blowing correction estimated by that procedure and by the evaluation of Marxman's expression (equation 2.35). Also some experimental results as reported by Marxman are included in the figure. Marxman's method is in very good agreement with the experimental results whereas the blowing correction estimated by Legelle's more exact profile overestimates the blowing factor, C_f/C_{f_o}, significantly. As a conclusion Marxman's result is inconsistent with the empirical zero blowing skin friction coefficient, but successfully estimates the variation of the relative skin friction with blowing. On the other hand, for case 2 in which we used Legelle's profile, we recover the correct result as blowing limits to zero, but inaccurate behavior for the blowing factor. This fact raises questions on the validity of the Prandtl's mixing length hypothesis for a boundary layer with blowing. We now attempt to develop a refined treatment that will yield the correct result both for the blowing factor and also for the skin friction value at the limit, $B \to 0$.

We start with the assumption that the blowing does not alter the eddy viscosity significantly. In this case we can write

$$\frac{\rho\varepsilon}{\mu} = \mathrm{Re}_\delta c' n \eta^{n+1} . \tag{2.37}$$

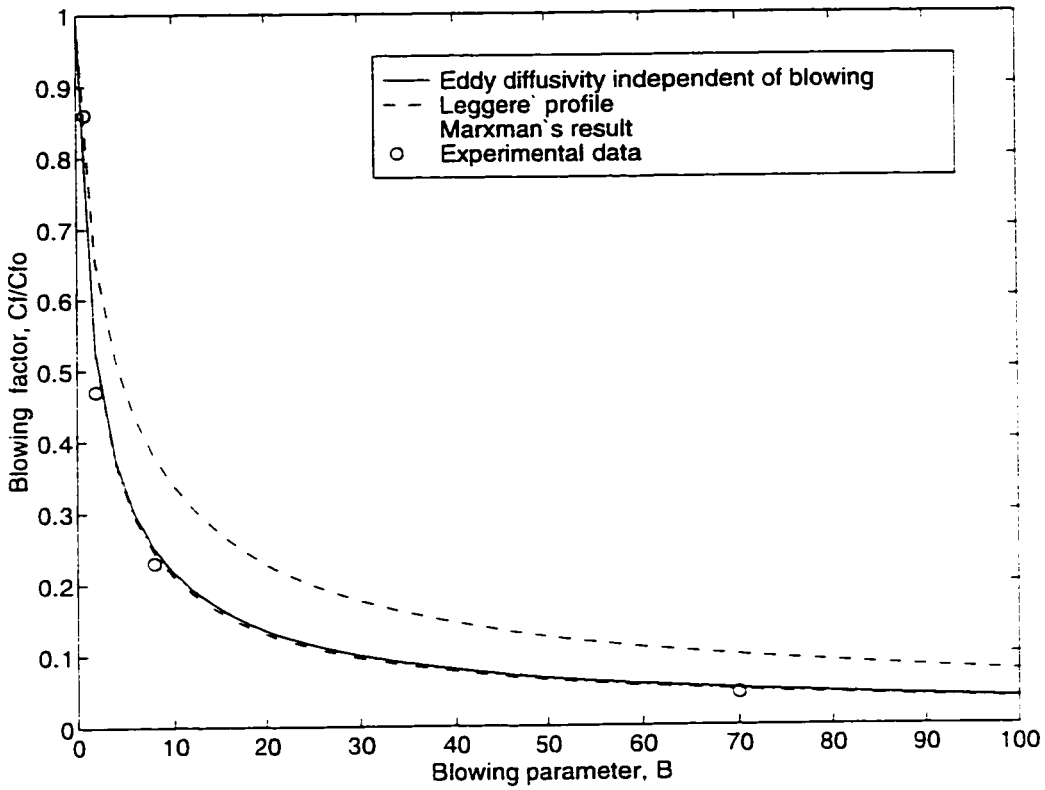

Figure 2.4. Variation of the blowing factor with the blowing parameter for various models.

We combine this with equation 2.14 to obtain

$$\frac{d\phi}{1+B\phi} = \frac{C_f}{2}\frac{\mathrm{Re}_\delta}{(n+1)\eta^n}\frac{dz}{1+\mathrm{Re}_\delta c' n z}. \tag{2.38}$$

where $z = \eta^{n-1}$. The quantity in this equation, η^n, can be solved from the exact velocity profile as

$$\eta^n = \frac{\ln(1+B\phi)}{\ln(1+B)} \tag{2.39}$$

After the substitution of η^n equation 2.38 takes the form

$$\frac{(1+B\phi)d\phi}{(1+B\phi)\ln(1+B\phi)} = \frac{C_f}{2}\frac{\mathrm{Re}_\delta}{(n+1)}\frac{dz}{1+\mathrm{Re}_\delta c' n z}. \tag{2.40}$$

Integration from the wall to boundary layer edge yields.

$$\frac{C_f}{2} = \frac{\ln(1+B)}{B} \frac{c'n(n+1)}{2\ln(1+\mathrm{Re}_\delta c'n)} \tag{2.41}$$

In the limit of $B \to 0$ equation 2.41 becomes equation 2.31, since Legelle's profile is identical to the zero blowing profile in this limit. Thus this last method, like Legelle's method, yields the correct skin friction coefficient with no blowing.

After the application of the preceding procedure, the blowing correction turns out to be the same as Marxman's expression given by equation 2.35. Note that for the last treatment the momentum integral, I, is slightly different due to the use of the exact velocity profile. The blowing correction for this last case is also shown in figure 2.4. The result is in close agreement with Marxman's prediction and experimental data. The consistency of the result supports the assumption on the weak dependence of the eddy diffusivity on the blowing parameter.

For practical purposes it is convenient to express the blowing factor in a simple exponent form that approximates the blowing factor given by equation 2.41 for a given range of blowing parameter. A suitable form that is often encountered in the literature is

$$\frac{C_f}{C_{f_o}} \equiv qB^{-k}. \tag{2.42}$$

Marxman [7] suggested $q = 1.2$ and $k = 0.77$ for the range of $5 < B < 100$ which covers hybrid applications. Although these values are used extensively in hybrid research up to date, it is shown by Altman [11] that the selection of values $q = 1.0$ and $k = 0.68$ gives a better fit in the proposed range of blowing parameters.

2.3 Regression Rate Expression

Now we are in a position to write a practically more useful expression for the regression rate after the substitution of the approximate blowing correction (equation 2.42) in equation 2.11.

$$\dot{r}(z) = 0.03\frac{q}{\rho_f} B^{(1-k)} \rho_e u_e \mathrm{Re}_z^{-0.2} \tag{2.43}$$

In practice it is more convenient to relate the regression rate to the local mass flux, G and position rather than the Reynolds number.

$$\dot{r}(z) = 0.03\frac{q\nu^{0.2}}{\rho_f} B^{(1-k)} G^{0.8} z^{-0.2} \tag{2.44}$$

The only unknown in this regression rate expression is the blowing parameter. The determination of the blowing parameter requires the solution of the gas phase field equations with the regression rate equation as one of the boundary conditions. Fortunately this extremely difficult problem does not have to be solved in most hybrid rocket applications. Marxman obtained an approximate solution using the mixing length concept and showed that the blowing parameter does not change significantly with the axial distance for motors with length over the hydraulic diameter ratios smaller than 25 [7, 17, 18]. For that reason B can be treated as a constant for a given propellant combination. Moreover even if the blowing parameter is changing moderately, its effect on the regression rate is small, since it is raised to an exponent of $1-k$ which turns out to be small number. This fact can be regarded as the fundamental reason for the success of the diffusion limited theory.

Its important to realize that the blowing parameter plays a dual role during the steady-state operation of the motor (equation 2.9): 1) It is a thermochemical property of the selected propellants. 2) It is also an aerodynamic property, namely a similarity parameter of the boundary layer. This connecting feature of the blowing parameter disappears during unsteady operation. This fact will be discussed in detail in chapter 5 of this thesis.

Under the light of the preceding discussions the local regression rate equation for a purely convective system can be simplified to

$$\dot{r}(z) = AG^{0.8} z^{-0.2} \ . \tag{2.45}$$

Here A can be considered as a constant after the selection of the propellants.

It is illustrative to mention typical values of the boundary layer combustion parameters of hybrids. The blowing parameter is generally in the range of 7-15. Unlike laminar diffusion flames the hybrid boundary layer combustion does not take place at the stoichiometric mixture. It is significantly fuel rich [8, 19]. The turbulent diffusion flame which covers almost 10 % of the boundary layer thickness is located 15-20% of the thickness away from the wall. The flame temperature is significantly less then the adiabatic flame temperature at the stoichiometric ratio. The wall temperature ranges from 600 K to 1200 K for most of the polymeric fuels used in applications.

2.4 Pressure Effect

The regression rate law predicted by the diffusion limited model for hybrids, unlike the solid rockets, is independent of the chamber pressure. According to the equation 2.45 the regression rate of a hybrid is mainly a function of the oxidizer mass flux. However, it is reported in the literature that this prediction is consistent with the experimental findings only for an intermediate range of the mass fluxes. Namely if the mass flux is too low or too high the regression rate of the hybrid shows same pressure dependence [11, 20, 21, 22]. A schematic of the typical behavior of the hybrid regression rate to the variations in the oxidizer mass flux and pressure is shown in figure 2.5.

The physical reasons for the deviation from the diffusion limited model at two extremes are different. At low mass fluxes the convective heat transfer is no longer large compared to the radiative heat transfer. In that regime the purely convective heat transfer assumption fails and the radiative transfer must also be included in the total wall heat flux. A simple model for the radiation is proposed by Marxman *et al* [8]. The model assumes the fuel grain as a gray body and the flame zone as a radiative continuum. According to the model radiative heat flux to the wall can be written as

$$\dot{Q}_r = \sigma \varepsilon_w \left(\varepsilon_g T_r^4 - T_w^4 \right). \tag{2.46}$$

Here ε_w is the absorptivity of the wall, ε_g is the emmisivity of the radiative continuum and T_r is the effective radiation temperature of the gas. Assuming a one dimensional emitting gas, the emmisivity of the continium can be written as

$$\varepsilon_g = 1 - e^{-\alpha_r N z} = F(P). \tag{2.47}$$

In this expression, N is the number density of the emitting particles and z is the optical path length. The parameters α_r and T_r are required to be determined empirically for a specified system. In absence of the metal additives in the fuel grain the radiation is emitted only from the hot gas molecules. In this case the number density of the particles can be replaced by the chamber pressure making the regression rate pressure dependent. Also note that the emmisivity of the gases depends explicitly on the scale of the motor. The practical significance of that is, in larger motors the contribution of radiation is likely to be more significant.

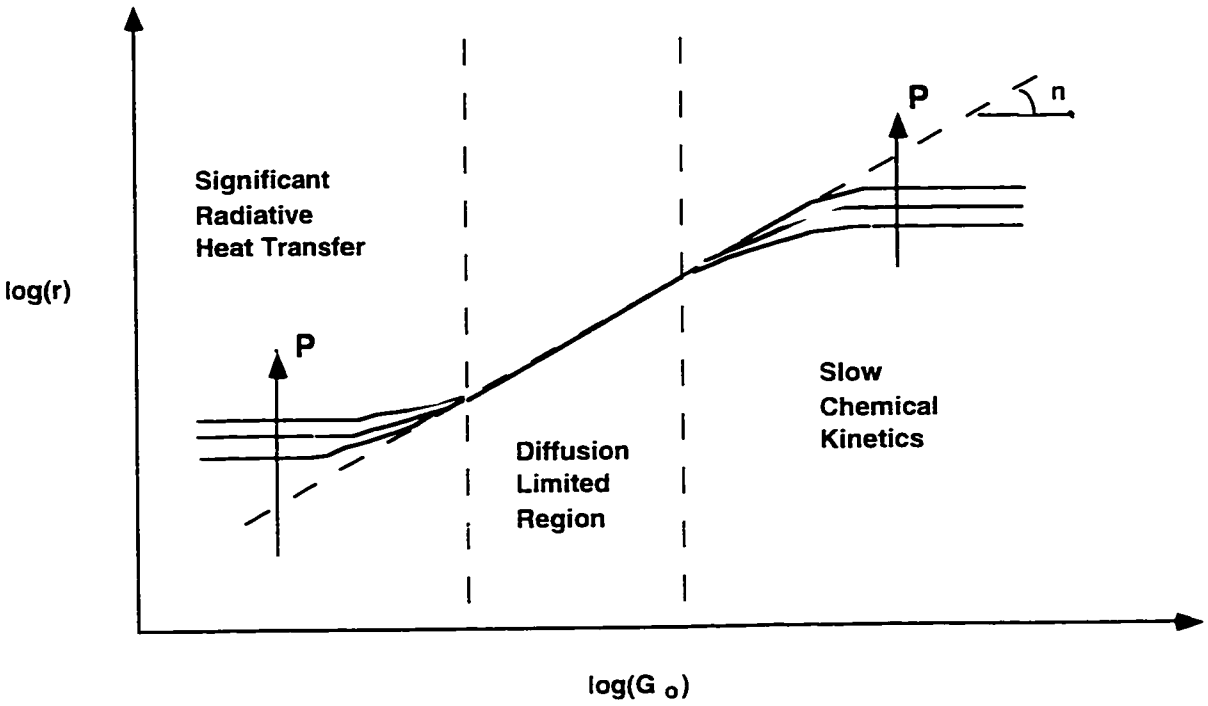

Figure 2.5. Illustration of the chamber pressure effect on the regression rate for hybrids.

The contributions of the radiative and convective heat transfers on the regression rate is not simply additive. This is due to the blowing effect. For example, an increase in radiative heat transfer increases the regression rate but the increased regression rate decreases the convective heat transfer due to increased blocking. However a formula, equation 2.48, that takes account of the blowing effect can easily be developed [12].

$$\dot{r} = \frac{\dot{Q}_c}{\rho_f h_v}\left[e^{-Q_r/Q_c} + \frac{\dot{Q}_r}{\dot{Q}_c}\right]. \tag{2.48}$$

If the radiative contribution to the total wall heat flux is small, than the following formula for the regression rate is a fairly good approximation .

$$\dot{r}(z) = AG^{0.8}z^{-0.2} + \frac{\dot{Q}_r}{\rho_f h_v} \tag{2.49}$$

It is fair to say that in most hybrid applications with fuels with no metal additives the radiative contribution on the regression rate is negligible.

At the other extreme of very high mass fluxes the boundary layer transport times become comparably large with respect to the reactions times in the gas phase, giving a pressure dependent operation through the kinetic effects. Note that in both of the pressure dependent regions, an increase in pressure enhances the regression rate.

2.5 Scaling Laws for Hybrids

In practice the regression rate data from the motor tests is in the space time averaged form. For that reason very occasionally the hybrid regression rate law is expressed in the following averaged formula [11, 20, 23, 24]

$$\dot{r} = aG_o^n L^m . \tag{2.50}$$

In this formula G_o is the mean oxidizer mass flux during the run and L is the length of the fuel grain. The coefficients a, n and m are determined empirically as a result of curve fitting to the experimental data. For classical hybrids the mass flux exponent is in the range of 0.5 to 0.8 whereas the length exponent is, in general, a much smaller value.

It is instructive to derive this averaged form the local regression rate expression given in section 2.3. Expression 2.45 for the local regression rate can be combined with the mass balance considerations in the port to determine the local mass flux through the port

$$G = \left[G_o^{0.2} + \frac{\alpha}{2} z^{0.8} \right]^5 \tag{2.51}$$

where $\alpha = 4\rho_f A/D$.

Next with use of the local mass flux information we take the average of the local regression rate expression over the length of the fuel grain.

$$\bar{r} = \frac{1}{L}\int_0^L a\left[G_o^{0.2} + \frac{\alpha}{2} z^{0.8} \right]^4 z^{-0.2} dz$$

This integral yields.

$$\bar{r} = aG_o^{0.8} L^{-0.2}\left(1.25 + 2.5\alpha + 2.5\alpha^2 + 1.25\alpha^3 + 0.25\alpha^4\right) = aG_o^{0.8} L^{-0.2} f(\alpha) \tag{2.52}$$

The global O/F ratio of the motor can expressed in terms of α as follows.

$$(O/F)_g = 1/4\alpha f(\alpha) \tag{2.53}$$

From this relation α can be solved to a forth order accuracy as

$$\alpha = \left(-1 + \sqrt{-1 + 2\sqrt{1 + 0.8/(O/F)_g}} \right) \Big/ 2.$$

This yields $\bar{r} = a\left((O/F)_g\right) G_o^{0.8} L^{-0.2}$.

For simplicity, we used specific values for the mass flux and distance exponents derived for the flow over a flat plate. However, in a hybrid rocket, the boundary layer developing over the fuel grain merges in a relatively short distance. For that reason, the diffusion limited model developed in this chapter needs to be modified due to the reasons such as the depletion of the oxidizer along the center line of the port and the change in the blowing parameter with the axial distance. It is convenient to use the following general form for the local regression rate formula.

$$\dot{r}(z) = Az^{-m}G^{n} \tag{2.54}$$

The preceding procedure developed to determine the average regression rate can be applied to the general form to yield a similar result.

$$\dot{r} = a\left((O/F)_{e}\right)G_{o}^{n}L^{m}. \tag{2.55}$$

This result indicates that the global regression rate expression such as equation 2.50 that is commonly encountered in the literature can only be used confidently for motors operating within the same O/F ratio range. This fact is not realized in most of the previous scaling consideration of hybrids.

A more general form for the empirical regression rate expression that allows for the pressure dependence that is commonly used in the hybrid literature is [23]

$$\dot{r} = aG_{o}^{n}L^{m}P^{k}. \tag{2.56}$$

We finally note that the pressure exponent for conventional hybrids with no metal additives is small.

Chapter 3

Classification of Hybrid Transients

In the development of hybrid motors as a propulsive system for practical space missions, two problems areas related to the transient response have been encountered. These are the motor instability (especially non-acoustic low frequency modes) and delayed transients in ignition, throttling and shut-down. Our objective is to study the transient characteristics of hybrid combustion to illuminate these problem areas.

In this chapter we will give an introduction to the important aspects of the transient events. We will specifically concentrate on the low frequency stability issue because of its practical importance. Later in this chapter we will discuss our overall approach on the transient modeling of the hybrid system.

3.1. Relevant Transient Events

In order to follow the thrust requirements of a specified mission, a hybrid motor has to operate in a sequence of isolated transient events which are classified and briefly discussed in the following paragraphs.

3.1.1. Ignition

The techniques used for the ignition of hybrids are based on the heating of the oxidizer flow by some kind of short duration heat source such as a slug of hypergolic fluid, a solid squib or spark ignition of a small amount of gaseous fuel. During ignition, the heated oxidizer quickly vaporizes fuel at the forward end of the grain, thus establishing an early combustion zone in the initial portion of the boundary layer. Subsequent portions of the fuel port will experience lower heating rates while vaporization proceeds downstream.

However, since the transient times in the chamber are generally less than those of the thermal lag times in the solid fuel, the latter will be controlling. During this early transient, the combustion gases leaving the motor are oxidizer-rich approaching the steady-state O/F ratio in the local flame front toward the end of the transient. In contrast, the O/F ratio during a conventional solid propellant transient is constant. Of the various time elements involved in this process, the longest time lags are those that establish the combustion boundary layer and the thermal lag in the solid fuel. Thus, the time lag required to establish a steady-state in the hybrid motor is observed to be at least twice as long as for the solid rocket.

3.1.2. Throttling

In a hybrid, throttling is accomplished by simply changing the oxidizer flow rate. The steady-state corresponding to each flow rate sets a new regression rate based on the regression rate law. Although there has been some research work in the early hybrid literature on the quasi-steady-state analysis of the throttling event [25], the full transient phenomenon is not studied. During this event, the gas velocity, temperature and density distributions in the hybrid combustion chamber and the thermal contour in the solid fuel require a lag time to readjust to the new equilibrium. It is clear that a quantitative understanding of this lag is important for predictable impulse management and maneuvering of the vehicle.

3.1.3. Instability

Instability of a rocket motor is defined as the operation when the chamber pressure oscillates in a recognizably coherent form with an amplitude of at least 5% of its mean value [26]. Discussion of the instabilities is deferred to a later section in this chapter due to their practical importance and complex nature.

3.1.4. Thrust Termination

During shutdown, the response time is basically the characteristic emptying time of the motor. The time lag associated with this emptying process can be calculated as about 0.01 to 0.1 seconds for typical motors. During this relaxation, the accumulated heat in the solid is slowly transferred to the surface, leading occasionally to further vaporization or "chuffing", which in the rarefied space environment can contribute a small additional

impulse. The relaxation time is generally greater than the emptying time and therefore controls the shutdown impulse. An understanding and ability to specify this impulse on shutdown is obviously important for precise control of vehicle velocity.

3.2 Hybrid Rocket Instabilities

The pressure oscillations observed in hybrids are bounded in amplitude. In that sense, unlike solid motor instabilities, hybrid instabilities do not introduce the possibility of catastrophic consequences such as the blow up of the whole motor. However they generate unpredictable burning rates and also introduce thrust oscillations. It is known that the oscillatory combustion enhances the mean regression rate (DC shift) [27, 28] and it may cause unpredictable regression of the fuel and also the insulation material. In fact a low frequency instability induced enhancement of the regression of the fuel lining in the pre-combustion chamber caused the failure of one of the AMROC DM-01 motors by burning a hole in the motor casing [29]. The thrust oscillations as a consequence of the pressure oscillations are harmful to the launch vehicle structure and the payload itself. Thus for practically acceptable hybrids, these oscillations must be controlled.

Instabilities are generally classified by the frequency range and their driving mechanisms. Some of the instabilities according to their driving mechanisms can be listed as:

a) Low Frequency: These instabilities are in the range of 0-60 Hz. This is the type of instability that the hybrids typically exhibit. The driving mechanisms for the instabilities in this range are 1) feed system coupling, 2) char layer formation and break-off at very low regression rates (the frequencies of that kind of instabilities are typically in the range of 1-2 Hz.), 3) low frequency instabilities intrinsic to hybrids [19]. This last type of instabilities with an unknown driving mechanism are observed over a wide range of hybrid motors operating with both liquid and also gaseous oxidizer [26, 27, 29, 30, 31]. In this study our objective is to explore this important class of instabilities.

b) Medium Frequency: These are in the range of 50-1000 Hz. This kind of instabilities are mainly longitudinal acoustic modes of the chamber. Medium frequency range oscillations are also observed in hybrids and they are generally accompanied by the low frequency oscillations [27, 29, 30, 31]. It is important to note that a nonlinear disturbance leads to the excitation of the acoustic modes of the chamber.

c) **High Frequency:** These are 'screaming' type oscillations and they are related to the transverse acoustic modes of the chamber. This high frequency portion of the hybrid pressure spectrum is generally inactive.

3.2.1 Characteristics of Low Frequency Instabilities

It is instructive to discuss the nature of the low frequency pressure oscillations observed in hybrid motors. We will base our discussion mainly on various size AMROC motor tests and 11 and 24 inch JIRAD tests, since the data obtained for those tests are relatively reliable and complete. Note that in any of the instabilities discussed in this section, it is shown that the feed system coupling is not the reason for the instability. It is also clear that the regression rates of all of those test are large enough, so that char layer formation and break-off (cooking of the propellant) can not play a role in the instability.

For AMROC DM-01 tests that showed instability, the observed frequency range was 2-3 Hz and the oscillation amplitudes were about 15-20% of the mean pressure. The JIRAD motors were also susceptible to low frequency instabilities [27, 30, 31]. Many of these tests showed pressure oscillations in the frequency range of 8-15 Hz and oscillation amplitudes of 5-60% mean pressure. As an example, Figure 3.1a represents a typical time history of the chamber pressure during unstable operation for an 11 inch JIRAD motor [27]. Figure 3.1b shows the high frequency content of the pressure signal for the same test.

An important observation is that low frequency instabilities were not detected in early hybrids which characteristically did not possess a pre-combustion chamber. The pre-combustion chamber is introduced in modern motors to create a warm uniform oxidizer flow field into the fuel port to increase the combustion efficiency. The introduction of the pre-combustion chamber for improvement in performance generated a major side effect, the low frequency pressure oscillations.

In fact it is commonly accepted by researchers that the stability level of the motor is controlled by the conditions in the pre-combustion chamber such as the chamber volume, flow configuration or heating. It is reported that the effect of the post-combustion chamber on the instability is not significant [30, 32, 33]. Boardman [27, 30] carefully investigated the effect of the pre-combustion chamber flow conditions on the stability level of motor. In

the experiments for the 11 inch GOX motors, he showed that axial injectors enhanced the stability over the radial and 45 degree inclined injectors. It is also reported by independent researchers that for gaseous systems the volume of the feed system downstream of the sonic choke or venturi influences the nature of the stability. Specifically an increase in this volume enhances the instability of the system. In that respect the downstream portion of the feed system volume acts as a part of the pre-combustion chamber.

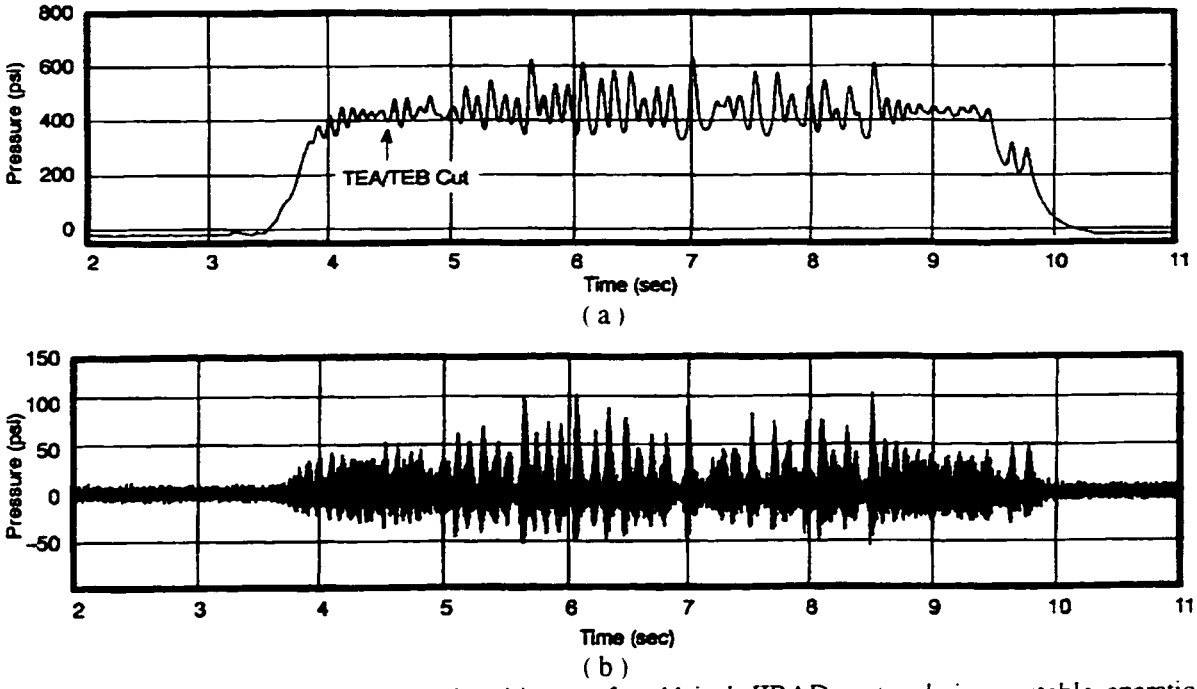

Figure 3.1. (a) The chamber pressure time history of an 11 inch JIRAD motor during unstable operation is shown. (b) The high frequency content of the signal for the same test is plotted.

The pressure oscillations are in the nature of a limit cycle phenomenon. As indicated before, their amplitude is bounded. The oscillations are not simple in the frequency domain. Namely, they possess a range of frequencies rather than a single frequency.

Another interesting observation is that the pressure oscillations may appear or disappear in the middle of a run. Specifically, in AMROC DM-01 tests the low frequency oscillations started after a pressure spike and decayed rather slowly. This indicates that, at least for this specific case, the hybrid motor as a system, possess natural response components with a small damping coefficient at the low frequency range of interest. The pressure spike which may be caused by a brief blockage of nozzle throat or explosion of a fuel oxidizer mixture stored in the pre-combustion chamber serves as a disturbance to activate the system's natural response.

In both JIRAD and AMROC tests the low frequency oscillations are accompanied by higher acoustic frequencies, mainly the first longitudinal (1-L) mode [29, 30]. The pressure-time history for another JIRAD 11 inch motor test [30] which is shown in figure 3.2 clearly indicates this phenomenon. However it is not clear from the pressure history data wether the high frequency is driving the low frequency or vise versa. The pressure data show that the shape of the low frequency oscillations are nonlinear, namely the pressure plot is different from the sinusoidal wave form. Thus these nonlinearities in the low frequency oscillations may very well be perturbing the acoustic modes of the combustion chamber.

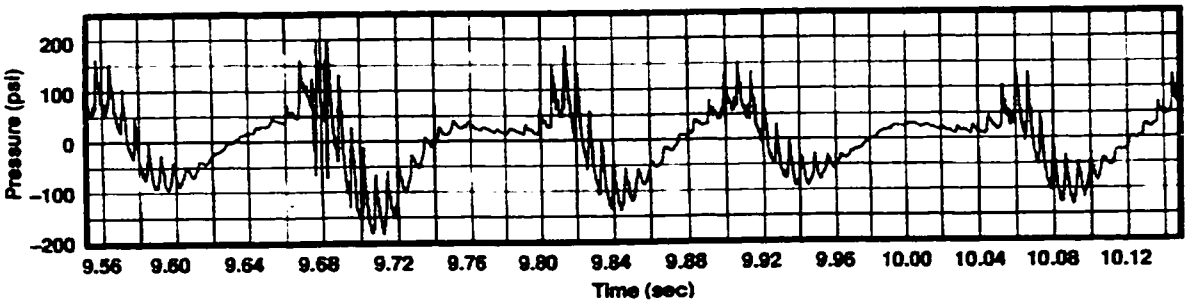

Figure 3.2. Pressure-time history for a different JIRAD 11 inch test.

All those information leads us to believe that even though the low frequency instabilities may be generated by a linear mechanism, their amplitudes are controlled by nonlinear effects. In our studies we will first explore the possible linear couplings that may generate unstable oscillations at the observed frequencies and scale the frequency with the motor operating conditions and geometry. Later we will discuss the nonlinearities that may limit the growth of the unstable modes of the system.

3.2.2. Instability Theories Suggested for Hybrids

Atomization/Mixing: It is claimed by some researchers that the atomization/vaporization lags of the liquid oxidizer may couple with the combustion and gasdynamics to generate the low frequency oscillations. The researchers also stated that the instability can be suppressed by increasing residence time of the droplets in the pre-combustion chamber - for example by employing vorticity - [26] or by providing a rapid means of vaporization as with a hypergolic fluid or igniter. This mechanism is only applicable to a liquid system. However the sames types of instabilities are observed in both liquid and also gaseous systems. Thus this is not a satisfactory explanation for the low frequency instabilities which are probably related intrinsically to the hybrid internal ballistics. Moreover Boardman [27] recently

showed that the increased pre-combustion chamber heat release does not improve the stability of the motor.

Mass Flux Coupling: Since the burning rate is mainly mass flux dependent, the flux coupling may provide the energy feeding mechanism in the hybrid. This is in contrast to solid rockets where pressure coupling is dominant. In the low frequency regime, where hybrids have shown a particular susceptibility to unstable behavior, there is the distinct possibility of mass flow velocity coupling with the hybrid burning rate. This is due to the fact that the thermal lag is typically in the range of tenths of seconds rather than milliseconds which is characteristic of gas phase combustion lags.

Chuffing/Chugging: Chuffing is the instability which has been associated with the accumulation and break off of char or melted layers on the fuel surface. This low frequency instability (1-2 Hz) has been observed during the low regression rate operation of the small hybrid test system in the Aero Fluid Mechanics Laboratory at Stanford University.

Pressure Coupling: There are two operating conditions where the regression rate of the hybrid is pressure dependent, namely at high oxidizer mass fluxes where chemical kinetics effects become rate determining, and in the low mass flux region where radiation becomes important relative to convection. In these regions pressure coupling may provide the energy feeding mechanism to create the pressure-coupled combustion instability. This kind of medium frequency instability is reported in the early literature [35, 36]. The solid propellant instability literature on the combustion pressure coupling effect is quite extensive and a reasonable understanding of this contribution has been demonstrated [37]. It is expected, however, that this type of instability will be evidenced only in those hybrids showing a distinct pressure effect on the burning rate. This kind of instability is first observed by Marxman [36] for a system with metal loading above a certain critical port diameter. The observed mean frequency of the oscillations were about 600 Hz for a 0.75 meters long motor. This frequency corresponds to the 1-L acoustic mode of the system.

Vortex Shedding: This instability is linked with the vortex shedding in regions of rapid expansion such as the mixing chamber of the motor [32, 33, 34]. These frequencies are generally in the medium range and so may not be primary in the hybrid motor.

DC Shift Theory: Boardman [36] suggested that the low frequency instabilities are generated by the high frequency (acoustic) active packages through the DC shift effect.

They claim that the high frequency pressure oscillations are generated by the back and forth oscillation of the leading edge of the hybrid diffusion flame, since it is not stabilized adequately for some hybrid configurations. However, this theory can not explain why the high frequency wave packages are modulated at a well defined range of frequency. Moreover it is also possible the cause and effect are reverse, namely the nonlinear low frequency wave forms may be driving the high frequency acoustic modes. The feasibility of this latter alternative is successfully demonstrated in chapter 6 of this thesis. Another evidence against the reality of this model is the sensitivity of the stability of the motor on the feed system volume downstream of the choked throat. Evidently the feed system volume can not have a direct effect on the stabilization of the flame leading edge.

L* Theory: There have been several attempts to develop a L^* instability theory for the hybrids as an analog to the solid rocket L^* model [26, 34]. The details of this possibility are discussed in the next section in which we compare hybrids with the solid and liquid systems from the perspective of low frequency instabilities.

3.2.3. Comparison of Liquid, Solid and Hybrid Rocket Low Frequency Instabilities

The low frequency instability mechanisms for liquid and solid rockets are reasonably well understood. Theories to predict the frequency and the nature of those instabilities have been successfully developed and used in the design of rockets for almost four decades. On the contrary, for hybrid rockets a low frequency theory that explains the widely observed low frequency oscillations is still not available. This is partly due to the late development of hybrids compared to the other chemical systems. In our opinion another important reason is the weak dependency of the combustion on the pressure in hybrids. It is well known that conventional hybrids operate, unlike the solids and the liquids, in a diffusion limited combustion regime which makes the regression rate a strong function of the mass flux not the chamber pressure. This lack of explicit dependence of the mass generation rate on the chamber pressure, prevents one from coupling the bulk mass balance in the chamber to the combustion through the pressure dependent regression rate. In this section we will discuss this issue in detail by summarizing the solid and liquid rocket low frequency instability theories and assessing the applicability of the fundamental principles of those theories to the hybrids.

The low frequency instability theory (L^* theory) for the solid rockets was first developed by Beckstead and Price [38, 39] and improved by many other researchers [37, 40]. The model depends on the bulk mass balance in the rocket chamber which can be written as equation 3.1 in terms of the normalized pressure ($\bar{p}$) and mass generation ($\bar{m}$)

$$\tau_c \frac{d\bar{p}}{dt} + \bar{p} = \bar{m} \tag{3.1}$$

where τ_c is the residence time of the fluid particles in the chamber.

The essence of the theory is to represent the mass generation term as an explicit function of the chamber pressure. This can only be done when the fuel generation rate (regression rate) is an explicit function of pressure which is a valid approximation for solid motors. It is well known that the regression rate expression for solid motors has a form $\dot{r} = ap^n$ during the steady-state operation and it is fair to state that the regression would still depend on the pressure during these low frequency oscillations. After the linearization of the mass generation rate, equation 3.1 can be written as

$$\tau_c \frac{d\bar{p}(t)}{dt} + \bar{p}(t) = R\bar{p}(t+\tau). \tag{3.2}$$

Here a lead time between the pressure and regression rate is applied. This lead time is due to the thermal profile changes in the solid grain. We know from thermal lag theory that for a frequency range the regression rate leads the wall heat transfer. Moreover the wall heat transfer can be expressed in terms of pressure if one assumes quasi-steady gas phase processes which is a good assumption in the low frequency range of our interest.

The system dynamic behavior at low frequencies can be investigated with the use of equation 3.2. We start by taking the Laplace transform of this linear equation.

$$\left(\tau_c s + 1 - \mathrm{Re}^{n}\right)\theta = 0. \tag{3.3}$$

The term in the parenthesis is the characteristic equation of the system. The roots of this equation determines the time response (natural) of the system. Since this is an analytic function in the s plane, the stability can easily determined by investigating the location of

the poles in the s plane. In short, if the system has any pole in the right halfplane, it is unstable. By dividing this equation into its real and imaginary parts, $s = \alpha + i\omega$ and defining $R' = \mathrm{Re}^{\pi\alpha}$ one can obtain the stability equations given by Backstead and Price [38].

$$\tau_c \alpha + 1 = R' \cos(\tau\omega) \tag{3.4.a}$$

$$\tau_c w = R' \sin(\tau\omega) \tag{3.4.b}$$

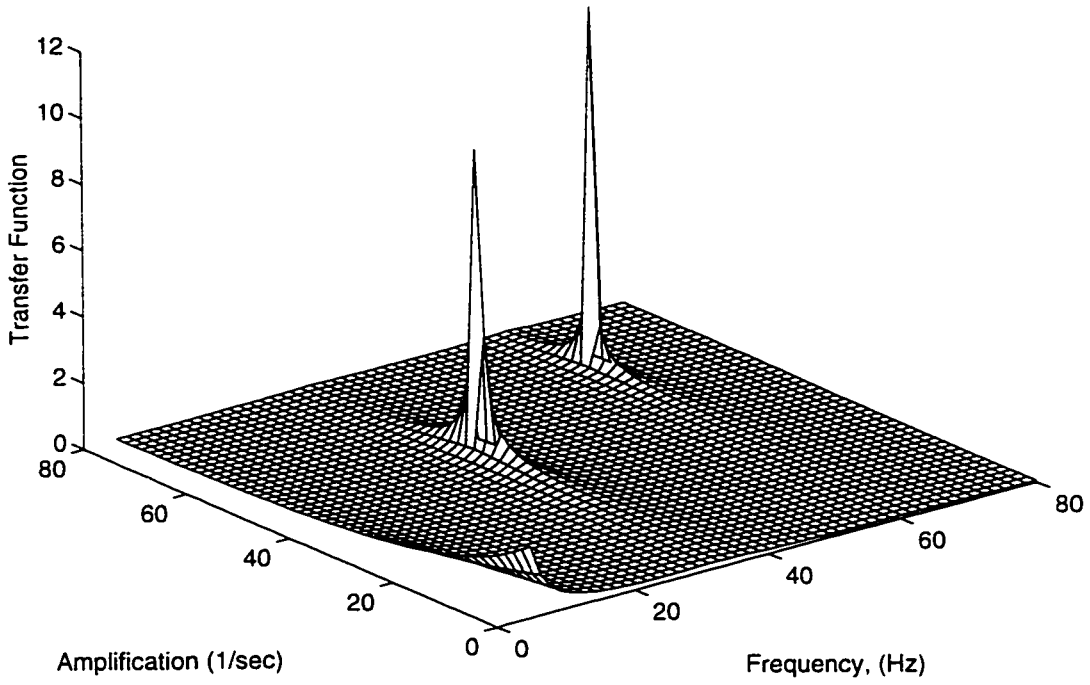

Figure 3.3. The poles of the L^* instability model.

In reference 38 these equations are investigated carefully and it is shown that for a range of τ (positive), the amplitude of oscillations grow indefinitely. As an example, the characteristic equation is plotted in figure 3.3 for the typical values of $\tau_c = 30$ $m$sec, $R = 1.3$ and $\tau = 35$ $m$sec. It obvious from figure 3.3 that the system has at least two poles in the positive real s halfplane. A more careful investigation shows that the equation has an infinite number of poles in the positive s plane. But only the pole with the smallest frequency (fundamental mode) has practical significance because for the high frequency poles the assumptions of the theory does not hold. In fact in experimental investigation of this phenomena only the smallest frequency is observed.

A similar development can also be performed for the low frequency instabilities of liquid rocket engines [41, 42]. An extensive discussion of the treatment is given by Corocco and Cheng [41]. Here we will give a brief outline of the model. Parallel to the solid rocket case, the bulk mass balance in the liquid engine combustion chamber can be written in the nondimensional form as

$$\tau_c \frac{d\bar{p}}{dt} + \bar{p} = \bar{m}_b \tag{3.5}$$

where $\bar{m}_b$ is the nondimensionalized mass of burnt gases generated in unit time. Similar to the solid motor, in a liquid engine the combustion rate (combustion of liquid droplets) will be a strong function of the chamber pressure. It can be shown as in reference 41 that the generation rate of hot gases in the combustion chamber can be expressed to the first order accuracy as

$$\bar{m}_b(t) = \bar{m}_i(t - \tau_t) + n\left[\bar{p}(t) - \bar{p}(t - \tau)\right] \tag{3.6}$$

Here $\bar{m}_i$ is the injection rate of the propellants into the chamber and n is the pressure sensitivity coefficient. Unlike the solid rocket L^* instability theory, in this model two types of time delays τ_t and τ are introduced. Although both of these delays represent the time lag between the injection of the propellant and the generation of the burned gases, τ is the pressure sensitive contribution whereas τ_t is the insensitive contribution to the total delay τ_t. Second term in equation 3.6 is available only for the variable delay case (pressure sensitive case). Equations 3.5 and 3.6 can be combined to obtain the linear response of the system at low frequencies.

$$\tau_c \frac{d\bar{p}(t)}{dt} + \bar{p}(t) = \bar{m}_i(t - \tau_t) + n\left[\bar{p}(t) - \bar{p}(t - \tau)\right] \tag{3.7}$$

The stability investigations can be performed with the Laplace transformation technique for the system represented with equation 3.7. It is shown in reference 41 that there are at least two types of low frequency instabilities that can be generated. If the feed system dynamics is very rigid, namely the injection mass flow rate is constant (decoupled from the chamber pressure), the liquid engine can sustain amplified oscillations of chamber

pressure for reasonably high values of the pressure sensitivity coefficient and for a realistic range of the combustion delays. This kind of feed system independent instability is called the 'intrinsic instability' and it is due to the existence of variable (sensitive) delay. A second type of instability can occur if the pressure sensitivity coefficient is zero but the feed system is coupled to the chamber pressure. Note that unlike the solid rocket motors, in general, in liquids the combustion delay (not the lead) generates the instability.

After summarizing the models of low frequency oscillations for solid and liquid rockets, we can return to the central point of our argument, namely the applicability of the fundamental principles of these highly accepted theories to hybrid rocket motors. In the literature there has been some attempts to apply the L^* analysis for solid rockets to the hybrids with some minor modifications [26, 34]. Specifically in reference 34 a reasonably detailed derivation of the analogous L^* theory is performed. After writing the bulk mass balance in a hybrid chamber (to our knowledge which was first performed by Marxman [36]), following the L^* derivation, the investigators introduced a lead time between the combustion and the chamber pressure. We believe that this is not a valid step for hybrids which, in general, do not possess regression rates with a strong explicit dependence on the chamber pressure. It can be argued that the regression rate for hybrids depends on pressure through the mass flux which is a product of density and fluid velocity where density is a linear function of the chamber pressure with use of the ideal gas law. However the response of the chamber thermodynamic properties to the changes in the pressure during these slow transients is not known off hand. For example, an increase in pressure (with a rate that is relevant to a low frequency oscillation) does not necessarily lead to a significant increase in the mass flux, since the flow velocity can also arrange (which is a very likely possibility at the low frequencies of interest) itself to keep the changes in the mass flux small. The preliminary results of our investigations on a quasi-1D unsteady gasdynamic model of the motor chamber, confirm this weak dependence of the mass flux on the pressure. In the absence of a coupling between the regression rate and the pressure, the principles used in solid rocket (or liquid rocket) instability modeling can not generate instabilities. For that reason, we believe that there is no analog (i.e. analog to L^*) low frequency theory for hybrids that will yield the instabilities.

3.4. Subsystems of a Hybrid Rocket Motor

Our approach on modeling the dynamic behavior of the hybrids is to isolate the subsystems of the motor and consider every single subsystem individually. For a full description of motor transients one has to consider the following subsystems.

a) Feed System: In a hybrid system the oxidizer is in liquid or gaseous phase. Thus oxidizer needs to be fed to the combustion chamber through some kind of a feed system. In reality the feed system response time is finite due to the capacity of the elements in the system. The accurate response depends on the details of the system which is likely to be significantly different for every design. For this reason we will bypass the feed system dynamics in our investigations by assuming the oxidizer mass flow rate as the input parameter.

b) Vaporization of the Liquid Oxidizer: The vaporization of the oxidizer droplets in the combustion chamber requires a time lag. In our investigations we will assume that this time is small compared to the other characteristic times of interest.

c) Diffusion and Combustion in the Hybrid Boundary Layer: It is requires some lag time for the hybrid boundary layer properties to adjust to the changes in the port velocity. The associated dynamics will be discussed in detail in chapter 5.

d) Thermal Profile Changes in the Solid Grain: A change in the wall flux to the hybrid fuel grain can not be followed by the temperature contour in the solid and also the regression rate of the fuel.

e) Chamber Gasdynamics: The chamber pressure responds to the changes in the mass flow in a time scale proportional to the filling time of the chamber.

In the subsequent chapters the last three of these subsystems will be modeled and investigated individually. Eventually these subsystems will be coupled to give the overall system response.

The order of magnitude estimates of the time scales of some of the important processes encountered in hybrids are listed in table 3.1.

Physical Phenomenon:	**Time Scale:**	**Explanation:**
1) Solid phase kinetic times	$\tau_{sp} < 10^{-3}$ sec	Degradation mechanisms of the polymer
2) Gas phase kinetic times	$\tau_{gp} < 10^{-3}$ sec	Hydrocarbon-O2 combustion mechanisms
3) Acoustic times	$\tau_a \propto L/c \approx 10^{-3}$ sec	Propagation of the acoustic waves
4) Evaporation times	$\tau_{evap} = f(U_\infty, T_1, d_p)$	Evaporation process of the LOX
5) Thermal lags in solid	$\tau_{tl} \propto \kappa/\dot{r}^2 \approx 10^{-1}$ sec	Thermal profile changes in the solid grain
6) Turbulent boundary layer diffusion lags	$\tau_{bl} \propto L/u_{ave} \approx 10^{-1}$ sec	Turbulent boundary layer diffusion processes
7) Gasdynamic filling times	$\tau_{fill} \propto L^*/c^* \approx 10^{-1}$ sec	Global mass flow balance

Table 3.1. The transient time scales of various phenomena in a typical hybrid rocket.

Chapter 4

Thermal Lags in the Solid

The regression rate of the hybrid fuel grain cannot respond to changes in the wall heat flux instantaneously due to the finite thermal conductivity of the solid fuel. The transient heat flow in the solid determines the dynamics of the regression rate response during wall heat flux variations. This phenomenon will be investigated (both analytically and numerically) in this chapter.

The hybrid combustion mechanism differs from the solid rocket in two respects [1, 19]: the flame front is an appreciable distance from the solid surface and there are no exothermic chemical reactions at the surface. As a consequence, the regression rate is low. The lower regression rate significantly increases the thermal profile variation lags in the solid. Thus, among the various response times discussed in the previous chapter, the thermal lags in the solid fuel is potentially the rate-limiting (slowest) step during transient operation. This fact can be seen from the characteristic thermal lag time $\tau_{tl} = \kappa/\dot{r}^2$ whose values lie typically in the range of 0.1 to 1 sec, corresponding to frequencies in the 1 to 10 Hz range. Since this is a common range observed in the low frequency instability of hybrids [26, 30], it is highly suggestive that the thermal lag in the solid may play an important role in the mechanism.

An early treatment of the thermal lags in hybrids was carried out by Marxman [19]. In his analysis, in order to obtain a closed form solution Marxman assumed: 1) constant wall temperature, 2) constant wall heat flux, 3) third order polynomial shape for the temperature profile, 4) small initial heating time. For that reason, this solution can only be used for the simulation of the ignition events with constant heat input. Furthermore, even for this specific case the solution is not exact, as a result of the imposed profile shape and fixed wall temperature approximations. Thus, in this chapter we focus our investigations on the thermal lags in the solid. We develop a physical model for that phenomenon and

study several analytical and numerical solution techniques for the associated mathematical problem.

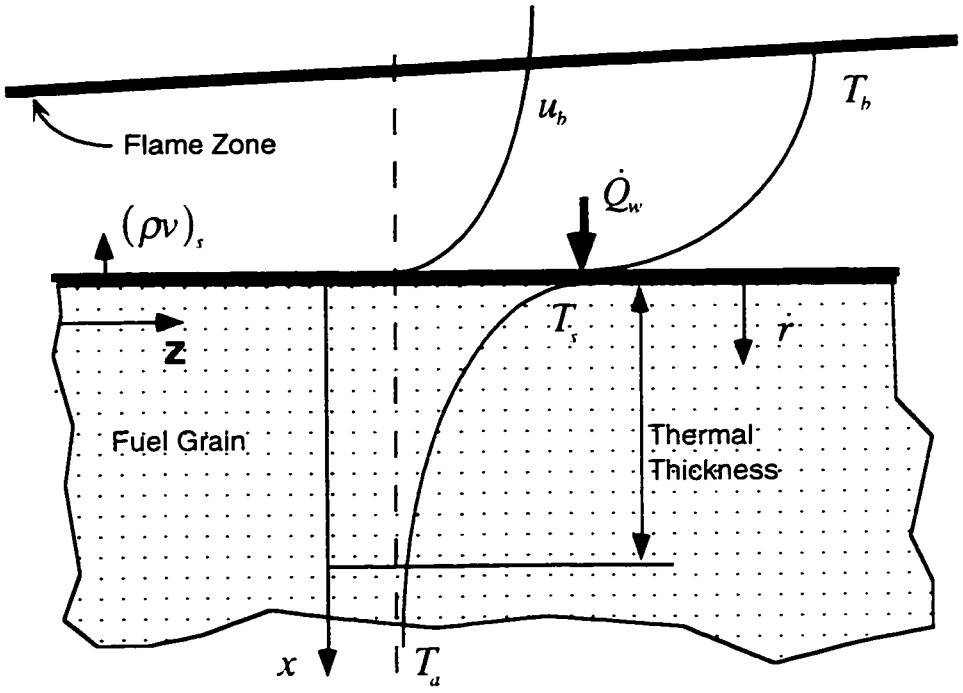

Figure 4.1: Schematic of the thermal lag model

4.1 Thermal Lag Model

Our model for the thermal lag in the solid is shown in figure 4.1. Major assumptions of the model are 1) the penetration depth of the temperature profile is small compared to the web thickness of the fuel, 2) the port radius is large compared to the thermal penetration thickness, 3) all solid phase reactions companying fuel vaporization occur in a thin layer next to the regressing surface*, 4) thermophysical properties (such as the thermal diffusivity) of the fuel grain are assumed to be constant, 5) the temperature gradient in the axial direction is small compared to the gradients in the normal direction. Under these conditions the suitable heat diffusion equation expressed in the x-coordinates moving with the regressing surface is

$$\frac{\partial T}{\partial t} = \kappa \frac{\partial^2 T}{\partial x^2} + \dot{r}(t) \frac{\partial T}{\partial x} \,. \tag{4.1}$$

* This assumption is a good one for large activation energies, since the reaction zone thickness in the solid is inversly proportional to the activation energy (see appendix B).

Landau [42], using Green's theorem, showed that for this kind of a semi-infinite region problem, Dirichlet or Neumann types of boundary conditions can be used alternatively, namely:

$$x \to \infty \qquad T = T_a \qquad \text{or} \qquad \frac{\partial T}{\partial x} = 0 \tag{4.2}$$

The second boundary condition can be derived from the energy balance at the surface which involves the latent heat of gasification, L_v (The latent heat of vaporization and solid phase reaction energies are lumped together to define the latent heat of gasification.).

$$x = 0 \qquad \dot{Q}_w(t) = -\lambda\left(\frac{\partial T}{\partial x}\right)_s + \rho\, \dot{r}(t) L_v \tag{4.3}$$

Note that these boundary conditions, with the appropriate form of the wall heat transfer, are common for every transient event. However, the initial condition which is the temperature distribution at the start of the event is case dependent.

A constitutive relation modeling the surface processes is required to close the set of equations representing the mathematical formulation of thermal lag theory. We propose two distinct models for the surface phenomena.

4.1.1 Constant wall temperature model (CWT)

In this case the surface temperature is independent of the regression rate and is kept fixed to a value which is assumed to be known *a priori*. Note that the constant specified wall temperature condition replaces the surface boundary condition and equation 4.3 becomes a determining relation for the regression rate.

4.1.2 Variable wall temperature model (VWT)

In reality, the gasification and pyrolysis reactions at the surface are both generated by an exponential of the Arrhenius type. For chemical reactions, the exponential constant is

an activation energy, whereas in vaporization it is the latent heat. To describe this behavior, we assign an average effective activation energy resulting in:

$$\dot{r} = A\exp\left(-\frac{E_a}{R_g T_s}\right) \qquad \text{if} \qquad T_S > T_i$$
$$\dot{r} = 0 \qquad \text{if} \qquad T_S < T_i \tag{4.4}$$

where T_i represents the temperature below which vaporization is negligible. This can be caused by pyrolysis, depolymerization or any other reaction with relatively high activation energy. In the case of a simple non-polymeric solid such as wax, for instance, T_i would be close to the ambient.

Here, we inherently assumed that once initiated, these reactions are fast compared to thermal diffusion. For typical values of E_a in the range of 10-60 kcal/mole, the percent change in T_s is small justifying the CWT model as a first approximation.

In our thermal lag model, we represent various transient events with the suitable selection of the initial conditions and the wall heat transfer variations. Our goal is to obtain the response of the regression rate during those simulated events. This requires the solution of the coupled equations 4.1, 4.2, 4.3 and 4.4. Note that this moving boundary problem is nonlinear and an exact closed form solution is not available (to our knowledge).

4.2 Methods of Solution

In this study we are interested in developing approximate solutions to the thermal lag problem posed in the previous section. We concentrate on three different methods.

4.2.1 Self-Similar Temperature Profiles Approximation

This approach which is introduced by Marxman is based on assuming a time invariant functional form for the temperature contour. In this treatment the wall heat transfer and surface temperature are assumed to be constant. Thus, the method is only capable of

generating solutions for the CWT model for fixed heat input case and is only good for simulating a special category of ignition events.

Although Marxman's analysis is limited to a third order polynomial form for the temperature profile, it is fairly straightforward to generalize the method to arbitrary contours. We assume the following form for the temperature profile

$$\frac{T - T_a}{\Delta T} = F(x/\delta). \tag{4.5a}$$

Here δ is the thickness of the thermal boundary layer in the solid and $\Delta T = T_s - T_a$. F can be any function satisfying the boundary conditions

$$\begin{aligned} x &= 0, & F &= 1 \\ x &\to \infty, & F &= 0 \quad \text{and} \quad \frac{\partial F}{\partial x} = 0. \end{aligned} \tag{4.5b}$$

There are several reasonable contours that can be selected. One is the contour that exists at the end of the heating cycle before vaporization occurs. This profile is given by an inverse error function (ierfc). Another is the exponential contour that describes the steady-state. A third is a simple polynomial.

For constant heat input, the energy balance at the surface can also be written as

$$\dot{Q}_w = \rho\, \dot{r}_{ref}\, h_v = \rho\, \dot{r} h_v + \rho\, C\, \frac{\partial}{\partial t} \int_0^{\delta} (T - T_a)\, dx \tag{4.6}$$

For this method the symbol $\dot{r}_{ref}$ refers to the steady-state regression rate associated with $\dot{Q}_w$. Integrating equation 4.1 over x from zero to infinity after substitution of the energy balance equation and profile function with the use of the boundary conditions yields the following first order ordinary differential equation for δ

$$\left(\frac{E_L}{E_L + 1}\right) \alpha_1 \frac{d\delta}{dt} - \frac{\alpha_2 \kappa}{\delta} = -\dot{r}_{ref}. \tag{4.7}$$

where, α_1 and α_2 are the shape parameters of the assumed profile and E_L is the ratio of the gasification energy to the energy consumed for heating the solid up to the surface temperature.

$$\alpha_1 = \int_0^\infty F(x')dx' \qquad \alpha_2 = \left(\frac{\partial F}{\partial x}\right)_s \tag{4.8}$$

$$E_L = \frac{L_v}{C\Delta T} \tag{4.9}$$

The shape factors α_1 and α_2 resemble the capacity and the surface slope of the selected profile, respectively. The values of α_1 and α_2 for various temperature contours are listed in table 4.1.

T-x Relation	*Shape factor* α_1	*Shape factor* α_2
exponential	1	1
ierfc	0.443	1.772
second order polynomial	0.33	2
third order polynomial	0.25	3

Table 4.1. Shape parameters for various profiles.

If we integrate equation 4.7 with the use of the initial condition, $\delta(0) = \delta_0$, we obtain the final result

$$\bar{t} = -\alpha_1 \alpha_2 \left(\frac{E_L}{E_L + 1}\right)\left(\ln\left(\frac{1-\bar{\delta}}{1-\bar{\delta}_0}\right) + \bar{\delta} - \bar{\delta}_0\right) \tag{4.10a}$$

$$R = 1 - \frac{1}{E_L}\left(\frac{1-\bar{\delta}}{\bar{\delta}}\right) \qquad \text{where} \qquad \bar{\delta} = \frac{\delta}{\alpha_2 \delta_{ref}}. \tag{4.10b}$$

Note that $E_L/(E_L+1)$ is equal to L_v/h_v where $h_v = L_v + C\,\Delta T$.

The variables of the problem are nondimensionalized with the use of the reference regression rate and the characteristic time and length associated with that reference point in the following way:

$$\bar{t} = t/\tau_{ref} , \qquad R = \dot{r}/\dot{r}_{ref} \tag{4.11}$$

where

$$\tau_{ref} = \kappa/\dot{r}_{ref}^2 , \qquad \delta_{ref} = \kappa/\dot{r}_{ref} . \tag{4.12}$$

For constant wall heat flux transient case, it is convenient to use the steady-state as the reference point.

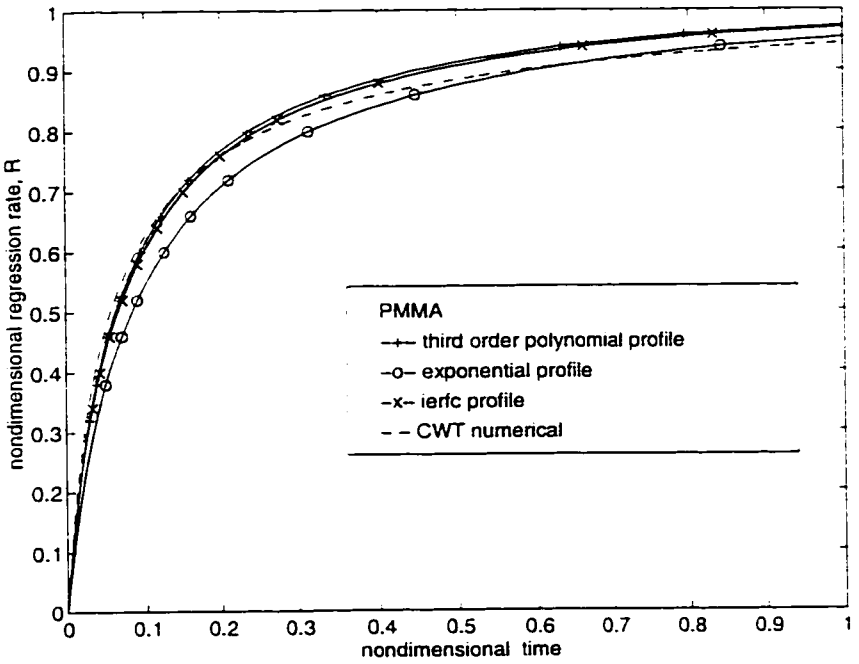

Figure 4.2. Effect of the temperature profile selection on the analytical solution for the ignition with constant heat transfer case. Initial heating period is neglected. Reference: $\dot{r}_{ref} = 0.05$ cm/sec and $\tau_{ref} = 0.4$ sec.

Equations 10a and 10b indicate that $\bar{\delta}$ serves as a free parameter that links the regression rate to the time. Thus the response of the regression rate only depends on the energy parameter, E_L, and the product of the two shape factors. Upon the selection of a profile shape and fuel type, equations 4.10a and 4.10b can be used to generate the solution.

Figure 4.2 shows the transient curves for three distinct profile functions, namely: ierfc function, exponential function and a third order polynomial, for PMMA material.

4.2.2 Numerical Solutions

The self-similar temperature profiles approximation approach is inadequate to generate solutions for all possible kinds of transients. Furthermore, in certain cases this treatment introduces extra assumptions that may generate significant errors. For this reason, we develop a numerical solution procedure for both of the models for surface phenomena. We start with normalizing the variables to obtain a nondimensional form of the problem.

The nondimensional time and regression rate are defined in equation 4.11. The remaining variables are normalized in the following way:

$$\bar{T} = \frac{T - T_a}{\Delta T}, \qquad \bar{x} = \frac{x}{\delta_{ref}} \tag{4.13}$$

The application of the simple stretching transformation defined by equations 4.11 and 4.13, yields the nondimensional form of the field equation

$$\frac{\partial \bar{T}}{\partial \bar{t}} = \frac{\partial^2 \bar{T}}{\partial \bar{x}^2} + R(\bar{t})\frac{\partial \bar{T}}{\partial \bar{x}} \tag{4.14}$$

and the boundary conditions

$$\text{for} \quad \bar{x} \to \infty: \quad \bar{T} = 0 \quad \text{or} \quad \frac{\partial \bar{T}}{\partial \bar{x}} = 0 \tag{4.15}$$

$$\text{for} \quad \bar{x} = 0: \quad \left(\frac{\partial \bar{T}}{\partial \bar{x}}\right)_s = E_L R(\bar{t}) - \bar{Q}(\bar{t}) \tag{4.16}$$

where $\bar{Q}(\bar{t}) = \dfrac{\dot{Q}_w(t)}{\dot{r}_{ref}\rho\, C\, \Delta T}$.

In the process of normalization, we introduced the nondimensional heat loading, $\overline{Q}$, which is defined as the ratio of the heat input per unit mass to the energy required to elevate the temperature of the fuel from T_a to T_s. $\overline{Q}$ is, in general, time dependent through the input and unlike E_L, it is not a property of the fuel alone.

We prefer the following nondimensional form for equation 4.4:

$$R = A\exp\left(-\frac{a}{\overline{T}_s + b}\right) \qquad \text{if} \qquad \overline{T}_s > \overline{T}_t$$
$$R = 0 \qquad \text{if} \qquad \overline{T}_s < \overline{T}_t \tag{4.17}$$

where

$$A = \exp\left(\frac{E_a}{(\overline{T}_s)_{ref} R_{gas}}\right). \tag{4.18}$$

$$a = \frac{E_a}{\Delta\overline{T}_{ref} R_{gas}}, \qquad b = \frac{\overline{T}_a}{\Delta\overline{T}_{ref}}. \tag{4.19}$$

Since the nature of the CWT and VWT problems are significantly different, we treat them separately.

4.2.2.1 CWT Simulations

In this case, the surface temperature boundary condition is replaced by a simple Dirichlet type of condition, $\overline{T}(\overline{x} = 0) = 1$, and equation 4.18 becomes a determining equation for the nondimensional regression rate.

We start by dividing the $\overline{x}$ coordinates into a uniform mesh and replacing the space derivatives with the second-order central differencing approximations. For simplicity, the Euler explicit time marching scheme [44, 45], which is first order in time, is selected for

the time accurate integration of the set of ODE's obtained after the space differencing. In the CWT problem the numerical stability criterion† which is,

$$\Delta\bar{t} \le \frac{2}{(2/\Delta\bar{x})^2 + (R/2)^2} \tag{4.20}$$

requires the selection of small time steps. Thus, even for this first order scheme, time accuracy is not an issue. Typical values for $\Delta\bar{x}$ and $\Delta\bar{t}$ are 0.05 and 0.001, respectively. In our algorithm, we update the temperature field using the differenced version of equation 4.14 and impose the suitable Dirichlet type boundary conditions at the boundaries. The calculations in a single time step will be completed upon the determination of the regression rate with use of equation 4.16 and the new temperature distribution.

As an example, an output of the run for the ignition with constant heat input case is shown in figure 4.3. The appropriate initial condition [46] is

$$\bar{T}(\bar{x}) = \sqrt{\pi}\, ierfc\left(\frac{\bar{Q}\bar{x}}{\sqrt{\pi}}\right). \tag{4.21}$$

This is the profile at the end of the surface heating period in which the surface of the fuel is heated from the ambient temperature up to the pyrolysis temperature at a constant heat load. Initial heating period is, in general, small compared to the total ignition transient time, but, if necessary, can easily be estimated by the use of the formula

$$\frac{t_{ih}}{\tau_{ref}} = \frac{\pi}{4\bar{Q}^2}. \tag{4.22}$$

4.2.2.2 VWT Simulations

The formulation of the VWT problem allows the simulation of any transient event with the proper selection of the heat loading. Thus, we focused our investigations on the numerical solution of this problem for any arbitrary heat input functions and initial conditions. In general, the selection of the reference point is also arbitrary. A convenient

† This condition is derived for the locally linearized form the field equation and for periodic boundary conditions. Thus, it is a necessary, not a sufficient condition for stability.

way of determining the reference state is to pick a reference heat transfer, $(\dot{Q}_w)_{ref}$, and to calculate the remaining reference quantities such as, $\dot{r}_{ref}$, $(\overline{T}_s)_{ref}$, $\Delta\overline{T}_{ref}$ from the steady operating conditions. This procedure requires iteration on the surface temperature, which turns out to be fairly straightforward. The nondimensional form of the equations remains valid for this arbitrary reference state. Since, equation 4.4 enters the VWT problem, this equation has to be normalized in order to close the set of nondimensional equations. The preferred form for that is also given by equation 4.17.

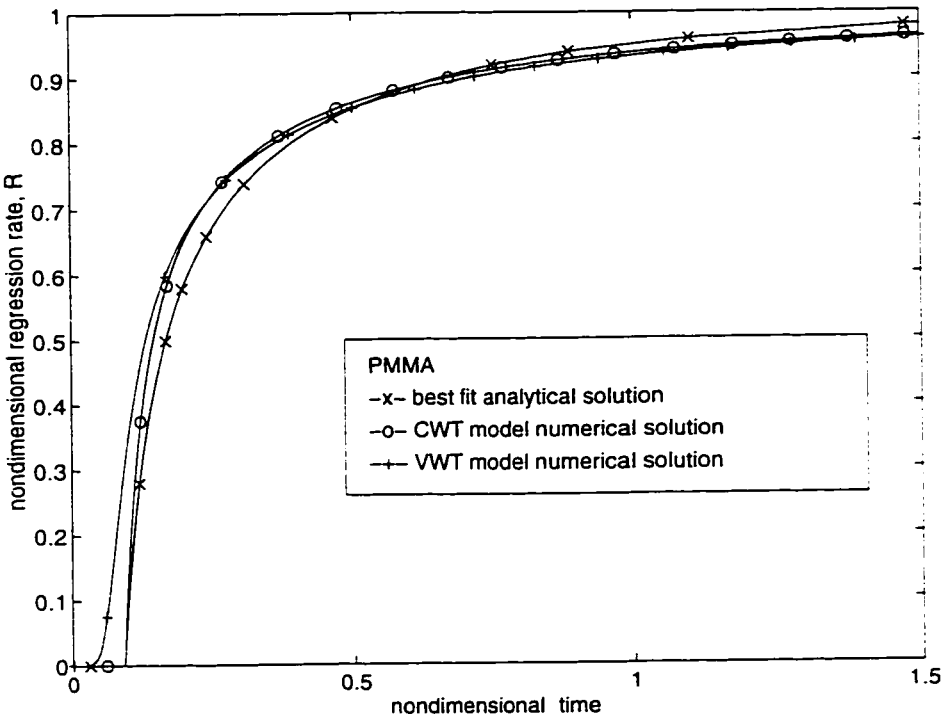

Figure 4.3. Comparison of various methods for the ignition with constant heat transfer case. Initial heating period is included with use of 4.21 in the analytical and CWT numerical solutions. E_s=30 kcal/mole, T_i=310 K for VWT numerical solution. Reference: $\dot{r}_{ref}$ =0.05 cm/sec and τ_{ref} =0.4 sec.

Note that the surface boundary condition for the VWT problem, given by equation 4.16, unlike the CWT case, is a mixed type.

We use the finite difference method to obtain numerical solutions for this well-posed problem given by equation 4.14 to equation 4.17. The space differencing is kept the same as the CWT case. But, since our intention is to generate long time solutions for the VWT problem, the global time error may be significant even for relatively small time steps imposed by the stability condition. For that reason, we implemented an adaptive RK4 scheme [44], which is fourth order accurate, for the time integration. The adaptive control

of the time step size increased the robustness of the thermal lag code (TLC). This property is important, since integration of TCL to a transient hybrid code that may be developed in the future requires this feature. The long term accuracy of the code is tested by checking the ability to follow a steady-state within a reasonable tolerance. The results for several transient simulations with the perturbation solutions are also in perfect agreement.

The TLC is capable of calculating the regression rate for any given initial temperature profiles and heat loadings. Also, the initial heating period or any such event without regression can be simulated with the present algorithm.

Since an adaptive time marching scheme is used, we did not encounter any apparent numerical instabilities. But, when the calculations were in an numerically unstable region the efficiency of the code reduced significantly. This is basically due to the reduced time step size to force the integration scheme into the stable region. These inefficient operating regions are encountered when the nondimensional regression rate is high. This fact can be seen from equation 4.20, namely as R increases, the domain of stability shrinks. Thus, we find it convenient to select the reference state in such a way that R is always less than an upper bound (which is roughly 1.3) during the course of the simulation. It is necessary to note that as $(\dot{Q}_w)_{ref}$ increases, the characteristic time and the physical simulation time decreases. This suggests that there is an optimum value for $(\dot{Q}_w)_{ref}$ that minimizes computer time for a given simulation.

4.2.3 Perturbation Solutions

In this section we develop perturbation solutions for the VWT problem. The results of this perturbation analysis are useful in determining the effects of various parameters on the response, in understanding the system behavior and in verifying the numerical solutions. Although this treatment requires small perturbations in the variations of the heat input around a reference point, the functional form of the heat load perturbation is arbitrary.

We apply a small perturbation, with an arbitrary form in time, to the wall heat flux around the reference steady-state value

$$\overline{Q}(\bar{t}) = (\overline{Q})_{ref} + \varepsilon . f(\bar{t}) \tag{4.23}$$

where $\varepsilon << 1$.

Let's assume regular perturbation [47] on the temperature and the regression rate.

$$\bar{T}(\bar{x},\bar{t}) = \bar{T}_{ref}(\bar{x}) + \varepsilon.\bar{T}_1(\bar{x},\bar{t}) + \varepsilon^2.\bar{T}_2(\bar{x},\bar{t}) + O(\varepsilon^3) \tag{4.24}$$

$$R(\bar{t}) = R_{ref} + \varepsilon.R_1(\bar{t}) + \varepsilon^2.R_2(\bar{t}) + O(\varepsilon^3) \tag{4.25}$$

But, the definitions of the reference state can be used to write

$$\bar{T}_{ref}(\bar{x}) = \exp(-\bar{x}), \qquad R_{ref} = 1. \tag{4.26}$$

Upon substituting equation 4.23 to equation 4.26 in the exact VWT problem and collecting the order of ε terms together, we obtain the following linear initial-boundary problem for the first order perturbation quantities.

$$\frac{\partial \bar{T}_1}{\partial \bar{t}} = \frac{\partial^2 \bar{T}_1}{\partial \bar{x}^2} + \frac{\partial \bar{T}_1}{\partial \bar{x}} - E_{E_s}\,\bar{T}_1\big|_{\bar{x}=0}\exp(-\bar{x}) \tag{4.27}$$

Boundary conditions become

$$\left.\frac{\partial \bar{T}_1}{\partial \bar{x}}\right|_{\bar{x}=0} - E_L E_{E_s}\,\bar{T}_1\big|_{\bar{x}=0} = -f(\bar{t}) \tag{4.28}$$

$$\bar{T}_1\big|_{\bar{x}\to\infty} = 0. \tag{4.29}$$

Initial condition takes the form

$$\bar{T}_1 = 0. \tag{4.30}$$

Regression rate equation becomes

$$R_1 = E_{E_a} \left. \frac{\partial \overline{T}_1}{\partial \overline{x}} \right|_{\overline{x}=0} . \tag{4.31}$$

Here, E_{E_a} is the third energy parameter which is proportional to the activation energy.

$$E_{E_a} = \frac{a}{(1+b)^2} = \frac{E_a (\Delta T)_{ref}}{R_g (T_s)^2_{ref}} \tag{4.32}$$

The linear initial-boundary value problem defined for the first order perturbation quantities is solved with use of the Laplace transformation technique [48]. The transfer function between the regression rate perturbation and the applied heat flux perturbation which is a result of practical importance is given as ($R_L(s)$ and $Q_L(s)$ are the Laplace transforms of the regression rate perturbation and the wall heat flux perturbation, respectively).

$$\frac{R_L(s)}{Q_L(s)} = \frac{2E_{E_a} s}{\left(1+\sqrt{4s+1}\right)\left(s+E_{E_a}\right) - 2E_{E_a} + 2E_L E_{E_a} s} \tag{4.33}$$

The first observation on the form of the derived transfer function is that it not a simple ratio of two polynomials. In fact the denominator is an irrational function. Another property is that the system has only one pole at s=0 for the real and positive values of the energy parameters. In the present study, we investigated the unit step heat input and oscillatory heat loading cases. The results will be discussed later in this chapter.

The collection of the ε^2 order terms yields the second order perturbation problem which can be expressed as follows.

$$\frac{\partial \overline{T}_2}{\partial \overline{t}} = \frac{\partial^2 \overline{T}_2}{\partial \overline{x}^2} + \frac{\partial \overline{T}_2}{\partial \overline{x}} + \overline{R}_1 \frac{\partial \overline{T}_1}{\partial \overline{x}} + \overline{R}_2 \exp(-\overline{x}) \tag{4.34}$$

Boundary conditions are

$$\left.\frac{\partial \bar{T}_2}{\partial \bar{x}}\right|_{\bar{\tau}=0} - E_L \bar{R}_2 = 0 \tag{4.35}$$

$$\bar{T}_2\big|_{\bar{\tau}\to\infty} = 0. \tag{4.36}$$

Initial condition can be written as

$$\bar{T}_2(\bar{x},0) = 0. \tag{4.37}$$

The second order regression rate equation has the form

$$\bar{R}_2 = E_{E_1}\bar{T}_2\big|_{\bar{\tau}=0} + \beta\left(\bar{T}_1\big|_{\bar{\tau}=0}\right)^2 \tag{4.38}$$

where $\beta = \dfrac{a(a+b+1)}{2(1+b)^4}$.

The solution for the second order perturbation problem stated above is presented in appendix C.

4.3 Discussion of Results

The methods described in the previous section are applied to generate simulations for various cases. The material properties used in the calculations are shown in table 4.2 [49, 50, 51, 52]. We follow the classification of the transient events in organizing the discussion of results.

4.3.1 Ignition

The ignition with constant heat transfer case for PMMA for various models is presented in nondimensional form in figure 4.3. For comparison purposes, in each calculation the same value for the constant heat flux is used. The shape parameters of the self-similar temperature profile model is tuned for the best match with the solution of the CWT problem. In the analytical and the numerical CWT solutions the initial heating time is included with the use of equation 4.22. While the overall shapes of the response curves for

the analytical model and numerical CWT cases look similar, the VWT model, which couples the wall temperature to the regression rate, yields a rather different response curve during the early stages of the transient. However the numerical solutions for the CWT and VWT models match perfectly at large times. The nondimensional time ($\tilde{t}_{90}$) corresponding to the 90% steady-state regression rate is observed to be 0.67. This value is rather different from 0.5 which was predicted by Marxman. This is due to the assumption on the shape of the profile, the exclusion of the initial heating period and secondarily to differences in material properties. In fact, numerical solutions for the CWT model show that the temperature profile is not self-similar in time, as it starts as an ierfc and relaxes to the equilibrium exponential distribution. Furthermore, the third order polynomial profile shape selected by Marxman does not give a good match to the numerical solution for PMMA, as figures 4.2 and 4.3 suggest.

Fuel Type	C *cal/gr-K*	ρ *gr/cm*^{3}	κ *mm*^{2} / sec	L_v *cal/gr*	T_s ‡ *K*	E_a § *kcal/mole*	E_{E_a} **	E_L
PMMA	0.37	1.1	0.11	231	620	30 - 40	12.6 -14.7	1.94
HTPB	0.57	0.93	0.098	433	820	12 - 60	4.7 - 23.4	1.45

Table 4.2. Thermophysical properties of the propellants used in the calculations.

It is important to notice that the form of the regression rate curves in the nondimensional coordinates for the constant heat transfer case depend only on the energy parameter, E_L. This suggests that E_L, which is a property of the fuel is also a similarity parameter of the thermal lag problem. In order to exhibit the effect of E_L on this specific transient, two numerical solution curves for PMMA (E_L=1.94) and HTPB (E_L=1.45) are shown in figure 4.4. It can easily be observed that an increase in E_L reduces the response time. This result is not restricted to this special case and it can be generalized to all types of transients. A possible explanation for this fact can be deduced from the physical interpretation of E_L, which is defined as the ratio of two possible energy modes for conversion of the total heat input. One mode is associated with the surface processes which are assumed to be infinitely fast in our model. The other mode is related to a slow process,

‡ These are the wall temperatures at a specified regression rate, which is 0.05 cm/sec for PMMA and 0.075 cm/sec for HTPB.

§ Instead of a single value, we give a range that covers the data in the literature.

namely the heat diffusion in the solid. Thus, E_L can also be treated as a parameter that shows the relative importance of the fast phenomena with respect to the slow phenomena.

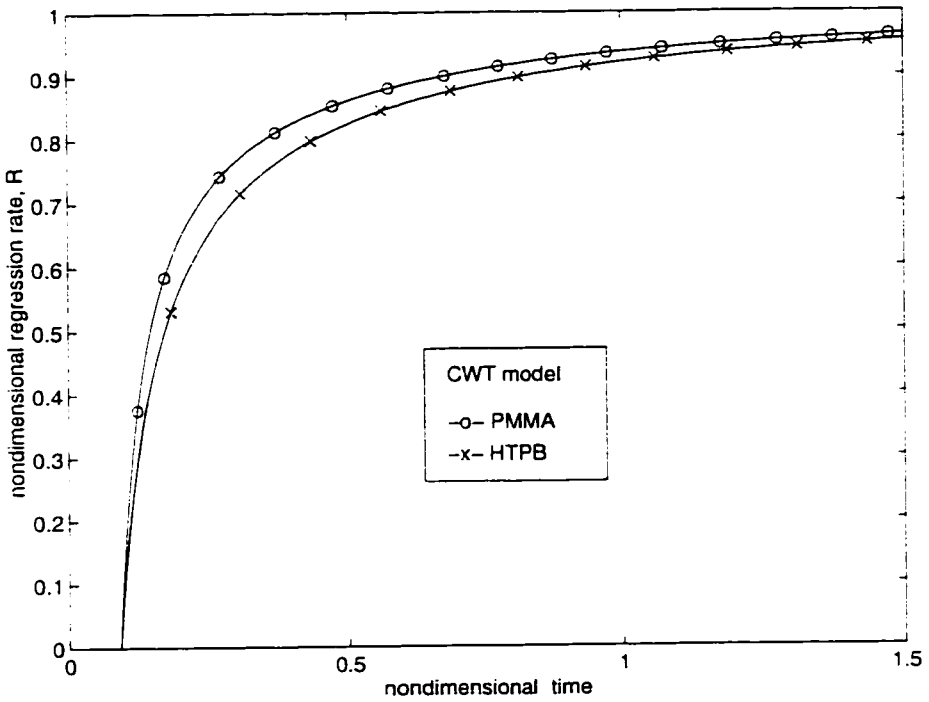

Figure 4.4. Effect of the energy parameter, E_L on the response for ignition with constant heat transfer. Reference: $\dot{r}_{ref} = 0.05$ cm/sec and $\tau_{ref} = 0.4$ sec. Initial heating period is included.

4.3.2 Throttling

TLC is used to simulate numerous throttling events of interest. We first studied the sharp throttling cases which were modeled by step functions for the heat loading. Figure 4.5[**] shows a 10:1 ratio throttle up simulation for PMMA. The response seems to follow the sudden increase perfectly, but it overshoots its asymptotic value by approximately 25% and ultimately relaxes to the second equilibrium, in a relatively long period of time, which appears to be proportional to the characteristic time, τ_{tl}.

A careful investigation on the temperature profiles at various stages of the transient is helpful in understanding this interesting phenomenon. For that reason, the regression rate response and the temperature profiles at certain instants of that response are plotted in

[**] Ambient temperature is taken 300 K in the calculations.

nondimensional parameters for a throttling ratio of 1.5:1 for PMMA, in figure 4.6. In the figure, points A, B and C corresponds to the initial equilibrium, maximum regression rate and final equilibrium times of the throttling transient, respectively. It is obvious from figure 6 that after a short time period from the sudden change in the input, only a small region of the temperature profile next to the wall responds rapidly, while the rest of the profile remains unchanged. In fact, the surface temperature and the surface temperature gradient are matched to their correct asymptotic values (point C), at a point in between A and B. The overall temperature profile is significantly different from the near equilibrium profile corresponding to point C.

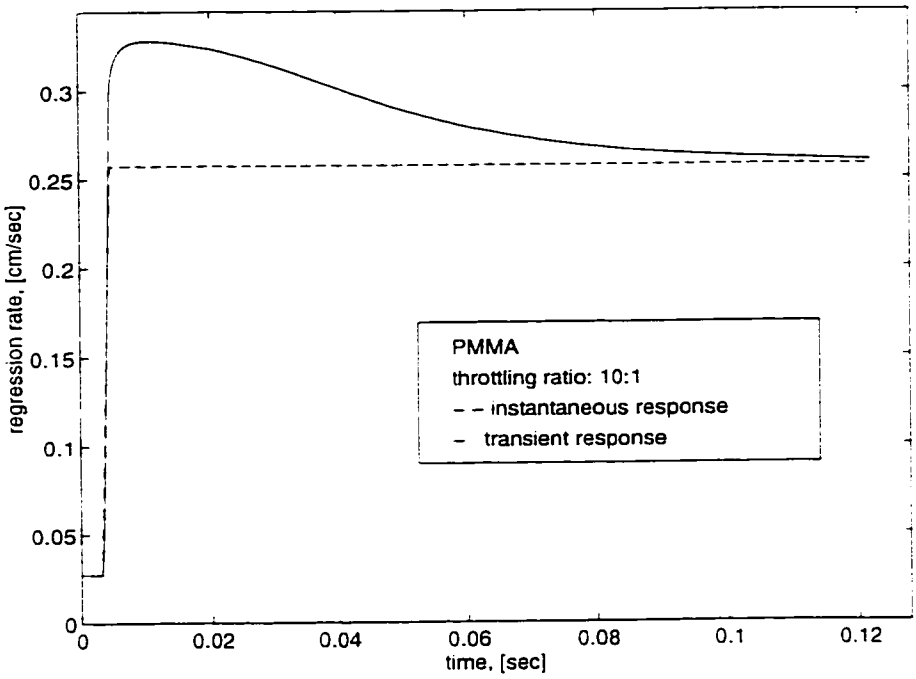

Figure 4.5. Illustration of the overshooting phenomenon for a sharp 10:1 throttling. The overshooting of the regression rate is approximately 25% of its asymptotic value

These observations indicate that the thermal lag system has two time scales. The surface time scale is related to the sudden adaptation of the temperature profile in a small zone next to the wall. The overshooting phenomenon occurs within this surface time scale. The larger time scale is the well known thermal relaxation time of the thermal profile in the solid. The thermal time scale governs the relaxation process of the temperature profile and the regression rate to their equilibrium state from the exited state.

[†] The instantaneous response curves included in figures assume zero thermal lag. So, they represent the shape of the heat input.

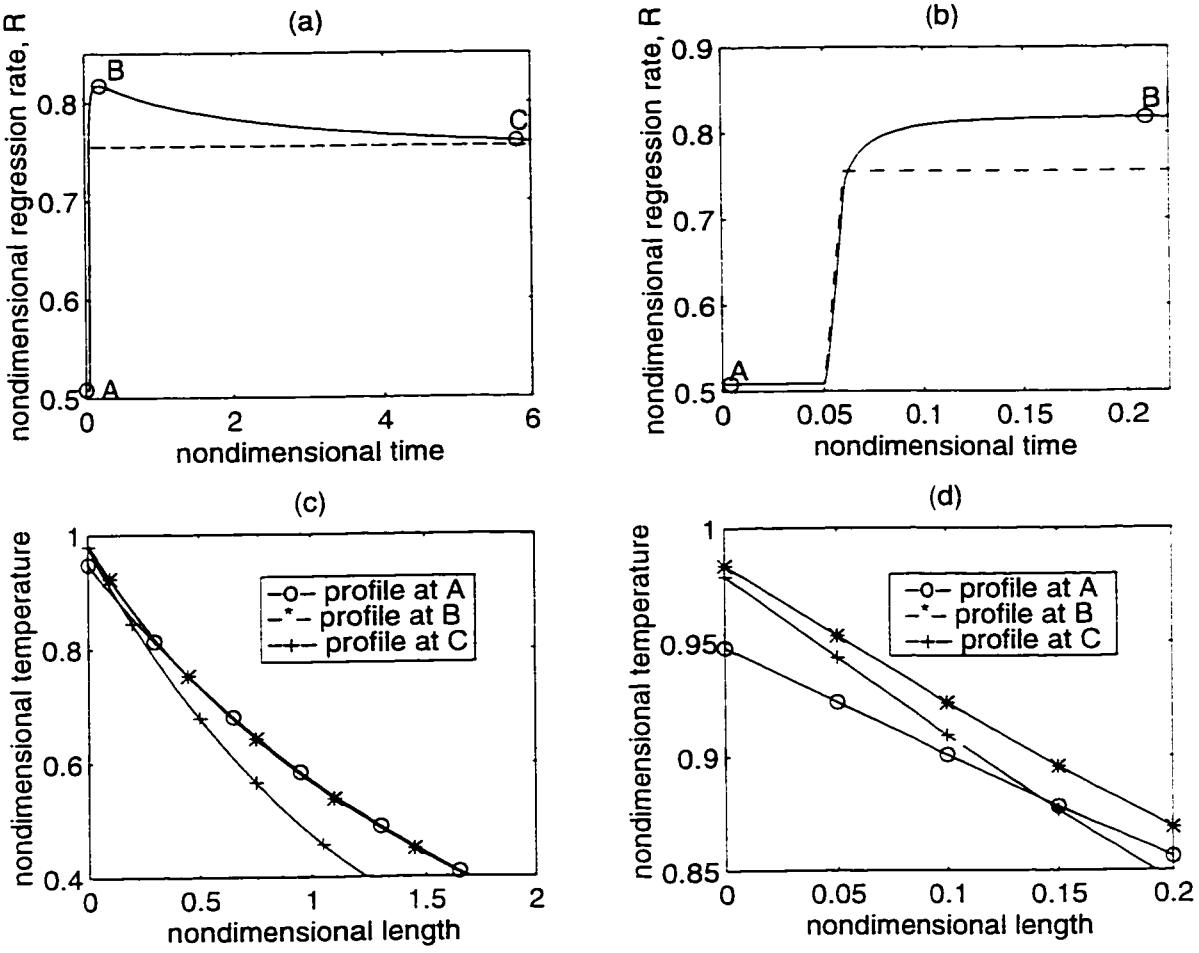

Figure 4.6. Explanation of the overshooting phenomenon: (a) Response of regression rate for a 1.5:1 ratio sharp throttle up transient for PMMA. (b) Close up to the rapid change region. (c) Temperature profiles at the instants tagged in plot (a). (d) close up to the near wall region of the temperature profiles. All the plots are in nondimensional variables as defined in 4.11 and 4.13. Reference: $\dot{r}_{ref}$ = 0.106 cm/sec, τ_{ref} = 0.091 sec and δ_{ref} = 0.0096 cm.

As a literature survey will confirm [51, 53, 54], reliable data on the activation energy is not available for the fuel types of interest. Thus the dependence of response on the activation energy is studied parametrically for PMMA and HTPB fuel types. The regression rate response for various activation energies for a throttling ratio of 1.5:1 of PMMA and HTPB fuels are shown in figures 4.7 and 4.8 respectively.

It can be observed from the figures that the activation energy alters the behavior of the response significantly. The common feature of the transients at different activation energy levels, is the overshooting and the relaxation back to the target equilibrium state. However, at high activation energies the regression rate overshooting which is defined as

$\left|\dot{r}_{\max} - \dot{r}_f\right| / \dot{r}_i$ is more apparent and the regression rate takes its maximum value in a rather short time compared to the thermal relaxation time. An interesting observation from figure 4.7 is for infinite activation energy which represents the constant wall temperature situation. The solution here is singular at the discontinuity of the input. At this point the regression rate jumps from its initial value to the maximum regression rate, which is approximately 50% higher than the final regression rate for this specific throttling ratio. Thus, the surface time scale is zero. The rest of the response is simply a monotonic relaxation to the second equilibrium in a period on the order of the thermal relaxation time, τ_{ref}. As shown in figure 4.7 the constant wall temperature case is an envelope for family of the response curves generated by the finite activation energies and it determines the upper bound for the overshoot for a specified throttling ratio. In the other extreme of very low activation energies as shown in figure 4.8, the overshooting phenomenon is less significant and the response is similar to the behavior of a first order system.

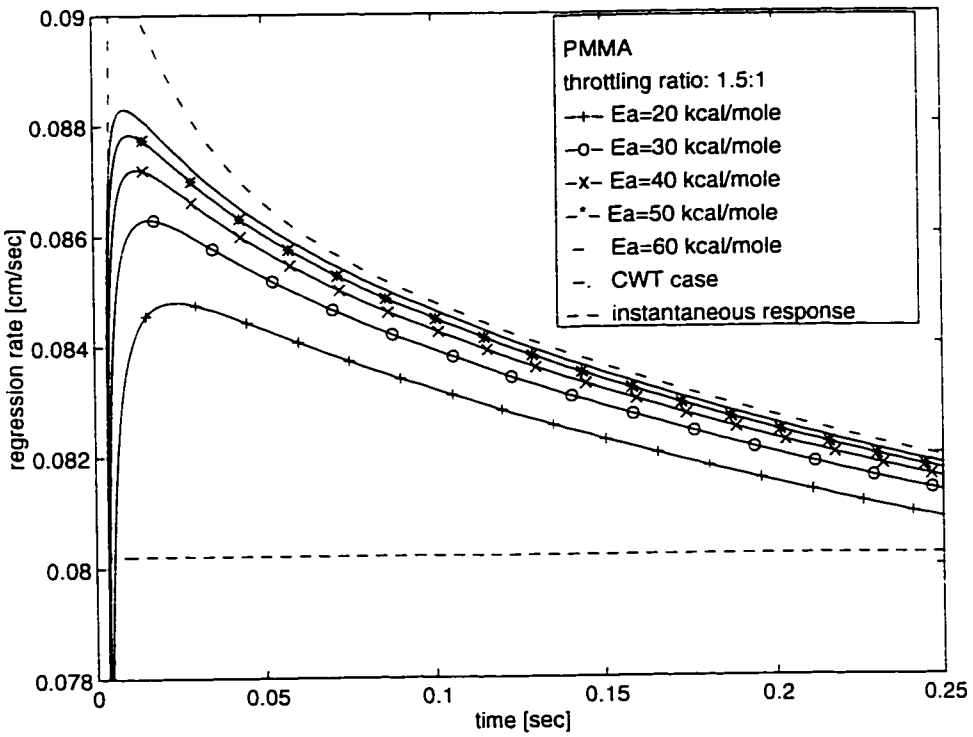

Figure 4.7. Effect of activation energy on the shape of the response for PMMA fuel. Note that CWT case envelopes the other solutions.

The effect of activation energy on these time scales is of fundamental importance. The surface time scale is influenced by the surface phenomenon and must be related to the activation energy. In fact, it is clear from the simulation results that increasing activation

energy reduces the surface time scale. However, the thermal time scale is unaffected by the activation energy, since it is essentially related to the heat diffusion process in the solid. At high activation energies for which the surface time scale is much smaller than the thermal time scale, very little diffusion takes place over the span of the surface time scale. As a result of this, the overshooting is significant. In the opposite extreme of low activation energies the surface time scale becomes comparable to the thermal time scale. In this regime the thermal diffusion makes the overshooting less apparent.

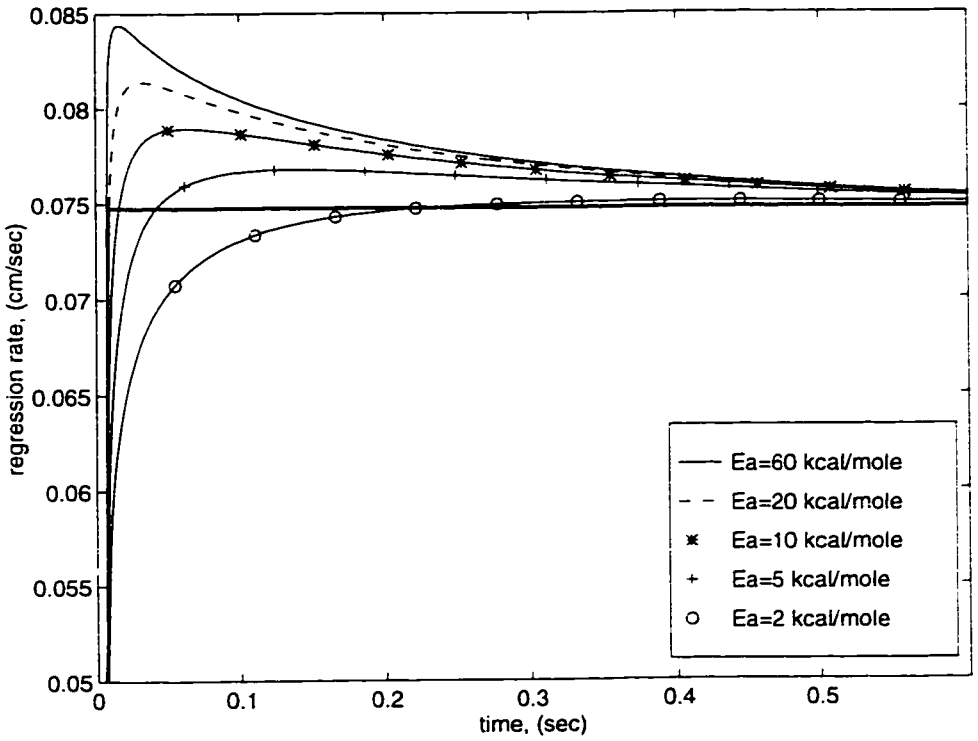

Figure 4.8: Effect of activation energy on the regression rate response for throttling event for a HTPB system with τ_{ref}=0.4 seconds. Throttling ratio is 1.5:1.

In order to support the preceding argument we will derive a scaling expression for the surface time scale in terms of the activation energy and the throttling ratio. We start with noting that the instantaneous regression rate response intersects the quasi-steady line at a point between A and B. For simplicity, we arbitrarily define the surface time scale as the time interval from the start of the transient to the intersection point. This definition of the surface time scale simplifies the treatment, since at the intersection point the surface temperature is equal to the final equilibrium temperature. Moreover from the energy balance at the surface, it can be argued that the surface temperature gradient must also be equal to

the surface gradient at the final equilibrium state. Thus at this point of intersection we can write the following expression for the surface length scale

$$\delta_s = \frac{T_{sf} - T_{si}}{|\partial T/\partial x|_{sf}}$$

Here the subscripts si and sf stand for the surface values at the start and the end of the transient.

The gradient term can easily be determined from the final equilibrium profile.

$$\delta_s = \frac{T_{sf} - T_{si}}{T_{sf} - T_a}\delta_{tl}$$

The Arrhenius expression can be used to write this equation in terms of the throttling ratio and the activation energy.

$$\frac{\delta_s}{\delta_{tl}} = \frac{T_{si}^2 \ln(\dot{r}_f/\dot{r}_i)}{T_{si}T_a \ln(\dot{r}_f/\dot{r}_i) + (T_{si} - T_a)E_a/R_g} \tag{4.39}$$

After noting that $\tau = \delta/\dot{r}$, we can express the ratio of time scales as

$$\frac{\tau_s}{\tau_{tl}} = \frac{T_{si}^2 \ln(\dot{r}_f/\dot{r}_i)}{T_{si}T_a \ln(\dot{r}_f/\dot{r}_i) + (T_{si} - T_a)E_a/R_g}. \tag{4.40}$$

It is clear from equation 4.40 that as the activation energy increases, the surface time scale gets smaller with respect to the thermal lag time scale. This results supports the previous arguments. The scaling expression also predicts that the surface time scale and the thermal lag time scale are on the same order during an ignition event which serves as an explanation why the overshooting phenomenon is not observed during ignition.

The effect of the throttling ratio, $\dot{r}_f/\dot{r}_i$, on the relative overshooting is an other issue of practical importance and demonstrated in figure 4.9 for PMMA and E_a=30 kcal/mole. The conclusions can be generalized to other types of polymeric fuels in use. For

the throttle up situation, the relative overshooting increases monotonically with the throttling ratio. However, in the throttle down case the relative excursion increases up to a maximum value and then decreases to zero at zero throttling ratio ($\dot{r}_f/\dot{r}_i = 0$) which represents the thrust termination event. Although, the first order perturbation analysis indicates that throttling up response is a mirror image of the throttling down response, the numerical studies show asymmetry (unless the throttling ratio is small). This nonlinear effect can be captured with higher order perturbation solutions.

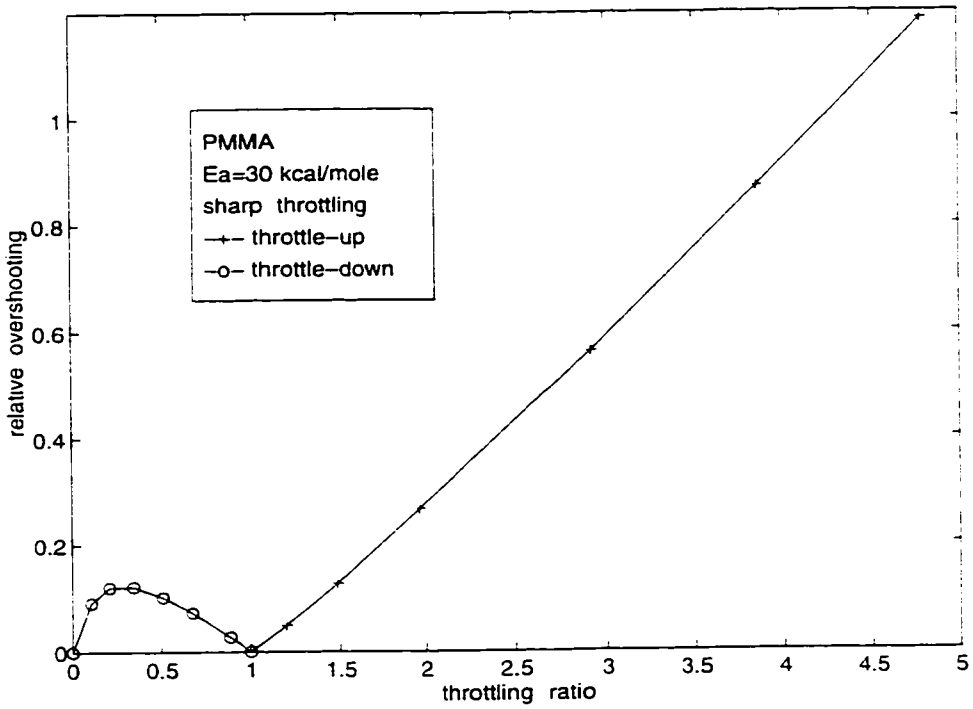

Figure 4.9. Effect of the throttling ratio, $\dot{r}_f/\dot{r}_i$, on the relative overshooting, $|\dot{r}_{max} - \dot{r}_i|/\dot{r}_i$. The nature of the throttle up and throttle down cases are significantly different.

In the previous paragraphs, we discussed the instantaneous throttling case which corresponds to an infinite rate of throttling. It is instructive to consider the more practical case of finite throttling response of the thermal lag system, since, in reality, the sudden increase of the heat input cannot be achieved because of the time lags related to the other transient phenomena in the rocket motor. Moreover finite throttling serves as a bridge to the situation of sinusoidal heat loading which will be investigated later in this chapter. Figure 4.10 shows three numerical simulation results for different throttling rates. The important observation is that for small throttling rates the transient response anticipates the heat input. Similar behavior will be observed in the sinusoidal heat loading case. Figure 4.10b indicates that for all rates there is a finite time range right after the start of the heat loading

when the response lags the input. The extent of this lag region increases as the throttling rate increases.

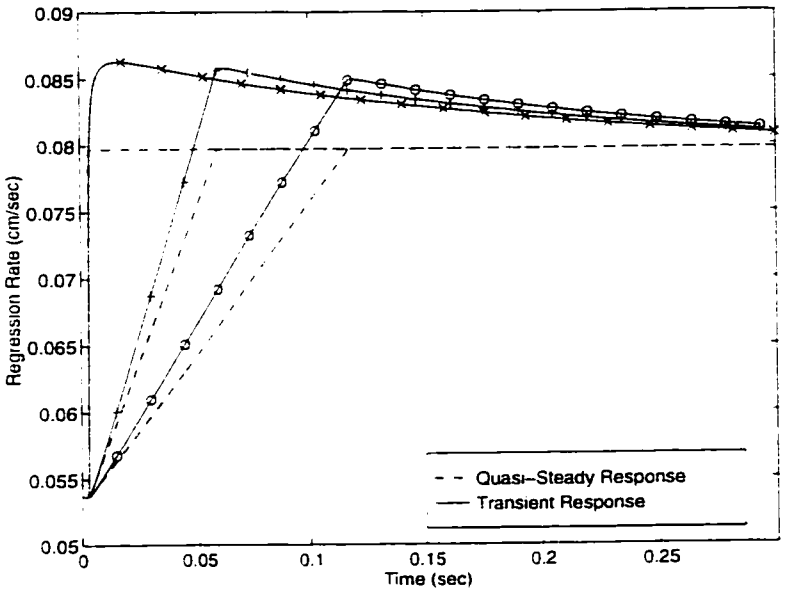

(a)

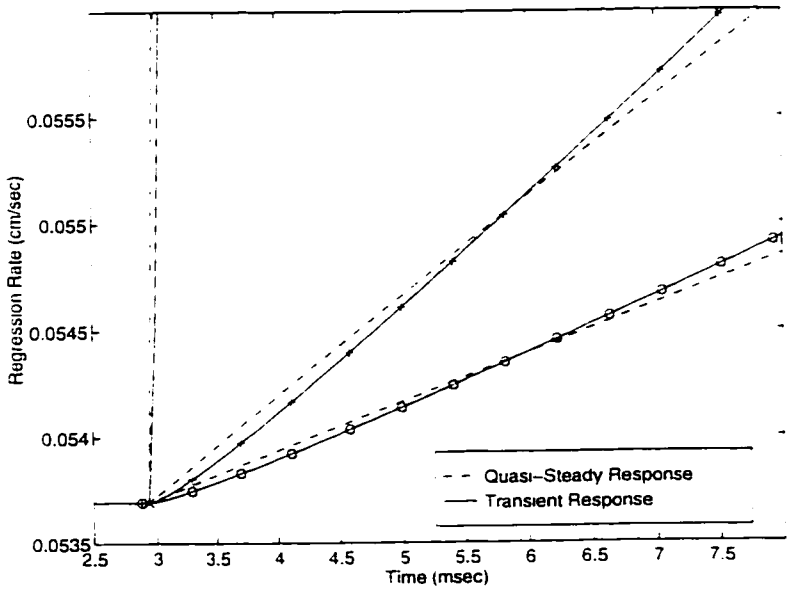

(b)

Figure 4.10 : Effect of throttling rate on the regression rate response. PMMA system with τ_{ref} =0.4 sec. E_a=30 kcal/mole and a throttling ratio of 1.5:1. a) Global response b) Initial response.

Next we applied a unit step input that simulates the sharp throttling event to our linearized thermal lag solution in order to confirm the numerical simulation results. The substitution of $Q_L(s) = 1/s$ yields the proper response function in the s domain.

Unfortunately, an easy way of inverse transformation back to the physical domain is not available. Thus, we will study only the limiting cases of step input solutions. The application of the final value theorem [55] gives

$$R_1(\infty) = \lim_{s\to 0} s\frac{R_L(s)}{Q_L(s)}\frac{1}{s} = \frac{E_{E_1}}{1 + E_{E_1} + E_L E_{E_1}}. \tag{4.41}$$

Note that $R_1(\infty)$ is the equilibrium regression rate corresponding to the new heat input and it can be shown that $R_1(\infty)$ satisfies the steady-state energy balance at the surface.

We now apply the small expansion theorem, in order to obtain the short time response. For large values of Laplace transform variable, s, we obtain the following expression for the transform of the regression rate

$$R_L(s) \approx \frac{E_{E_1}}{s\left(\sqrt{s} + E_L E_{E_1}\right)}.$$

This equation can be inverted with use of the transform tables to yield the following time response which represents the early portion of the transient.

$$R_1''(\bar{t}) = \frac{1}{E_L}\left[1 - \exp\left(\left(E_L E_{E_1}\right)^2 \bar{t}\right) erfc\left(E_L E_{E_1}\sqrt{\bar{t}}\right)\right]$$

It is easy to evaluate the large time limit of this expression

$$R_1''(\infty) = \lim_{\bar{t}\to\infty} R_1''(\bar{t}) = \frac{1}{E_L}. \tag{4.42}$$

The comparison of equation 4.41 with equation 4.42 yields the result which is valid for the practical values of the energy parameters.

$$R_1''(\infty) > R_1(\infty)$$

We claim that this inequality serves as a proof for the overshooting phenomenon observed in the numerical calculations, where $R_1^o(\infty)$ can be treated as an upper bound for the overshooting.

4.3.3 Oscillatory Combustion

The application of the sinusoidal heat input at a specific frequency simulates regression rate behavior during unstable motor operation. Due to its practical significance we investigated the frequency response of the linearized thermal lag system. In the calculations, a wall heat flux perturbation of the form of a sine wave with a specified amplitude and frequency is applied. Since the transfer function of the thermal lag system is already known, the response of the regression rate can easily be calculated.

We apply a sinusoidal heat input, $Q_1(\bar{t}) = \sin(\bar{\omega}\,\bar{t})$ which has the Laplace transformation

$$Q_L(s) = \frac{\bar{\omega}}{s^2 + \bar{\omega}^2}. \tag{4.43}$$

Note that $\bar{\omega}$ is the nondimensional frequency. The corresponding dimensional angular frequency is $\omega = \bar{\omega}/\tau_{tl}$ where τ_{tl} is the thermal lag time corresponding to the nominal operating point.

Coupling $Q_L(s)$ with the transfer function yields the response function of the regression rate, $R_L(s)$, in the s domain. Inverse transformation back to the time domain can be achieved with the use of the residue theorem [55, 56, 57]. In the analysis, we are only interested in the forced response, since the influence of the natural response is expected to be confined in a relatively small time period for practically significant applications. This fact is confirmed by the numerical simulations.

We will first consider the two limiting behaviors for which the explicit expressions can be obtained relatively easily. The first limit is the low frequency case ($\bar{\omega} \to 0$) in which the response simplifies to

$$R_1(\bar{t}) = R_1^{qs} \sin(\bar{\omega}\,\bar{t}) \tag{4.44a}$$

where the amplitude can be written as

$$R_1^{qs} = \frac{E_{E_1}}{E_L E_{E_1} + E_{E_1} + 1}. \tag{4.44b}$$

At very low frequencies the regression follows the variations in the wall heat flux in a quasi-steady manner. Namely, the amplitude of the regression rate is the steady value associated with the heat flux at the time of interest and the phase difference is zero. In the dimensional form the time dependent component of the regression rate has the form

$$\dot{r}(t) \propto \dot{r}^{qs} \sin(\omega\, t)$$

where $\dot{r}^{qs}$ is the quasi-steady response to the wall heat flux oscillation.

The other limit is the high frequency one where the response becomes

$$R_1(\bar{t}) = \frac{E_{E_1}}{\sqrt{\bar{\omega}}} \sin(\bar{\omega}\,\bar{t} - \frac{\pi}{4}). \tag{4.45}$$

In the other extreme of very large frequencies, the regression rate lags the wall heat flux with a 45 degree phase angle. The drop of the amplitude of the oscillatory component follows asymptotic form of $1/\sqrt{\omega}$ as indicated in the dimensional form of the asymptotic formula

$$\dot{r}(t) - \dot{r}_{ref} \propto \frac{1}{\sqrt{\omega}} \sin(\omega\, t - \frac{\pi}{4}).$$

The response at the intermediate frequencies is quite interesting. As a typical example we will consider the special case of a PMMA system (The physical properties used in the calculations are shown in table 4.2) with a thermal characteristic time of τ_{tl}=0.5 sec. The normalized regression rate amplitudes and phase differences between the regression rate and heat flux are plotted over a range of frequencies in figure 4.11. For convenience,

the amplitudes shown in the figure are normalized with respect to the quasi-steady response (by equation 4.44b). It is apparent that for relatively small frequencies, f <80 Hz, the regression rate oscillations are amplified. The amplitude of the regression rate increases from its quasi-steady value and takes a maximum value (at a small frequency close to 4 Hz). For this specific case, the maximum amplitude is approximately 25% larger than R_1^{qs}. At higher frequencies, the amplitude of the response monotonically decreases with the increasing frequency. At a moderate frequency, it crosses the quasi-steady amplitude after which it is attenuated. Eventually, the amplitude response reaches its asymptotic behavior at very high frequencies.

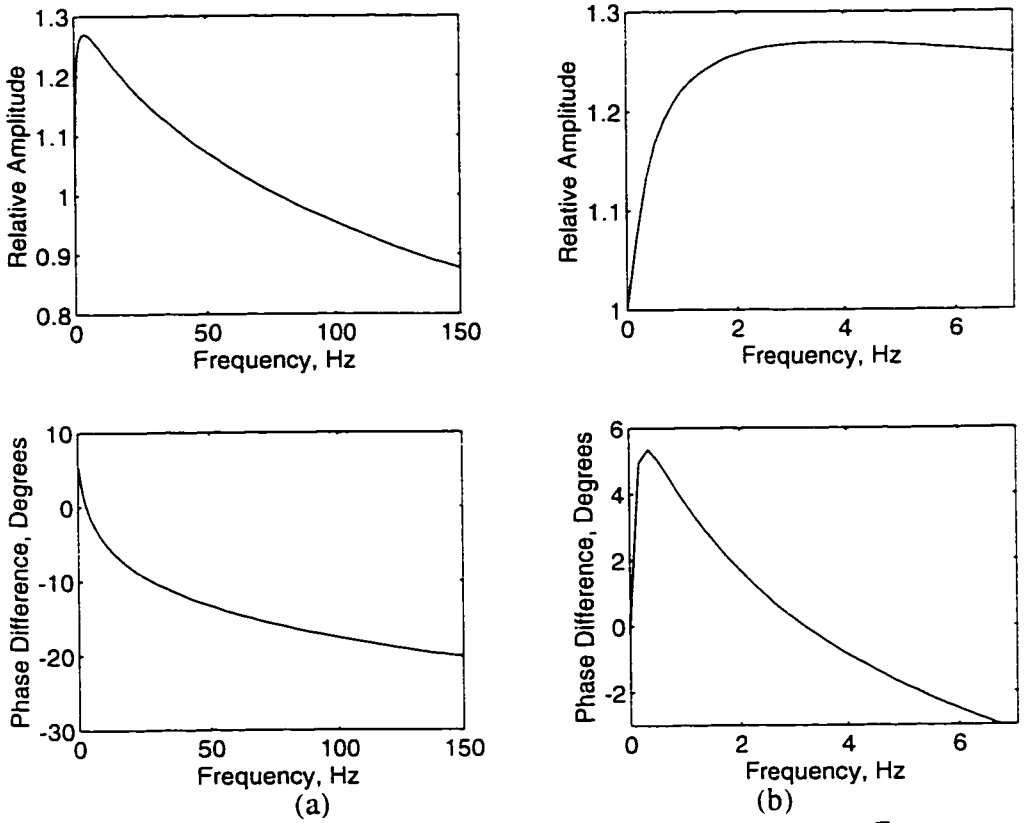

Figure 4.11. Frequency response for the thermal lag system. PMMA fuel with E_a=30 kcal/mole and τ_{ref}=0.5 sec. a) Wide frequency range b) Close up to the low frequency range. The relative amplitude is defined as R_1/R_1^{qs} where R_1^{qs} is the quasi-steady amplitude defined by equation 4.44b.

The nature of phase difference response is also worth noting. In a small range of frequencies close to zero, the regression rate leads the wall heat flux input. Specifically, the phase difference starting from zero at zero frequency, increases to a maximum phase lead which occurs at a small frequency. Later the phase difference starts decreasing and it crosses the zero axis (at which the regression rate and the heat flux are in phase one more

time). For the frequencies larger than this crossing frequency the regression always lags the heat flux input. Eventually the phase asymptotes to $-\pi/4$ monitonically at very high frequencies as mentioned previously. In short, for frequencies smaller than this crossing frequency, the regression rate leads the heat flux input, whereas, for higher frequencies it lags. The low frequency behavior, implying a lower rate of change of heat flux, parallels the $\dot{p}$ extinguishment in solid propellants where the burn rate "anticipates" the steady-state leading to a zero burn rate prior to the steady-state value.

The region of amplitude amplification is much wider than the region of the phase lead in the frequency domain. The amplification of the regression rate is on the order of 20-30% for the practical operating regimes of hybrids. We also note that no resonance behavior is observed for any set of parameters. For that reason, it can be stated that the thermal lag system is inherently stable at least in the linear regime and the thermal lags alone can not generate the low frequency oscillations observed in hybrids. However, it is shown that the thermal lag system favors the low frequency oscillations because of the amplification.

At this point it is instructive to discuss the relation of these results on the thermal lag response to the solid rocket low frequency instabilities. It is clear that the thermal lag model presented here, can also be applied to the solid rocket fuel grains. It is well known from solid rocket L^* theory [38] that a solid rocket may present low frequency instabilities, if the regression rate leads the pressure oscillations. Since for solids the combustion is pressure dependent, the wall heat flux will mainly be a function of the chamber pressure (even during the transients). Thus it is the phase lead of the regression rate as it is shown in this section that generates the L^* instabilities. But the essential ingredient of this type of an instability is the explicit dependence of the wall heat flux on the chamber pressure. However, the hybrids do not possess this ingredient, since the combustion is mainly diffusion limited and the wall heat flux fails to have significant dependence on the pressure. In short even though there may be some combustion leads generated by the thermal lags in the solid, hybrids do not appear to possess low frequency instabilities in the L^* theory framework. This is of course due to the lack of direct coupling of chamber pressure with those combustion lead times.

The different selection of the parameters such as heat of gasification, activation energy or the characteristic thermal lag time (i.e. L_v, E_a and $\kappa/\dot{r}$) does not alter the

qualitative nature of the frequency response. However various quantitative features of the thermal lag response such as the width of the phase lead region or the amplification region. that can influence the overall dynamics of the system, depend on those parameters. For that reason. it is desirable to perform a parametric investigation to explore the effect of each relevant parameter.

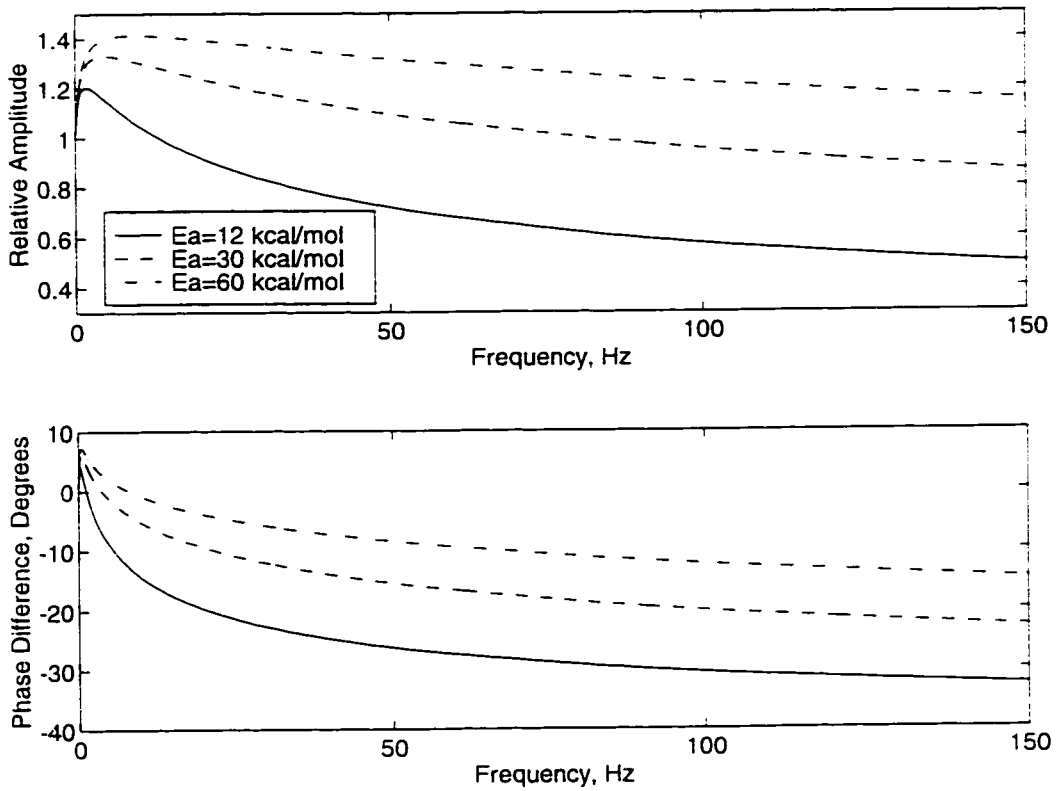

Figure 4.12. Effect of activation energy on the frequency response of the thermal lag system. The plot is for a HTPB system with τ_{ref} =0.4 seconds. The relative amplitude is defined as R_1 / R_1^{qs} where R_1^{qs} is the quasi-steady amplitude defined by equation 4.44b.

The influence of the activation energy is shown in figure 4.12 for an HTPB system operating at a nominal condition corresponding to a characteristic time of τ_{tl}=0.4 seconds (Note that $\tau_{tl} = \tau_{ref}$). The effect of increasing activation energy is to enlarge the amplification and the phase lead regions in the frequency domain. As the activation energy increases the magnitude of the relative amplification and also the value of the maximum phase lead increases. This observation is related to the overshooting phenomenon discussed in the context of throttling. At high activation energies, as described in the preceding section, the surface time scale is small and overshooting is significant. The response can lead and amplify a faster changing input through the overshooting phenomenon. Thus the phase lead and amplification domains get larger as the activation

energy increases. In the limiting case of infinite activation energy that corresponds to the constant wall temperature model (CWT), the phase lead and relative amplification covers the whole spectrum. Namely, the relative amplification and phase lead increase to their maximum values at zero frequency and they stay constant for the whole frequency spectrum. For very small activation energies the frequency response behaves like the response of a first order system which does not possess any amplification or phase lead regions.

It is determined that the effect of the energy parameter, E_L, on the frequency response is secondary for the fuels typically used in hybrid applications. The influence of the thermal lag time is to linearly stretch the frequency axis of the response curves such that a system with smaller thermal lag time will have a broader frequency range of amplification and phase lead.

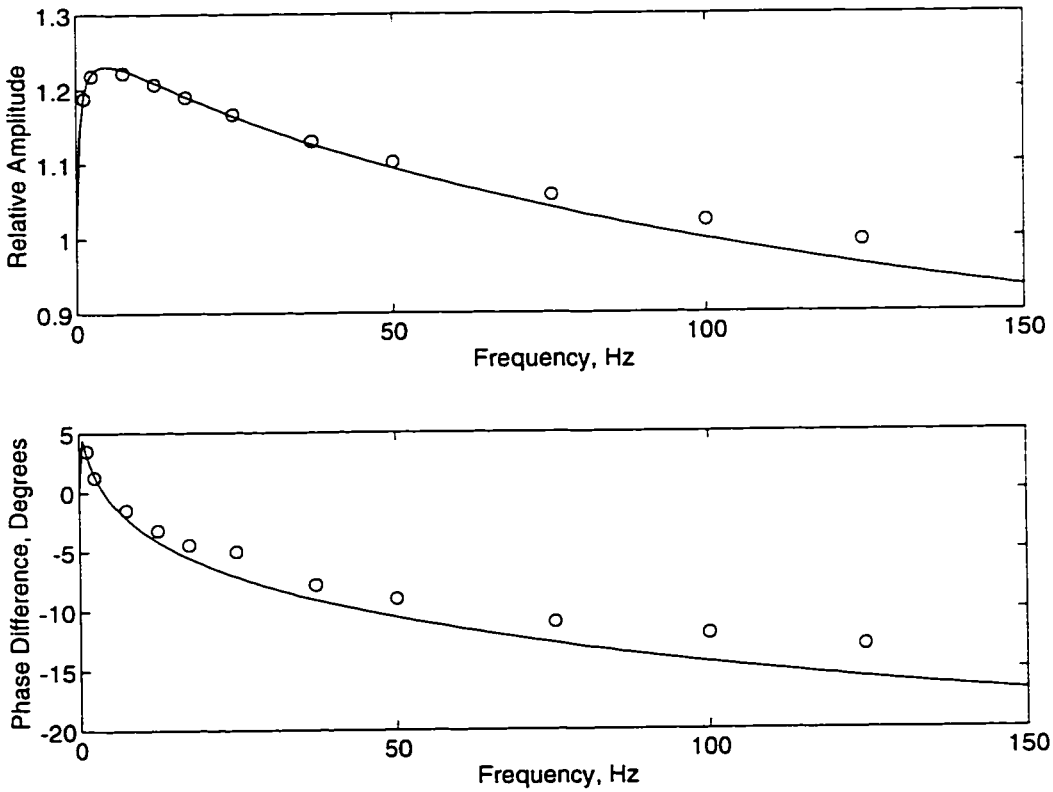

Figure 4.13. Comparison of numerical simulation results with the perturbation estimates. The plot is for a system with E_L=2.333, E_a=30 kcal/mole and τ_{ref}=0.4 seconds. For the numerical calculations a heat flux oscillation with an amplitude of 40% of the mean is used.

In order to explore the possible nonlinear effects on the response and to confirm the perturbation analysis results, we performed some numerical simulations of the sinusoidal heat input case. The details of the numerical algorithm used in the simulations are discussed in section 4.2.2.

We first note that the results of this perturbation analysis are in good agreement with the numerical simulations even for relatively high oscillation amplitudes such as 40% of the mean value. The comparison of the perturbation results with the numerical simulations for various frequencies is shown in figure 4.13. We believe that the larger errors at high frequency values is mainly due to the inaccuracies in the amplitude and phase difference calculations made from the numerical simulation data.

Another important observation that is made from the numerical simulation results is the existence of a small shift of the mean regression rate above the mean quasi-steady value. This is consistent with the experimental findings indicating increased mean regression rates during the oscillatory modes of combustion.

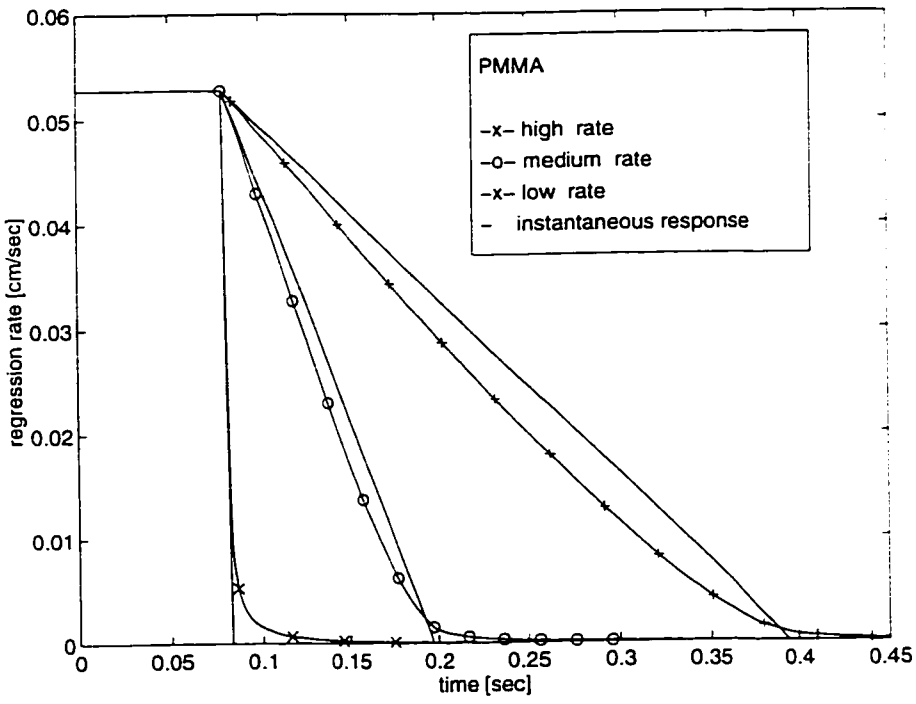

Figure 4.14. Thrust termination response for various thrust termination rates.

4.3.4 Thrust Termination

The thrust termination case is simulated using a heat input model that gradually drops from a constant value to zero. The proper initial condition is the steady-state temperature distribution at the initial heat input. Figure 4.14 indicates that for sudden thrust termination cases, the regression rate closely follows the heat input except in a region next to the zero regression rate point. As the rate decreases the transient response starts to lead the instantaneous response. This behavior is well known in solid rockets [58].

4.3.5 Combined Simulation

In order to prove the capability of the TLC, we tried a combination of several transient events (ignition, throttle up and thrust termination) in a single run. The simulation result is shown in figure 4.15.

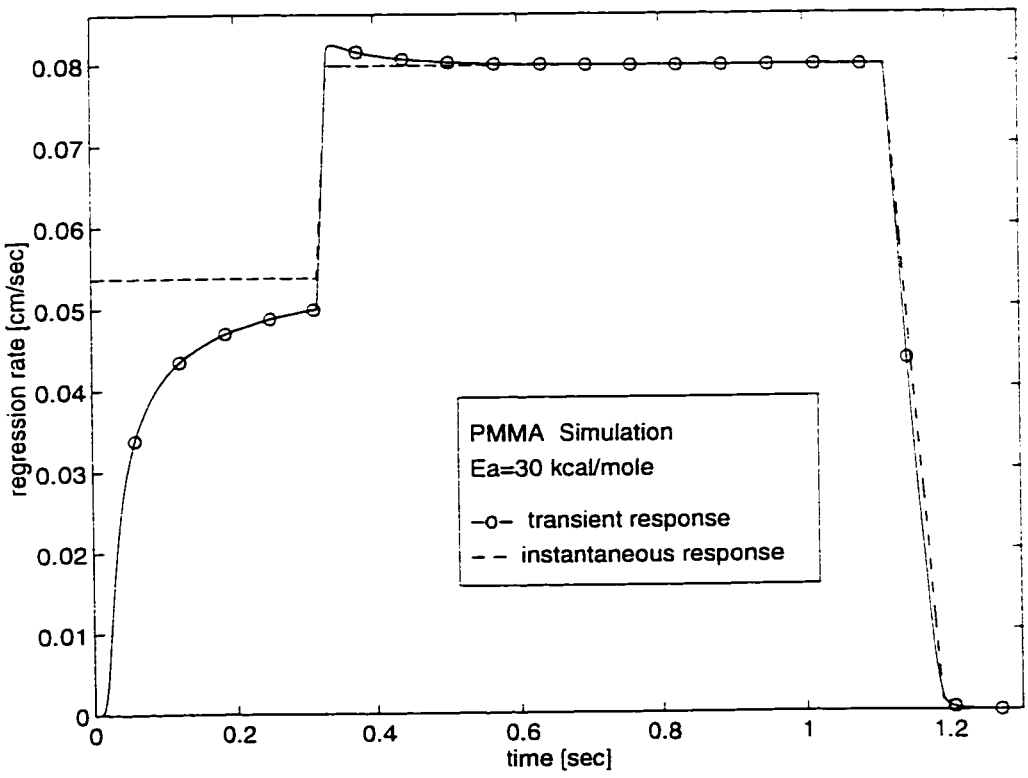

Figure 4.15. Combined transient case.

4.4 Conclusions for the Thermal Lag Theory

In this chapter study, the thermal lags in the solid are extensively investigated. Two analytical methods for the solution of the thermal lag problem are developed. Although, their usage is limited to the treatment of only some special transient events, they yield significant information which enhanced the understanding of various interesting phenomena. However, the numerical solution techniques can be applied to a much broader spectrum of transient events. In fact, TLC is capable of estimating the response of the regression rate for almost all practically important events with high accuracy and within a reasonable amount of computer time. However, we believe that the efficiency of the code may still be increased.

It has previously been recognized that the thermal transients in the solid are slow, but this study is indicating a new insight with regard to the influence of an effective activation energy which determines the variation in wall temperature with a variation in heat flux. As shown here, the percent of the sudden increase in $\dot{Q}_w$, which results in a sudden increase in regression rate depends on how much of the heat flux increase goes into gasification and how much into thermal heating of the solid. It is shown here that this split depends on both the activation energy and the vaporization energy which is related to the E_L parameter.

The thermal lag model introduced in this paper can be improved by relaxing some of its assumptions. It may be worth exploring the effect of the temperature dependence of thermal properties, especially the thermal diffusivity, on the response. Another improvement might be the application of the theory in the polar coordinates. The introduction of another length dimension (hydraulic diameter of the port) will allow one to investigate the scaling effects on the thermal response time.

In our analysis, we treated the wall heat transfer as the input of the problem. However, in a hybrid system the heat transfer is an internal parameter and can not be directly controlled during the operation of the motor. Thus, a complete transient hybrid theory should relate the wall heat transfer to the controllable parameters of the problem, such as the oxidizer mass flow rate. In the next two chapters, we develop models for the transient phenomena other than the thermal lags in order to obtain a more mature understanding of the dynamics of the hybrid combustion system. In that respect, the

thermal lag theory developed in this chapter, which is an essential component of the full transient picture, is not complete by itself.

Chapter 5

Transient Hybrid Combustion Theory and TC Coupling

In the previous chapter we investigated the thermal lags in the solid fuel grain and developed a model to calculate the variations in the regression rate for specified changes in the wall heat flux that simulates various transient events. This model inherently treats the wall heat flux as a parameter that can directly be controlled. However, in a hybrid motor, the actual control parameter is the oxidizer mass flow rate whereas the wall heat flux is just an internal parameter that will be adjusted after the specification of mass flow rate and other relevant parameters such as the geometry.

The actual response of the motor to a change in the oxidizer mass flow is rather complicated. As the oxidizer mass flow rate of the motor changes, the mass flux at a characteristic point in the port reacts to the change with a certain dynamics that is determined by the gasdynamic characteristics of the rocket motor. Meanwhile the turbulent boundary layer developed over the fuel surface responds dynamically to the changes in the port mass flux. In this section we will focus on the modeling of the boundary layer combustion dynamics and investigate its interactions with the thermal lags in the solid. The treatment of the gasdynamic response of the combustion chamber is delayed to the next chapter.

5.1 Quasi-Steady Combustion Theory

In our preliminary model we will assume that the boundary layer response is quasi-steady, namely the boundary layer diffusion lag times are small compared to the thermal lag times. Later in this section we will relax this simple assumption by considering the

boundary layer diffusion dynamics with use of simple constant delays. Under the quasi-steady assumption we will be able use to Marxman's classical approach [6, 7, 8] to calculate the response of the wall heat flux to the changes in mass flux. However, the results of classical hybrid theory can not be used directly due to the fact that the convective heat transfer to the wall is affected by the regression rate through the blocking generated by the blowing of the gaseous fuel from the surface. In the presence of the thermal lags the blocking generates a coupling mechanism in the gas phase between the regression rate and the wall heat flow.

In this section we follow the classical approach to derive the relation between the wall heat flux, regression rate and local mass flux. In our analysis we assume that the system is purely convective (i.e. the radiative heat transfer is small compared to the convective transfer) and the boundary layer properties are constant. We also make use of the key steady-state assumption that the boundary layer responds rapidly compared to other transient processes involved in the problem such as the thermal lags.

During any transient the energy balance at the surface can be written as

$$\dot{Q}_c(t) = \dot{r}(t)\rho_f L_v - \lambda\left(\frac{\partial T}{\partial x}\right)_s \tag{5.1}$$

Here, $\dot{Q}_c(t)$ is the convective heat flux from the gas to the fuel surface and λ is the heat conduction coefficient in the solid. Next we define the heat transfer coefficient C_H at time t as

$$\dot{Q}_c(t) = C_H \rho_b u_b (h_b - h_w) = C_H \rho_b u_b \Delta h \tag{5.2}$$

where h_b and h_w are enthalpies at the flame and at the wall respectively. Note that all variables are functions of time.

We now assume that the Reynolds analogy is still valid during this quasi-steady operation mode. This allows us to express the heat transfer coefficient in terms of the skin friction coefficient as

$$C_H = \frac{1}{2} C_f \frac{\rho_e u_e^2}{\rho_b u_b^2} \tag{5.3}$$

After the elimination of the heat transfer coefficient, we obtain the following expression for the wall heat flux.

$$\dot{Q}_c(t) = \frac{1}{2} C_f G \frac{u_e}{u_b} \Delta h \tag{5.4}$$

where G is the total mass flux $\rho_e u_e$.

At this point it is useful to define an aerodynamic blowing parameter (also known as the mass transfer number) as

$$B_a = \frac{(\rho v)_w}{G C_f/2} = \frac{\dot{r}\rho_f}{G C_f/2} \tag{5.5}$$

The skin friction coefficient can be written as the skin friction coefficient for no blowing multiplied by a correction factor, C_f/C_{fo}, for the blocking which, in general, is a function of the aerodynamic blowing parameter, B_a. For the blowing correction we use the general formula discussed in chapter 2.

$$\frac{C_f}{C_{fo}} = q B_a^{-k} \tag{5.6}$$

We define the thermochemical blowing parameter as

$$B_t = \frac{u_e}{u_b} \frac{\Delta h}{h_v} \tag{5.7}$$

which is equal to B_a at steady-state as in chapter 2.

Combining equations 5.4, 5.5, 5.6 and 5.7 one gets the following expression for wall heat flux

$$\dot{Q}_c = \frac{1}{2} C_{fo} q h_v G B_a^{-k} B_t . \tag{5.8}$$

Note that since the ratio of the velocities at the free stream and the flame can be written in terms of the enthalpy ratio, $\Delta h/h_v$ and the oxidizer mass fraction in the free stream [19], the thermochemical blowing parameter is a function of the thermochemical properties alone. Thus it is a known parameter for a given selection of the propellants. However during a transient the thermochemical blowing parameter is not equal to the aerodynamic blowing. There are two distinct blowing parameters, because during the transients in the solid grain the energy balance at the surface has an extra time dependent term that represents the heat conduction to the solid, which depends on the slope of the transient temperature profile in the solid fuel at the surface. In the strictly steady case, the temperature profile and thus the heat conduction is known apriori and its contribution can be included in the regression rate term of the energy balance by simply replacing the latent heat of gasification, L_v, with the effective heat of gasification, h_v, which includes energy required to heat the solid fuel from the ambient temperature to the surface temperature.

Since during a transient, the aerodynamic blowing parameter at a given operating condition of a rocket motor cannot be determined by equating it to the thermochemical blowing parameter, we need to derive an expression for it in terms of the other parameters of the problem. This can be easily done with the use of the definition of the aerodynamic blowing parameter and the skin friction expression (equations 5.5 and 5.6).

$$B_a = \frac{\dot{r}\rho_f}{G q B_a^{-k} C_{fo}/2} \tag{5.9}$$

From this equation B_a can be solved as

$$B_a = \left(\frac{\dot{r}\rho_f}{q G C_{fo}/2} \right)^{1/(1-k)} . \tag{5.10}$$

Now a more useful form of the heat conduction expression can be found upon the substitution of B_a and the commonly used form of the skin friction coefficient for the turbulent boundary layers [15],

$$C_{fo}/2 = 0.03(Gz/\mu)^{-0.2} \tag{5.11}$$

in equations 5.8 and 5.10.

$$\dot{Q}_c(t) = \left(\frac{0.03q}{\mu^{-0.2}}\right)^{1/(1-k)} \left(\frac{B_t h_v}{\rho_f^{k/(k-1)}}\right) z^{-0.2/(1-k)} G^{0.8/(1-k)} \dot{r}^{-k/(1-k)} \tag{5.12}$$

Here z is the local distance from the entrance of the port.

Note that the terms in the parentheses in equation 5.12 are functions of the boundary layer properties and combustion characteristics. Thus they can be treated as constants after the propellants are selected and the expression for the heat flux reduces to the following form where A' is a constant for a given propellant combination (includes terms μ, B_t, h_v and ρ_f).

$$\dot{Q}_c(t) = A' z^{-0.2/(1-k)} G^{0.8/(1-k)} \dot{r}^{-k/(1-k)} \tag{5.13}$$

So far we have developed a formula that relates the wall heat flux at a specified location of the port to the regression rate and mass flux at that location. However, in practice for a specific propellant combination, the coefficient A' is best determined empirically. Very frequently the available data is based on the average regression rate in terms of the oxidizer mass flux [4, 23, 31]. Let's consider, for simplicity, a propellant combination with the average regression rate expression, $\dot{r} = aG_o^n$, where the empirical constants are obtained by experimentation. Note that the following analysis can equally be performed for other forms of the regression rate expressions used for hybrids.

Now we assume that the global heat flux expression can be written analogously to the local equation 5.13 as

$$\dot{Q}_c(t) = eG_o^{n/(1-k)} \dot{r}^{-k/(1-k)} \tag{5.14}$$

where e is a constant that replaces A' and the space average of the z term and n replaces the classical exponent 0.8. The constant e can be excluded from the formula with the use

of the steady-state condition $\dot{Q}_c = \dot{r}\rho_f h_v$. After the elimination of the unknown constant e in the favor of the known experimental constant a, the final form of the global formula becomes

$$\dot{Q}_c(t) = \rho_f h_v a^{1/(1-k)} G_o^{n/(1-k)} \dot{r}^{-k/(1-k)}. \tag{5.15}$$

Note that the heat flux from the gas to the wall depends on the port mass flux and also the regression rate.

In order to be able to couple the heat flux expression with our thermal lag formulation, we nondimensionalize with respect to the reference state $(G_o)_{ref}$ and $\dot{r}_{ref}$ $(= a(G_o)_{ref}^n)$ which is selected to be the nominal operating point. For the following definition of the normalized mass flux the heat flux equation takes the form of equation 5.17.

$$\overline{G}_o = G_o / (G_o)_{ref} \tag{5.16}$$

$$\overline{\dot{Q}}_c(\bar{t}) = E_h \overline{G}_o^{n/(1-k)} R^{-k/(1-k)} \tag{5.17}$$

Note that $E_h = h_v / C\Delta T = 1 + E_L$ and the rest of the nondimensional variables and parameters used in this expression are defined in chapter 4. Since we are dealing with a purely convective system $\dot{Q}_w$ (which includes radiation) can be replaced with $\dot{Q}_c$ in this formulation.

Next we linearize this equation around the reference point by expanding

$$\begin{aligned}
\overline{\dot{Q}}_c(\bar{t}) &= 1 + \varepsilon Q_1(\bar{t}) + O(\varepsilon^2) \\
R(\bar{t}) &= 1 + \varepsilon R_1(\bar{t}) + O(\varepsilon^2) \\
\overline{G}_o(\bar{t}) &= 1 + \varepsilon G_1(\bar{t}) + O(\varepsilon^2).
\end{aligned}$$

The first order terms in ε can be collected to give the linear version of the relation to be used in the first order perturbation analysis.

$$Q_1(\bar{t}) = E_h\left(\left(\frac{n}{1-k}\right)G_1(\bar{t}) - \left(\frac{k}{1-k}\right)R_1(\bar{t})\right) \tag{5.18}$$

Note that in the absence of the blocking effect ($k = 0$ and $q = 1$), the heat flux becomes a function of the oxidizer mass flux alone.

5.2 Thermal Lags and Combustion Coupling (TC Coupling)

In the development of the transient hybrid combustion theory we assumed that the boundary layer responds to the changes in the mass flux fast compared to the other transient time scales in the rocket motor such as the gasdynamic lags or the thermal lags. This assumption fails to be valid especially for large hybrid motors. In order to develop a realistic model for the dynamics of the hybrid motor, the boundary layer lags must be considered. At least to the authors knowledge there is not sufficient information in the literature on the response of the turbulent boundary layers with chemical reactions and blowing (i.e. hybrid rocket combustion scheme) to the changes in the free flow conditions. Since this complex dynamic phenomenon is extremely difficult to investigate both theoretically and also experimentally, we will consider a much simpler case of a standard incompressible turbulent boundary layer with no blowing or chemical reactions. This will hopefully lead us to a reasonable estimation of the time lags associated with the boundary layer diffusion/transport processes. This scaling information on the boundary layer response time will be inserted as simple delays in the quasi-steady wall heat flux expression. This crude model for the gasdynamic response will later be coupled with the thermal lag system in order to perform stability investigations on the coupled system.

The extent of information even on the transients of the incompressible turbulent boundary layers is very limited in the literature. The previous research performed is almost exclusively experimental. Here we will briefly summarize the results of some of those papers reported on the unsteady turbulent wall flows.

It is important to note that due to the insufficient length of the port and continuous mass addition, a hybrid motor port flow field never becomes a fully developed pipe flow. However, in our brief summary we will also include the results for the fully developed pulsating turbulent pipe flow, since some of those results can be adapted to the boundary

layer case. In the pipe flow case, almost all of the investigations deal with the response of the turbulent flow mean and statistical properties to the periodic changes in the mean velocity [59, 60, 61]. It is instructive to first discuss the well understood case of the pulsating laminar pipe flow which is considerably simpler compared to the turbulent case. It is shown in numerous early studies (i.e. reference 15), the nature of oscillating component of the laminar pipe flow depends only on the frequency parameter [61] defined as $\Omega = (\omega/\nu)^{1/2} D/2$ where ν is the kinematic viscosity of the fluid. When this non-dimensional frequency is very small, the velocity oscillations follow the pressure gradient oscillations in a quasi-steady manner. At the other extreme of very high frequencies, the flow in the pipe, except in a small annular region next to the wall, moves like a solid plug with a constant amplitude of modulation. Unlike the laminar case, the turbulent unsteady flow depends on at least two parameters: [59, 61] (when the oscillation amplitude is small with respect to the mean flow velocity) the nondimensional frequency and the time-mean Reynolds number. If the oscillation amplitude is large, the amplitude must be considered (due to the nonlinear nature of the turbulent flow) as a third parameter that controls the physics of the flow. In all major investigations it is shown that at low frequencies (frequencies below a first critical value which depends on the steady flow properties) the wall layer behaves in a quasi-steady manner, namely global properties (i.e. mean velocity profile) and the statistical properties (i.e. velocity fluctuation correlations) of the turbulent boundary layer are at their equilibrium values associated with the free stream velocity at any time of the transient. In the other extreme, when the frequency is larger than a second critical frequency, the properties of the boundary layer can not follow the fast changes in the free stream velocity and the properties such as Reynolds stresses and turbulence intensity become frozen in most of the core of the pipe cross section away from the wall. However, the turbulent flow properties in a small region next to the wall show large variations within an oscillation cycle. In the limit of infinite frequency, a quasi-laminar state of the oscillatory component of the flow can be reached. Namely, the oscillatory component becomes totally independent of the turbulent nature of the flow. If the imposed oscillation frequency is at an intermediate level between the critical frequencies, the situation is much more complicated and the response is neither frozen nor in equilibrium. In this case the frequency is close to the burst frequency of the boundary layer and the turbulent flow structure interacts more strongly with the modulated oscillations [59, 60]. The critical frequency levels for the pipe flow are reported in terms of the mean bulk Reynolds number by references 60 and 61.

A correct modeling of the hybrid boundary layer for the low frequency oscillations , requires the determination of the oscillatory regime (i.e. the position of the oscillation frequency with respect to the critical frequencies) that the hybrids operate. This will require knowledge of the critical frequencies for hybrid boundary layers. However, to our knowledge no such information for the boundary layers analogous to the pipe flow, is available in the literature.

An important set of experiments [62] was performed by abruptly changing the free stream velocity over a turbulent boundary layer from one value to an other (such as throttling) and by measuring the time average velocity profile and the fluctuations in the velocity components at various axial locations. The researchers concluded that the time required to reach from the initial equilibrium profile to the final equilibrium profile at any axial location was proportional to the time of flight of a fluid particle from the leading edge of the boundary layer to the specific axial location at the speed of the free stream flow. This very important result can be formulated for hybrid boundary layers as

$$\tau_{bl} = c' \frac{z}{u_e}. \tag{5.19}$$

Here c' is a constant that needs to be determined empirically. We will call this time required for equilibration, the characteristic response time of the boundary layer, τ_{bl}. It is important to note that the physical nature of the boundary layer transient time is not related to the propagation of the disturbances with the speed of the port velocity as it is suggested by expression 5.19. The delay rather depends on the diffusion time scale across the boundary layer which is proportional to the ratio of the local boundary layer thickness to the diffusion speed. The diffusion speed is defined in terms of the shear stress and mean gas density as $U^* = \sqrt{\tau_w / \bar{\rho}}$. The thickness to diffusion speed ratio, after the substitution of the standard turbulent boundary layer expressions for the shear stress and the thickness yields equation 5.19 with a coefficient c' which is a weak function of the local Reynolds number. In our investigations we assume that c' is constant. For an incompressible turbulent boundary layer on a flat plate at a local Reynolds number corresponding to typical hybrid operation, c' is estimated to be approximately 0.5. However, in a real hybrid boundary layer with combustion and blowing, c' can be different from this estimation and for that reason, we treat it as a parameter to be determined empirically.

For the purpose of this paper, it is convenient to consider an average boundary layer delay and replace the local distance z, with the length of the grain, L. Note that the empirical constant c' accounts for the correction to the inaccurate selection of the length scale, L. However, we recognize that in reality there is a range of boundary layer delay times that should be considered. Thus the significant observation here is that an erratic or variable low frequency instability can result. The exact determination of the average delay time is quite difficult, since the hybrid boundary layers merge at a point which has been estimated to be at an $L/D \approx 5$[18] Note that after they merge, the diffusion thickness for the oxidizer portion becomes a large fraction of the radius of the port which changes very slowly with the axial distance. However the diffusion thickness in the fuel side continues to increase due to the increasing distance of the flame from the wall.

In our studies we implement the response lag of the boundary layer to the changes in the mass flux by simply inserting time delays to our heat flux expressions derived under the assumption of quasi-steady response. The implementation of this idea in equation 5.18 yields

$$Q_1(\bar{t}) = E_h\left(\left(\frac{n}{1-k}\right)G_1(\bar{t}-\bar{\tau}_{bl1}) - \left(\frac{k}{1-k}\right)R_1(\bar{t}-\bar{\tau}_{bl2})\right) \tag{5.20}$$

where $\bar{\tau}_{bl1} = \tau_{bl1}/\tau_{tl}$ and $\bar{\tau}_{bl2} = \tau_{bl2}/\tau_{tl}$.

Here τ_{bl1} is the time delay between the oxidizer mass flux and the wall heat transfer and τ_{bl2} is the time delay between the regression rate and the wall heat flux. The scaling of the time delays τ_{bl1} and τ_{bl2} obey the general scaling law given by equation 5.19. However the coefficient c' for τ_{bl1} and τ_{bl2} is expected to be different since each of these delays represents a different adjustment mechanisms for the boundary layer.

Now, with the use of this relation the thermal lags in the solid can be coupled to the combustion transients in the boundary layer. This coupling will yield a transfer function between the oxidizer mass flux (input) and the regression rate (output).

The derivation of the transfer function is very similar to the derivation performed for pure thermal lags case discussed in the previous chapter. The only difference is the energy balance boundary condition at the surface must be modified. Substitution of

equation 5.20 in the surface boundary condition of the linearized thermal lag problem (equation 4.28) yields the correct boundary condition for the coupled problem.

$$\left(\frac{\partial T_1}{\partial x}\right)_{x=0} - E_L R_1(\bar{t}) - \sigma_1 R_1(\bar{t} - \bar{\tau}_{hl2}) = -\sigma_2 G_1(\bar{t} - \bar{\tau}_{hl1}) \tag{5.21}$$

Two new constants are introduced for convenience.

$$\sigma_1 = E_h(k/(1-k)), \quad \sigma_2 = E_h(n/(1-k)) \tag{5.22}$$

With this new boundary condition the linearized thermal lag problem can be solved in a similar way to the case with no delays, with the use of the Laplace Transformation technique. The transfer function between the regression rate ($R_{1L}(s)$) and the mass flux ($I(s)$) can be obtained as

$$\frac{R_{1L}(s)}{I(s)} = \frac{2E_{E_a}\sigma_2 e^{-\bar{\tau}_{hl1}s}s}{\left(1+\sqrt{1+4s}\right)\left(s+E_{E_a}\right) - 2E_{E_a} + 2E_{E_a}s\left(E_L + \sigma_1 e^{-\bar{\tau}_{hl2}s}\right)}. \tag{5.23}$$

The quasi-steady response (R_1^{qs}) can be obtained by taking the limit $s \to 0$ of equation 5.23.

$$\frac{R_1^{qs}}{I(s)} = \frac{E_{E_a}\sigma_2}{1 + E_{E_a} + E_{E_a}(E_L + \sigma_1)}. \tag{5.24}$$

By dividing equation 5.23 to the equation 5.24 the normalized (with the quasi-steady value) regression rate can be determined as

$$\frac{R_{1L}(s)}{R_1^{qs}} = \frac{2\left(1 + E_{E_a}(1 + E_L + \sigma_1)\right)\sigma_2 e^{-\bar{\tau}_{hl1}s}s}{\left(1+\sqrt{1+4s}\right)\left(s+E_{E_a}\right) - 2E_{E_a} + 2E_{E_a}s\left(E_L + \sigma_1 e^{-\bar{\tau}_{hl2}s}\right)}. \tag{5.25}$$

5.3 Results and Discussion

We are now in a position to investigate the behavior of the regression rate with repect to changes in the oxidizer mass flux with use of equation 5.25 which is a transfer function that resembles the combustion phenomenon which includes the dynamics of the thermal processes in the solid and approximates the combustion dynamics in the turbulent boundary layer of the rocket motor. The dynamic characteristics of the hybrid combustion system can be deduced from the properties of this transfer function. This transfer function includes the energy parameters E_L and E_{E_s}, the B and G exponents (k and n) and the delay times of the boundary layer. In that respect the dynamic behavior of the combustion depends on these parameters and in this section we will investigate the impact of those on the system dynamics.

One of the most important properties of the system of practical interest is the inherent stability of the hybrid combustion scheme. As discussed earlier, low frequency instabilities are widely observed in actual motors of various sizes. In general, for dynamic systems with analytic transfer functions, the stability feature of the system can be directly examined by the open loop transfer function with use of the Nyquist stability criterion [56]. For systems with time delays, Satche developed [41] a very clever technique which is a variation of the standard Nyquist criteria. However our system transfer function is significantly more complicated, since it is not an analytic function in the complex s domain [57]. This is a characteristic of the diffusive systems that yield a square root term, which automatically introduces a branch point, in their Laplace transforms. Since the transfer function is not an analytic function of the Laplace Transform variable s, the Cauchy integral theorem does not hold and the standard Nyquist stability criterion or the Satche criterion derived from it can not be applied directly [41]. However we prove in Appendix D that we can still state that the system will be unstable if at least one of poles of the transfer function is located in the right hand side of the s plane. In other words at least one of the poles of the system must have a positive real component for the system to be unstable. The poles can be determined by finding the roots of the characteristic equation (the denominator of the transfer function). The imaginary portion of the root is the oscillation frequency of the system whereas the real part is the amplification rate of the corresponding frequency [56]. In short the unstable oscillation frequency of the system will be the imaginary part of a pole with a positive real component.

We first observe (from equation 5.25) that the delay between the heat flux and the oxidizer mass flux, τ_{hl1}, does not affect the stability characteristics of the TC coupled system, since its appearance is limited to the numerator of the transfer function given by equation 5.25. We will start with the trivial case with no boundary layer delay between the wall heat flux and oxidizer mass flux. A careful analysis shows that, similar to the pure thermal lags case, the system with no boundary layer delays does not have any poles. This can be seen from figure 5.1 which is a plot of the transfer function for $\tau_{hl2} = 0$ over the complex plane. It is clearly a smooth function in the domain of interest except the origin. A systematic search for a pole is performed for various combinations of the parameters and no poles are found. We conclude that a system without delays is always stable.

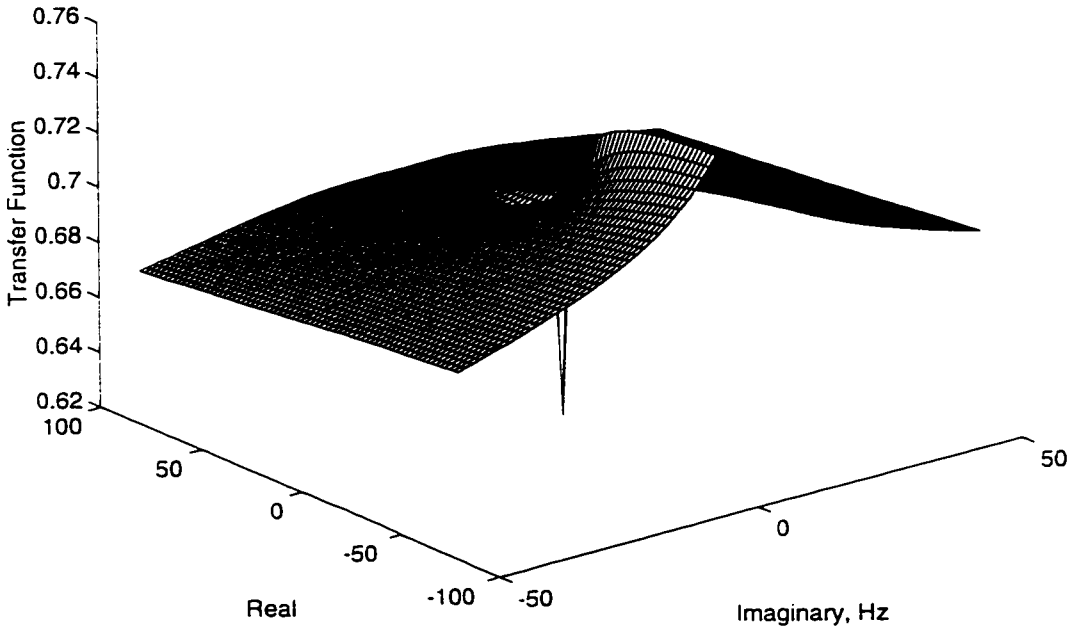

Figure 5.1. Plot of the transfer function of the TC coupled system with no delays ($\tau_{hl1} = \tau_{hl2} = 0$). This plot is for a HTPB system with E_a=15 kcal/mole.

On the contrary, a system with delay between the regression rate and the heat flux ($\tau_{hl2} \neq 0$) showed interesting behavior. As it can be seen from figure 5.2, which is also a plot of the transfer function over the s domain, the system has several poles in the positive real part of the s plane. These roots indicate that the system will possess an unstable time domain response. These calculations were made with a time delay (τ_{hl2}) of 66.7 msec that corresponds to a motor with an average gas velocity of 45 m/sec, a length of 6 meters and

c' of 0.5. Note that there is a series of unstable frequencies all with the same amplification rate and the smallest of those frequencies corresponds to the range of low frequency instabilities observed in practice for that motor size. We suggest that the higher frequency instabilities, although appeared at the same amplification rate as the lowest frequency as a result of the linear theory, will possibly be stabilized by the nonlinear effects and by the energy dissipation processes. It is also determined that the thermal lag time does not affect the value of the fundamental oscillation frequency of the system.

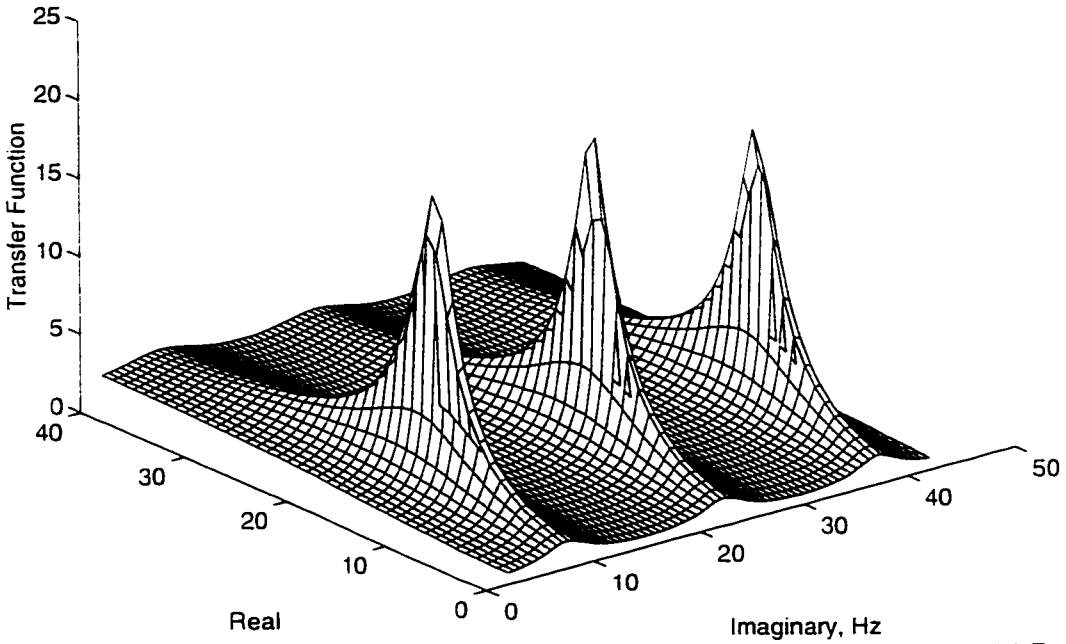

Figure 5.2. The unstable poles of the TC coupled system in the s plane for $\tau_{hl1} = 0$. $\tau_{hl2} = 66.7$ msec and $\tau_{tl} = 118.6$ msec. This plot is for a HTPB system with E_a=15 kcal/mole.

In order to explore the compatibility of the results of this linear model with the observations, we will perform three parametric studies and compare those with the test results from the actual motor runs. The first one of those is for the various size AMROC motors [82] which operated at various L^* levels. Since the information on the AMROC motors that can be found in the literature is limited to L^*, c^* and motor O/F ratio, it is desirable to express the boundary layer delay time, equation 5.19 in terms of those variables. The average velocity in the port can be approximated as

$$u_{ave} = \frac{G_t[(1+2O/F)/(1+O/F)]RT_{ave}}{2P}.$$

where RT_{ave} is an average value in the port. Substituting this expression in the delay formula and using the relations for the total mass flow rate $\dot{m}_t = G_t A_p$ and port volume $V_p = LA_p$ yields

$$\tau_{bl} = c' \frac{2V_p P}{\dot{m}_t[(1+2O/F)/(1+O/F)]RT_{ave}}.$$

With the use of the total mass flow relation, $\dot{m}_t = PA_n/c^*_{\exp}$ and the definition $L^* = V_m/A_n$. the delay equation can be written as

$$\tau_{bl} = 2c' \frac{V_p}{V_m} \frac{[(1+O/F)/(1+2O/F)]}{RT_{ave}} L^* c^*_{\exp}. \tag{5.26}$$

Here V_p/V_m is the ratio of the port volume to the motor volume which is estimated to be approximately 0.8 for AMROC DM-01 motor [82]. We assume that all AMROC motors possess the same average gas constant temperature product, RT_{ave} and volume ratio, V_p/V_m. Various properties of the AMROC motors [26, 82] are listed in table 5.1. After noting that all motors operate at very similar O/F ratios and $c^*_{\exp}$ values, it can be stated that in the series of tests the boundary layer characteristic delay time is proportional to L^*.

AMROC Motor (thrust)	O/F	c^*_{theo} (ft/sec)	$c^*_{\exp}$ (ft/sec)	L^* (in)	f (Hz)
S Motor (10k)	1.45	5584	5361	570	11
Half-Scale (33k)	1.45	5584	5361	1305-1430	4.8
H-500 (75k)	1.45	5584	5361	1770-2340	4.0
DM-01 (250k)	1.55	5700	5472	2168	2-3.5

Table 5.1. Summary of parameters used in the frequency estimations for AMROC motors.

We estimated the fundamental oscillation frequencies predicted by the linear theory for various boundary layer delays. The result is shown in figure 5.3 which is a plot of the calculated unstable oscillation frequency versus the boundary layer delay of the motor. The AMROC motor data is also included in this figure. A c' value of 0.79 is selected to provide a best fit between the linear theory predictions and the observed frequencies of the AMROC motor tests. As indicated in the figure for this selected delay coefficient, the linear theory estimates the AMROC motor instability frequencies with good accuracy.

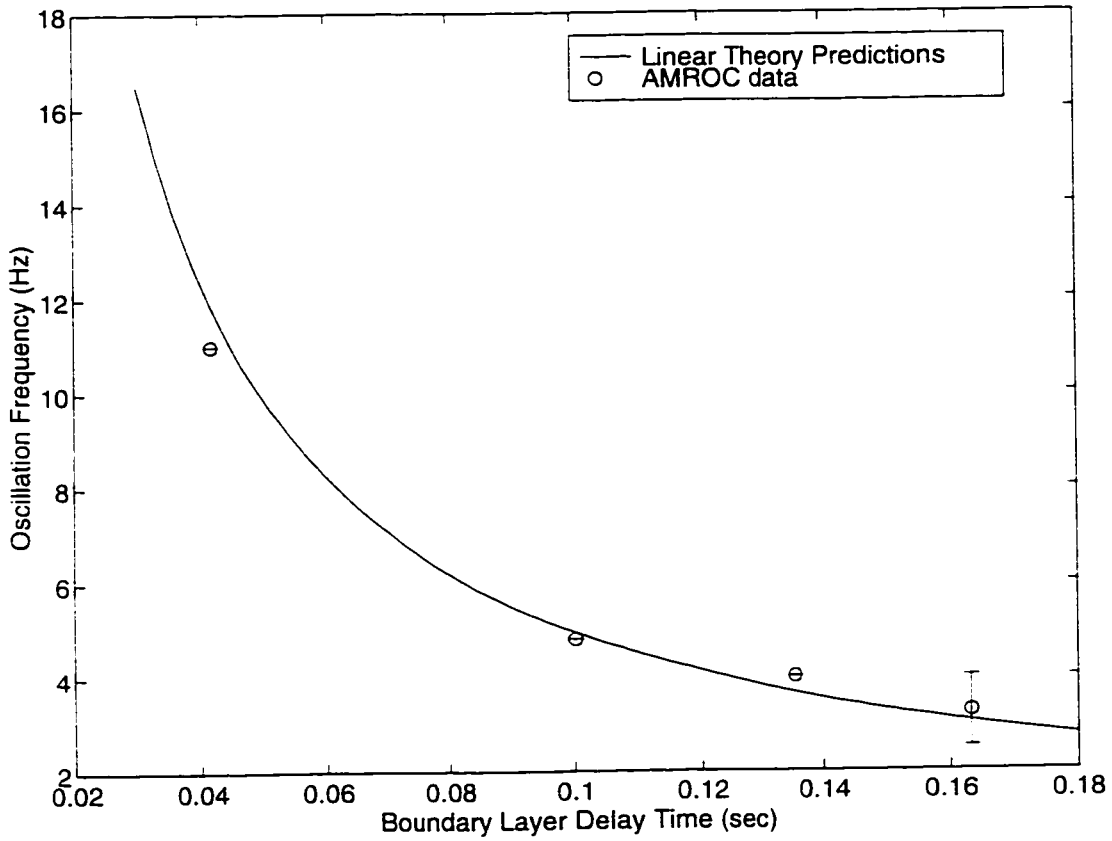

Figure 5.3. The effect of motor size on the oscillation frequency. Comparison of the TC coupled theory with the AMROC motors stability data.

The plot clearly shows the inverse relation between the boundary layer delay time and the fundamental oscillation frequency. Moreover when figure 5.3 is plotted in the log-log scale the oscillation frequency shows a linear variation with the boundary layer delay time. This suggests that the frequency is inversely proportional to the delay time or $f = const/\tau_{bl}$ where the constant has a value of 0.495 for this specific case. For AMROC motors which operate at approximately the same O/F levels, the frequency becomes inversely proportional to L^*. This relation has been previously observed [34].

A different test of the model can be performed by comparing the predictions of the model with actual experimental results for motors with the same port length but running at different operating points (i.e. chamber pressure, oxidizer mass flux, port diameter). To treat this case, the port velocity can be replaced by an average value $(G_o + G_t)/2\rho_{ave}$ with ρ_{ave} given by the gas law $P/\rho_{ave}R_g T_{ave}$ to yield finally for the boundary layer lag:

$$\tau_{hl} = c' \frac{2LP}{(G_o + G_t)RT_{ave}}. \tag{5.27}$$

Equation 5.27 gives the scaling law for the boundary layer delay in terms of the operating points of the rocket motor and also with the size of the motor. This states that delay increases with increasing chamber pressure, port length and decreases with increasing mass flux in the port. An important conclusion that can be drawn from those observations is that an increase in the chamber pressure or a decrease in the port mass flux act to decrease the oscillation frequency of this type of TC coupled system.

Test No.	$\overline{D}$ (in)	$\dot{m}_{ox}$ (lb/sec)	G_{ox} (lb/ in^2-sec)	G_{tot} (lb/ in^2-sec)	$\overline{P}_c$ (psi)	$\overline{O/F}$	f (Hz)	ΔP_{osci} (psi)	τ_{hl} (msec)
1 (GOX)	4.25	6.0	0.423	0.571	600	2.85	13	200	44
2 (GOX)	4.25	5.7	0.402	0.541	550	2.89	8	300	42
7 (GOX)	4.20	4.7	0.339	0.458	440	2.89	15	100	40
8 (GOX)	4.22	5.1	0.365	0.492	260/280	2.87	20	400	23
1 (LOX)	-	-	0.222	0.31	435	2.51	8	250	58

Table 5.2: Summary of parameters used in the frequency estimations for the 11 inch Hybrid motor tests. Grain length is 102 inches.

To test these predictions, we will mainly use the 11 inch GOX/Hybrid Motor Tests which are performed with HTPB/Escorez fuel grains [30] Only the tests that exhibit combustion instability and performed with single port motors are considered. The runs with the rearward-facing steps at the port entrance are also excluded in this study, since in

these tests the flow field in the port is significantly altered which may cause to a major change in the boundary layer delay time coefficient. We also include test #1 of 11 inch LOX motor data in the analysis [83]. We only consider test 1 since it is the only run with a chamber configuration identical to GOX motors used in the calculations. A summary of the test conditions and the observed frequencies are presented in table 5.2.

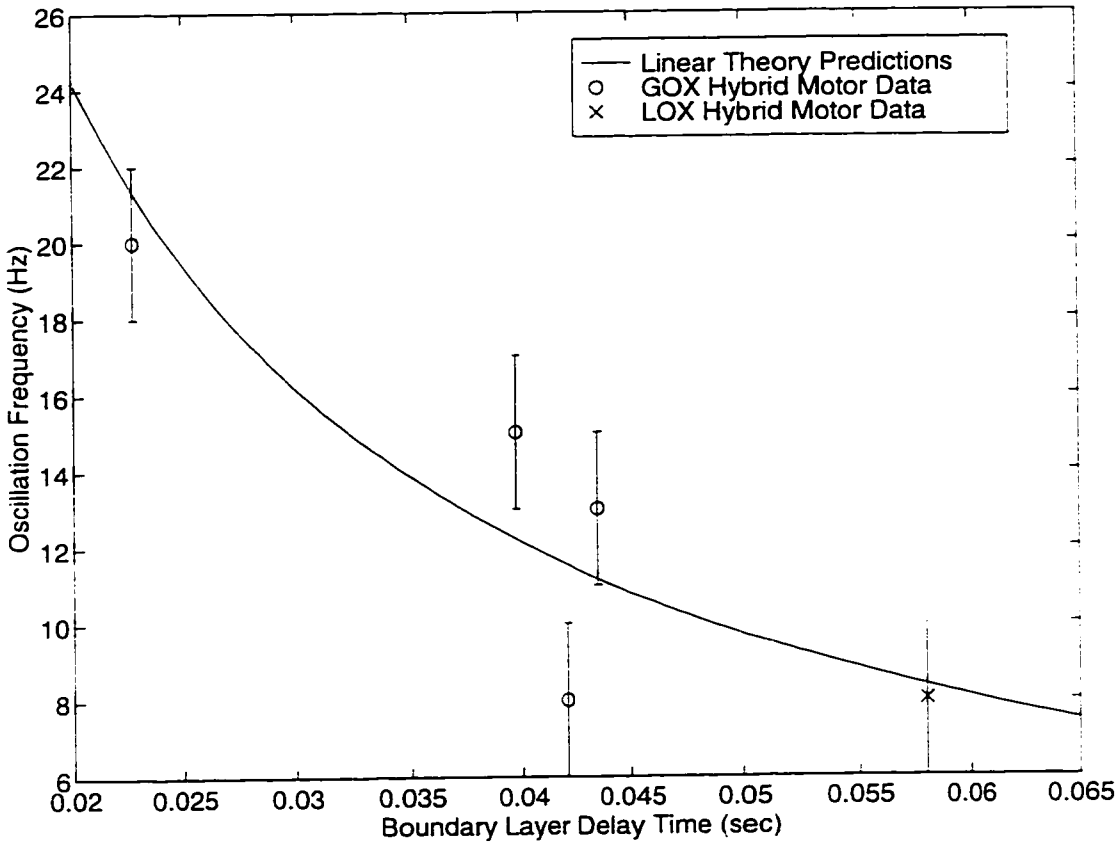

Figure 5.4. Comparison of the linear theory results with the experimental data for 11 inch hybrid motors.

The estimation of the unstable frequencies is performed similarly by determining the smallest unstable pole of the system transfer function (fundamental mode) given by equation 5.25. The delay constant in the calculations is determined to be 0.63 by fitting the experimental data to the theory predictions. Both the experimental results and also the calculation results are shown in figure 5.4. The error bars are introduced in the experimental data, since the observed oscillation frequencies cover a range. The agreement between the estimates and the experimental data is reasonable considering the experimental uncertainty. The greatest deviation is in test #2 where it is reported that a diffuser plate was inserted in the pre-combustion chamber. The purpose of the diffuser plate is to reduce the turbulence level of the flow entering the port which possibly decreases the turbulent scalar

diffusion in the boundary layer. The effect of the reduced transport in the boundary layer would be to increase the boundary layer delay time and would shift the test #2 value to the right providing better agreement.

Finally we use a different set of 11 inch GOX/Hybrid experimental data (NASA/MSFC program), which were also performed with HTPB/DDI/Escorez fuel grains [29, 31]. Only the tests that exhibit combustion instability and performed with single port motors are considered here. A summary of the operating conditions and instability data are presented in table 5.3.

Test No.	$\overline{D}$ (in)	L (in)	$\dot{m}_{ox}$ (lb/sec)	G_{ox} (lb/in^2-sec)	G_{tot} (lb/ in^2 in-sec)	$\overline{P}_c$ (psi)	$\overline{O/F}$	f (Hz)	ΔP_{osci} (%)	τ_{hl} (msec)
4	3.4	102	3.44	0.38	0.527	745	2.6	6-10	15	70.8
3	4.3	102	3.36	0.23	0.325	325	2.4	10-20	20	50.8
10	3.7	102	8.36	0.78	1.024	750	3.2	10-15	12	35.8
6	5.3	102	3.41	0.15	0.22	335	2.1	6-15	15	78.0
9	5.7	102	3.87	0.15	0.209	850	2.6	2-5	60	204
8	6.1	102	6.34	0.28	0.392	215	2.6	6-20	33	27.6
11	5.4	108	10.20	0.45	0.599	1025	3.0	4	10	89.4
7	6.1	102	5.93	0.20	0.278	215	2.6	10-25	5	38.7

Table 5.3. Summary of parameters used in the frequency estimations for the NASA/MSFC 11 inch Hybrid motor tests.

Both the observed and also the calculated frequencies are shown in figure 5.5. Note that the delay time coefficient c' is taken to be 0.75 for the calculations. The agreement between the estimates and the experimental data is very good except for test number 11. However in test number 11 it is reported that the GOX venturi is not choked and the instability mechanism for this run is most likely the coupling between the feed system and the chamber gasdynamics, not the TC coupling.

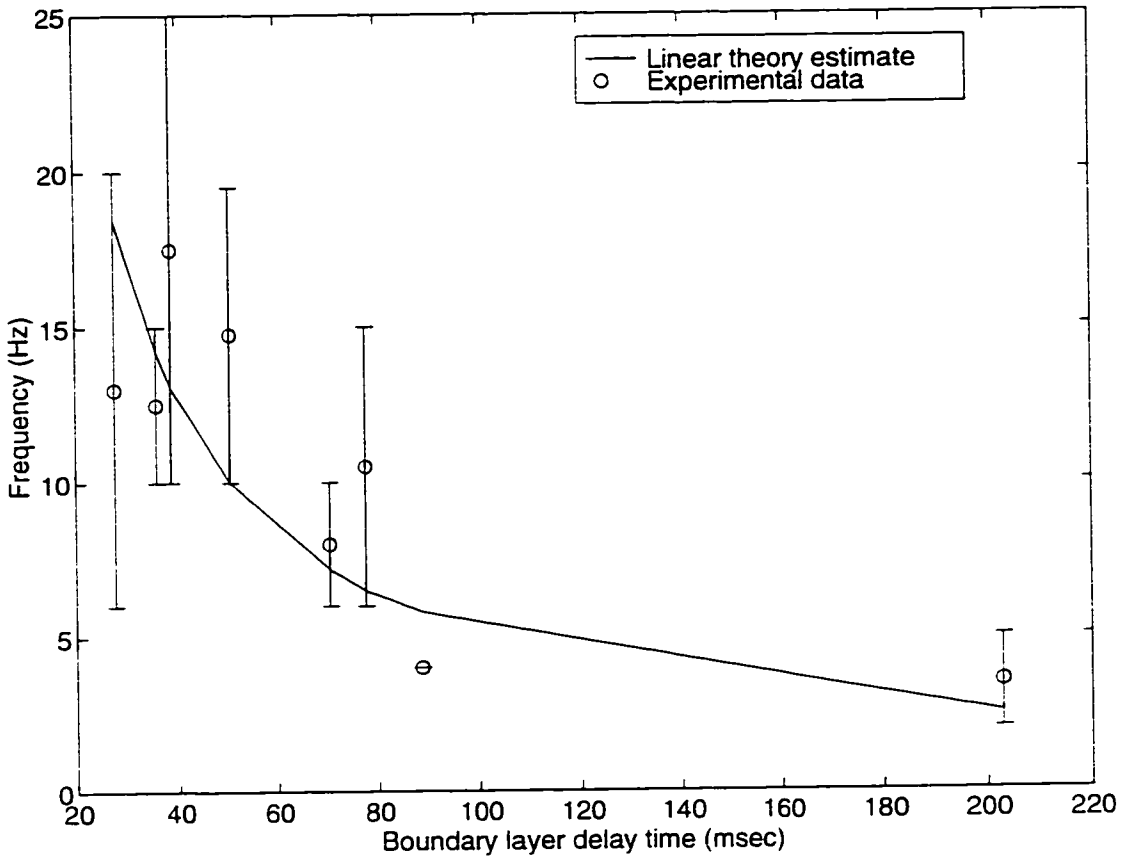

Figure 5.5. Comparison of the linear theory results with the experimental data for NASA/MSFC program.

It is significant that the boundary layer delay coefficients obtained for both the AMROC motors and also for the 11 inch motors are reasonably close to each other and also to the theoretically predicted value of 0.5 for an incompressible turbulent boundary layer with no blowing.

The impact of the parameters other than the thermal lag time and the boundary layer delay time (such as the fuel properties or the mass flux and blowing exponents) on the oscillation frequency is determined to be small. It is also observed that decreasing activation energy (E_a) and decreasing blowing exponent (k) decreases the amplification rate (real component of the poles) of the oscillatory modes. The effect of the other parameters such as the mass flux exponent and the latent heat of gasification on the amplification rate is negligible. In the extreme case of no blocking effect (k=0) the system does not possess an oscillatory component in its natural response (either stable or unstable). Thus, for highly radiating combustion gases where the effective k values are diminished, we might expect that the tendency for instability from this mechanism would be decreased. Within the practically feasible range of variations in the activation energy and the blowing exponent,

the changes in the amplification rate is small. This may serve as an explanation on why the low frequency oscillations are encountered for a wide range of motors.

5.4 Conclusions for Transient Hybrid Combustion Theory

The agreement between the experimental observations and the predictions of the theory suggests that the regression rate wall heat flux coupling through the boundary layer processes and the thermal diffusion in the solid possibly play a central role in the generation of the low frequency instabilities in hybrids. However this linear theory can only predict the range of the frequencies that is expected, it cannot predict the amplitude of the oscillations nor can it (at least directly) tell when the instability will be present. The linear theory, of course, can only yield an unlimited increase of the oscillation amplitude through exponential growth in time. The energy dissipation processes in a motor must be considered to determine the limiting amplitudes in the instabilities. The amplitude of the pressure oscillations in a hybrid motor chamber during the instability is bounded and it has the character of a limit cycle process. This suggests the existence of nonlinear processes controlling the amplitude of oscillations that are generated by the linear mechanism (at least in the early stages of the development of the instability). A full hybrid stability theory requires a good understanding of those nonlinear effects and should include the interaction with the gasdynamics in the chamber involving pre and post-combustion chambers.

Chapter 6

Chamber Gasdynamics and TCG Coupling

In the preceding chapters the dynamic models for the thermal lags and the hybrid combustion are developed. In addition, these subsystem models are coupled to obtain the response of the fuel mass generation to the changes in the mass flux in the port. However, practically significant parameters of the rocket operation such as the chamber pressure, specific impulse and thrust cannot be obtained solely from the TC coupled system. These variables can only be determined after introducing a model for the gasdynamics which will be discussed in detail in this chapter. A gasdynamic model, in general, should use the oxidizer mass flow rate and the fuel mass generation rate as the inputs and it should yield the parameters that are more closely related to the performance of the motor such as the chamber pressure and the motor O/F ratio as the outputs.

In our specific model (2V-port model) we divide the chamber into three components, pre-combustion chamber, port volume and the post-combustion chamber. We treat the pre and post combustion chambers as zero dimensional volume elements, but consider the variation of state variables along the axis of the port. The mathematical formulation is obtained after the application of the conservation laws for the three volume elements. The set of equations resembling our model is solved analytically after linearization and as a result of that operation, a transfer function for the gasdynamic subsystem is obtained. Some numerical simulations are also performed to determine the validity of the approximations used in the perturbation solutions. Later the gasdynamic model is integrated with the TC coupled system to determine the TCG coupled response. The TCG coupled system yields the performance of the rocket (such as chamber pressure) for some given input of oxidizer mass flow rate which is a fundamental control parameter in hybrid rockets. For that reason, it is fair to state that the TCG coupled system represents the most fundamental dynamic behavior of the hybrid rocket.

6.1 Two Volume-Port Model

The simplest gasdynamic model for a hybrid motor is just a single zero dimensional volume element attached to a nozzle. This single volume model captures the filling/emptying processes associated with the volumetric capacity of the motor cavity. It, of course, fails to resolve the acoustic behavior. This is, in fact, the model most commonly used in transient modeling of hybrids in the past [34, 36].

We claim that the single volume model is not satisfactory for hybrids even for the slow transients for which the acoustic behavior is not important. Unlike the solid rockets, a hybrid motor combustion chamber has extreme temperature variations between the pre-combustion chamber where the cold oxidizer is injected and the exit of the post combustion chamber where the combustion of reactants is complete to a large extent. Thus a single volume with a mean temperature assumption is an oversimplification for hybrids. In this study we will develop a more sophisticated model for the chamber gasdynamics that captures the longitudinal acoustic modes and also the nonuniformity of the temperature in the motor.

In our model the motor is divided into four subsections: 1) pre-combustion chamber, 2) port volume, 3) post-combustion chamber, 4) nozzle. A schematic of the gasdynamic model is shown in figure 6.1. Each component is approximated appropriately with one or zero spatial dimensional models. The subscripts 1 and 2 are used for the physical properties in the pre and post combustion chambers respectively. Various stations of significance are also distinguished by use of subscript notation. Namely the entrance station of the gaseous oxidizer into the system is represented by a subscript o, the nozzle entrance is denoted by n and the port entrance and exit are shown by a and b, respectively. Our models for these subsections are discussed in the next section.

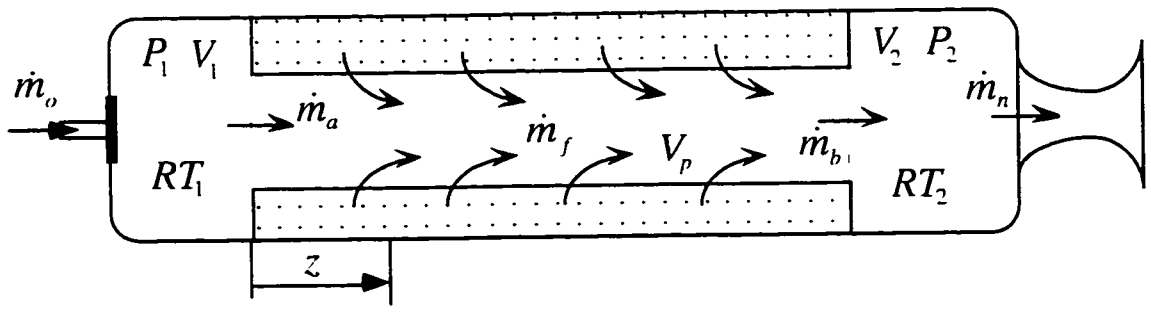

Figure 6.1. The schematic of the 2V-port model.

6.1.1 Pre-Combustion Chamber

We use a zero dimensional gasdynamic model for the pre-combustion chamber. Thus the momentum equation and the energy equations reduce to the mean state information on the pressure and temperature in this volume. But, the mass balance equation is nontrivial and it can be written as

$$V_1 \frac{d\rho_1}{dt} = \dot{m}_{in} - \dot{m}_{out}. \tag{6.1}$$

Note that the size of the volume is assumed to be constant over the burn time. We further assume a constant molar mass and a polytropic process, $P \propto \rho^{n_p}$ in the chamber. Here n_p is the polytropic exponent. We believe that these are reasonable assumptions for this cold volume which accommodates negligible combustion. Under these stated conditions and with the use of the ideal gas law, equation 6.1 can be reduced to

$$a_1 \frac{dP_1}{dt} = \dot{m}_{in} - \dot{m}_{out} \qquad \text{where} \qquad a_1 = \frac{V_1}{n_p R_1 T_1}. \tag{6.2}$$

6.1.2 Port Chamber

In our model we treat the port as a quasi-1D tube with continuous mass and heat addition. The conservation of mass can be written as the following differential equation [63].

$$\frac{\partial \rho}{\partial t} = -\frac{\partial G}{\partial z} + \dot{m}_f \tag{6.3}$$

Here $\dot{m}_f$ is the mass generated at the axial location z of the port. At this stage we prefer to express the mass generation term in the general functional form.

$$\dot{m}_f = f(G, z)$$

The momentum equation in the port can be written in terms of the local mass flux, G, the local pressure, P and the local density, ρ.

$$\frac{\partial G}{\partial t} = -\frac{\partial (G^2/\rho)}{\partial z} - \frac{\partial P}{\partial z} - \left(\frac{C_f C}{2A_p}\right)\frac{G^2}{\rho} \tag{6.4}$$

Note that the last term in this expression is included to capture the effect of the skin friction on the force balance. Here C_f stands for the skin friction coefficient at location z. A_p as the port area and the C for the circumference of the port. All the geometrical properties are assumed to be independent of time and axial dimension. This is a reasonable approximation for typical hybrids which possess a uniform distribution and slow regression of the fuel grain [17].

We further assume that the ideal gas law holds locally in the port.

$$P = \rho RT \tag{6.5}$$

The closure of the system requires the energy equation. For the sake of simplicity we replace the energy equation with the following linear variation of temperature gas constant product in the port.

$$RT(x) = (RT)_1 + \left((RT)_2 - (RT)_1\right) z/L \tag{6.6}$$

Note that for the simplicity of notation we treat the gas constant temperature product as a single dependent variable.

Furthermore we assume that the gas constant temperature product at the exit of the port volume is a fraction of the nozzle entrance value RT_c which can be calculated from the equilibrium chemistry at the operating O/F ratio of the motor.

$$RT_2 = f_b RT_c \tag{6.7}$$

In short, we specify the whole temperature field in the motor chamber for a given operating point and we ignore the variations in the temperature field during the transients. In that respect 2V-port is an isothermal gasdynamic model.

6.1.3 Post-Combustion Chamber

Similar to the pre-combustion chamber treatment, we assign uniform thermodynamic properties for the gas in the post-combustion chamber volume. Therefore the dynamics can be represented with the mass balance which takes the following form after the fixed volume assumption.

$$V_2 \frac{d\rho_2}{dt} = \dot{m}_h - \dot{m}_n \tag{6.8}$$

Here $\dot{m}_h$ is the mass flow rate entering the hot volume and $\dot{m}_n$ is the mass flow rate exiting the volume through the nozzle. Note that we have inherently assumed that post-combustion chamber behaves like a well stirred reactor with the reactions fast compared to the transient rates of concern. Equation 6.8 can be written as

$$a_2 \frac{dP_2}{dt} = \dot{m}_h - \dot{m}_n \qquad \text{where} \qquad a_2 = \frac{V_2}{RT_2}. \tag{6.9}$$

We have approximated the gas constant temperature product in the post-combustion chamber with product at the port exit.

6.1.4 Nozzle

We first assume that the nozzle flow is quasi-steady which is only valid at very slow transients. We also assume that through out the operation of the motor, the nozzle is always choked, namely at any time the ratio of the chamber pressure to the ambient pressure is larger than the critical value associated with the properties of the expending gas. After these simplifying assumptions the nozzle flow rate can be expressed with use of the classical quasi-1D gasdynamic formula [63]

$$\dot{m}_n = \frac{A_n \Gamma_c P_2}{\sqrt{RT_c}} \qquad \text{where} \qquad \Gamma_c = \sqrt{\gamma_c}\left(\frac{2}{\gamma_c + 1}\right)^{\frac{\gamma_c + 1}{2(\gamma_c - 1)}}. \tag{6.10}$$

Here γ_c is the ratio of the specific heats of the combustion products.

At moderate frequency oscillations (such as the acoustic modes of the motor), the acoustic admittance of the nozzle must be considered and a more sophisticated behavior must be considered. For our purposes, it is adequate to adapt Crocco's expression [41] for the nozzle transfer function which is valid for small deviations from the mean chamber pressure and for moderate frequencies.

$$\frac{\tilde{\dot{m}}_n}{\tilde{P}_2} = \frac{A_n \Gamma_c \tilde{P}_2}{\sqrt{RT_c}} + k_n \frac{d}{dt} \tag{6.11}$$

Here k_n represents the effect of inertia of the gas in the convergent portion of the nozzle in causing a phase difference between the oscillation of the velocity and pressure at the entrance of the nozzle.

$$k_n = \frac{c_*}{\gamma_c \left(c_*^2 - u_e^2\right)} \int \left(\frac{c_*}{u} - \frac{\gamma_c - 1}{2} \frac{u}{c_*} \right) dx \tag{6.12}$$

This integration is being performed on the whole convergent portion of the nozzle. Note that c_* is the critical sound velocity, u is the local gas velocity in the nozzle, u_e is the gas velocity at the nozzle entrance.

Equations 6.9 and 6.11 and the ideal gas law can be combined to relate the pressure perturbation directly to the mass flow rate perturbation at the exit of the port.

$$\left(a_2 + k_n\right) \frac{d\tilde{P}_2}{dt} = -\left[\left(\frac{V_2}{\left(RT_c\right)^2} \right) \frac{d\left(RT_c\right)}{dt} + \frac{A_n \Gamma_c}{\sqrt{RT_c}} \right] \tilde{P}_2 + \dot{m}_b \tag{6.13}$$

Note that a fraction of the nozzle volume adds to the post-combustion chamber volume to account for the inertial effects of the gas in the nozzle. For typical hybrids the effective nozzle volume is small compared to the post-combustion chamber volume. We finally indicate that for our isothermal treatment the temperature derivative term is identically zero.

Equation 6.13 includes some properties of the combustion products which are not known offhand. These properties are calculated from chemical equilibrium considerations

with use of the code STANJAN for the selected propellants. A sample calculation result of the product, RTc with the motor O/F ratio for HTPB-oxygen system is shown in figure 6.2.

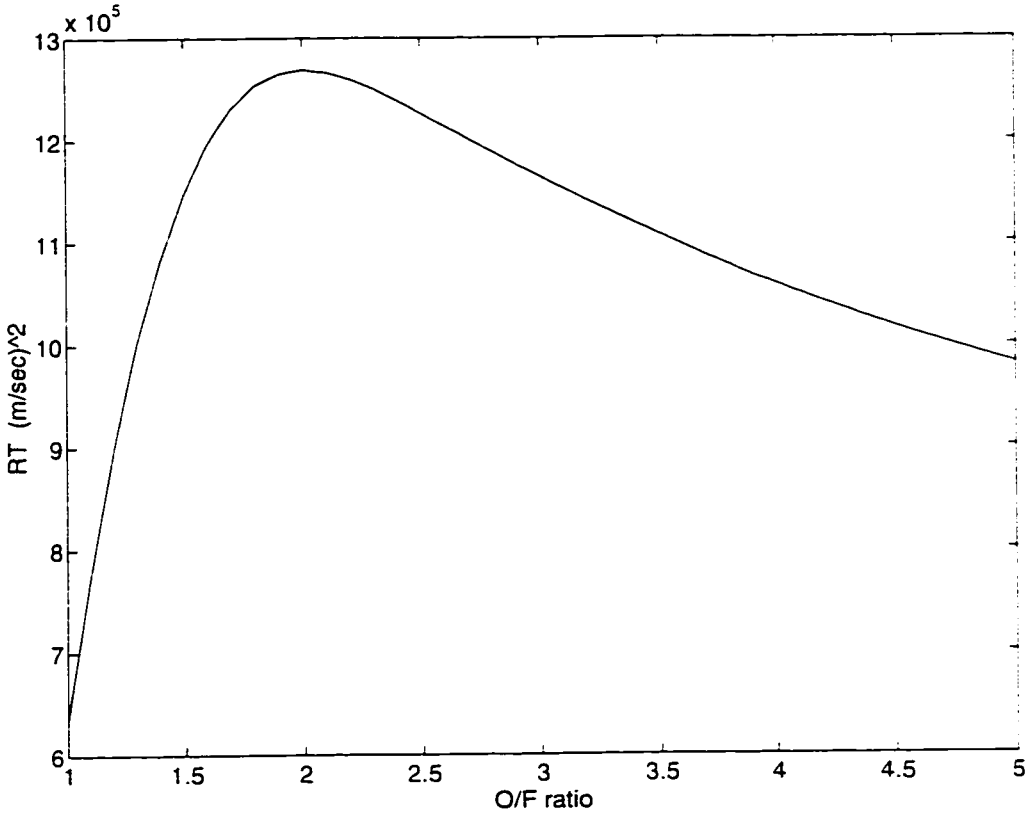

Figure 6.2. The variation of the product, RT_c , with the motor O/F ratio for a HTPB-oxygen system.

6.2 Solution Techniques

In this section we develop small perturbation solutions and also numerical solutions for the system of equations derived for the 2V-port model .

6.2.1 Perturbation Solutions

We determine perturbation solutions around a nominal operating point of the rocket for the gasdynamic system of equations described in the previous paragraphs. These perturbation solutions will be used to obtain a transfer function representing the linear

response of the gasdynamic system. The transfer function uses the oxidizer mass flow rate as the input and the system pressure for the output.

We start with perturbing the port equations around a nominal operating point as

$$\rho = \bar{\rho} + \tilde{\rho}, \qquad G = \bar{G} + \tilde{G}, \qquad P = \bar{P} + \tilde{P}, \qquad m_f = \bar{m}_f + \tilde{m}_f .$$

Note that the terms with the bars are the nominal values which are independent of time. The perturbation terms are assumed to be much smaller compared to the mean variables and, in general, they are functions of both time and the axial coordinate.

After substituting these expressions in the port equations and collecting the terms of the zeroth order, one obtains the following set of equations that describes the steady-state operation of the motor

$$\frac{\partial \bar{G}}{\partial z} = \bar{m}_f \tag{6.14a}$$

$$\frac{\partial \bar{P}}{\partial z} = -\frac{\partial\left(\bar{G}^2/\bar{\rho}\right)}{\partial z} - \left(\frac{CC_f}{A_p}\right)\frac{\bar{G}^2}{\bar{\rho}}\frac{a\rho_f S_w}{A_p} \tag{6.14b}$$

$$\bar{P} = \bar{\rho} RT \tag{6.14c}$$

$$\bar{m}_f = \alpha \bar{G}^n \tag{6.14d}$$

where $\alpha = a\rho_f S_w / A_p$. Here we assumed a steady-state regression rate law of the commonly used form $\dot{r} = aG^n$.

Equation 6.14a can easily be integrated to obtain the mass flux distribution in the port.

$$\bar{G}(z) = \left[(1-n)\alpha z + \bar{G}_o^{1-n}\right]^{1/(1-n)} \tag{6.15}$$

In the absence of the skin friction term the steady-state pressure distribution can also be expressed in a closed form

$$\overline{P}(z)=\frac{1}{2}\left[\frac{\overline{G}_b^2 RT_c}{\overline{P}_c}+\overline{P}_c+\sqrt{\left(\frac{\overline{G}_b^2 RT_c}{\overline{P}_c}+\overline{P}_c\right)-4G^2(z)RT(z)}\right] \tag{6.16}$$

where $\overline{P}_c=\dfrac{\sqrt{RT_c}}{\Gamma_c}\dfrac{A_p\overline{G}_b}{A_n}$.

We perform the calculations of this chapter for a motor which has the properties listed in table 6.1. This properties resemble the characteristics of the 250,000 lb. thrust AMROC DM-01 motor [29].

Geometry:			
Length L (m)	Relative Pre-Combustion Chamber Volume, V_1/V_p	Relative Post-Combustion Chamber Volume, V_2/V_p	Relative Nozzle Throat Area, A_n/A_p
8.5	0.05	0.08	0.178
Model Parameters:			
Temperature, T_1 (K)	Gas Constant, R_1	Skin friction, C_f	Polytropic exponent, n_p
1200	320	0.0001	1
Combustion (HTPB-Oxygen)			
Fuel density	Regression rate law exponent, n	Regression rate law coefficient, a	
920	0.681	$30.48\ 10^{-6}$	
Operating Conditions:			
Oxidizer Mass Flux G_o, (kg/m^2-sec)	Pre-Combustion Chamber Pressure P_1, (atm)	Post-Combustion Chamber Pressure, P_2, (atm)	O/F ratio
200	27.94	27.64	2.1

Table 6.1. The list of parameters for the motor used in the gasdynamic calculations.

Figure 6.3 shows the pressure distribution along the port axis for the test motor. The pressure field is calculated with the use of the inviscid approximation and also with the numerical integration of equation 6.14b for $C_f=0.001$. Note that the effect of friction on the pressure field is negligible for typical hybrid operating conditions. Namely the pressure

drop is mainly due to the fuel mass addition. The variation of the mean velocity along the axis of the motor is determined to behave almost linearly. Thus, we will use a linear mean velocity profile for the first order perturbation formulation. The mean flow Mach number is typically less than 0.2 for every point in the port.

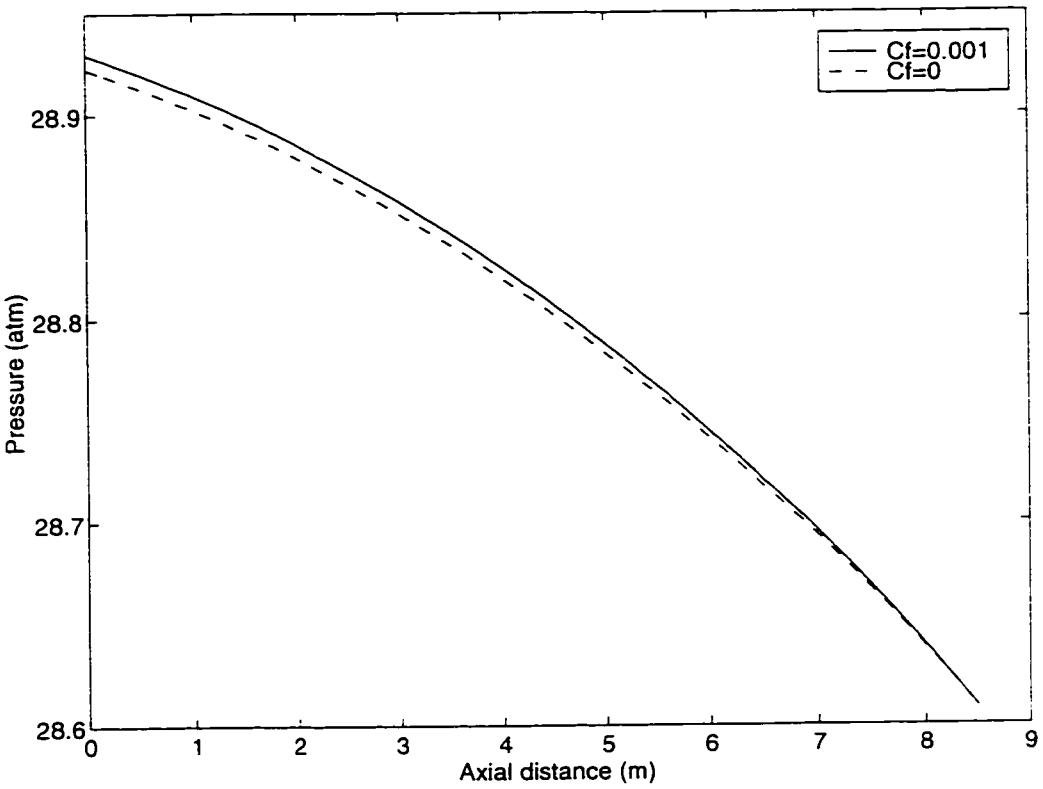

Figure 6.3. The pressure distribution along the port length for the cases of inviscid flow and viscous flow with $C_f = 0.001$.

After determining the nature of the base flow defined by the zeroth order equations, we now focus on the first order perturbation problem around the equilibrium. The first order terms can be collected to yield the following set of perturbation equations.

$$\frac{\partial \tilde{\rho}}{\partial t} = -\frac{\partial \tilde{G}}{\partial z} + \tilde{m}_f \tag{6.17a}$$

$$\frac{\partial \tilde{G}}{\partial t} = -2\bar{u}\frac{\partial \tilde{G}}{\partial z} - RT\frac{\partial \tilde{\rho}}{\partial z} - \lambda \tilde{G} + \beta \tilde{\rho} \tag{6.17b}$$

where

$$\lambda = 2\frac{\partial \overline{u}}{\partial z} + 2\overline{u}\left(\frac{CC_f}{A_p}\right) \qquad \beta = \frac{\partial \overline{u}^2}{\partial z} + \overline{u}\left(\frac{CC_f}{A_p}\right) - \frac{dRT}{dz}. \tag{6.17c}$$

The proper initial conditions for the first order problem are

$$\tilde{G}(z,0) = \tilde{\rho}(z,0) = 0. \tag{6.18}$$

The boundary conditions are

$$\tilde{G}(0,t) = \tilde{G}_a \text{ and } \tilde{\rho}(0,t) = \rho_a. \tag{6.19}$$

We apply the Laplace transformation technique for the solution of the first order perturbation problem. In the solution we assume that the fuel mass generation is independent of the axial position, namely we use an average regression rate for every axial location. The application of the Laplace transformation on the time variable yields the following set of ODE's.

$$s\Psi = -\frac{d\Phi}{dz} + M \tag{6.20a}$$

$$s\Phi = 2\overline{u}(z)\frac{d\Phi}{dz} - RT(z)\frac{d\Psi}{dz} - \lambda(z)\Phi + \beta(z)\Psi \tag{6.20b}$$

Here the Laplace transform variables are defined as

$$\Psi = L[\tilde{\rho}] \qquad \Phi = L[\tilde{G}] \qquad M = L[\tilde{m}_f].$$

The boundary conditions become

$$\Psi(0) = \Psi_a \qquad \text{and} \qquad \Phi(0) = \Phi_a. \tag{6.21}$$

The set of equations can be combined to give the following linear second order ODE for the variable Φ.

$$f_2(z)\frac{d^2\Phi}{dz^2} = f_1(z)\frac{d\Phi}{dz} + f_o(z)\Phi \tag{6.22}$$

The coefficient functions are defined as

$$f_o(z) = s^2 + \lambda s - F_{TC}\beta \qquad f_1(z) = 2\bar{u}(z)s + F_{TC}RT(z) + \beta \qquad f_2(z) = RT(z). \tag{6.23}$$

Note that F_{TC} is the transfer function of the TC coupled system defined as $F_{TC} = M/\Phi$.

For the linear variation of the mean velocity and the RT function along the axis of the port, the coefficients λ, β and f_o, f_1, f_2 become linear functions of z. For this special case a closed form solution for equation 6.22 can be found in terms of hypergeometric functions. However for the purposes of our study, these solutions are too complicated. We introduce another simplifying assumption at this point. We replace variables for the velocity and the RT function with their average values in the port. The validity of this assumption will be discussed in section 6.3 where we compare the numerical simulations with the perturbation solutions.

For convenience we rewrite the differential equation for Φ in the following format.

$$\frac{d^2\Phi}{dz^2} - (a_\Phi + F_{TC})\frac{d\Phi}{dz} - (sb_\Phi - F_{TC}a_\Phi)\Phi = 0 \tag{6.24}$$

Here the parameters are defined as

$$a_\Phi = \frac{\beta + 2\bar{u}_{ave}s}{RT_{ave}} \qquad \text{and} \qquad b_\Phi = \frac{\alpha + 2\bar{u}_{ave}F_{TC} + s}{RT_{ave}}. \tag{6.25}$$

The general solution for equation can be easily found to be

$$\Phi(z) = c_1 e^{(a_\Phi + F_{TC} + \Delta)z/2} + c_2 e^{(a_\Phi + F_{TC} - \Delta)z/2} \tag{6.26}$$

where $\Delta = \sqrt{(a_\Phi - F_{TC})^2 + 4sb_\Phi}$.

The boundary conditions. the differential equation for Ψ and the general solution for Φ can be combined to give the specific solution that we are interested in finding.

$$\Phi(z) = \frac{e^{(a_\Phi - F_{TC})z/2}}{\Delta}\left\{-2s\sinh\left(\frac{\Delta z}{2}\right)\Psi_a + \left[(F_{TC} - a_\Phi)\sinh\left(\frac{\Delta z}{2}\right) + \Delta\cosh\left(\frac{\Delta z}{2}\right)\right]\Phi_a\right\} \quad (6.27a)$$

$$\Psi(z) = \frac{e^{(a_\Phi - F_{TC})z/2}}{\Delta}\left\{\left[-(F_{TC} - a_\Phi)\sinh\left(\frac{\Delta z}{2}\right) + \Delta\cosh\left(\frac{\Delta z}{2}\right)\right]\Psi_a - 2b_\Phi\sinh\left(\frac{\Delta z}{2}\right)\Phi_a\right\} \quad (6.27b)$$

These relations can be evaluated at $z = L$ where L is the length of the port. to obtain the relation for the flow variables between the entrance and the exit of the port.

$$\Psi_b = \frac{e^{(a_\Phi - F_{TC})L/2}}{\Delta}\left\{\left[-(F_{TC} - a_\Phi)\sinh\left(\frac{\Delta L}{2}\right) + \Delta\cosh\left(\frac{\Delta L}{2}\right)\right]\Psi_a - 2b_\Phi\sinh\left(\frac{\Delta L}{2}\right)\Phi_a\right\} \quad (6.28a)$$

$$\Phi_b = \frac{e^{(a_\Phi - F_{TC})L/2}}{\Delta}\left\{-2s\sinh\left(\frac{\Delta L}{2}\right)\Psi_a + \left[(F_{TC} - a_\Phi)\sinh\left(\frac{\Delta L}{2}\right) + \Delta\cosh\left(\frac{\Delta L}{2}\right)\right]\Phi_a\right\} \quad (6.28a)$$

It is convenient to replace the density variables which appear in these equations with the pressure variables. We use the ideal gas law. $\tilde{P} = \tilde{\rho}RT$ or in the transformed format $\Theta = \Psi RT$ where the Laplace transform of pressure perturbation is defined as $\Theta = L\left[\tilde{P}\right]$. The density transform variable at the entrance and at the exit of the port can be written as $\Psi_a = \Theta_1 RT_1$ and $\Psi_b = \Theta_2 RT_2$, respectively. We remind that subscript 1 corresponds to pre-combustion chamber and subscript 2 corresponds to post-combustion chamber.

The port equations can be also be expressed in the following compact form.

$$\Phi_b = F_1(s)\Theta_1 + F_2(s)\Phi_a \quad (6.29a)$$

$$\Theta_2 = F_3(s)\Theta_1 + F_4(s)\Phi_a \quad (6.29b)$$

Here the functions are defined as

$$F_1(s) = -RT_1 \frac{e^{(a_\Phi + F_{TC})L/2}}{\Delta} 2s\sinh\left(\frac{\Delta L}{2}\right) \tag{6.30a}$$

$$F_2(s) = \frac{e^{(a_\Phi + F_{TC})L/2}}{\Delta}\left[(F_{TC} - a_\Phi)\sinh\left(\frac{\Delta L}{2}\right) + \Delta\cosh\left(\frac{\Delta L}{2}\right)\right] \tag{6.30b}$$

$$F_3(s) = \frac{RT_2}{RT_1}\frac{e^{(a_\Phi + F_{TC})L/2}}{\Delta}\left[-(F_{TC} - a_\Phi)\sinh\left(\frac{\Delta L}{2}\right) + \Delta\cosh\left(\frac{\Delta L}{2}\right)\right] \tag{6.30c}$$

$$F_4(s) = -RT_2 \frac{e^{(a_\Phi + F_{TC})L/2}}{\Delta} 2b_\Phi \sinh\left(\frac{\Delta L}{2}\right). \tag{6.30d}$$

We next consider the pre-combustion and post-combustion chamber response. Since the pre-combustion chamber equation is already linear in nature, we directly apply the Laplace transformation.

$$a_1 s\Theta_1 = I - \Phi_a \tag{6.31}$$

Here the I is the Laplace transform of the oxidizer mass flow rate perturbation injected into the chamber and a_1 is defined as L_1/RT_1 where L_1 is the characteristic length of the pre-combustion chamber volume, $L_1 = V_1/n_p A_p$.

We simplify the post combustion chamber response and obtain the following equation.

$$a_2 s\Theta_2 = -e'\Theta_2 + \Phi_b \tag{6.32}$$

Similarly a_2 can be written as L_2/RT_2. Note that the characteristic length of the post-combustion chamber is defined as $L_2 = (V_2 + V_n)/A_p$. V_n is the portion of the nozzle volume that needs to be added to the post combustion chamber volume to account for the inertial effects in the nozzle. The nozzle discharge behavior is represented by the coefficient e' given by

$$e' = \frac{A_n}{A_p}\frac{\Gamma_c}{\sqrt{RT_c}}. \tag{6.33}$$

Equations 6.29a, 6.29b, 6.31 and 6.32 form a linear system for the four unknown variables, namely the pressures and the mass fluxes at the entrance and the exit of the port volume. The pre-combustion chamber pressure variable can easily be solved from this linear system to give

$$\Theta_1 = \frac{RT_1\left\{\Delta + \left[(F_{TC} - a_\Phi) + 2b_\Phi(L_2 s + e)\right]\tanh(\Delta L/2)\right\} I}{\left[(L_1 + L_2)s + e\right]\Delta + \left\{\left[L_1(F_{TC} - a_\Phi) + 2\right]s + \left[2L_1 b_\Phi s - (F_{TC} - a_\Phi)\right](L_2 s + e)\right\}\tanh(\Delta L/2)}. \tag{6.34}$$

Note that we define

$$e \equiv e' RT_2 = \frac{A_n}{A_p} f_h \Gamma_c \sqrt{RT_c} = \frac{A_n}{A_p} f_h c^*. \tag{6.35}$$

Although equation 6.34 is a transfer function specifically between the oxidizer mass flux input and the pre-combustion chamber pressure output, it represents the overall nature of the response for gasdynamic system. Similar expressions for the other variables can be also derived, but for the purpose of our arguments this expression is adequate.

6.2.2 Numerical Simulations

In order to check the validity of the assumptions used in the perturbation solutions, we also perform numerical simulations on the 2V-port model described in the previous section. We start with the finite differencing of the special derivative terms and use the second order central differencing over a uniform mesh along the axis of the port [44]. For the time marching we use the Runge-Kutta fourth order method. The boundary conditions for the port equations are obtained from the pre and post combustion chamber dynamic equations. The numerical method used in the calculations gave stable and accurate results for a typical time step of 3 10^{-4} seconds and 80 mesh points in the port. The details of the numerical scheme is discussed in appendix E.

The simulation code is applied to various transient events such as the throttling and the sinusoidal oxidizer flow rate case. The results are discussed in the following section.

6.3 Discussion of Results for Pure Gasdynamics

The response of the gasdynamic system for a hybrid motor can be deduced from the gasdynamic system transfer function. For example, the stability features of the system are revealed by the roots of the denominator of the transfer function which is the characteristic equation. However any investigation of the gasdynamic system response requires an input for the combustion response that is represented by the F_{TC} term.

In this section we use the simplest quasi-steady combustion model. Namely, all the transient effects including the thermal lags in the solid and also the boundary layer delays except the gasdynamics are ignored in this model. For that reason, this model which does not allow any dynamic coupling between the sub-systems of the rocket is highly desirable to isolate the investigations to purely gasdynamic phenomena. The combustion response function can easily be derived from the general regression rate law after linearization and Laplace transformation.

$$F_{TC} = \alpha_1 n \bar{G}^{n-1} \tag{6.36}$$

For the case of the quisi-steady combustion the gasdynamic system transfer function is plotted in figure 6.4. The operational parameters of this motor are listed in table 6.1. The plot shows a pole on the negative real axis and a row of imaginary poles also in the negative real halfplane. The real pole resembles the volumetric capacity of the chamber, whereas the imaginary poles represent the longitudinal acoustic nature of the cavity. Note that all the poles have negative real parts, namely the both acoustic and also the global response components decay in time. The conclusion is that the pure gasdynamic system is stable in nature.

In order to test the validity of the transfer function we consider the trivial case of no mass addition and no temperature or velocity gradients in the port. In this case the transfer function simplifies to

$$\Theta_1 = \lim_{(F_{TC}-a_\Phi)\to 0} \frac{RT_c I}{\left[(L_1+L_2)s+e\right] + \dfrac{2s}{(F_{TC}-a_\Phi)} \tanh\left[(F_{TC}-a_\Phi)L/2\right]}. \tag{6.37}$$

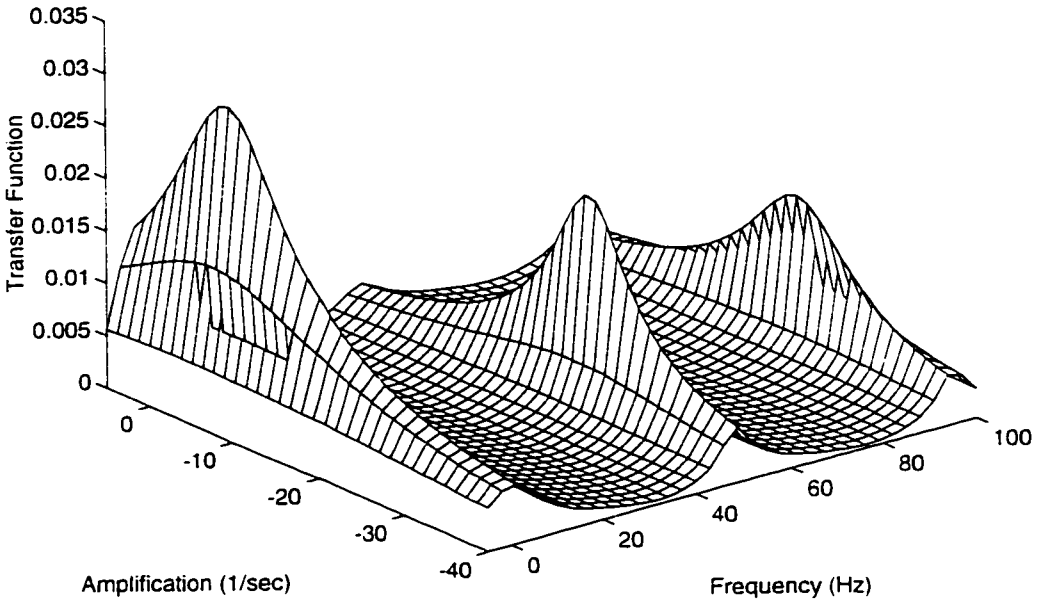

Figure 6.4. The plot of the transfer function for the pure gasdynamic system.

After the application of the L'Hospital's rule one obtains the well known transfer function for a simple single volume system.

$$\Theta_1 = \frac{RT_c I}{(L_1 + L_2 + L)s + e} = \frac{(RT_c/\theta c^*)}{\tau_f s + 1} \tag{6.38}$$

Here $\tau_f = L^*/c^*$ is the characteristic filling time of the motor chamber. The other parameters are defined as $L^* = V/A_p$ and $c^* = \Gamma_c\sqrt{RT_c}$ which are commonly used in rocket literature [4]. Note that the total volume of the motor combustion chamber can be written as $V = (L_1 + L_2 + L)A_p$. This is the transfer function generally used (especially in the industry) in hybrid dynamic modeling.

The preceding equation does not predict the filling/emptying time scale of a hybrid rocket accurately. For that reason we develop a better estimate by the following argument. In the region of the s plane that the pole for the filling/emptying process is expected to be located, the following approximations can be made.

$$a_\phi \equiv \frac{\beta}{RT_{ave}} \qquad b_\phi \equiv 0 \qquad \Delta \equiv \left|a_\phi - F_{TC}\right| \tag{6.39}$$

Under these approximations the gasdynamic transfer function simplifies to

$$\Theta_1 = \frac{RT_1\left\{1+\tanh\left(\left|F_{TC}-a_\phi\right|L/2\right)\right\}I}{\left\{L_1+L_2+\left[L_1-L_2+2/\left(F_{TC}-a_\phi\right)\right]\tanh\left(\left|F_{TC}-a_\phi\right|L/2\right)\right\}s+e\left[1-\tanh\left(\left|F_{TC}-a_\phi\right|L/2\right)\right]}. \tag{6.40}$$

Note that since $F_{TC}-a_\phi$ term is independent of s, this transfer function represent the behavior of a first order system with a characteristic time of

$$\tau_f = \frac{L_1+L_2+\left[L_1-L_2+2/\left(F_{TC}-a_\phi\right)\right]\tanh\left(\left|F_{TC}-a_\phi\right|L/2\right)}{e\left[1-\tanh\left(\left|F_{TC}-a_\phi\right|L/2\right)\right]}. \tag{6.41}$$

The throttling response for a throttling ratio of 1.2 of the motor with specifications listed in table 6.1 is calculated with different methods and plotted in figure 6.5. Figure shows the time variation of the nondimesional pre-combustion chamber pressure defined as $\left(P_1(t)-P_1^i\right)/\left(P_1^f-P_1^i\right)$ where P_1^i is the initial pressure and P_1^f is the final pressure. The striking observation is that the perturbation solution with the filling time defined by equation 6.41 is in excellent agreement with the numerical simulation result. This shows that equation 6.41 gives a good estimate for the filling time of the motor chamber within the context of the 2V-port model. The response according to the simple transfer function is also shown in figure 6.5. It is obvious from the figure that the simple filling time argument for the hybrid combustion chamber is not valid.

Figure 6.6 shows the variation of the characteristic filing time as a function of the port volume length. Figure indicates that both models present linear behavior with the motor size, but equation 6.38 estimates are significantly larger than the single volume predictions.

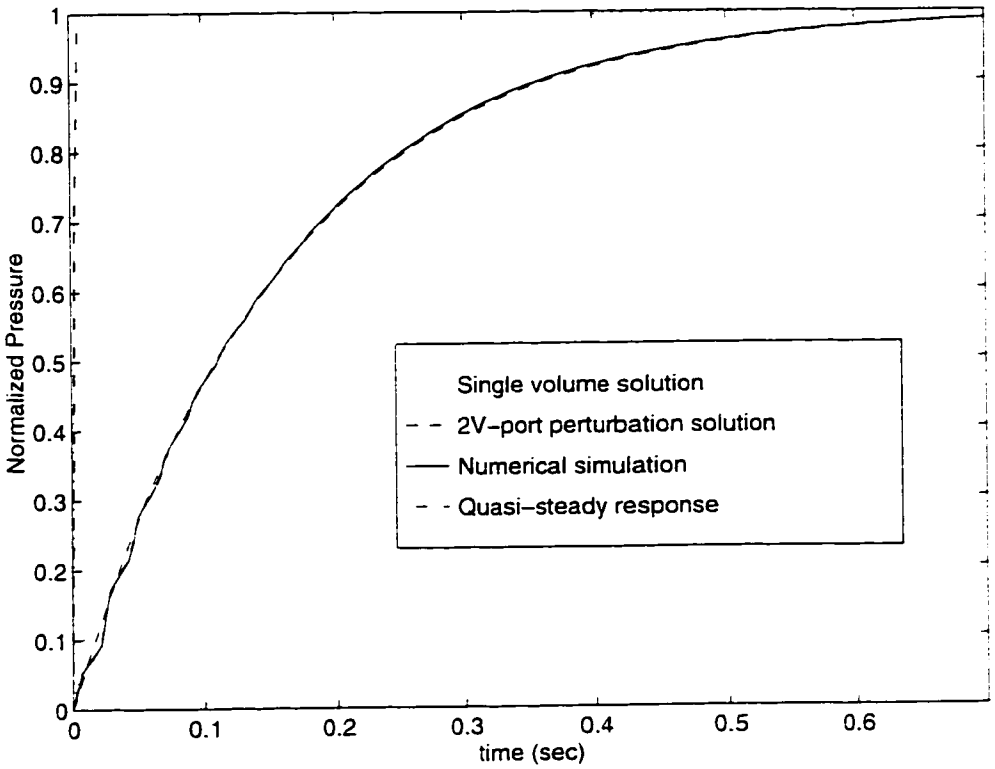

Figure 6.5. The throttling response for the pure gasdynamic system.

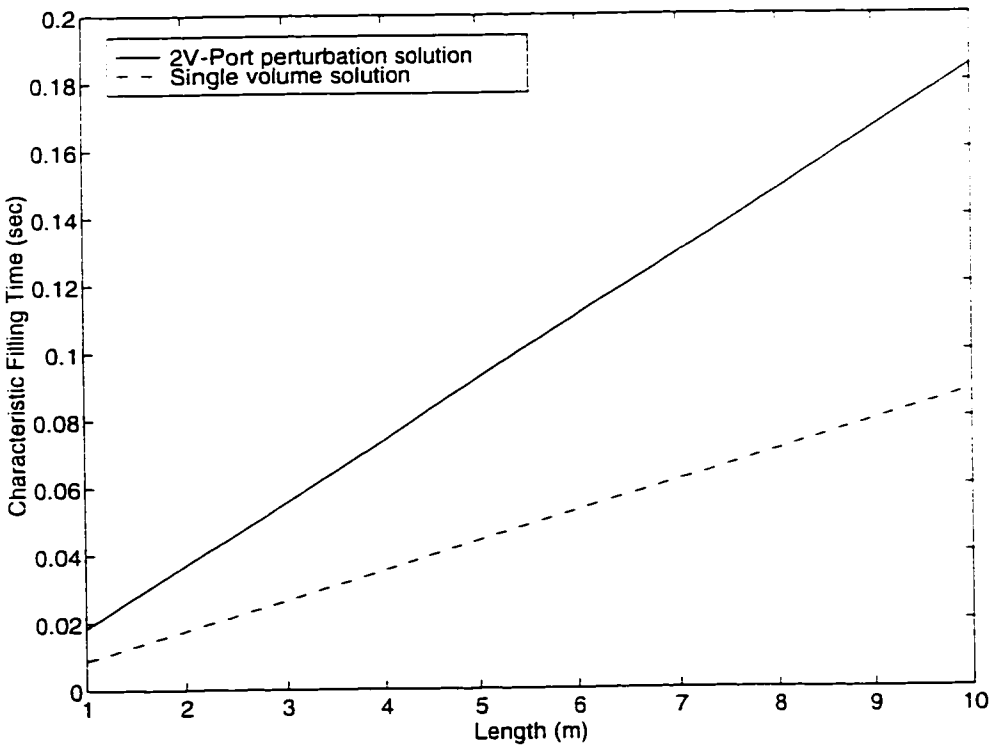

Figure 6.6. The characteristic filling time τ_f as a function of the port length for two models represented by equations 6.38 and 6.41.

Another observation from figure 6.5 is that the numerical simulation result shows oscillatory behavior in the early stages of the throttling event. This oscillatory behavior is due to the excitation of the acoustic modes of the cavity by the disturbance caused by the sudden increase in the oxidizer mass flow rate. The oscillation frequency and the damping time scale of this mode of motion is consistent with the longitudinal acoustic mode findings for the same motor.

This kind of behavior is commonly observed in AMROC DM-01 motors [29]. Namely, a nonlinear disturbance causes the well damped oscillation of the chamber pressure at the longitudinal acoustic frequencies. The exciting disturbances in the actual tests are believed to be caused by: 1) a sudden blockage of the nozzle throat area by some disintegrated fuel fractions. 2) the ignition of a bulk of fuel oxidizer mixture captured in the pre-combustion chamber or 3) the low frequency oscillations of chamber pressure.

We compare the predictions of our gasdynamic model for the acoustic frequencies of the chamber with the AMROC DM-01 motor test data. Table 6.2 shows the first five longitudinal frequencies determined by the perturbation solutions. Since our model is isothermal, these frequencies are corrected by multiplying with the factor of $\sqrt{\gamma}$. An average γ value of 1.2 is used for the calculations. Note that the corrected frequencies falls in the range of observed frequencies for every calculated acoustic mode.

Longitudinal Acoustic Mode	Estimated (Isothermal) Frequency (Hz)	Corrected Frequency (Hz)	Observed Frequency (Hz)	Estimated Amplification (1/sec)
1st	48.4	53.0	50-55	-22
2nd	96.7	103.9	100-110	-22
3rd	142.6	156.1	150-165	-21
4th	191.1	209.3	200-220	-19
5th	240.7	263.6	250-275	-18

Table 6.2. The estimated and observed longitudinal acoustic frequencies for AMROC DM-01 motor.

The gasdynamic code developed to perform simulations on the 2V-Port model is used to confirm the findings of the perturbation solutions on the frequency response of the system. In the simulations, sinusoidal oxidizer mass flow rate inputs at various frequencies are applied as the forcing function and the phase and the amplitude of the chamber pressure

oscillations are determined. The agreement between the perturbation solutions and the numerical simulations for the frequency response of the system is also found to be satisfactory. The results are reported in detail in reference 64.

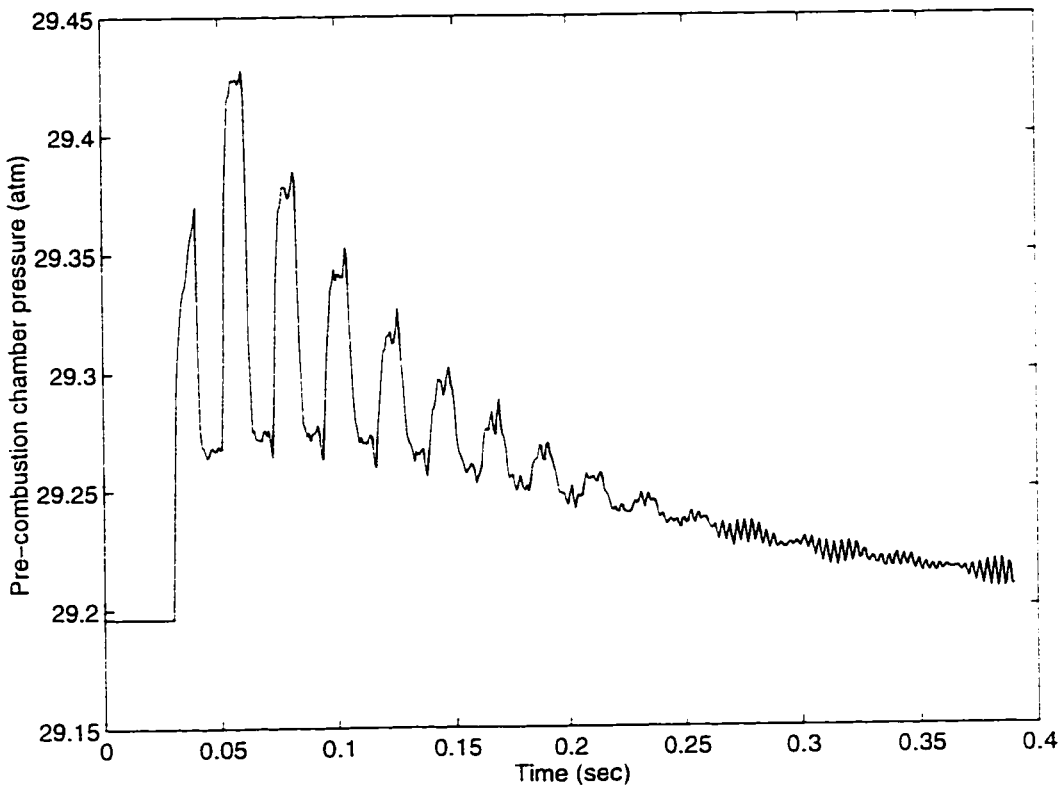

Figure 6.7. The response of the pre-combustion chamber pressure to a disturbance of the oxidizer mass flow rate.

The simulation code is also used to investigate the response of the gasdynamic system to a disturbance. The oxidizer mass flow input is suddenly increased 10% above its operating value and held at its elevated level for 0.03 seconds before its suddenly reduced to its original value. The pressure time history for this simulation is shown figure 6.7. It is clear that the disturbance excites the acoustic modes of the chamber similar to the previous observations. These exited modes decay in a moderate time scale as it was observed in the AMROC tests. A similar simulation is performed to determine the effect of nozzle blockage on the stability by reducing the nozzle throat area for a brief period of time. The results for the nozzle area perturbation case are identical in nature to the results of the oxidizer mass flow rate perturbation. In short, a nonlinear disturbance causes the ringing of the hybrid chamber which decays in time. This fact potentially explains why the low frequency

instabilities which are nonlinear waveforms are accompanied by the acoustic frequency pressure oscillations.

Finally a simple delay (τ_c) on the combustion response is applied to the gasdynamic system.

$$F_{TC} = \alpha_1 n \overline{G}^{n-1} e^{-\tau_c s} \tag{6.42}$$

Both the perturbation solutions and also the numerical simulations indicate that any positive combustion delay have negligible effect on the satbility nature of the system.

6.4 TCG Coupling

In the previous section we considered the quasi-steady combustion approximation with and without delay. These considerations were instructive on the behavior of the isolated gasdynamic system and on the possible influence of a delay on the response. However, a much more complete description of the dynamics of the hybrid rocket can be obtained by using the combustion model developed in chapters 4 and 5 along with the gasdynamic transfer function derived in this chapter. We call the resulting system as the thermal lag-combustion-gasdynamics coupled (TCG coupled) system.

The schematic of the hybrid subsystems and the information flow between the subsystems in the context of TCG coupling are shown in figure 6.8. Note that the lower block in the schematic represents the TC coupled system. The input for the TC coupled system is the local mass flux information and the output is the mass generation or the regression rate. The upper block shows the 2V-port gasdynamic model. The gasdynamic model takes the oxidizer flow rate and the mass generation rate information and reveals the important performance parameters such as the chamber pressure and specific impulse. The TCG coupled system can be considered as an overall model for the dynamics of a hybrid propulsion system that utilizes gaseous oxidizer which is delivered by a very stiff feed system.

The generalization of the TCG coupled system to a liquid hybrid with significant feed system dynamics can be achieved easily. Namely two more modules for the liquid droplet evaporation and the feed system dynamics must be added to the front end of the

TCG model. We finally note that the phenomena such as the low frequency instabilities unique to hybrids do not involve either of the evaporation lags or the feed system dynamics.

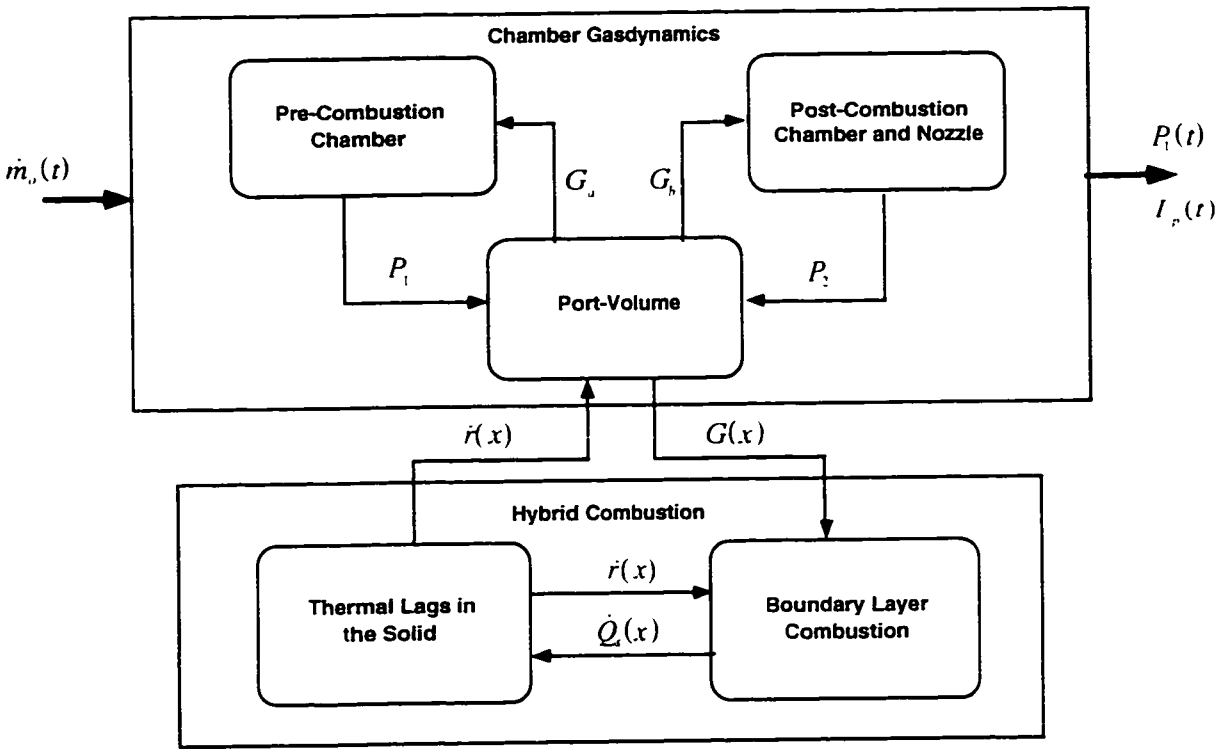

Figure 6.8. The schematic of the TCG coupled system.

A plot of the TCG coupled system transfer function for the motor with properties listed in table 6.1 is shown in figure 6.9. Since the form of the plot in the negative real halfplane behaves very similar to the pure gasdynamic transfer function, we focus only on the first mode in the positive real halfplane. An important observation is that the unstable pole generated by TC coupled system persists after the interaction with the gasdynamics. However after the interaction with the gasdynamics, the single pole splits into many poles in a relatively small neighborhood in the s plane. In this special case the poles are distributed between 3.4 and 3.7 Hz. Similar behavior is also observed at higher frequency poles of the system. This pole splitting phenomenon is consistent with the erratic nature of the measured frequencies in the motor tests [30].

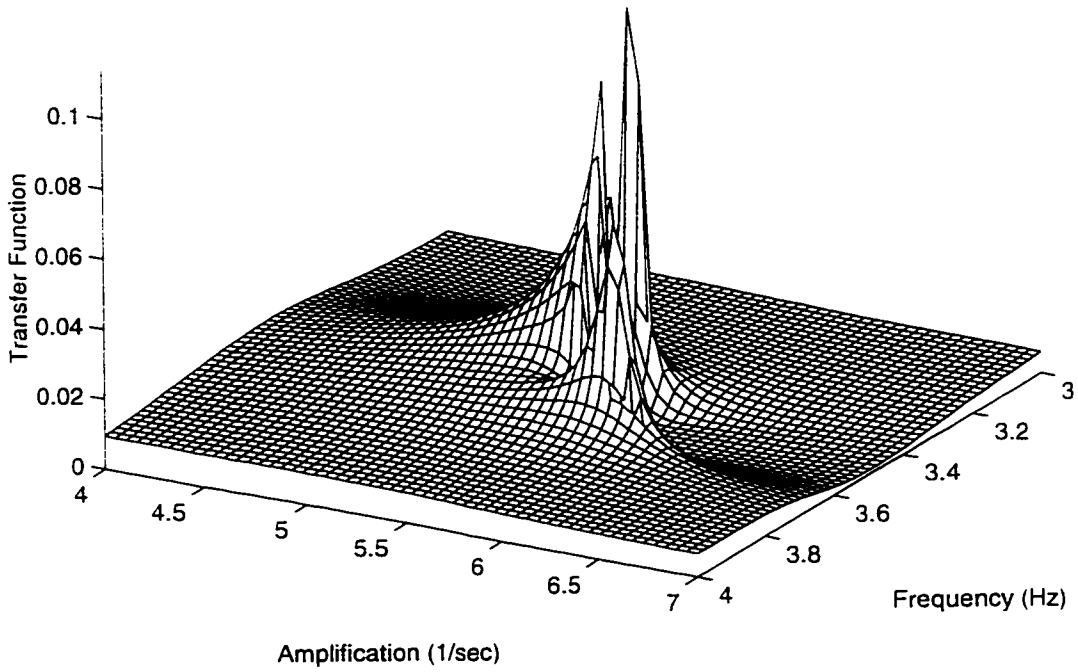

Figure 6.9. The unstable poles of the TCG coupled transfer function.

6.5 Conclusions for Chamber Gasdynamics

In this chapter we developed an isothermal gasdynamic model (2V-Port) for the hybrid rocket combustion chamber. In our model we treated the port as a quasi-1D tube with continuous mass and heat addition. In order to simplify the problem, we assumed a time invariant temperature field in the port (the energy equation is decoupled). We linearized the field equations and obtained a transfer function for the whole system. The combustion dynamics is represented as a general transfer function in the model. In order to isolate the gasdynamic phenomena, we initially assumed a quasi-steady combustion response. The perturbation results showed that the model successfully represents the longitudinal acoustic behavior as well as the volumetric nature of the chamber. Acoustic frequencies estimated by the model and corrected for the isothermal assumption agreed well with the AMROC DM-01 test results. All modes of the pure gasdynamic system are determined to be stable with or without the application of a positive time delay for the combustion response.

Some numerical simulations are also performed mainly to verify the results of the perturbation solutions. The analytical solutions determined to be in perfect agreement with the numerical simulation results. The numerical results also showed the decaying ringing of the chamber after the application of a nonlinear disturbance. This phenomenon which is observed in actual motor tests is generated by the excitation of the acoustic modes by some nonlinear disturbance. Ringing may serve as a possible explanation for the mutual existence of the low frequency oscillations and the acoustic modes which is often encountered in hybrid tests.

Finally, the gasdynamic model is coupled with the TC system to obtain a more complete response for the hybrid motor. The TCG coupled system splitted each of the unstable poles predicted by the TC coupled system in a small neighborhood in the s plane. It can be stated that TCG coupled system successfully predicts the generation of the low frequency oscillations in hybrids. However, at least the linear implementation of the model, fails to limit the growth of the unstable oscillations. We believe that a nonlinear gasdynamic model that includes the effects of the O/F shift during the transients is essential to capture the limit cycle behavior of the hybrid low frequency oscillations [65].

Chapter 7

Liquid Layer Hybrid Combustion Theory

In this chapter, the classical hybrid combustion theory is generalized for the hybrid rocket fuels that burn by forming a significant liquid layer on the solid grain. The most important application of the theory is to cryogenic hybrids [9, 66, 67] with frozen hydrocarbon liquids as fuels which do not involve a depolymerization energy for their gasification. The theory is based on the possibility of a separate mass transfer mechanism for the hybrid fuel regression other than the evaporation due to the convective and radiative heat transfer from the flame to the grain surface. The additional mechanism proposed in this study is the entrainment of the liquid droplets of fuel from a melt layer formed over the solid. The entrainment, as it will be shown in this chapter, is due to the liquid layer instabilities which arise from the high velocity gas flow in the port.

7.1 Cryogenic Hybrids

Despite their safety and cost advantages over the solid and liquid systems, hybrids, at least the conventional ones, possess a significant shortcoming. That is the low thrust densities associated with the low regression rates. The limit on the regression rate for the hybrid combustion configuration is set by the physical phenomenon of heat transfer from the relatively remote and cool flame zone to the fuel surface. As a consequence, the regression rates of modern hybrids that utilizes polymers as the fuel are significantly less than the conventional solid rocket burning rates [3, 11, 31].

Various methods for the enhancement of the hybrid regression rate performance is suggested in the past. One obvious method is to reduce the effective heat of gasification of the selected fuel. However, this is not satisfactory, since the variation of the effective heat of gasification is small over the range of feasible fuel types. Moreover the change in the fuel thermochemical properties may also alter other important parameters that also affect the regression rate such as the flame temperature and the flame location in the boundary layer.

A much more effective method is to use of propellants that form a melt layer at the combustion surface which are usually non-polymerized substances that liquify on heating. Obvious members of this class of propellants are fluids at standard conditions which when solidified form the classical "cryogenic propellants". However it is clear that same ballistic behavior can be experienced by solids at standard conditions if they form melt layers at the combustion surface. Thus typical members of this class range from H_2, a deep cryogen, to the long chain hydrocarbon waxes. "Reverse" hybrids in this class would be solid oxygen, N_2O_4, HNO_3, etc.

The increased regression rates by several hundred percent have been observed with solid pentane and O_2 [9, 29]. The higher regression rates opens a new vista of potential performance improvement in hybrid since it permits thicker webs resulting fewer ports for large motors and therefore increased volumetric fuel loading and simpler fabrication. In addition, higher I_{sp} values can now be realized with short chain hydrocarbons and amine compounds because of their low molecular mass gases. In contrast to liquid propellant rockets, which also use these ingredients, the frozen fuels can incorporate energetic metals to further increase performance and density. Adding metals to liquid has always been a problem due to storage instability of the slurry mixture, i.e. settling of metals. The resulting cryogenic hybrid still retain their classical advantages of non-explosiveness, safe handling, on-off operation, simplified throttling.

The regression rate model developed for these propellants, in addition to the classical gasification, is based on a mass transfer mechanism resulting entrainment of liquid droplets from the melt layer over the solid. As will be discussed the droplet formation is due to the liquid layer instabilities which result from the high velocity gas flow in the port. The purpose of this paper is to explore the development of the liquid layer at the burning surface and determine the conditions for the onset of the entrainment so that its occurrence can either be invoked or avoided. It can be expected, further, that there may be conditions where excessive sloughing occurs relating in nonuniform combustion which should be avoided.

In the next section we will investigate the regression rate characteristics of the solid cryogenic propellants burned with gaseous oxygen in hybrid configuration.

7.2 Experimental Findings

Recently some lab scale cryogenic hybrid tests were performed at Edwards Air Force Base [9, 66, 67]. A small tube burner with a 1.4 cm inner diameter was used to investigate the performance of various frozen hydrocarbon liquids at the liquid nitrogen temperature. These were burned with gaseous oxygen in a hybrid scheme. In this section, we are mainly interested in finding the dependence of burning rates on the port oxidizer mass flux (the burning law) for the cryogenic motors tested.

The primary observed variables in the performed tests were the chamber pressure-time history and oxidizer mass flow rate which was held constant with use of a venturi in the oxygen feed system [66]. However, the instantaneous space averaged regression rates, which are of primary interest for us, were not measured (or estimated) directly in the previous studies. For that reason we develop procedures to determine the regression rates from the pressure history and the oxidizer flow rate information.

In our calculations we primarily concentrate on the tests performed with pentane as the fuel. A summary of the data for the tests of concern are reported in table 7.1 [66]. We start with the calculation of the time averaged regression rate for each test. In general for a hybrid rocket, the space time average regression rate can be calculated approximately from the global mass balance considerations which is given by the following formula.

$$\bar{\dot{r}} = \frac{M_f}{\rho_f S_w t_b} \tag{7.1}$$

Here M_f is the total mass of the fuel, t_b is the burn time, S_w is the average burn area over the burn time. The average regression rates are calculated for five different pentane runs and plotted against the oxidizer mass flux in figure 7.1. Note that the oxidizer mass flux is also calculated with use of an average port area which is consistent with the burn area used in the regression rate estimation. Figure 7.1 indicates that the averaged regression rate law for this set of experiments has an oxidizer mass flux exponent value of slightly larger than one. This result is in contrast with the classical diffusion limited theory that predicts a mass flux exponent in the range of 0.5 to 0.8 [11].

Test No.	Solid Propellant	Nozzle Area (cm^2)	Burn time (sec)	$\dot{m}_{ox}$ (g/sec)	Maximum Pressure (psi)
100	Pentane	0.2056	4.5	11.4	225
101	Pentane	0.2056	3	21.0	440
103	Pentane	0.100	3	19.8	800
118	Pentane	0.2056	7.5	4.8	90
102	Pentane	0.1	4.5	10.2	420
105	2,2,5 tmh	0.0993	4.75	10.2	425
108	Acetone	0.0964	4.5	10.3	475
121	HFI	0.128	8	10.3	350
107	Isopropanol	0.993	9	10.3	425

Table 7.1. Summary of data for several cryogenic experiments.

Unlike conventional hybrid rocket test results, the pressure-time history for the cryogenic experiments do not possess a time period of slow variation of pressure. A typical pressure time history is shown in figure 7.4a for test 103 [9]. Initially, the pressure rapidly increases to a maximum value over a period of approximately one third of the total burn time. During this time period it is likely that the transients in the motor such as the heating of the cold fuel grain govern the response. After the maximum pressure point is attained, the pressure decreases rapidly and for most cases almost linearly in time. It is likely that this period of the burn is dictated by the increase in the port area, reduction in the oxidizer mass flux and consequently the decrease in the mass generation rate. In most of the pentane runs this period covers the middle one third of the total burn. The rapid decrease in the chamber pressure in the cryogenic tests unlike the conventional hybrids is most likely related to the large regression rates and small port diameters used in the cryogenic experiments. In the remaining period of the burn times the pressure levels are low and the pressure decreases even more rapidly. These high reduction in the pressure is likely to be caused by a decrease in the total burn area of the fuel grain due to the uneven depletion of the fuel both in the axial and also in the azimutal directions. In our studies we are interested in the stationary operation of the cryogenic motor. For that reason only the middle third of the tests are likely to be useful for the purpose of our studies. Therefore we believe that the average regression rate analysis based on the whole test period is not adequate to yield the data to obtain a stationary burning law for the cryogenic hybrids. A more sophisticated

method for the determination of the regression rates during the stationary operation of the motor will be developed in the next paragraph.

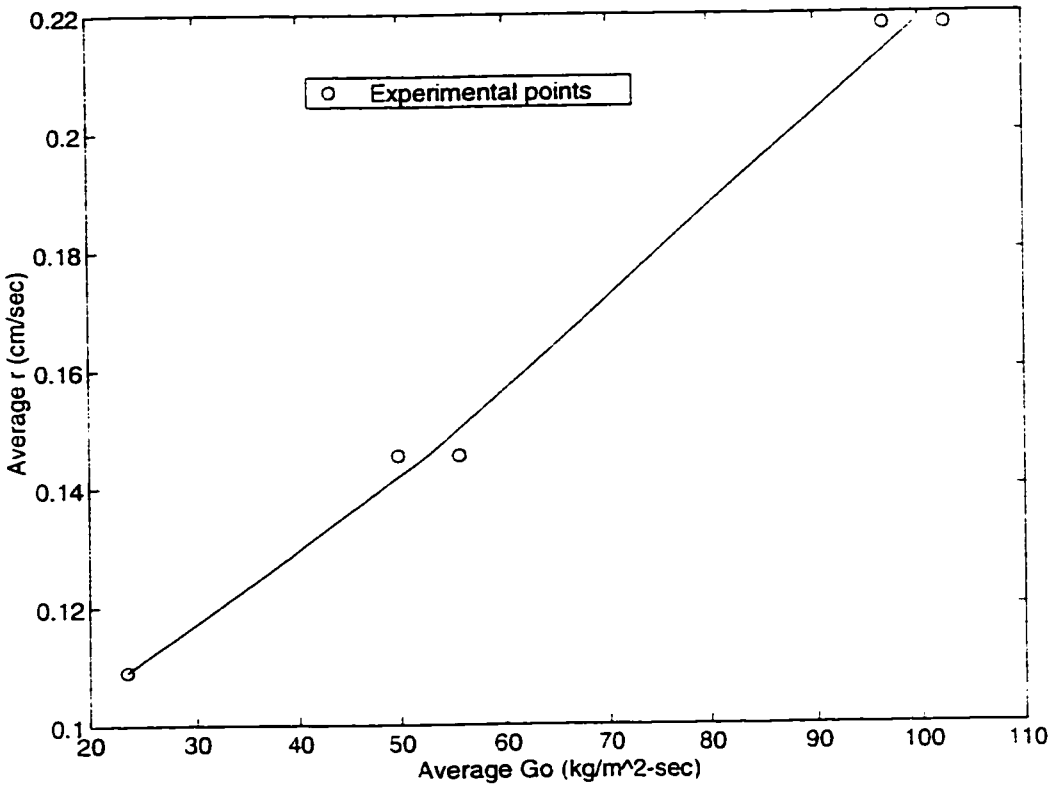

Figure 7.1. The average regression rates are plotted versus the average oxidizer mass fluxes in the port. The tests used in this plot are 100 101, 102, 103 and 118 [66].

We start with the steady-state global mass balance in the chamber which can be formulated as

$$\dot{m} = \dot{m}_{ox} + \dot{m}_f = \dot{m}_{ox}\left(1 + \frac{1}{O/F}\right) = \frac{P_c A_n c_d}{c^* \eta_{c^*}}. \tag{7.2}$$

Here $\dot{m}_{ox}$ is the oxidizer mass flow rate, $\dot{m}_f$ is the fuel mass flow rate, O/F is the oxidizer to fuel ratio of the motor. The discharge coefficient, c_d, the combustion efficiency, η_{c^*}, are also included in the equation to account for the nozzle flow losses and the combustion inefficiencies, respectively. Note that c^* is the theoretical characteristic velocity and its variation with the motor O/F ratio for the pentane-oxygen system is shown in figure 7.2.

Next, we rearrange equation 7.2 in the following form to isolate the terms depending on the O/F ratio.

$$c^{+}(O/F) \equiv \left(1 + \frac{1}{O/F}\right) c^{*}(O/F) = \frac{P_c A_n c_d}{\dot{m}_{ox} \eta_c} \tag{7.3}$$

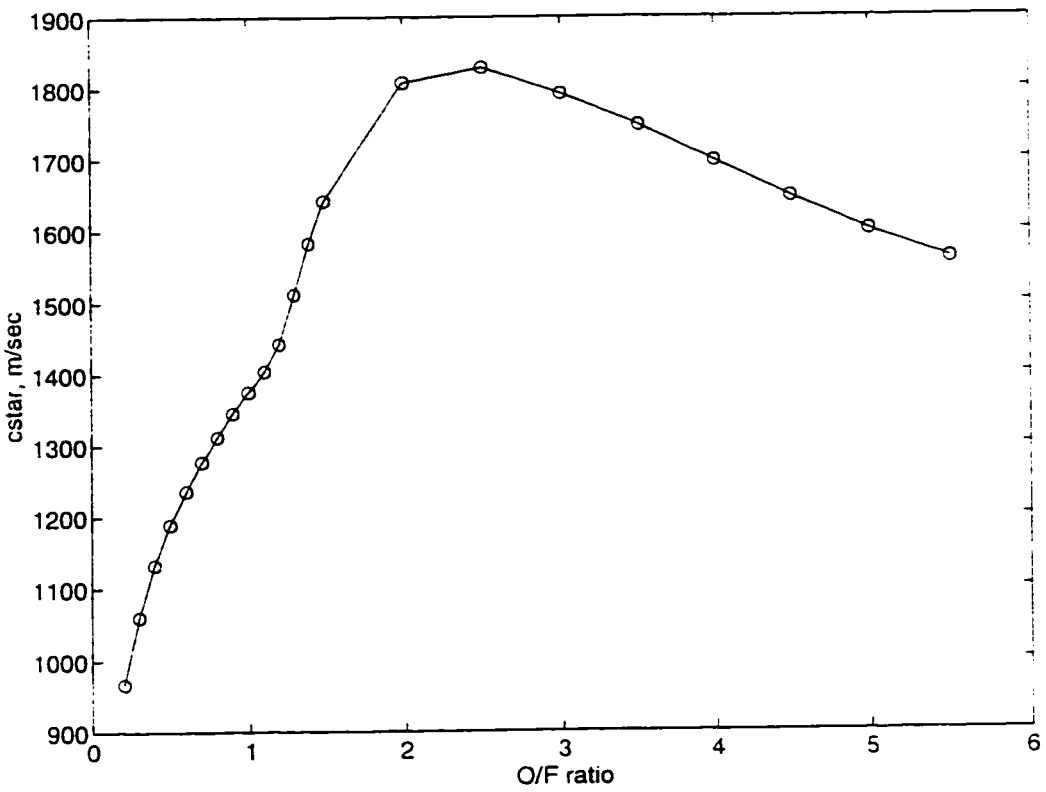

Figure 7.2. The characteristic velocity c^{*} is plotted with respect to the O/F ratio for a pentane-oxygen system.

In this expression c^{+} is another characteristic speed corrected for the relative mass flow rate of the oxidizer and the fuel which only depends on the motor O/F ratio for a selection of propellants. We assume that both η_c and also c_d are independent of the O/F ratio. Under these conditions the right hand side of equation 7.3 becomes a known function of time for a specified experiment. Thus the problem is reduced to the solution of equation 7.3 for the O/F ratio for every time step. Since the oxidizer mass flow rate is specified, the fuel mass flow at each time can also be estimated with use of the O/F ratio. Next the estimated fuel mass flow rate variation can be used to determine the change of the average diameter of the port and also the space averaged regression rate as a function of time.

The variation of c^* with O/F ratio, which plays a central role in the inversion process, for the pentane/GOX system in shown in figure 7.3. For simplicity we use a curvefit relation rather than the exact c^* expression for the solution for the O/F ratio. The variation of the curvefit expression with the O/F ratio is also shown in figure 7.3. We note that the exact c^* for pentane is not a monotonic function of the O/F ratio. For that reason, for a range of operating conditions the inversion process is ambiguous. Although, the curvefit expression for the inversion is a rough approximation, it is a single valued function of the O/F ratio. (This characteristic simplifies the inversion process significantly.)

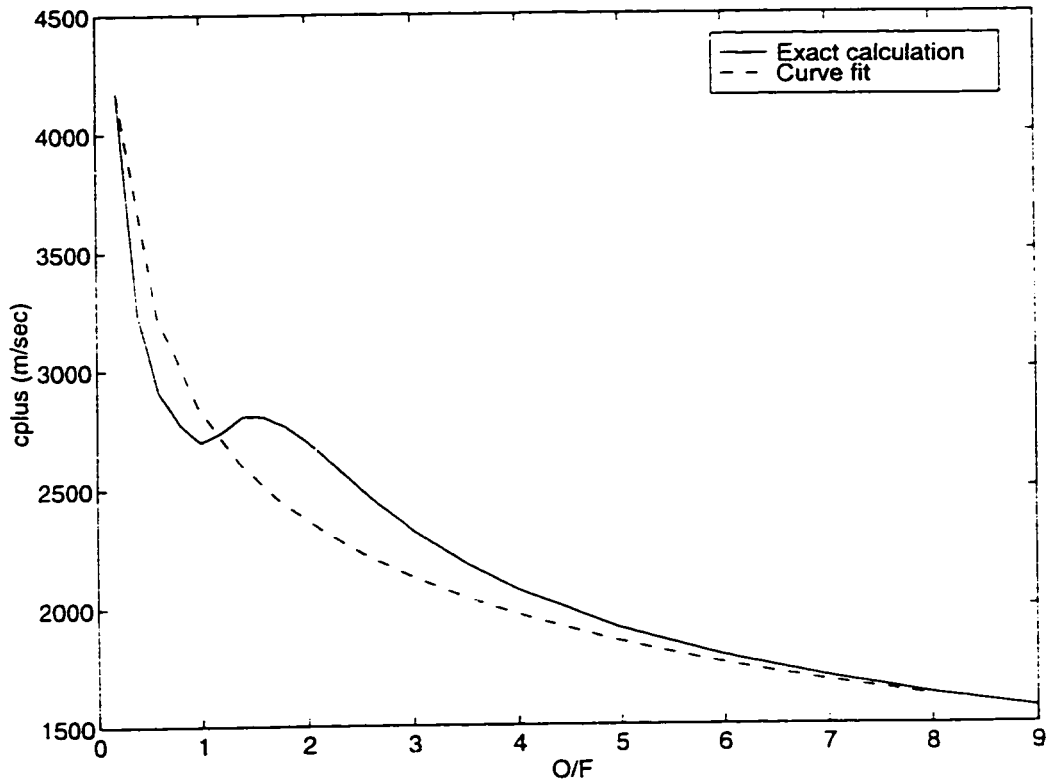

Figure 7.3. The characteristic velocity c^* is plotted with respect to the O/F ratio for a pentane/GOX system. The solid line is the exact calculation whereas the dotted line represents a curvefit to the exact line.

In our calculations we assume that the combustion efficiency is constant over the extent of the run. For each run, this constant efficiency can be determined by iteration to match the initial fuel mass to the total estimated mass of the fuel consumed over the whole burn period. For all calculations we used the constant value of 0.9 [67] for the discharge coefficient. Figure 7.4 shows an example of the results of the preceding procedure for the estimation of the regression rate from pressure data for the specific test 103. For this test the fuel mass matching required a combustion efficiency of approximately 0.81.

Figure 7.4 indicates that the regression rate takes its maximum value approximately at 0.8 seconds after the ignition. The regression rate drops rather rapidly after that time due to the increase in the port diameter as discussed earlier. We believe that around this maximum regression rate the steady-state characteristics of the tests are represented to some extend. Therefore we first use the maximum regression rates and the corresponding oxidizer mass fluxes for tests of concern as the data points. The maximum regression rates and the oxidizer mass fluxes at the maximum regression rates for other tests are estimated similarly. The results are shown in figure 7.5 which is a plot of the maximum regression rate versus the corresponding oxidizer mass flux.

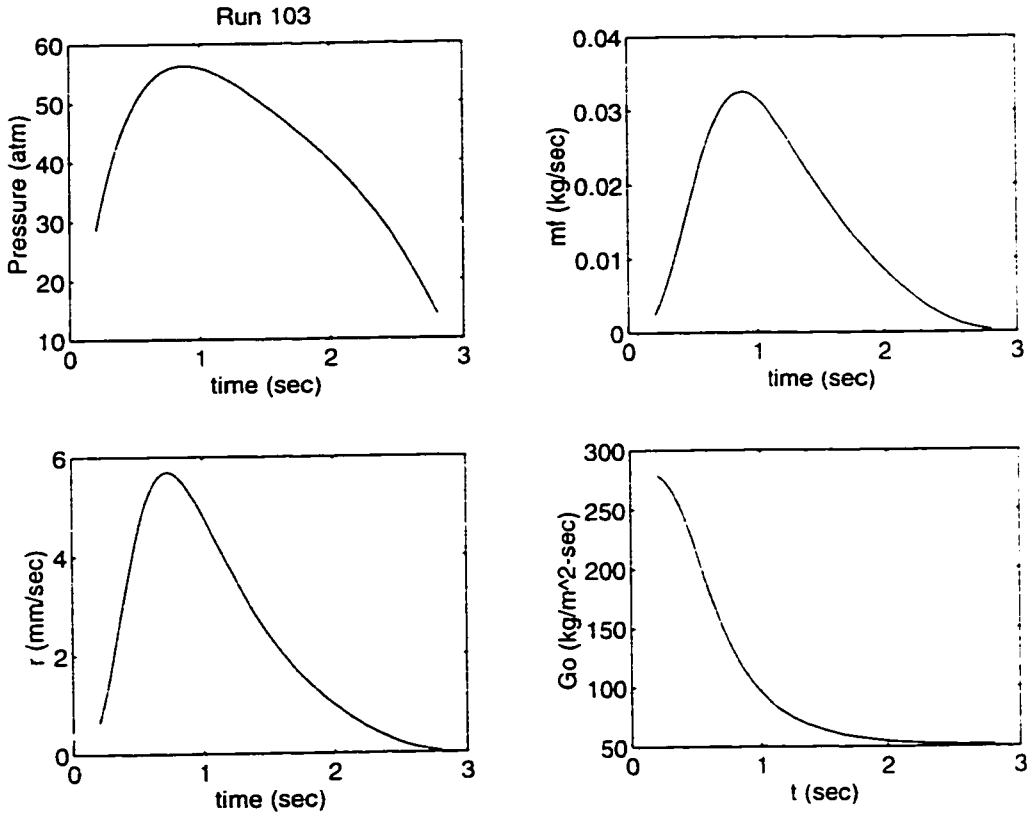

Figure 7.4. The pressure-time history and the time history of the calculated properties, fuel mass flow rate, regression rate and oxidizer mass flux are shown for the test 103.

For comparison purposes, we also calculate the regression rates predicted by the classical theory. The only unknown quantity in the calculation of the classical regression rate is the blowing parameter for the pentane-oxygen system. For the purposes of this argument, the blowing parameter can be roughly estimated with use of the following formula derived by Marxman *et al* [19].

$$B = \frac{1 + \left[1 + (O/F)_f\right] \Delta h / h_v}{(O/F)_f} \tag{7.4}$$

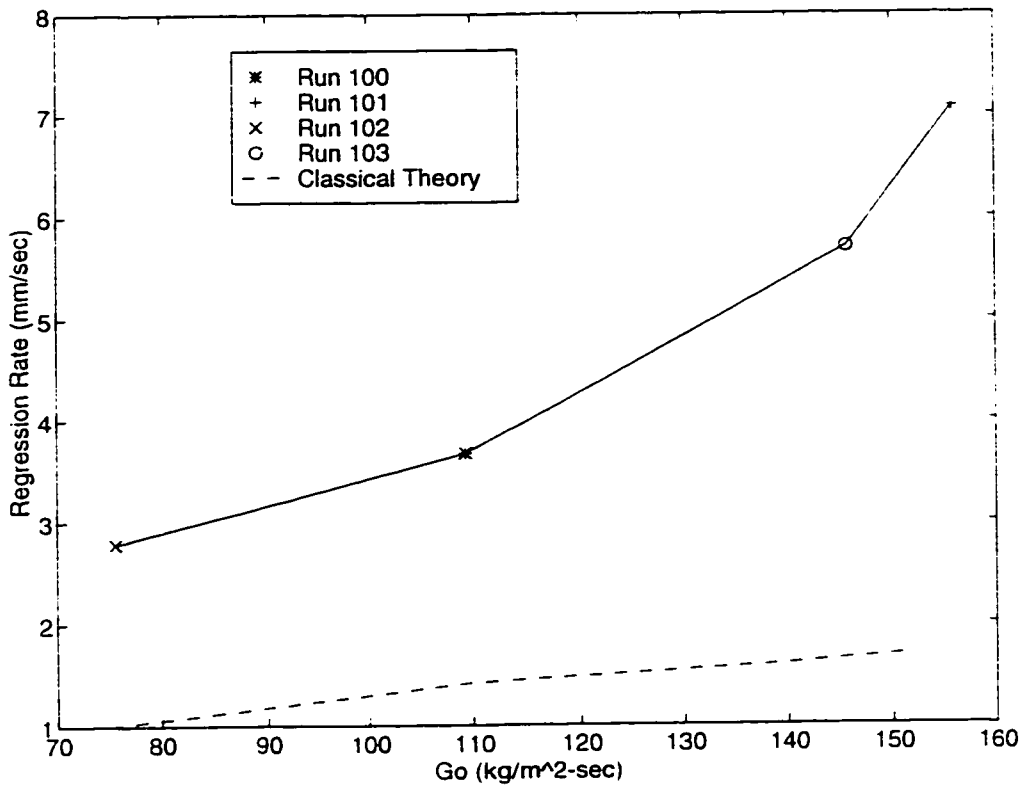

Figure 7.5. The maximum regression rates are plotted versus the corresponding oxidizer mass fluxes for the tests 100 101, 102 and 103.

Here $(O/F)_f$ is the oxidizer to fuel ratio of the hybrid diffusion flame, Δh is the enthalpy difference between the flame and the surface and h_v is the effective heat of gasification. Note that Δh is also a function of the flame O/F ratio. The blowing parameter for a pentane-oxygen system is calculated according to this formula and plotted as a function of flame stoichiometry in figure 7.6

The classical regression rate expression is evaluated with the maximum value of the blowing parameter to obtain an upper limit for the classical regression rate prediction. We also increased the diffusion limited regression rate estimates by 20% to account for the effect of radiation. The classical theory predictions are also shown with the experimental data in figure 7.5.

It is obvious that the experimental regression rates obtained by using the pressure time history and the oxidizer mass flux information are much higher than even the upper limit of the rates that are predicted by the classical theory. Moreover, the mass flux exponent that is obtained from the experimental data appears to be larger than unity which is higher than the maximum value of 0.8 predicted by the classical diffusion limited theory. These observations serve as a motivation for the exploration of another mass transfer mechanism from the fuel grain that could increase the regression rates above the range predicted by the classical diffusion limited model.

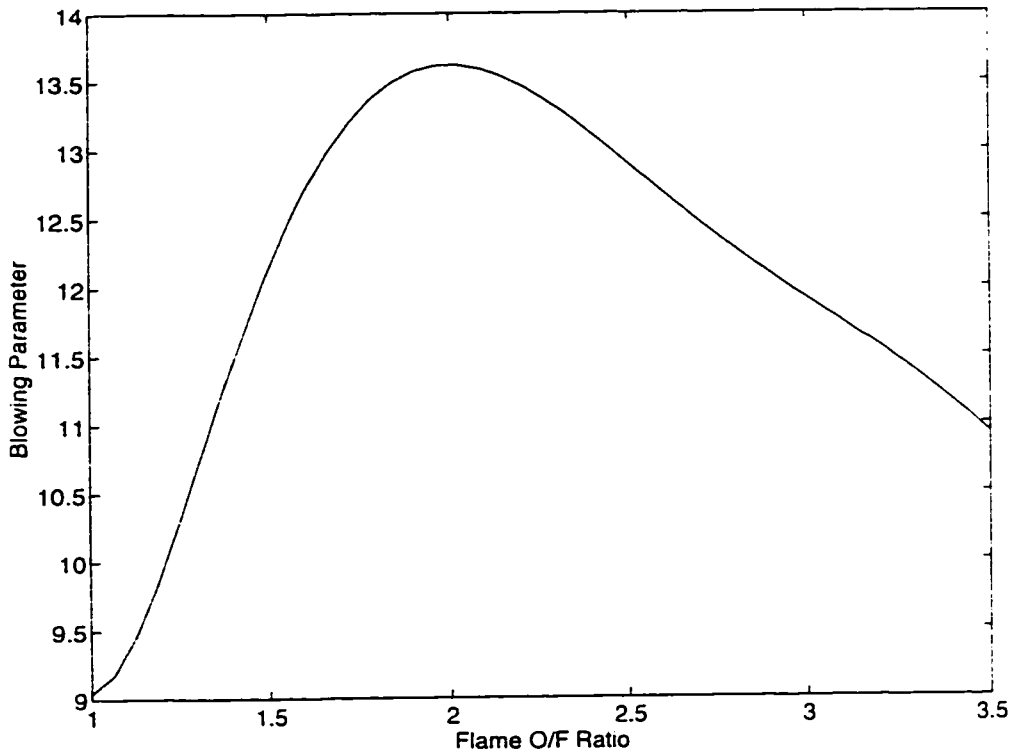

Figure 7.6. The blowing parameter variation for a pentane-oxygen system with the flame O/F ratio.

Moreover the cryogenic test data also revealed that the combustion efficiencies for the motors were around 0.8 which is small compared to the conventional hybrid efficiencies [4]. This fact can also be explained with the entrainment of liquid droplets into the gas stream. Note that depending on the droplet size and the residency time in the motor, the evaporation and combustion of some of these droplets may not be completed in the combustion chamber. This incomplete combustion of the fuel is a feasible explanation for the observed low c^* efficiencies for cryogenic hybrids.

We also plotted the estimated space averaged regression rates with respect to the corresponding mean port mass fluxes for several points in the middle one third of each run which best resembles the steady-state operation of the cryogenic motor. The result is shown in figure 7.19 for runs 100, 101, 102 and 103. Note that all points other than run 100 data lie on a very smooth curve. It can be inferred from the curve that the mean mass flux exponent of the regression rate is slightly larger than one. Note that regression rates predicted for different runs at the same mass flux level are significantly close to each other. This fact justifies the use of the regression rate estimation technique developed in this paper. The regression rate levels predicted for run 100 are slightly below the other test results. We claim that these lower regression rates can be attributed to the lower chamber pressure level of test 100. This pressure dependency is an indicator of the significant radiative heating of the fuel surface.

7.3 Development of the Theory

In this section we will develop a theory that can be used to explain the phenomena observed in the cryogenic hybrids and that will extend the applicability of the hybrid combustion theory to the fuels that may form a significantly thick liquid layer during their combustion. Due to the complexity of the problem, we will perform the development in three stages. In the first stage, we will investigate the possibility of the formation of a reasonably thick melt layer on the fuel grain. In the second stage, we will start with linear stability analysis of the melt layer under the strong shear of a gas flow. Our linear stability model includes the effect of the injection of liquid at the liquid-solid interface due to the regression of the fuel slab. Later in this stage the linear stability results will be linked to the entrainment of liquid droplets with use of some experimental results and some semi-empirical relations developed in the nuclear engineering literature. Eventually in the final stage, the classical theory will be extended to the case of liquid droplet entrainment. It is shown that the primary effect of the entrainment mass transfer is to increase the regression rate of the fuel without increasing the thermochemically defined blowing parameter. Note that the thermochemical blowing parameter can only be altered, to some degree, by changing the thermochemical properties of the propellants or the combustion parameters such as the local flame O/F ratio.

7.3.1 Thickness of the Melt Layer-Thermal Analysis

In this section the film thickness formed on a burning slab under the combined heating of convection and radiation is considered. Physically, the thickness of the liquid layer is determined by the energy transfer relations both in the solid and also in the liquid. The schematic of our thermal model for the slab configuration is shown in figure 7.7. In this investigation we are solely interested in the steady-state regression of the fuel slab. For that reason in our formulation the velocity of the liquid-gas interface and the solid-liquid interface are assumed to be equal and constant. This, of course, implies that the thickness of the melt layer is also constant. For the sake of simplicity we further assume that the thermophysical properties of the material both in the liquid phase and also in the solid phase are uniform. The effect of convection in the liquid layer is also ignored. This assumption can be justified for small melt layer thicknesses for which the Reynolds numbers are relatively small (a couple of hundreds) and the temperature gradients are fairly large.

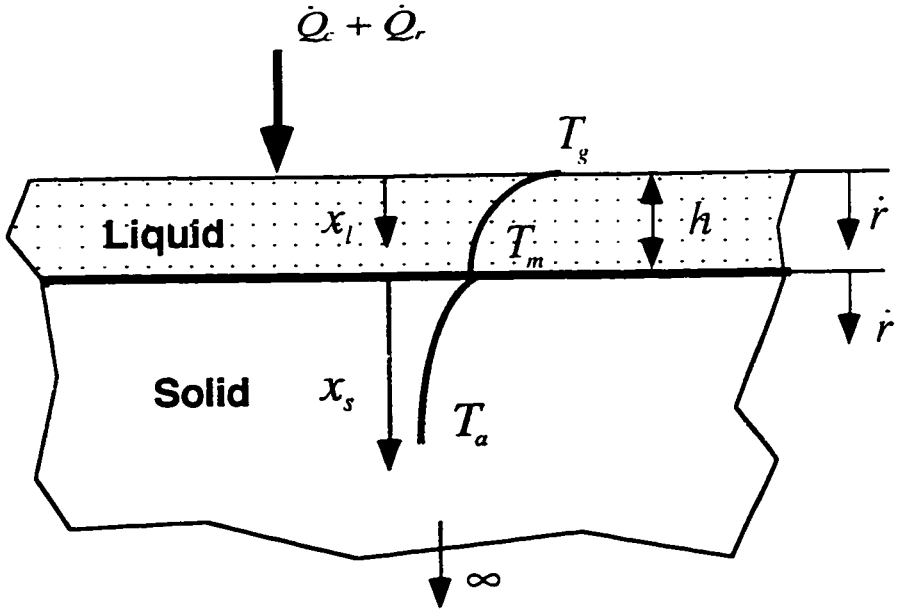

Figure 7.7. Schematic of the thermal model.

In the analysis the possibility of the penetration of the thermal radiation into the slab is considered. Several simplifying assumptions are introduced in our radiation treatment. First, the radiative flux field is assumed to be one dimensional. Since the temperature levels in the slab are small, the contribution of radiation emitted by internal material to the radiative intensity is negligible. The absorbing character of both the liquid and also the solid material are assumed to behave like a gray body, namely the absorption coefficient is

independent of the frequency of the radiation. Note that the absorption characteristics for typical hydrocarbons used in cryogenic hybrid applications, such as pentane, are reasonably flat in the medium IR range of the spectrum [68, 69]. Even if this is not the case, the use of a constant absorption coefficient obtained by averaging over the band of the spectrum of the incoming radiation can be justified [70]. Furthermore the non-collimated effects of the incoming radiation to the fuel slab surface is neglected.

Under these simplifications the radiative energy flux in the liquid and solid phases of the slab can be written as [70]

$$q_r(x_l) = \dot{Q}_r e^{-a_l x_l} \qquad q_r(x_s) = \dot{Q}_r e^{-a_l h} e^{-a_s x_s} = q_r^h e^{-a_s x_s}. \tag{7.5}$$

Here a_s and a_l are the gray body absorption coefficients of the solid phase and liquid phase respectively. These absorption properties of the material are also taken to be uniform. $\dot{Q}_r$ is the total collimated radiative flux impinging on the surface. The flux is generated by the emission from the hot combustion products in the gas phase. In hybrids it is reported that the effective radiation temperatures of the gases fall in the range of 1500-2000 K [8, 35]. Note that the radiation levels from the gas phase are significantly elevated in the presence of solid emitting particles in the gas flow. These solid particles can either be metal additives to the solid fuel or the soot which is a natural product of hydrocarbon combustion at fuel rich stoichiometries.

The radiative heating of material at any position can be expressed as the divergence of the radiative flux, $-\nabla.\mathbf{q}_r$. In our one dimensional model the radiative heating in the solid and the liquid become

$$-\frac{dq_r}{dx_s} = a_s \dot{Q}_r e^{-a_l h} e^{-a_s x_s} \qquad -\frac{dq_r}{dx_l} = a_l \dot{Q}_r e^{-a_l x_l}. \tag{7.6}$$

Note that it can be shown by the following integral that the total heating of the fuel by radiation matches the radiative heat input.

$$\int_0^h a_l \dot{Q}_r e^{-a_l x_l} dx_l + \int_0^\infty a_s \dot{Q}_r e^{-a_l h} e^{-a_s x_s} dx_s = \dot{Q}_r$$

We will now consider the energy equations in the liquid and in the solid phases. The liquid layer energy equation can be written as [46]

$$\frac{d^2T}{dx_l^2}+\frac{1}{\delta_l}\frac{dT}{dx_l}=-\frac{a_l\dot{Q}_r}{\kappa_l\rho_l C_l}e^{-a_l x_l} \tag{7.7}$$

where the characteristic thermal thickness in the liquid phase is defined as $\delta_l=\kappa_l/\dot{r}$. Here ρ_l is the density of the liquid, C_l is the specific heat of the liquid and κ_l is the thermal diffusivity of the liquid which can be written as $\kappa_l=\lambda_l/\rho_l C_l$. Note that λ_l is the thermal conductivity in the liquid.

The general solution for this linear ODE can be easily found as

$$T(x_l)=c_1e^{-x_l/\delta_l}+c_2+Ae^{-a_l x_l} \tag{7.8}$$

where

$$A=-\frac{\dot{Q}_r}{\rho_l C_l\dot{r}}\left(\frac{1}{a_l\delta_l-1}\right).$$

The boundary conditions appropriate for the liquid layer are

$$x_l=0 \qquad T=T_s$$
$$x_l=h \qquad T=T_m.$$

Under these boundary conditions the temperature gradients at the two boundaries can be determined as

$$\left.\frac{dT}{dx_l}\right|_{x_l=0}=\frac{1}{\delta_l}\left[-\frac{\Delta T_1}{1-\phi}+\frac{1-\varphi}{1-\phi}A-R_lA\right] \tag{7.9}$$

$$\left.\frac{dT}{dx_l}\right|_{x_l=h}=\frac{1}{\delta_l}\left[-\frac{\phi}{1-\phi}\Delta T_1+\frac{\phi}{1-\phi}(1-\varphi)A-\varphi R_lA\right]. \tag{7.10}$$

The parameters appear in these expressions are

$$\Delta T_l = T_s - T_m \qquad R_l = a_l \delta_l \qquad \phi = e^{-h/\delta_l} \qquad \varphi = e^{-a_l h}.$$

Next, a similar treatment is performed for the solid phase. The energy equation in the solid is

$$\frac{d^2T}{dx_s^2} + \frac{1}{\delta_s}\frac{dT}{dx_s} = -\frac{a_s \dot{Q}_r}{\kappa_s \rho_s C_s} e^{-a_s x_s} \tag{7.11}$$

where the thermal thickness in the solid is defined as $\delta_s = \kappa_s / \dot{r}$. Note that all other parameters are defined as their liquid phase analogs.

Similarly, the general solution for the solid case is

$$T(x_s) = c_1 e^{-x_s/\delta_s} + c_2 + B e^{-a_s x_s} \tag{7.12}$$

where

$$B = -\frac{\dot{Q}_r \varphi}{\rho_s C_s \dot{r}} \left(\frac{1}{a_s \delta_s - 1} \right).$$

The boundary conditions for the solid phase are also Dirichlet type

$$x_s = 0 \qquad T = T_m$$
$$x_s \to \infty \qquad T = T_a.$$

Here T_a is the ambient temperature of the solid fuel grain. The temperature gradient at the liquid-solid interface can easily be determined upon the application of these boundary conditions on equation 7.12.

$$\left.\frac{dT}{dx_s}\right|_{x_s=0} = \frac{1}{\delta_l}\left[-\Delta T_2 - BR_s + B\right].$$

The recently introduced parameters are

$$\Delta T_2 = T_m - T_a \qquad R_s = a_s \delta_s .$$

Now we will consider the energy balance at the liquid-solid interface. Namely, the energy transfer from the liquid to the interface must be equal to the heat conducted into the solid from the interface and the energy required for the phase transformation. In mathematical terms this can be expressed as

$$-\lambda_l \left.\frac{dT}{dx_l}\right|_{x_l=h} + \lambda_s \left.\frac{dT}{dx_s}\right|_{x_s=0} - L_m \rho_s \dot{r} = 0. \tag{7.13}$$

Here L_m is the heat of fusion for the fuel material of interest.

The temperature derivative expressions derived previously can be inserted in this energy balance formula. After several simplifications one obtains the following relation between the variables ϕ and φ.

$$\phi = \frac{L_m + \Delta T_2 C_s + \dfrac{Q_r}{\rho_s \dot{r}\,(R_l - 1)}\dfrac{\varphi}{}}{L_m + \Delta T_2 C_s + \Delta T_1 C_l (\rho_l/\rho_s) + \dfrac{\dot{Q}_r}{\rho_s \dot{r}\,(R_l - 1)}\dfrac{1}{}} \tag{7.14}$$

From a practical point of view, it is desirable to replace the regression rates appearing in this expression with a commonly used parameter, the effective heat of gasification. We will further follow the energy considerations to derive a relation for the effective heat of gasification.

The energy balance at the liquid-solid interface requires that the convective heat transfer from the gas to the interface must be equal to the conductive heat transfer into the liquid and the heat required for the phase transformation, namely

$$\dot{Q}_c - \lambda_l \left.\frac{dT}{dx_l}\right|_{x_l=0} - L_v \rho_s \dot{r}_c = 0. \tag{7.15}$$

In this formula we allowed for the possibility of entrainment mass transfer from the liquid surface other than the mass transfer by evaporation. This feature is, in fact, the basis of our liquid layer combustion theory. Thus $\dot{r}_c$ which appears in the energy balance expression represents the evaporative contribution of the total regression rate since only the evaporative mass transfer contributes to the thermal energy balance.

Next we add the energy balance equations at the liquid-solid and gas-liquid interfaces together. The final result of this operation is strikingly simple.

$$\dot{Q}_w = \dot{Q}_c + \dot{Q}_r = \Delta T_1 C_l \rho_l \dot{r} + \Delta T_2 C_s \rho_s \dot{r} + L_m \rho_s \dot{r} + L_v \rho_s \dot{r}_c \tag{7.16}$$

This can be interpreted as the total energy transferred from the surroundings must be equal to the total energy absorbed in the slab with its components being the energy required to heat the liquid and solid and the heat required for the phase transformations.

Now with use of equation 7.16, we define the effective heat of gasification as it is commonly used in the hybrid literature.

$$h_v \equiv \frac{\dot{Q}_w}{\rho_s \dot{r}} = \Delta T_1 C_l (\rho_l / \rho_s) + \Delta T_2 C_s + L_m + L_v (\dot{r}_c / \dot{r}) \ . \tag{7.17}$$

Eventually, note that the variables ϕ and φ are related according to the simple relation, $\varphi = \phi^{R_l}$.

After combining equations 7.14 and 7.17, we obtain a nonlinear equation for the thickness parameter ϕ.

$$\phi = \frac{1 + \dfrac{L_m}{\Delta T_2 C_s} + h_v \left(\dfrac{\dot{Q}_r / \dot{Q}_c}{1 + \dot{Q}_r / \dot{Q}_c} \right) \dfrac{\phi^{R_l}}{(R_l - 1)}}{1 + \dfrac{L_m}{\Delta T_2 C_s} + \dfrac{\Delta T_1 C_l \rho_l}{\Delta T_2 C_s \rho_s} + h_v \left(\dfrac{\dot{Q}_r / \dot{Q}_c}{1 + \dot{Q}_r / \dot{Q}_c} \right) \dfrac{1}{(R_l - 1)}} \tag{7.18}$$

An explicit solution for this algebraic nonlinear equation for the general case could not be attained. We first focus on the following two limiting cases of practical interest. Note that R_l is the ratio of the thermal thickness to the radiative penetration thickness in the liquid layer.

1) $R_l >> 1$: The absorption of the radiation in the liquid layer is very large. In this extreme case of an opaque liquid layer. all the radiative heat is absorbed at the liquid gas interface. The thickness can be solved explicitly as

$$h = \delta_l \ln \left[\frac{1 + L_m / C_{ps} \Delta T_2 + \rho_l C_{pl} \Delta T_1 / \rho_s C_{ps} \Delta T_2}{1 + L_m / C_{ps} \Delta T_2} \right] \tag{7.19a}$$

where the characteristic thermal thickness of the liquid layer is $\delta_l = \kappa_l / \dot{r}$. In this case the film thickness is inversely proportional to the regression rate. Note that all the thermophysical properties of the fuel material are lumped in the logarithmic term and $\dot{Q}_r / \dot{Q}_c$ ratio does not affect the thickness.

For a given fuel type, the only control parameter that can be altered to effect the thickness of the melt layer is the ambient temperature of the fuel slab. (Note that the ambient temperature appears in ΔT_2.) Figure 7.8 shows the plots of the melt layer thickness versus the regression rate for various ambient temperatures for a pentane fuel slab. The material properties used in the calculations in this chapter are given in appendix F. Note that an increase in the ambient temperature of the fuel slab results in an increase in the melt layer thickness. The maximum film thickness for a given regression rate is attained when the ambient temperature is equal to the melting temperature.

2) $R_l << 1$: In this other extreme. the absorption of the radiation in the liquid phase is small. Here the thickness of the thermal layer in the liquid is much smaller compared to the radiative thickness in the liquid and as a consequence all the radiative flux is absorbed in the

solid. The effect of the entrainment mass transfer on the thickness is also included in this formulation. Unlike the other extreme, in this case the film thickness depends on the ratio of the radiative heat flux to the convective heat flux and it can be expressed as

$$h = \delta_l \ln\left[\frac{1+\dfrac{L_m}{C_{ps}\Delta T_2}+\dfrac{\rho_l C_{pl}\Delta T_1}{\rho_s C_{ps}\Delta T_2}-\dfrac{h_v}{C_{ps}\Delta T_2}\left(\dfrac{\dot{Q}_r/\dot{Q}_c}{1+\dot{Q}_r/\dot{Q}_c}\right)}{1+\dfrac{L_m}{C_{ps}\Delta T_2}-\dfrac{h_v}{C_{ps}\Delta T_2}\left(\dfrac{\dot{Q}_r/\dot{Q}_c}{1+\dot{Q}_r/\dot{Q}_c}\right)}\right]. \tag{7.19b}$$

Note that the dependence of the thickness on $\dot{r}_v/\dot{r}$ comes from the effective heat of gasification that appears explicitly in this formula. Another interesting observation is that for this extreme case of transparent liquid, the thickness is independent of the absorbtivity of the solid material. Namely R_s does not appear in the expression for the thickness.

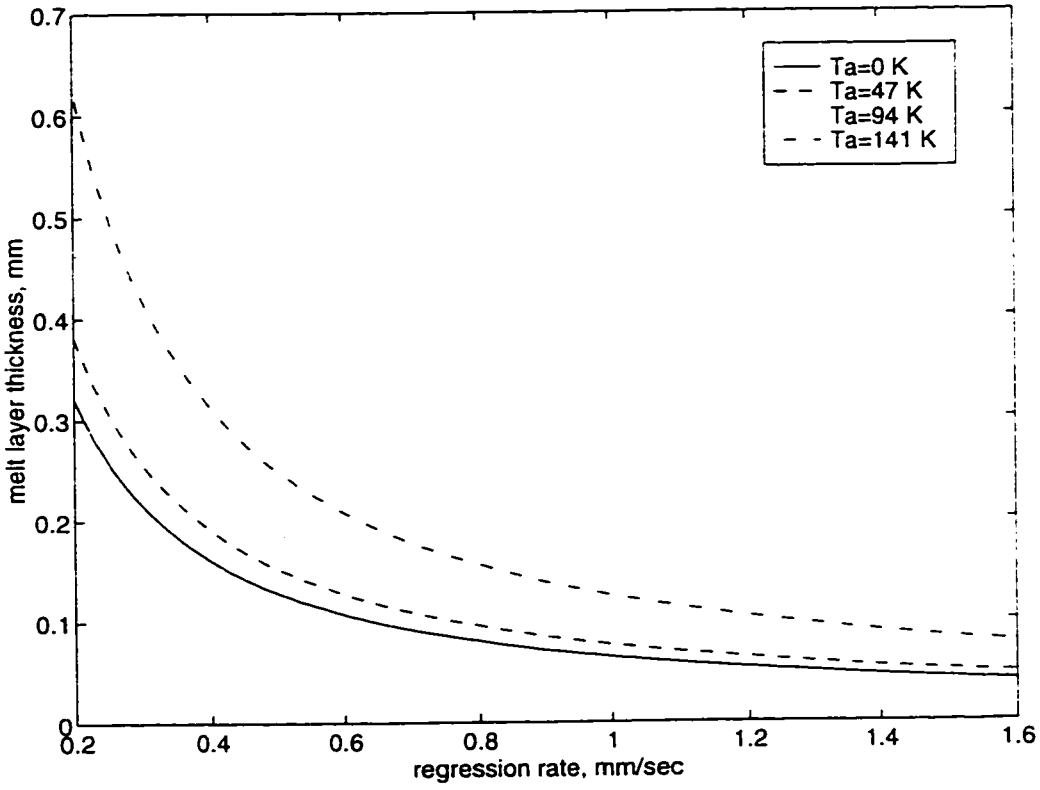

Figure 7.8. Effect of ambient temperature of the fuel slab on the melt layer thickness.

A plot of the variation of the film thickness with the radiative heat flux factor, $\dot{Q}_r/\dot{Q}_c$, for a pentane system is shown in figure 7.9. The figure reveals the interesting

phenomenon that at a critical value of the radiation factor (around 0.35 for no entrainment), the steady-state film thickness grows indefinitely. This fact can easily be seen from equation 7.20, namely at the critical value of the factor the numerator of the argument of the logarithm diminishes. In physical terms, during this critical operation, the energy balance at the liquid-solid interface requires zero conductive heat transfer from the liquid side. This condition imposes a zero temperature gradient on the liquid side of the interface, which can only be achieved with an infinite thickness of the liquid layer.

The effect of the entrainment mass transfer is to reduce the thickness at a given radiation factor and to increase the critical value of the radiation factor. These are also indicated in figure 7.9 in which various thickness curves are plotted at different levels of the entrainment parameter $\dot{r}_{ent}/\dot{r}$.

The conclusion of this stage of the development is that under certain conditions the melt layer formed on the solid fuel grain of a hybrid motor can be significantly thick.

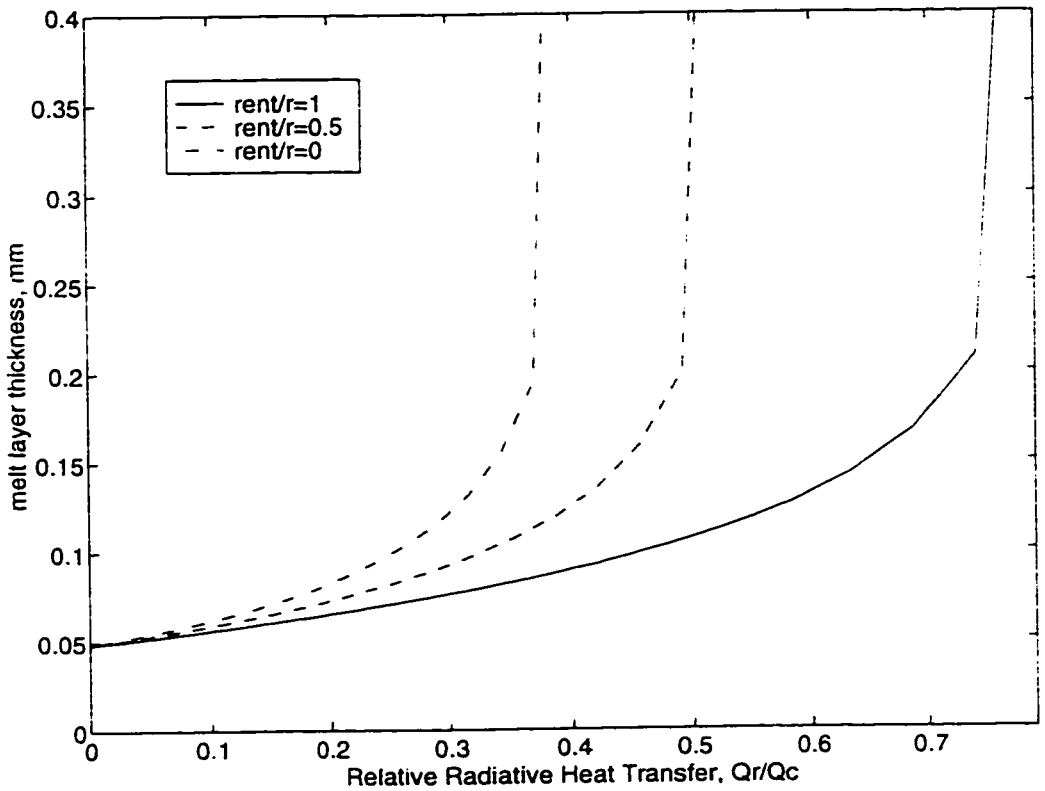

Figure 7.9. Effect of radiation and entrainment mass transfer on the thickness of the melt layer for the pentane fuel grain at a regression rate of 1 mm/sec.

For practical purposes, it is desirable to obtain an expression for the outer web temperature of the propellant. However this requires a transient thermal analysis, since the semi-infinite thickness slab geometry assumption, which is essential for the simplified steady-state treatment pursued here, rules out the use of a finite web thickness. We will bypass this difficult transient moving boundary problem by simply approximating the outer web temperature with the infinite slab temperature given by equation 7.18 evaluated at the web thickness. After this simplification the inner wall temperature can be written in the following nondimensional form:

$$\frac{T_{iw}-T_a}{\Delta T_2} \cong e^{-\Delta/\delta_s}\left[1+\frac{h_v}{C_s\Delta T_2}\frac{\varphi \dot{Q}_r/\dot{Q}_c}{(1-R_s)\left(1+\dot{Q}_r/\dot{Q}_c\right)}\left(e^{-(1-R_s)\Delta/\delta_s}-1\right)\right]. \tag{7.20}$$

Here Δ/δ_s is the nondimensional web thickness at a certain time during the course of the run.

7.3.2 Stability of the Melt Layer

Knowing from the previous section that a melt layer with a reasonable thickness is formed on the solid grain, we can now investigate the stability of this liquid layer under the effect of strong shear force generated by the gas flow in the port [71, 72, 73]. The schematic of our liquid layer stability model is shown in figure 7.10.

In our investigations, we ignore the effect of density variations and all chemical reactions in the gas phase on the stability. In the calculations we adapt the linearized gas phase equations derived by Benjamin [75] for the incompressible flow over a wavy wall. Since our predictions for the Reynolds numbers for the hybrid liquid films are on the order of a couple of hundreds, both the small Reynolds number and also the high Reynolds number approximations [15, 71] as the solution techniques for the film stability equation introduced in the literature are not satisfactory. For that reason we develop new solution techniques for the liquid layer aspect of the problem.

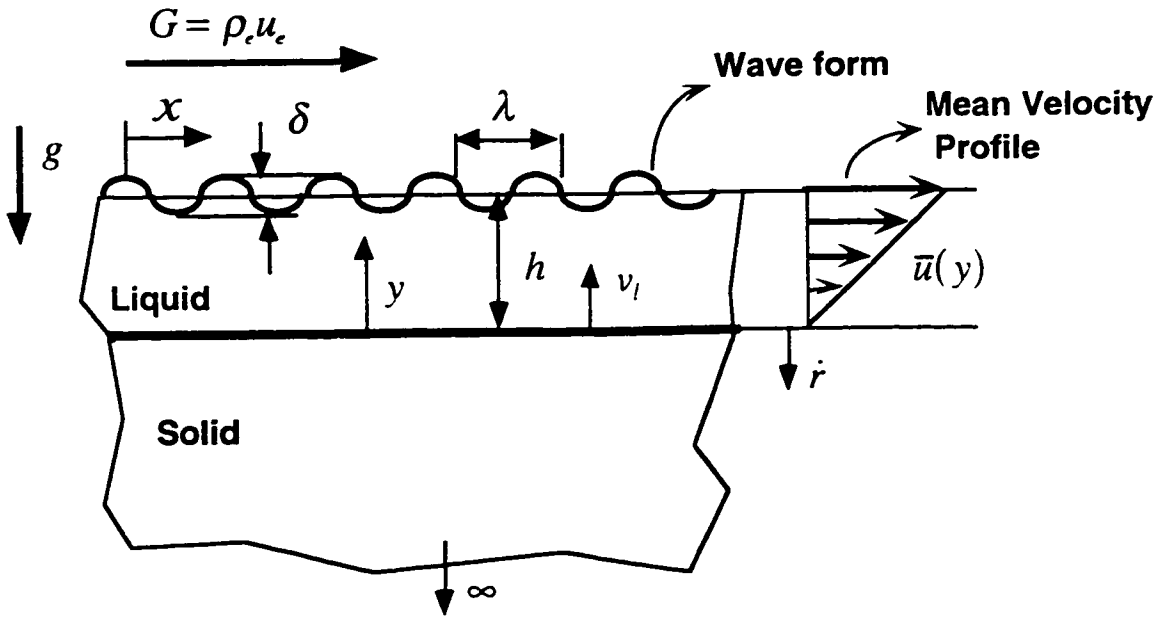

Figure 7.10. The schematic of the stability model.

7.3.2.1 Derivation of the Liquid Phase Stability Equation

In this section the hydrodynamic stability equation for the liquid layer formed on the solid fuel grain is derived. For typical hybrid applications the liquid layer Reynolds numbers defined with respect to the liquid layer thickness are estimated to be on the order of a couple hundreds. Thus the liquid flow in the layer can be assumed to be laminar in nature. In our analysis we ignore the variations of the fluid properties across the thickness of the layer. We believe that the effect of these variations are small on the stability behavior of the film.

We start with the incompressible Navier-Stokes equations for a fluid with constant physical properties [15].

$$\frac{\partial u}{\partial t} + u\frac{\partial u}{\partial x} + v\frac{\partial u}{\partial y} = \frac{\mu}{\rho}\nabla^2 u - \frac{1}{\rho}\frac{\partial P}{\partial x} \tag{7.21a}$$

$$\frac{\partial v}{\partial t} + u\frac{\partial v}{\partial x} + v\frac{\partial v}{\partial y} = \frac{\mu}{\rho}\nabla^2 v - \frac{1}{\rho}\frac{\partial P}{\partial y} \tag{7.21b}$$

$$\frac{\partial u}{\partial x} + \frac{\partial v}{\partial y} = 0 \tag{7.21c}$$

The film stability model for a hybrid motor must take into account the generation and injection of liquid at the solid interface and removal of the liquid at the gas interface. During the steady-state operation for which the film thickness is constant, the removal rate must be equal to the injection rate. In our study we concentrate on the this steady-state situation described above. Even in this simple state of operation, the liquid layer equations with respect to the rocket frame of reference does not possess a steady-state component. In order to simplify the analysis, the problem has to be formulated in a frame of reference that is fixed to the moving interfaces which are translated at a constant speed with respect to the rocket frame. The new set of governing equations with respect to this moving reference frame can be obtained upon the application of the following translational transformation on the Navier-Stokes equations.

$$x' = x \qquad y' = y + \dot{r}t \qquad u' = u \qquad v' = v + \dot{r}$$

It is showed in appendix G that the Navier-Stokes equations are invariant under this transformation, namely the equations keep their forms with the new set of primed variables defined in the transformation equations. (For the sake of simplicity, from now on we drop the prime notation.) For that reason equations 7.21 also govern the dynamics of the fluid motion with respect to the moving reference of frame and these will be used in the stability investigations.

In the moving reference of frame, there exists a steady component of the flow field. It is reasonable to assume the following base flow which is the steady part of the flow field in the liquid layer.

$$v_o(x,y,t) = v_l \qquad u_o(x,y,t) = U_o(y) \tag{7.22}$$

Here v_l is the mean velocity of the liquid in the film in the direction normal to the liquid surface. In our investigations this component of the velocity is assumed to be uniform in the whole domain. Moreover, the parallel component of the mean velocity is considered to be independent of the axial dimension. The substitution of the base flow expressions in the Navier-Stokes equations yields

$$v_l \frac{dU_o}{dy} = \frac{\mu}{\rho}\frac{d^2U_o}{d^2y} - \frac{1}{\rho}\frac{\partial \overline{P}}{\partial x} \qquad \frac{\partial \overline{P}}{\partial y} = 0. \tag{7.23}$$

We further assume that the mean pressure is uniform in space, namely $\overline{P}$ is a function of time alone. This simplifies the mean flow description of the flow to the following ODE for the parallel velocity component.

$$\frac{\mu}{\rho}\frac{d^2U_a}{d^2y} - v_l\frac{dU_a}{dy} = 0 \tag{7.24}$$

This equation is separable and it can easily be integrated twice to give

$$U_a(y) = c_1 + c_2 e^{(v_l\rho/\mu)y}. \tag{7.25}$$

The integration constants can be determined with use of the boundary conditions. First boundary condition is the no slip requirement at the wall.

$$U_a(0) = 0 \tag{7.26}$$

The second condition is the shear force balance at the gas-liquid interface that can written as

$$\tau_g = C_f P_d = \mu\frac{dU_a}{dy}\bigg|_{y=h}. \tag{7.27}$$

Here τ_g is the mean shear stress exerted by the gas flow on the liquid surface, C_f is the skin friction coefficient of the gas flow and P_d is the dynamic pressure of the gas flow.

Under these conditions the velocity distribution can be expressed in terms of the gas phase conditions and the physical properties of the film as

$$U_a(y) = \frac{\tau_g}{\rho_l v_l}e^{-(v_l\rho/\mu)h}\left[e^{(v_l\rho/\mu)y} - 1\right]. \tag{7.28}$$

Note that the mean y-component velocity of the liquid flow can be written in terms of the regression rate of the slab after a simple mass balance consideration. Namely, the mass balance on the control volume placed at the liquid-solid interface requires $v_l = \dot{r}\rho_s/\rho_l$.

At this point it is useful to define a regression rate parameter (which is a also liquid phase blowing parameter), b, as

$$b \equiv \frac{v_l h}{\nu} = \frac{\rho_s}{\rho_l}\frac{h}{\delta_m} \tag{7.29}$$

where the momentum thickness for the liquid layer is defined as $\delta_m = \mu/\rho\dot{r}$. For typical operating conditions of hybrids the liquid blowing parameter falls in the range of 0.1-1.0. The velocity expression takes a more compact form when it is written in terms of b, namely

$$U_u(y) = U_l''\left[e^{b(y/h)} - 1\right]/be^b \tag{7.30}$$

where $U_l'' = \tau_s h/\mu$.

In the limit of zero liquid blowing ($\dot{r} = 0$), the application of the L'Hospital's rule yields the following linear velocity profile of the standard Couette flow as expected.

$$U_u(y) = U_l''\, y/h = \tau_s y/\mu \tag{7.31}$$

According to equation 7.30 the liquid velocity at the surface is

$$U_u(h) \equiv U_l = U_l''\left[e^b - 1\right]/be^b. \tag{7.32}$$

In figure 7.11 the plot of the velocity profiles according to equation 7.30 and equation 7.31 are shown for a typical blowing parameter value of 0.4. It is apparent that the exact velocity profile is quite different from the simple Couette flow profile. However it is observed that for values of b smaller than 0.5, the exact solution is fairly close to a linear variation from the zero wall value to the maximum velocity predicted by equation 7.32. (Note that the first order effect of the injection is to reduce the surface velocity of the

liquid.). For that reason the following corrected linear profile is a good approximation for small blowing parameters.

$$U_{\parallel}(y) = U_l^o \frac{e^b - 1}{be^b} \frac{y}{h} \tag{7.33}$$

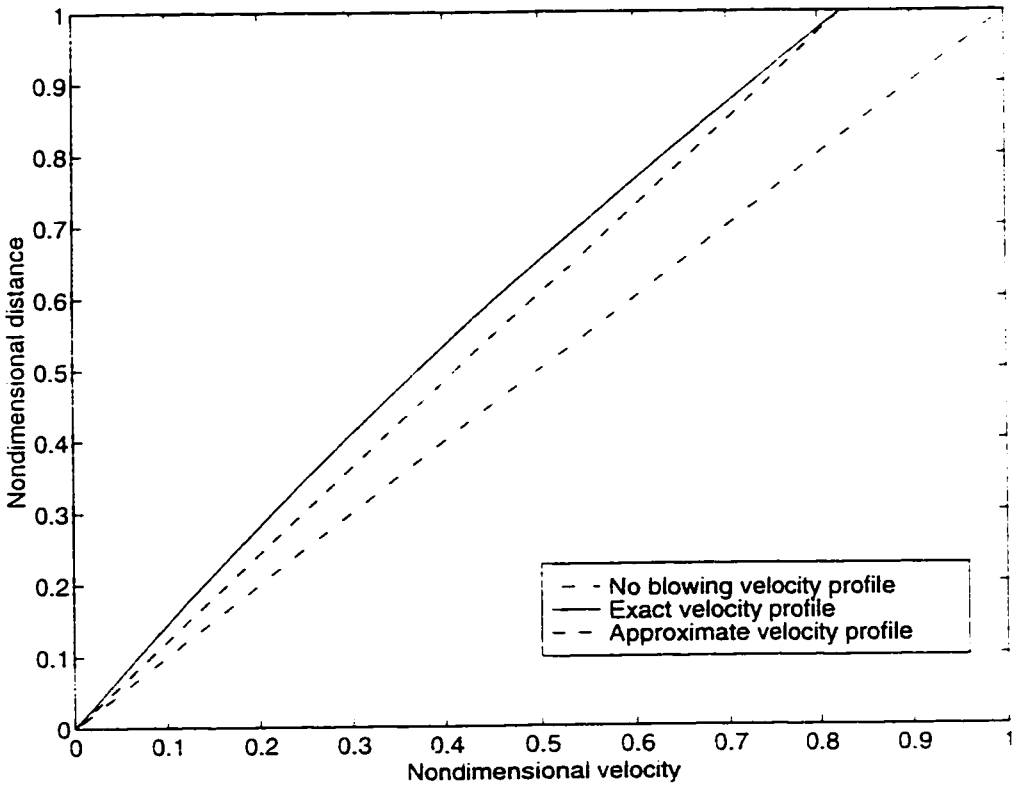

Figure 7.11. The exact velocity profile for the regression rate parameter of b=0.4. the linear approximation given by equation 7.33 and also the velocity profile with no blowing are plotted.

The corrected linear velocity profile given by equation 7.33 will be used in the linear stability investigations as an approximation for the base flow. This simplification is essential for the analytic development of an explicit stability expression for the film layer.

The total liquid mass flow rate in the film is also of practical importance. The mass flow rate per unit width can easily be calculated with the integral

$$\dot{m}_l = \rho_l \int_0^h U_{\parallel}(y) dy .$$

For the exact velocity profile this integral yields

$$\dot{m}_l = 2\dot{m}_l''\left(\frac{e^b - b - 1}{b^2 e^b}\right) \tag{7.34}$$

where $\dot{m}_l'' = \tau_e h^2 \rho / 2\mu$ is the standard Couette flow mass flow rate. The correction for mass flow rate, $\dot{m}_l / \dot{m}_l'' = f_m(b)$, is plotted as a function of the regression rate parameter in figure 7.12. Note that the effect of liquid blowing is to reduce the mass flow rate of the liquid in the layer.

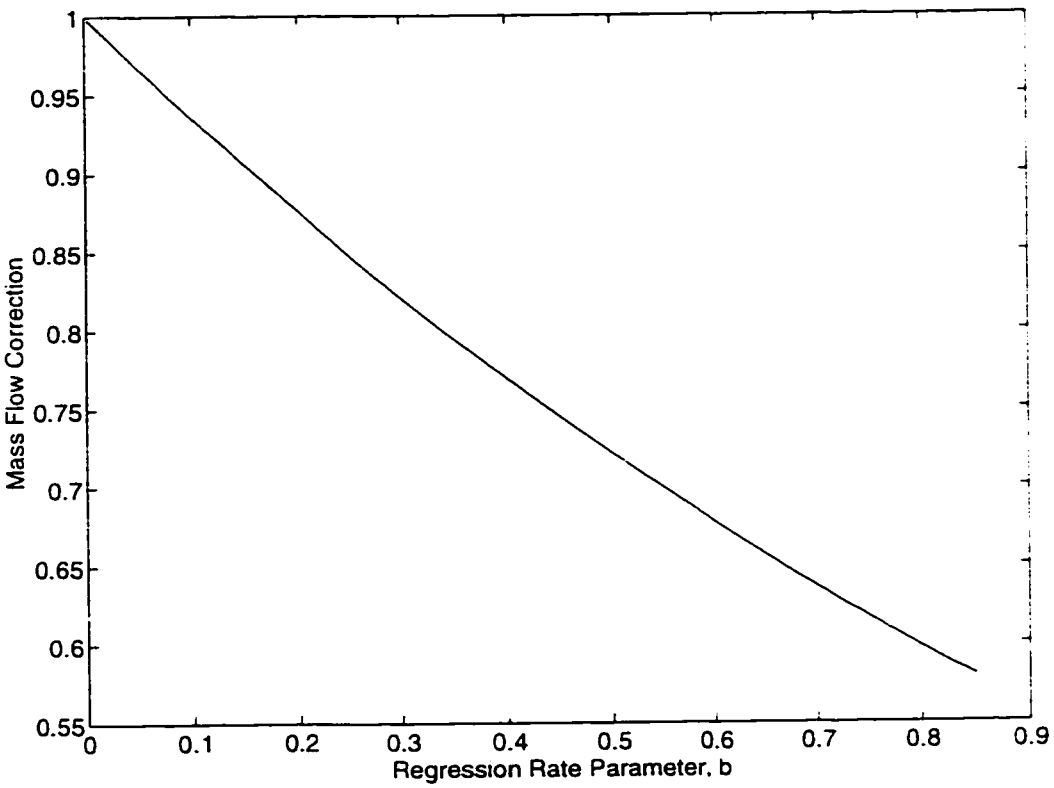

Figure 7.12. The mass flow rate correction plotted versus the regression rate parameter.

Now we perturb the liquid flow field around the base flow presented in the previous paragraphs. We separate the flow variables into their base flow components and perturbation components as

$$u = U_o(y) + \tilde{u}(x,y,t) \qquad v = v_l + \tilde{v}(x,y,t) \qquad P = \overline{P}(t) + \tilde{P}(x,y,t).$$

Next we substitute of these expressions in the Navier-Stokes equations. After collecting the terms to the first order and performing the simplifications on the base flow terms, we obtain the following linear equations.

$$\frac{\partial \tilde{u}}{\partial t} + U_{\infty}\frac{\partial \tilde{u}}{\partial x} + \tilde{u}\frac{dU_{\infty}}{dy} + \frac{1}{\rho}\frac{\partial \tilde{P}}{\partial x} = \frac{\mu}{\rho}\nabla^2\tilde{u} - \nu_l\frac{\partial \tilde{u}}{\partial y} \tag{7.35}$$

$$\frac{\partial \tilde{v}}{\partial t} + U_{\infty}\frac{\partial \tilde{v}}{\partial x} + \frac{1}{\rho}\frac{\partial \tilde{P}}{\partial y} = \frac{\mu}{\rho}\nabla^2\tilde{v} - \nu_l\frac{\partial \tilde{v}}{\partial y} - g$$

$$\frac{\partial \tilde{u}}{\partial x} + \frac{\partial \tilde{v}}{\partial y} = 0$$

The pressure terms can be canceled from the first two of these equations by cross differentiation and subtraction. In short notation resulting set of equations become

$$\tilde{u}_{ty} - \tilde{v}_{tx} + U''_{\infty}\tilde{u}_x + U_{\infty}\tilde{u}_{xy} - U_{\infty}\tilde{v}_{xx} + U''_{\infty}\tilde{v}_y + U'_{\infty}\tilde{v}_{yy} = \frac{\mu}{\rho}\left(\tilde{u}_{xxy} + \tilde{u}_{yyy} - \tilde{v}_{xxx} - \tilde{v}_{yyx}\right) - \nu_l\left(\tilde{u}_{yy} - \tilde{v}_{yx}\right) \tag{7.36}$$

$$\tilde{u}_x + \tilde{v}_y = 0.$$

We investigate the stability of the surface waves of the harmonic nature according to equations 7.36. We first assume the following wave form for the liquid-gas interface [71].

$$\eta(x,y,t) = \varepsilon e^{i(\alpha x - \beta t)} \tag{7.37}$$

Next we define a stream function of the following form which is consistent with the assumed surface wave.

$$\varphi(x,y,t) = \phi(y)e^{i(\alpha x - \beta t)} \tag{7.38}$$

$$\tilde{u} = \varphi_y \qquad \text{and} \qquad \tilde{v} = -\varphi_x$$

Note this definition of the stream function automatically satisfies the continuity equation and equation 7.36 becomes a linear fourth order ODE for the dependent variable ϕ.

$$(\alpha U_{\prime\prime} - \beta)(\phi'' - \alpha^2\phi) - \alpha U_{\prime\prime}''\phi = -i\frac{\mu}{\rho}(\phi^{IV} - 2\alpha^2\phi'' + \alpha^4\phi) + iv_l(\phi''' - \alpha^2\phi') \qquad (7.39)$$

This is the Orr-Sommerfeld equation that governs the stability of a film layer with the steady-state injection of the fluid. It is desirable to work with nondimensioanal quantities. For convenience, we introduce the following set of nondimensional variables.

$$\bar{\phi} = \frac{\phi}{U_l h} \qquad \bar{\alpha} = \alpha h \qquad \bar{y} = \frac{y}{h} \qquad \bar{\beta} = \frac{\beta h}{U_l} \qquad \bar{U}_{\prime\prime} = \frac{U_{\prime\prime}}{U_l}$$

The nondimensional version of Orr-Sommerfeld equation becomes

$$(\bar{\alpha}\bar{U}_{\prime\prime} - \bar{\beta})(\bar{\phi}'' - \bar{\alpha}^2\bar{\phi}) - \bar{\alpha}\bar{U}_{\prime\prime}''\bar{\phi} = -\frac{i}{\mathrm{Re}}\left[(\bar{\phi}^{IV} - 2\bar{\alpha}^2\bar{\phi}'' + \bar{\alpha}^4\bar{\phi}) - b(\bar{\phi}''' - \bar{\alpha}^2\bar{\phi}')\right] \qquad (7.40)$$

where the liquid layer Reynolds number is defined as $\mathrm{Re} = U_l h\rho/\mu$.

From now on we will drop the bars for the nondimesional quantities for simplicity in notation. We use the approximate mean velocity expression given by equation 7.32 which simplifies to $U_{\prime\prime} = y$ in the nondimensional form. Upon the substitution of this linear velocity profile and some minor rearrangements, the Orr-Sommerfeld equation can be written in the following convenient form.

$$\phi^{IV} - 2\alpha^2\phi'' + \alpha^4\phi - b(\phi''' - \alpha^2\phi') = i\alpha\,\mathrm{Re}(y - c)(\phi'' - \alpha^2\phi) \qquad (7.41)$$

Here c is defined as β/α. Note that this is a fourth order linear equation with variable coefficients. Thus a special solution of this equation requires four boundary conditions. In the next section we discuss the appropriate boundary conditions for the film stability problem.

7.3.2.2 Boundary Conditions

The first two of the required boundary conditions can be obtained from the velocity requirements at the solid-liquid interface. The physical statement of the requirements are: 1) The parallel component of the velocity at solid wall must be zero due to the no slip

condition. 2) The regression rate of the slab is steady. These requirements can be formulated as

$$\tilde{u}(0) = 0 \qquad \text{and} \qquad \tilde{v}(0) = 0.$$

These can be written in terms of the stream function formulation as

$$\phi(0) = 0 \qquad \text{and} \qquad \phi'(0) = 0. \tag{7.42}$$

Another requirement that needs to be satisfied by the solution is the kinematic boundary condition at the liquid-gas interface. In the linear form this can be written as [71]

$$v(1) = \frac{D\eta}{Dt} = \eta_t + \eta_x.$$

In terms of the stream function the kinematic condition simplifies to

$$\phi(1) = 1 - c. \tag{7.43}$$

There are two other constraints that limit the possibility of solutions which come from the dynamic conditions at the liquid-gas interface. These are the shear and the normal force balances at the liquid surface. The shear force balance in the linear form requires

$$\tilde{\tau}_g = \frac{\mu}{\rho}\left(\tilde{u}_y + \tilde{v}_x\right).$$

In this relation $\tilde{\tau}_g$ is the gas phase shear stress perturbation on the liquid interface. Note that the gas shear perturbation should be determined by solving the gas phase perturbation equations which will be considered at a later section. For present purposes we consider $\tilde{\tau}_g$ as a known input for the liquid layer stability problem. The definition of the stream function can be used to convert this equation into the stream function format as

$$\frac{\tilde{\tau}_g}{\eta} = -\frac{1}{\mathrm{Re}}\left(\phi''(1) + \alpha^2\phi(1)\right). \tag{7.44}$$

Finally the normal force balance at the surface requires

$$-\tilde{P}_g + \frac{2}{\mathrm{Re}} v_y = T\eta_{xx} + \left(\frac{\tilde{P}_g}{\eta} - G \right) \eta$$

Here $\tilde{P}_g$ is the gas phase pressure perturbation on the liquid surface. T is the inverse Weber number and G is the inverse Froud number.

$$T = \frac{\sigma}{\rho h U_l} \qquad G = \frac{gh}{U_l^2} \tag{7.45}$$

After converting this equation into the stream function format and coupling with the other boundary conditions, one obtains the following expression.

$$(1-c)\phi'(1) - \phi(1) - \frac{1}{i\alpha \mathrm{Re}}\left[\phi'''(1) - b\phi''(1) - 3\alpha^2\phi'(1)\right] = \left(T\alpha^2 + G - \frac{\tilde{P}_g}{\eta} \right) \frac{\phi(1)}{1-c}. \tag{7.46}$$

The equations 7.42, 7.43, 7.44 and 7.46 set five conditions on the fourth order differential equation, 7.41. Thus this is an overposed boundary value problem. The correct approach is to consider the Orr-Sommerfeld equation with those five conditions as an eigenvalue problem, the eigenvalue being the amplification parameter, c. The direct numerical solution of this eigenvalue problem is computationally expensive, since it requires many iterations (each iteration is a finite difference solution itself) for every selection of the parameters such as the Reynolds number, Froud number or the Weber number that might effect the stability of the layer. For that reason it is desirable to develop analytical solutions. We obtain solutions for the stability problem by using two independent techniques. We first developed a power series solution that can only be applied to films with Reynolds numbers less than unity. For the power series solution, we modified Craik's technique [71] which was originally applied to a simpler case of a layer with no blowing. Since in hybrid applications the film layer Reynolds numbers can be significantly larger than unity, we also formulated an exact solution for the liquid stability problem defined above. In the next section we discuss the development of the two distinct solutions.

7.3.2.3. Development of Solutions

7.3.2.3.1. Power Series Solution

Following Craik, we assume a regular power series solution for the Orr-Sommerfeld equation (7.41) of the form

$$\phi(y) = \sum_{n=0}^{N} A_n y^n . \tag{7.47}$$

Next, this power series is substituted in the Orr-Sommerfeld equation to obtain the following recurrence relation for the coefficients of the power series. (Note that this relation holds only for n>4. For smaller terms similar formulas exist.)

$$n(n-1)(n-2)(n-3)A_n = (n-1)(n-2)(n-3)bA_{n-1} + (n-2)(n-3)qA_{n-2} - (n-3)(n-4)pA_{n-3} - (n-3)\alpha^2 bA_{n-3} + \alpha^2(-rA_{n-4} + pA_{n-5})$$

where

$$p = -i\alpha\,\mathrm{Re} \qquad q = -ic\alpha\,\mathrm{Re} + 2\alpha^2 \qquad r = -ic\alpha\,\mathrm{Re} + \alpha^2$$

It can be argued that if the following order of magnitude relations are valid, the power series converges rapidly.

$$\alpha^2 << 1 \qquad p < O(1) \qquad q < O(1) \qquad r < O(1) \qquad b < O(1)$$

We truncate the series at n=6 under the assumption that the convergence rate is reasonably fast. The first seven coefficients of the series which are of our concern can be calculated with the use of the recurrence relations derived previously. Eventually, the stream function, ϕ can be expressed, to the first order, in terms of four unknown coefficients, A_0, A_1, A_2 and A_3.

$$\phi(y) = A_0 + A_1 y + A_2\left(y^2 + \frac{q}{12}y^4 - \frac{p}{60}y^5\right) + A_3\left(y^3 + \frac{b}{4}y^4 + \frac{q}{20}y^5 - \frac{p}{60}y^6\right) \tag{7.48}$$

This approximate general expression can now be used to solve the eigenvalue problem specified by the boundary conditions discussed in section 7.3.2.2. First, it is easy to see that the zero velocity conditions at the solid surface requires

$$A_n = A_1 = 0. \tag{7.49}$$

The remaining boundary conditions set a new eigenvalue problem with reduced dimensions which can be solved to yield the following condition on the eigenvalue c (to the first order) for the existence of a solution.

$$T\alpha^2 + G - \tilde{P}_g/\eta + \frac{3i\tilde{\tau}_g/\eta}{2\alpha} = (1-c)\left[\frac{3}{2}(1-c) - 1 + \frac{(3+3b+6\alpha^2)}{i\alpha\,\mathrm{Re}}\right] \tag{7.50}$$

This is the stability relation of the liquid film layer. For a selection of physical film parameters and gas flow conditions, the sign of the imaginary part of the eigenvalue c determines the stability of the layer. The stability behavior of the layer according to this relation will be discussed later in this study.

7.3.2.3.2. Exact Solution

The assumptions required for the convergence of the power series solution, limit the range of applicability of the solution to Reynolds numbers and regression rate parameters less than one. However the liquid layers formed on the walls of the hybrid fuel grain possess Reynolds numbers up to a couple of hundreds, due to the large shear forces exerted by the strong gas flow. In this range of moderate Reynolds numbers, the applicability of the high Reynolds number expansion solutions are also highly questionable. For that reason, we developed an exact solution for the eigenvalue problem stated above. In this section we present the outline of our derivation.

It is convenient to restate the Orr-Sommerfeld equation in the operator format

$$(D^4 - bD^3 - 2\alpha^2 D^2 + b\alpha^2 D + \alpha^4)\phi = [i\alpha\,\mathrm{Re}(y-c)](D^2 - \alpha^2)\phi \tag{7.51}$$

where the differential operator is defined as $D \equiv d/dy$.

The critical step in the derivation is the factorization of the operator on the left handside of the equation as

$$(D^2 - bD - \alpha^2)(D^2 - \alpha^2)\phi = [i\alpha \mathrm{Re}(y-c)](D^2 - \alpha^2)\phi. \tag{7.52}$$

After the factorization, this fourth order equation can be separated into two second order equations, namely

$$(D^2 - bD - \alpha^2)\theta = [i\alpha \mathrm{Re}(y-c)]\theta \tag{7.53a}$$

$$(D^2 - \alpha^2)\phi = \theta. \tag{7.53b}$$

In the standard ODE notation these can be written as

$$\theta'' - b\theta' - [\alpha^2 + i\alpha \mathrm{Re}(y-c)]\theta = 0$$

$$\phi'' - \alpha^2\phi = \theta.$$

We have managed to reduce the problem in to the solution of two second order equations. The first of these is a homogeneous linear equation with variable coefficients, whereas the second one is an inhomogeneous equation with constant coefficients. Our solution strategy is to first solve equation 7.53a and use the result to determine the particular solution of the second equation.

We start the solution procedure of equation 7.53a with the application of the following transformation

$$z = -\frac{\alpha^2 + i\alpha \mathrm{Re}(y-c)}{(\alpha \mathrm{Re})^{2/3}} \tag{7.54}$$

In terms of the transformed variable the equation becomes

$$\frac{d^2\theta}{dz^2} + B\frac{d\theta}{dz} - z\theta = 0 \tag{7.55}$$

where $B = -ib/(\alpha \mathrm{Re})^{1/3}$.

It occurs that equation 7.55 takes a simpler form in its reduced form $\theta = UV$. Here V variable is given by $V = e^{-(B/2)z}$ and U is the solution of the following ODE [74]

$$\frac{d^2U}{dz^2} - (z + B^2/4)\frac{dU}{dz} = 0. \tag{7.56}$$

The ODE for U can further be simplified after the transformation $\xi = z + B^2/4$.

$$\frac{d^2U}{d\xi^2} - \xi\frac{dU}{d\xi} = 0 \tag{7.57}$$

This equation commonly known as the Airy equation and the solution can be readily written in terms of the Airy functions Ai and Bi [74].

$$U(\xi) = c_1 Ai(\xi) + c_2 Bi(\xi) \tag{7.58}$$

Now we transform back to the original physical variables. First step is the transformation back to the z variable.

$$U(z) = c_1 Ai(z + B^2/4) + c_2 Bi(z + B^2/4) \tag{7.59}$$

With use of the definition of the normal form, the solution for equation 7.53a can be obtained as

$$\theta(y) = c_1 e^{-(B/2)z(y)} Ai[z(y) + B^2/4] + c_2 e^{-(B/2)z(y)} Bi[z(y) + B^2/4]. \tag{7.60}$$

Note that z is a linear function of y by equation 7.54.

We are now in a position to solve equation 7.53b which now becomes.

$$\frac{d^2\phi}{dy^2} - \alpha^2\phi = c_1 e^{-(B/2)z(y)} Ai\left[z(y) + B^2/4\right] + c_2 e^{-(B/2)z(y)} Bi\left[z(y) + B^2/4\right] \tag{7.61}$$

The homogeneous solution of this equation is quite simple

$$\phi_h(y) = c_1 e^{\alpha y} + c_2 e^{-\alpha y}. \tag{7.62}$$

The particular solution can be obtained with use of the technique of variation of parameters.

$$\phi_h(y) = -\phi_1 \int \frac{\phi_2 \theta}{W} dy + \phi_2 \int \frac{\phi_1 \theta}{W} dy \tag{7.63}$$

Here $\phi_1 = e^{\alpha y}$, $\phi_2 = e^{-\alpha y}$ and the Wronskien, W, is defined as

$$W = \begin{vmatrix} \phi_1 & \phi_2 \\ \phi_1' & \phi_2' \end{vmatrix}.$$

After some algebraic manipulations the total solution can be written as

$$\phi(y) = c_1 e^{\alpha y} + c_2 e^{-\alpha y} + \frac{c_3}{\alpha} \int_{y_0}^{y} \sinh\left[\alpha(y - \hat{y})\right] e^{-(B/2)z(\hat{y})} Ai\left[z(\hat{y}) + B^2/4\right] d\hat{y}$$

$$+ \frac{c_4}{\alpha} \int_{y_0}^{y} \sinh\left[\alpha(y - \hat{y})\right] e^{-(B/2)z(\hat{y})} Bi\left[z(\hat{y}) + B^2/4\right] d\hat{y}. \tag{7.64}$$

The solution can be expressed more conveniently as

$$\phi(y) = \sum_{n=1}^{4} c_n \varphi_n(y) \tag{7.65a}$$

where the four independent particular solutions of the Orr-Sommerfeld equation are

$$\varphi_1 = e^{\alpha y} \tag{7.65b}$$

$$\phi_2 = e^{-\alpha y} \tag{7.65c}$$

$$\phi_3(y) = \frac{1}{\alpha}\int_{y_w}^{y} \sinh\left[\alpha(y-\hat{y})\right] e^{-(B/2)z(\hat{y})} Ai\left[z(\hat{y}) + B^2/4\right] d\hat{y} \tag{7.65d}$$

$$\phi_4(y) = \frac{1}{\alpha}\int_{y_w}^{y} \sinh\left[\alpha(y-\hat{y})\right] e^{-(B/2)z(\hat{y})} Bi\left[z(\hat{y}) + B^2/4\right] d\hat{y} \ . \tag{7.65e}$$

In this format the boundary conditions can be written explicitly as

$$\sum_{n=1}^{4} c_n \phi_n(0) = 0 \tag{7.66a}$$

$$\sum_{n=1}^{4} c_n \phi_n'(0) = 0 \tag{7.66b}$$

$$\sum_{n=1}^{4} c_n \left[\phi_n''(1) - \alpha^2 \phi_n(1)\right] = \mathrm{Re}\frac{\bar{\tau}_s}{\eta} \tag{7.66c}$$

$$\sum_{n=1}^{4} c_n \left\{\phi_n'''(1) - b\phi_n''(1) - 3\alpha^2\phi_n'(1) + (i\alpha\,\mathrm{Re})\left[(c-1)\phi_n'(1) + \phi_n(1)\right]\right\} = i\alpha\,\mathrm{Re}\left(T\alpha^2 + G - \bar{P}_s/\eta\right) \tag{7.66d}$$

$$\sum_{n=1}^{4} c_n \phi_n(1) = c - 1 \tag{7.66e}$$

These boundary conditions with the analytical expressions for the independent solutions can now be used to solve the eigenvalue problem for the eigenvalue c. It is important to note that the selection of $y_w = 0$ significantly simplifies the solution since the first two of the boundary conditions require $c_1 = c_2 = 0$ and drop out of the system. (The derivatives of the solution required for the boundary conditions are listed in appendix G.) In this case the system is reduced to three equations for three unknowns, c_3, c_4, c. Note that even the reduced system involves difficult integrals and it is nonlinear in c. Thus the solution requires numerical integration and some iterative procedure on c. In order to perform the calculations, we developed a MATHEMATICA program that automates the solution procedure and iteratively solves the eigenvalue c, for any given selection of parameters. The time required for the solution at a specified point of the parameter space is less than a second with a modern desktop computer. Thus the analytic solution developed for the film stability problem is apparently very efficient in terms of the computation time over the numerical simulation of the Orr-Somerfeld equation or the Navier-Stokes equations.

7.3.2.4. Gas Phase Relations

The linear stability problem discussed in the previous section requires the gas phase response as the input. In this study we use the gas phase perturbation results (the surface stresses) that were first derived by Benjamin [75] and later adapted to the thin film stability problem by Craik [71]. For the case of surface velocity much smaller than the gas velocity the normal and the tangential stress parameters Π and Σ that represent the gas disturbance on the wavy liquid surface can be approximated by the following equations.

$$\Pi = \left(\alpha/\mathrm{Re}\, C_f\right)\left[I - \sqrt{3}s + i\left(2C_f - s\right)\right] \tag{7.67a}$$

$$\Sigma = \left(2\beta I/\sqrt{3}C_f\right)e^{\pi i/3}\alpha^3(\alpha\,\mathrm{Re})^{-4/3} \tag{7.67b}$$

$$s = 0.644\Delta I, \quad \Delta = \left(I/C_f\right)(\mu/\mu_e)^{2/3}(\alpha\,\mathrm{Re})^{-2/3}\alpha^2, \quad \beta = 1.188(\mu/\mu_e)^{2/3}(\rho_e/\rho)$$

$$I = \int_0^\infty (U/U_e)^2 e^{-\alpha y} d(\alpha y)$$

Here U is the mean boundary layer velocity profile of the gas flow, U_e is the free stream velocity and μ_e, ρ_e are the viscosity and the density of the gas respectively. Note that $\tilde{P}_s$ equals $\Pi\eta$ and $\tilde{\tau}_s$ equals $\Sigma\eta$. Therefore the real parts of stress parameters corresponds to the components of stress that are in phase with the wave displacement, whereas the imaginary parts of the stress parameters represent the stress components which are in phase with the wave slope.

The preceding expressions for the gas phase stress perturbations are derived for an incompressible gas flow with no blowing allowed. For that reason, it must be realized that the applicability of those relations to the hybrid boundary layer with combustion and strong blowing is a rough approximation. Moreover these estimates derived by Benjamin involves major assumptions even for the incompressible gas flow. The assumptions and the range of applicability of the solution given by equation 7.67 is discussed extensively by Craik.

7.3.2.5. Discussion of Results for Stability

In this section we discuss the results for the liquid layer stability problem that are obtained with the application of the solution techniques discussed in the previous section. First we compare the result of the exact solution with the power series solution for verification purposes. Figure 7.13 shows the amplification rate (imaginary part of c) as a function of the wave number for the power series solution and also for the exact solution. The figure is for a water film with a relatively low liquid Reynolds number of 2 and at a regression rate parameter of 0.2. As it can be induced from the figure, the exact solution is in good agreement with the power series predictions for the small Reynolds number used in the calculation within the range of small wave numbers as expected. Note that as the nondimensional wave number increases the error associated with the power series solution increases rapidly.

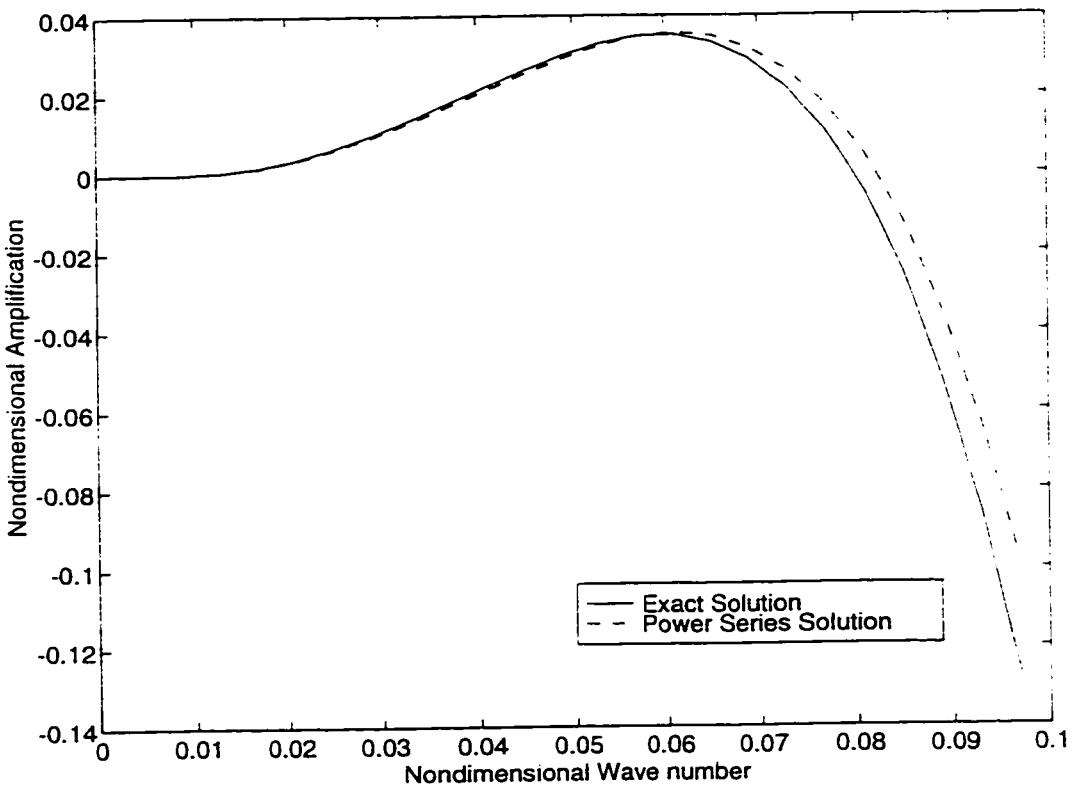

Figure 7.13. Nondimensional amplification rate of a surface disturbance versus the nondimensional disturbance frequency calculated with the power series method and the exact solution method. This case is for a water film with a thickness of 0.3 mm, a liquid Reynolds number of 2 and regression rate parameter of 0.2.

The most encouraging result of this linear theory is that even at very small film thickness there exists a finite range of amplified wave numbers, namely the layer is unstable over a finite range of wave numbers. The instabilities of that type were first discovered for thin water films in a wind tunnel by Craik [71] and they are called the "slow waves". These are generated by the interaction of the gas phase shear stresses acting on the liquid surface with the slope of the liquid layer surface. Figure 7.14 shows a typical form of the amplification rate versus the wave number within the content of the mentioned linear stability theory. As indicated in the figure, there is a positive amplification domain which lies between two cutoff wave numbers. The amplification takes a maximum value at a wave number between these two cutoff wave numbers. This is the most amplified wave number and the corresponding wave length is expected to be the observed size of the disturbance in the actual flow system [76].

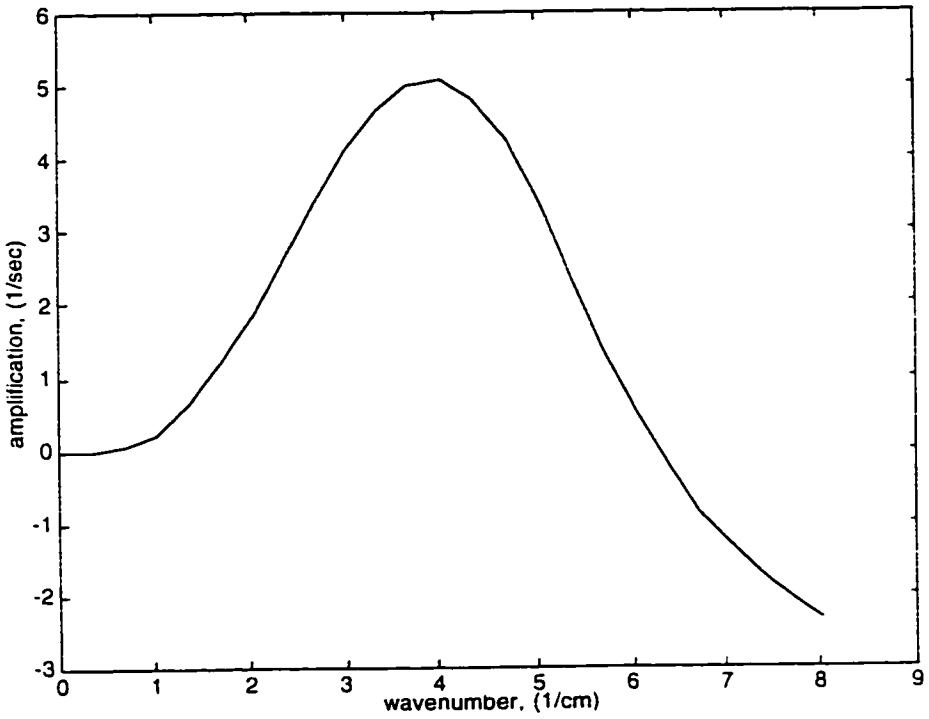

Figure 7.14. Amplification rate of a surface disturbance versus the disturbance frequency. This plot is for a water film with a thickness of 0.3 mm and film Reynolds number of 7.

Intuitively, the most important parameter that links the linear stability results to the entrainment rate of the liquid from the surface is the amplification rate of the disturbances. Figure 7.15 shows the effect of the Reynolds number on the amplification curves. Note that as the liquid layer Reynolds number (which is directly proportional to the gas stream

dynamic pressure) increases, the amplification rate increases. The Reynolds number also increases the most amplified wave number, meaning that at higher gas flow velocities the expected wave lengths of the instabilities are smaller. This latter result is in good agreement with the experimental findings for the nature of water waves formed on the surface of a thin film [76]. The body force (i.e. gravity) acting downwards on the liquid surface sets a threshold for the stability feature of the film. Namely, there is a critical Reynolds number below which all the wave lengths are stable. If the body force is zero this critical Reynolds number is also zero. Since in hybrid applications the gas flow dynamic pressures are high, the effect of gravity is negligible.

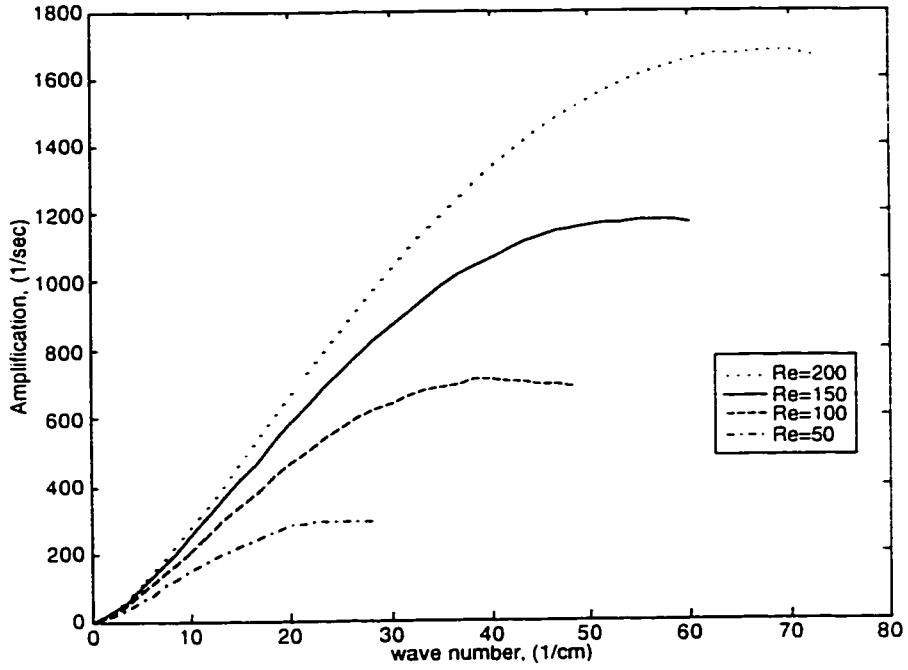

Figure 7.15. Amplification rate of a surface disturbance versus the disturbance frequency for various film Reynolds numbers. This plot is for a pentane film with a thickness of 0.3 mm.

The effect of the liquid injection on the film stability is shown in figure 7.16. The amplification rate as a function of the wave number for two values of regression rate parameter, b, is calculated with use of the exact solution. As indicated in figure 7.16, the final result is that the injection stabilizes the film. The power series solution also leads to the same conclusion.

The surface tension of the liquid fuel has also a stabilizing effect on the liquid film. Namely, for liquids with larger surface tension the amplification rates of the unstable wave

lengths are smaller. It is worth noting that viscosity has a similar stabilizing effect. The amplification curves for various liquids at a constant thicness of 0.3 mm are shown in figure 7.17. The Reynolds number for pentane is selected to be 5 and the Reynolds numbers for all the other liquid are calculated for the same dynamic pressure and film thickness. The material properties of the liquids used in the calculations are given in table F.1 of Appendix F. Note that liquids with higher viscosities such as isopropanol and HFI are more stable than the liquids with small viscosity values.

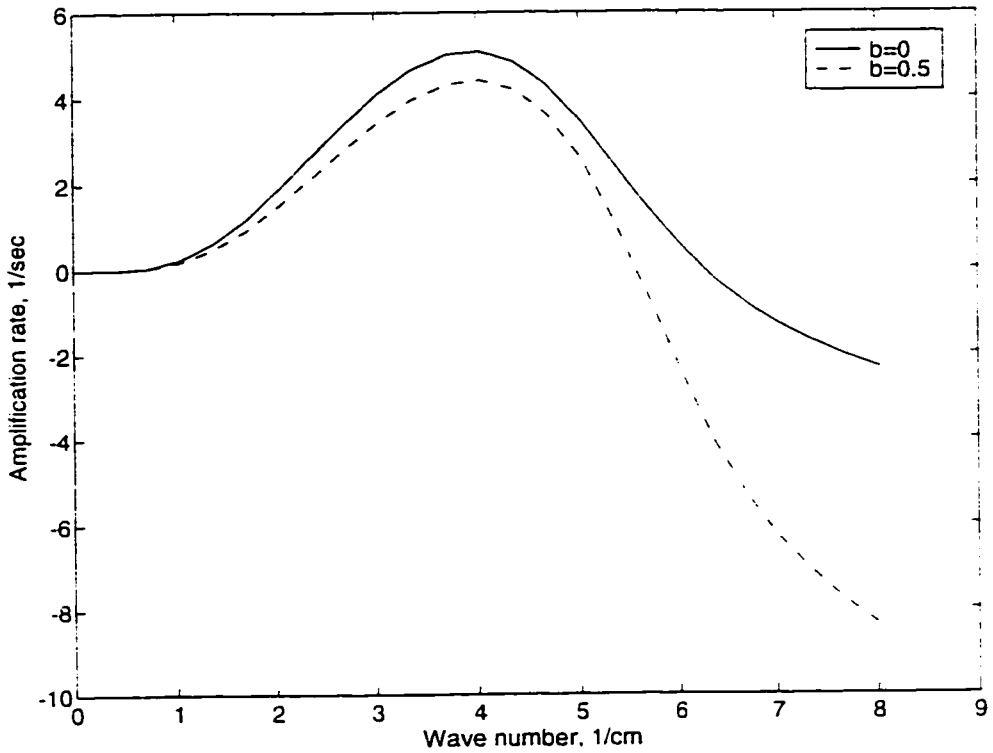

Figure 7.16. The effect of regression rate on the stability of the film is illustrated. This plot is for a water film with a thickness of 0.3 mm and a Reynolds number of 7.

In the preceding section we discussed the linear stability of the film layer. It is shown that the layer can be unstable over a wide range of parameters. Now this observation needs to be related to the entrainment phenomenon of the liquid droplets into the gas stream. The rigorous treatment of the entrainment problem requires a nonlinear investigation. In this study we avoid this difficulty by developing empirical relations for the entrainment with use of some experimental data and the linear stability results.

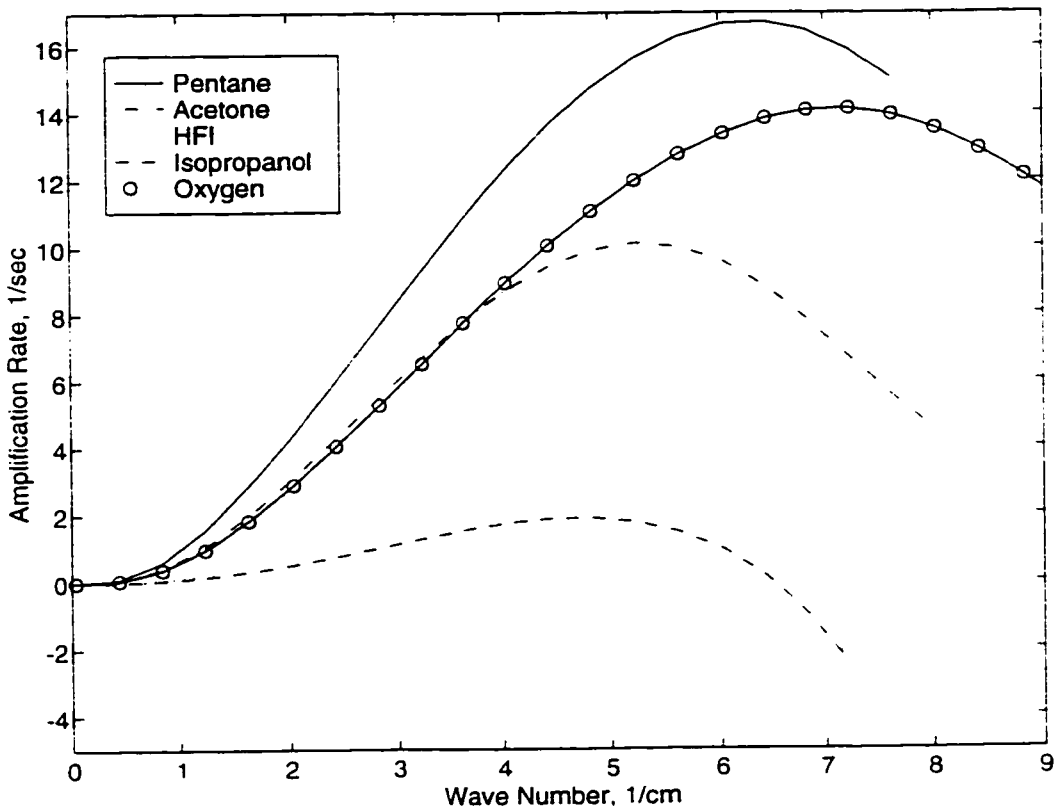

Figure 7.17. Amplification curves for various liquid materials at the same film thickness and gas shear stress level.

The most relevant experimental work on entrainment is reported by Gater and L'Ecuyer in an early paper [76]. In this study, the entrainment rates from thin films of various liquids (including some hydrocarbons such as RP-1, methanol) under strong gas flow in a wind tunnel are measured. The experiments are performed in a wind tunnel and some test are executed with hot gas flow. The most significant result of this study is that the entrainment mass transfer per unit area, $\dot{m}_{ent}$ is proportional to the mass flow rate per unit width in the liquid layer. The dimensional proportionality coefficient, e_{ent}, is formulated in terms of the dynamic pressure of the gas flow, P_d, surface tension, σ and a temperature ratio according to the following simple formula.

$$\dot{m}_{ent} = 13.3 e_{ent}(X_e)\dot{m}_l \qquad \text{where} \qquad X_e = \frac{P_d^{0.5}}{\sigma}\left(\frac{T_g}{T_s}\right)^{0.25} \tag{7.68}$$

Here T_g is the gas stream average temperature and T_s is the surface temperature. It is indicated that the temperature ratio is included as a correction for the density variation in the

gas. The following empirical formula can be used to calculate the entrainment mass transfer per unit area of liquid surface, $\dot{m}_{ent}$, in $kg/m^2\sec$, for a given mass flow rate per unit width of the liquid, $\dot{m}_l$, in units of $kg/m\sec$.

$$e_{ff}(X_c) = 1 - e^{-1.06(X_c - 2109)/10000} \tag{7.69}$$

In this relation the units of X_c is $N^{-1/2}$. Note that with use of the shear force balance at the liquid gas interface, liquid mass flow rate per unit width can easily be related to the properties of the gas flow and liquid film under consideration.

$$\dot{m}_l = \frac{P_{ff} c_f h^2}{2\mu} \tag{7.70}$$

Equation 7.68 for the entrainment mass transfer ignores the effect of reduction in the liquid mass flow rate along the axial direction. This may be a significant source of error at high mass transfer rates for which the decrease of the film thickness is important. For that reason we modify the entrainment expression to correct for this effect.

$$\dot{m}_{ent} = -13.3\ln(1 - e_{ff})\dot{m}_l \tag{7.71}$$

This expression shows that if the entrainment parameter e_{ff} is sufficiently large, the entrainment mass transfer rate, $\dot{m}_{ent}$, can be significantly larger than the liquid mass flow rate, $\dot{m}_l$, of the film. Upon the substitution of equation 7.69 in equation 7.71, the following expression for the entrainment mass transfer and entrainment regression rate is obtained.

$$\dot{m}_{ent} = \rho_l \dot{r}_{ent} = 1.41\,10^{-3}(X_c - 2109)\dot{m}_l \tag{7.72}$$

This relation or the original expression, equation 7.68, is only valid for $X_c < 2109$ ($N^{-1/2}$). Namely if the entrainment parameter is less than the critical value there is no entrainment mass transfer from the film. This threshold for entrainment roughly corresponds to a port gas mass flux of 50 $kg/m^2\sec$ for pentane fuel during a typical operation of the motor.

After the preceding correction the entainment mass transfer becomes proportional to a difference between the entrainment parameter, X_e and its critical value at the onset of entrainment. Note that this a form that is commonly found in the literature [78]. For hybrid applications with sufficiently large X_e, the entrainment mass transfer is approximately proportional to $P_d^{3/2}$.

The empirical result stated above is in good qualitative agreement with the linear stability theory predictions. First, the entrainment increases monotonically with the entrainment parameter. Thus similar to the linear stability, the gas dynamic pressure is destabilizing and the surface tension and viscosity are stabilizing. Moreover below a critical level of the entrainment parameter there is no entrainment observed. This is also consistent with the requirement for the interface disturbance to posses a minimum amplification rate to yield any entrainment.

In the nuclear reactor field there has been significant research on the entrainment mass transfer [77, 78], since it has importance in the emergency cooling of the reactors. Various models for entrainment are developed at various regimes of operation. At high Reynolds numbers which are more relevant to our case, a roll wave mechanism for the liquid entrainment is suggested [77]. In general, the experimental findings of those studies also confirm the results previously mentioned. However the form of dependence of the entrainment mass transfer on the parameters is somewhat different in every study. Thus it is fair to state that the proper form of scaling for the entrainment still needs to be resolved.

In the light of experimental findings and the results of the linear theory, we suggest the following general empirical expression for the entrainment rate of liquid droplets in terms of the relevant properties of the hybrid motor.

$$\dot{m}_{ent} \propto P_d^{\alpha} h^{\beta} \mu^{\gamma} \sigma^{\pi} \tag{7.73}$$

The experimental curvefits and the linear stability theory suggest that the dynamic pressure exponent is in the range of 1-1.5. For example Gater and L'Ecuyer [76] scaling for large mass fluxes indicates that α is approximately 1.5 and β is equal to 2. The viscosity and surface tension exponents are both predicted to be -1. The series of entrainment relations given Nigmatulin *et al* [78] suggest a weaker dependence on both the dynamic pressure and also the thickness ($\alpha = 1$ and $\beta = 1$). The scaling with respect to the

material properties is not estimated accurately by the entrainment relations given by Nigmatulin, since mainly water data was considered in the study.

A very useful empirical relation for the critical conditions for the onset of entrainment given by reference 84 is rearranged here in terms of the practical conditions in the motor.

$$G^{1.6}h^{0.8} = 2.5\ 10^{-3}\frac{\mu^{0.6}\sigma}{\rho_l}\frac{\rho_g^{1.2}}{\mu_g c_f} \tag{7.74}$$

Note that this relation only holds for a laminar film ($\mathrm{Re} < 300$). Unlike the entrainment relations this formula has correct scaling with the material properties of the liquid. Figure 7.18 shows the plot of the entrainment boundary for various liquid materials in the mass flux film thickness plane (See Appendix F for the material properties used in calculations). Note that for each liquid, the entrainment takes place in the region above the curve.

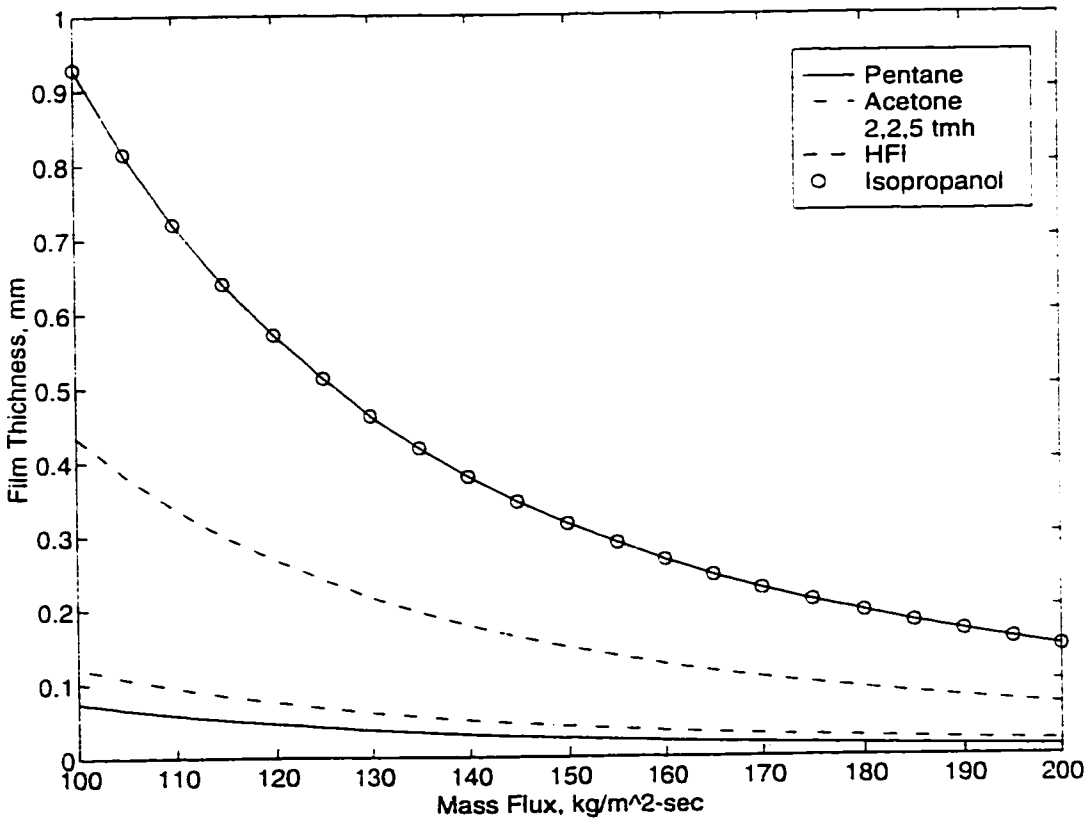

Figure 7.18. Entrainment onset boundaries for various liquids used in hybrid tests.

7.3.3 Extended Hybrid Theory

It has been shown in the previous sections that a liquid layer can be formed on the fuel grain and this liquid layer can be unstable over a reasonable range of parameters typical of hybrid operation. It is also indicated that the instabilities in the liquid layer may enhance the entrainment of liquid droplets into the gas stream. The final phase of the development involves the modification of the classical hybrid boundary layer combustion theory for the possibility of the entrainment mass transfer from the fuel grain.

The possibility of entrainment of droplets requires two major modifications in the classical hybrid theory.

1) The ratio of the enthalpy difference to the effective heat of gasification ($\Delta h/h_{\ell}$) that appears in the thermal blowing parameter expression is altered. The effective heat of gasification is reduced since the evaporation energy required for the fuel mass transfer from the surface is partly avoided by the mechanical entrainment of the liquid. Whereas, the enthalpy difference between the flame and the surface is also reduced, since some of the reactants are now in liquid phase. It is estimated that, the reduction in the effective heat of gasification is more dominant than the change in the enthalpy difference. Thus as a first approximation we assume that the reduction in the flame enthalpy is negligible.

2) The blocking factor, C_H/C_{H_0}, that modifies the convective heat flux to the surface is also altered due to the presence of the two phase flow. As a first approximation we ignore the effect of the liquid droplets on the momentum and energy transfer. Under this assumption the blocking factor can be expressed as a function of evaporation blowing parameter.

$$C_H/C_{H_0} = f(B_g)$$

The evaporation blowing parameter, B_g, includes only the gaseous phase mass transfer from the fuel surface. We assume that evaporation of the droplets released from the liquid surface into the gas stream does not take place beneath the flame sheet. This assumption is consistent with the flame sheet approximation which is a standard one in hybrid combustion modeling. Moreover, it is a reasonable approximation for typical hybrid

operating conditions that are characterized by high blowing rates and thus low residence time of droplets between the liquid surface and the diffusion flame.

In general, the total regression rate of a hybrid motor can be written as a combination of the evaporation regression rate that is generated by the vaporization of the liquid into the gas stream and the entrainment regression rate that is related to the mass transfer mechanically extracted from the liquid surface.

$$r = \dot{r}_v + \dot{r}_{ent} \tag{7.75}$$

For an arbitrary combination of the entrainment and evaporative mass transfer the energy balance at the liquid gas interface is

$$\dot{r}_v + R_h \dot{r}_{ent} = \frac{0.03\mu_g^{0.2}}{\rho_f}\left(1 + \dot{Q}_r/\dot{Q}_c\right) B \frac{C_H}{C_{H_0}} G^{0.8} z^{-0.2} \tag{7.76}$$

where $R_h = (h_v)_{ent}/h_v$.

Since entrainment mass transfer requires no vaporization energy, the entrainment heat of gasification is defined as $(h_v)_{ent} = h_v - L_v$. The blowing correction appearing in equation 7.76 can be estimated by the following formula which is a reasonable approximation for the exact blowing correction expression given by Marxman for a B_g range of 0-14

$$\frac{C_H}{C_{H_0}} \equiv \frac{2}{2 + 1.25B_g^{0.75}} = \frac{C_{B1}}{C_{B1} + C_{B2}\left(\dot{r}_v/\dot{r}_{cl}\right)^{0.75}} \tag{7.77}$$

Here the coefficients are defined as

$$C_{B1} \equiv \frac{2}{2 + 1.25B^{0.75}} \qquad \text{and} \qquad C_{B2} \equiv \frac{1.25}{2 + 1.25B^{0.75}}.$$

Note that B is the classical blowing parameter and $\dot{r}_{cl}$ is the classical regression rate of the system in the case of no entrainment. The classical regression rate can be written as

$$\dot{r}_{cl} = \frac{0.03\mu_g^{0.2}}{\rho_f}\left(1 + \dot{Q}_r/\dot{Q}_c\right) B\, C_{B1} G^{0.8} z^{-0.2}. \tag{7.78}$$

The energy equation, 7.76 simplifies significantly when it is expressed in terms of the classical regression rate.

$$\dot{r}_v + R_h \dot{r}_{ent} = \frac{\dot{r}_{cl}}{C_{B1} + C_{B2}\left(\dot{r}_v/\dot{r}_{cl}\right)^{0.75}} \tag{7.79}$$

Following the proceeding section's arguments the entrainment regression rate can be written in terms of the mass flux in the port and the total regression rate.

$$\dot{r}_{ent} = a_{ent} \frac{G^{2\alpha}}{\dot{r}^{\beta}} \tag{7.80}$$

Here we used the definition of the dynamic pressure ($P_d = G^2/2\rho_g$) and equation 7.20 for the film thickness expression. The coefficient a_{ent} is a function of the properties of the selected propellant and average gas density (ρ_g) in the chamber. For simplicity we will assume that is a constant for given propellant. In the calculations we use Gater and L'Ecuyer's modified empirical entrainment mass transfer relation to determine the unknown a_{ent} coefficient with a correction for the thickness exponent, β. The correction is performed since the Gater's empirical formula significantly overestimates β compared to predictions of the other scaling laws found in the literature (i.e. Nigmatulin).

Equations 7.75, 7.76 and 7.80 together with the blowing correction expression, equation 7.77, form a nonlinear set of algebraic equations which can be solved for a given propellant combination to obtain the total regression rate as a function of the axial location and local mass flux. For pentane as the frozen fuel, the regression rates are calculated iteratively from this nonlinear set of equations as a function of the mean mass flux in the port. Figure 7.19 shows both the estimated regression rates and also the reduced data for the pentane runs. In the calculations $\dot{Q}_r/\dot{Q}_c = 0.3$, $z = L/2 = 7.5$ (cm) and $\mu_g = 6.5\ 10^{-5}$ (N-sec/m^2) numerical values are used. Figure shows that the estimated regression rates are in good agreement with the regression rates reduced from the pentane data.

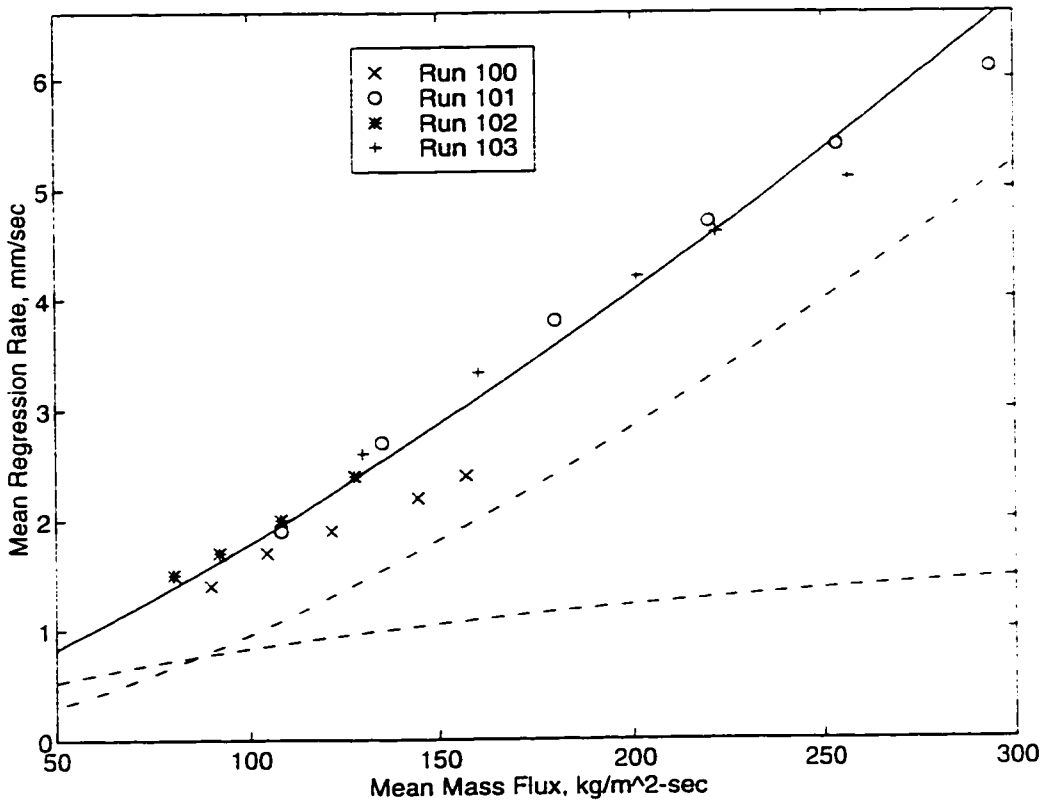

Figure 7.19. Regression rate of a cryogenic hybrid as a function of the mass flux. "-" : total regression rate, "--" : vaporization component of regression rate, "-." : entrainment component of regression rate.

It is desirable to obtain an approximate explicit expression for the total regression rate as a function of the local mass flux and axial location. In order to achieve that we first nondimensionalize the regression rate equations in the following way

$$\Phi = \Phi_v + \Phi_{ent} \tag{7.81a}$$

$$\Phi_v + R_h \Phi_{ent} = \frac{1}{C_{B1} + C_{B2}(\Phi_v)^{0.75}} \tag{7.81b}$$

$$\Phi_{ent} = \frac{R_{ent}}{\Phi^{\beta}} \tag{7.81c}$$

where the nondimensional variables are defined as

$$\Phi \equiv \dot{r}/\dot{r}_{cl}, \qquad \Phi_v \equiv \dot{r}_v/\dot{r}_{cl}, \qquad \Phi_{ent} \equiv \dot{r}_{ent}/\dot{r}_{cl}, \qquad R_{ent} \equiv a_{ent} G^{2\alpha}/\dot{r}_{cl}^{\beta+1}.$$

These equations can now be solved for the nondimensional total regression rate for each value of the nondimensional entrainment variable, R_{ent} and the gasification energy

ratio R_h. The result is presented in figure 7.20 which shows the universal family of nondimensional regression rate, Φ, versus R_{ent} curves for various values of the gasification energy ratio. Note that the effect of gasification energy ratio within its acceptable range of variation (from zero to one) is small.

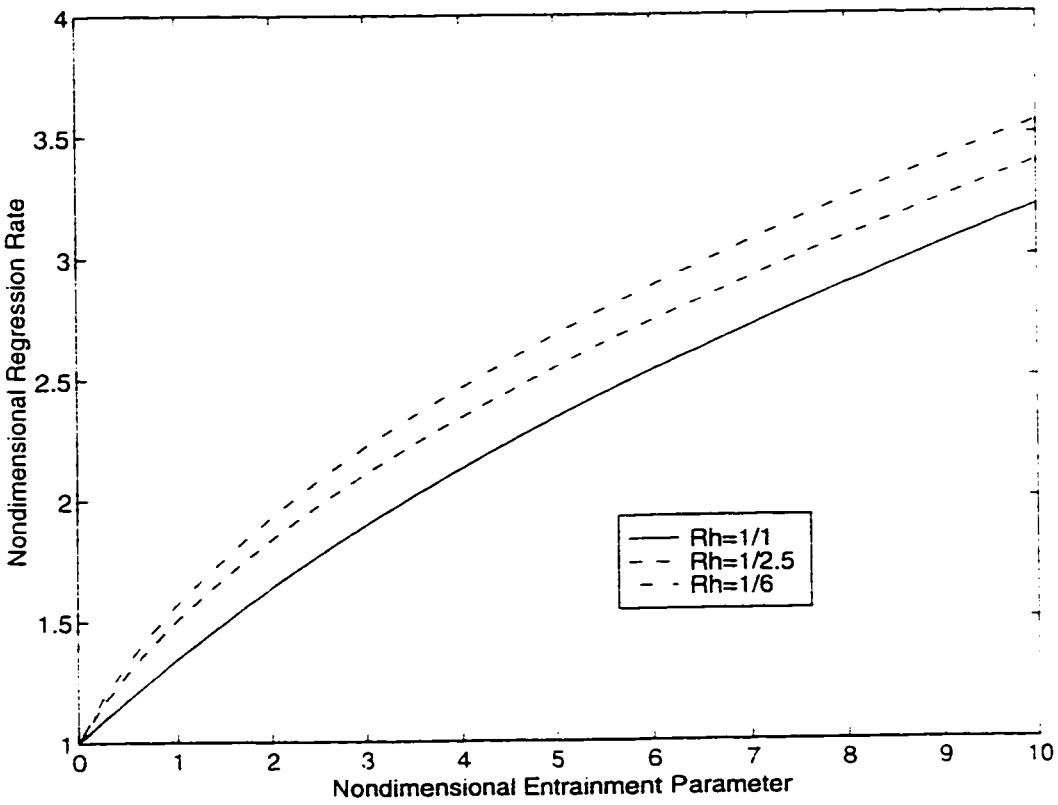

Figure 7.20. Universal curves for the nondimensional regression rate versus the entrainment parameter for various ratios of heat of gasification.

A reasonably accurate curvefit expression for the nondimensional regression rate curve for $R_h = 1/2.5$ (corresponding to pentane) is

$$\Phi \cong 0.53 R_{ent}^{0.75} + 1. \tag{7.82}$$

In terms of the dimensional variables, this expression takes the following form.

$$\dot{r} \cong 0.53 \frac{a_{ent}^{0.65} G^{1.3\alpha}}{\dot{r}_{cl}^{0.65\beta - 0.35}} + \dot{r}_{cl} \tag{7.83}$$

This equation shows that the total regression rate can be approximately written as a sum of the classical regression rate and the entrainment contribution. Note that for pentane ($\alpha = 1.5$ and $\beta = 1.18$) the mass flux exponent of the entrainment component is approximately 1.95 as opposed to the 0.8 exponent of the classical part. Thus the effective exponent of the total regression rate is between 0.8 and 1.95 as indicated by the pentane data. Note that since the gasification energy ratio alters the coefficient and the exponent of the curvefit expression slightly, equation 7.82 does not hold for every kind of propellant. However the general form of the approximate regression rate expression will be the same for any material selection.

It is useful to obtain an upper limit for the regression rate of a hybrid fuel forming a liquid layer. In the extreme case the evaporation from the liquid surface is negligible, namely all the mass is transferred to the gas flow in form of droplets. This upper bound can be quantitatively determined upon the consideration of equation 7.76. The maximum regression rate occurs when there is no evaporation at the surface takes place. Under the assumptions of our theory, for this extreme case, the blocking factor becomes unity. The maximum regression rate normalized with the classical value of the regression rate, for which no entrainment from the surface is allowed, becomes

$$\frac{\dot{r}_{max}}{\dot{r}_{cl}} = \frac{h_v}{C_{BI}(h_v)_{ent}}. \tag{7.84}$$

For pentane fuel the maximum regression rate is estimated to be approximately 15 times the classical regression rate. Note that for pentane calculations the blowing parameter value of 13.5 and heat of gasification ratio of 2.5 are used. This large upper limit for the amplification explains the experimentally observed regression rates that are determined to be 2-5 times larger than the expected (classical) values.

As shown in table 7.1 some hydrocarbons such as pentane, acetone and 2,2,5 tmh burn fast whereas some others such as isopropanol and HFI burn considerably slowly. This observation can also be explained within the context of the liquid layer hybrid theory developed in this section. Figure 7.18 shows the entrainment onset boundary for various propellants tried in the cryogenic hybrid configuration. It is clear that materials isopropanol and HFI, which are significantly more viscous compared to the other materials, require very large thresholds for entertainment. In order to reinforce this finding, we used equation 7.72 to calculate the entrainment regression rate as a function of the mass flux in the port

for the materials of our concern. The result is shown in figure 7.21. Similarly the entrainment regression rates of the viscous propellants (i.e. isopropanol, HFI) is one order of magnitude smaller than the other propellants. This finding reveals viscosity as a major parameter controlling the burning rate of a cryogenic hybrid propellant. In fact, viscosity of the imbedded propellant can be adjusted to tailor the regression rate of a cryogenic hybrid rocket during the course of its operation. Moreover it can be stated that oxygen, which is an interesting alternative solid cryogenic hybrid propellant, is also likely to be a fast burning material due to its low viscosity.

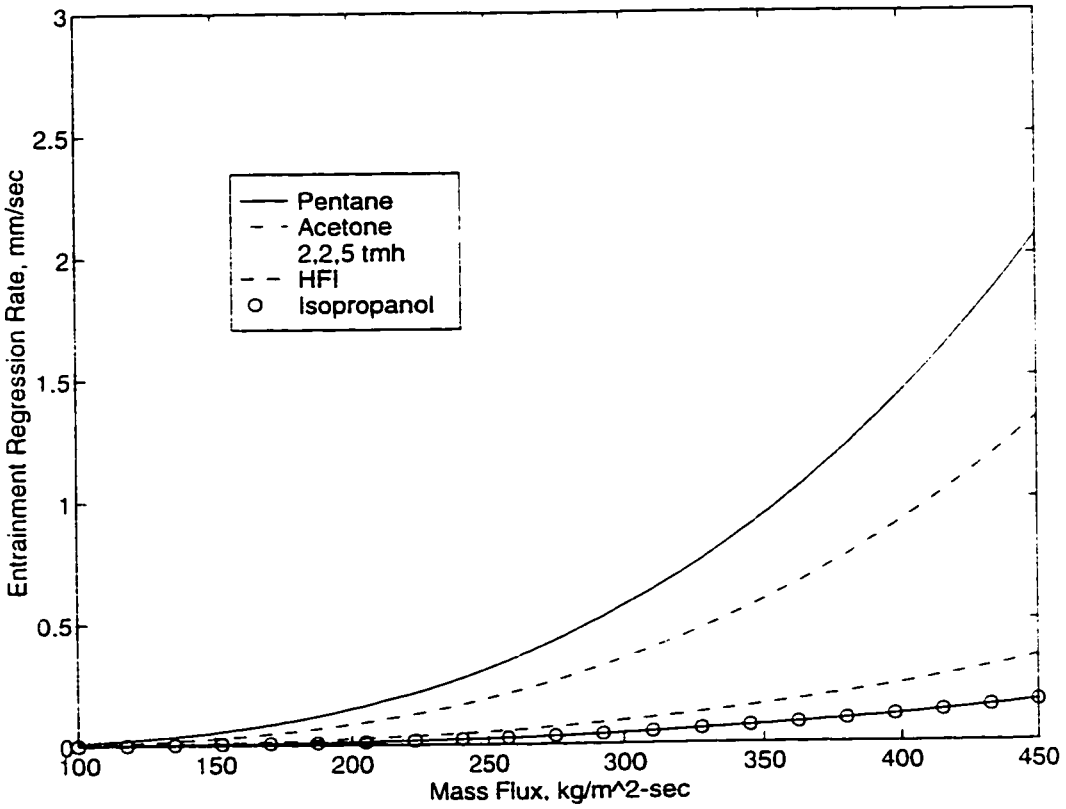

Figure 7.21. Entrainment regression rate according to eqaution 7.72 at a constant film thickness of 0.1 mm for various liquids.

Another important practical issue for the prediction of the performance of a propellant is its susceptivity to bulk heating by radiation penetrated through the slab. Specifically, it can be stated that the materials which have small radiative absorptivities in their solid phases, potentially burn in an uncontrolled fashion. This due to the possibility of sloughing of the propellant that is internally heated. In order to investigate this, outer web temperature is calculated as a function of nondimensional web thickness for a typical pentane run with use of equation 7.20. The result is shown for three different solid

absoptivities in figure 7.22. Evidently, the temperature measurement during a pentane test [67] taken at the inside wall of the tube burner is best resembled by calculations performed with $R_s = 0.02$. The wall temperature changes very little until the last quarter of the run after which it increases rapidly. Note that in the last quarter of the run the chamber pressure drops suddenly for the same test. This observation supports the possibility of sloughing due to bulk heating of the propellant. The extent of this uncontrolled operation mode over the whole burn time is expected to be more significant for propellants with smaller absorptivities of radiation. In fact for a propellant to be practical its absoptivity must be increased over a minimum value by possibly adding materials that are good absorbers of radiation (i.e. carbon black).

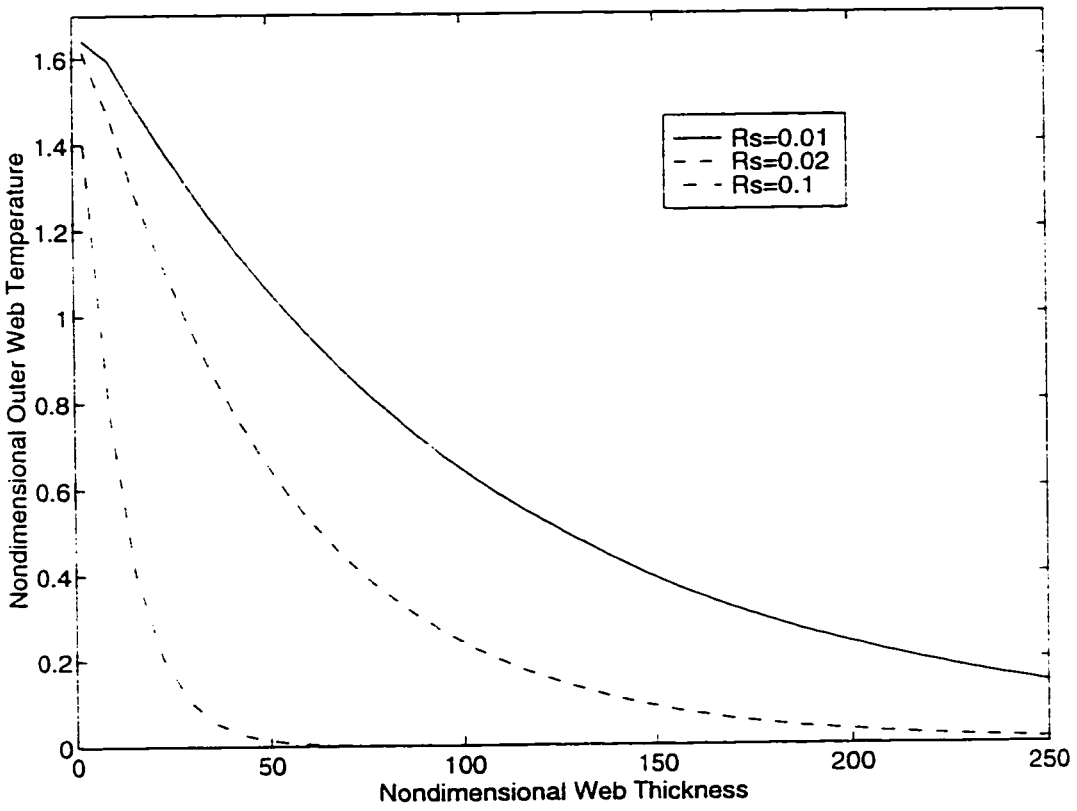

Figure 7.22. The variation of the nondimensional outer web temperature with the nondimensional web thickness for a typical pentane run at three different absoptivity values.

7.4 Wax Burning Rate Predictions

Although the liquid layer hybrid combustion theory was first developed for cryogenic propellants, it covers the combustion of non-cryogenic materials such as long chain hydrocarbons that might form a low viscosity melt layer on their burning surfaces.

Note that the combustion of the conventional polymeric fuels which burn with no entrainment is a subset of the liquid layer theory. It will be shown in this section that the theory predicts regression rates that are several times larger than the classical hybrid burning rates for some particular long chain normal hydrocarbons which are solid at ambient conditions. This family of fast burning materials such as paraffin waxes which do not require a cryogenic environment eliminates various disadvantages of classical hybrids which can be listed as

a) The higher regression rates will yield a more compact hybrid motor which can ultimately be comparable to conventional solid rocket systems. The volumetric loading will be significantly increased which will improve the performance of the overall propulsion system

b) Higher regression rates will eliminate the requirement of complex multi-port design. This leads to a reduction of the cost of the system due to the easy manufacturing of a single port motor. The use of a single port solves various practical engineering problems such as grain integrity. The performance will also be increased due to reduced fraction of the residual fuel at the burn out.

c) Single port design also eliminates the requirement for a pre-combustion chamber which will reduce the incidence of low frequency instabilities commonly observed in modern hybrids.

We now apply the liquid layer combustion theory for the long chain hydrocarbon materials that are in solid phase under ambient conditions. For simplicity, we will constraint our search, to linear hydrocarbon molecules (specifically n-paraffins), for which important material properties such as viscosity can be expressed as a function of the molecular weight and the temperature. In fact the melting, vaporization and average melt temperatures of the n-paraffins as functions of the molecular weight is shown in figure 7.23. Data points for the melting temperatures of three polyethylene waxes are included in the figure. Note that all three temperatures increase rapidly in the small molecular weight region, where as in the large molecular weight region they asymptote to a constant value. For large molecules the upper temperature limit is dictated by the pyrolysis rather than the vaporization, since the large molecules will tend to break up before the vaporization occurs. Note that the pyrolysis temperature for the high density polyethylene polymer is about 405

°C. Where as the melting temperature limit is the melting temperature of the infinite molecular weight polyethylene polymer which is 141 °C.

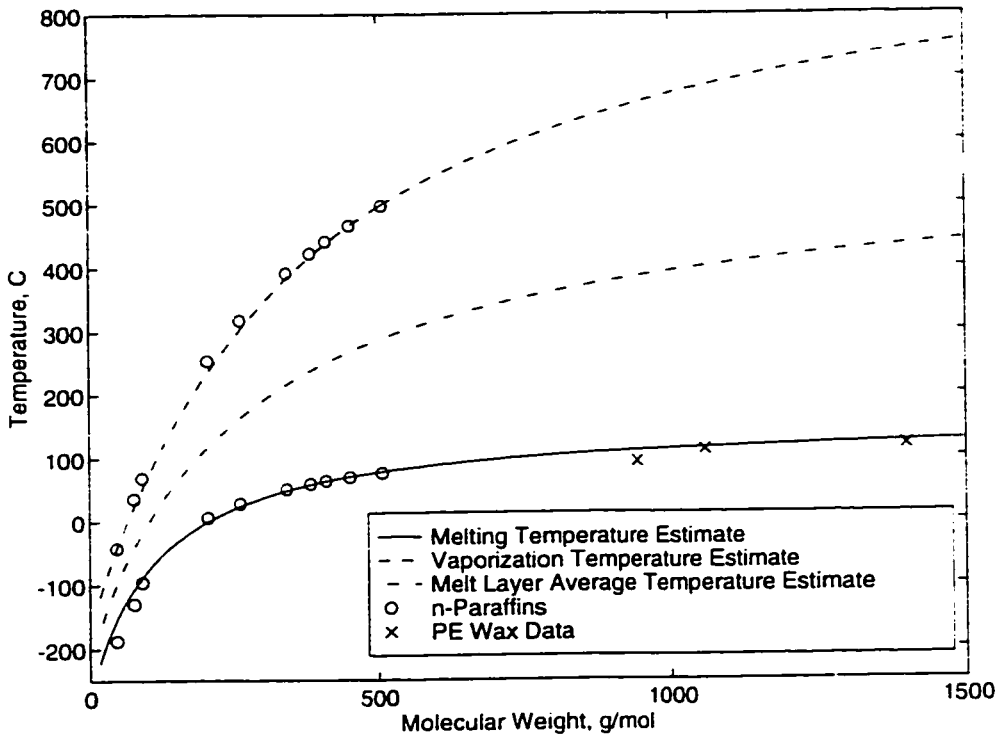

Figure 7.23. Melting, vaporization and average melt layer temperatures of n-paraffins as a function of molecular weight.

As discussed in the previous section, the most important parameters of a melting propellant that determines the entrainment and thus the total burning rate of a prospective propellant are the melt viscosity at an average temperature between the melting temperature and the liquid-gas interface temperature and the surface tension at the liquid-gas interface temperature. The plot of viscosity as function of the molecular weight of the normal hydrocarbons for three different temperatures are shown in figure 7.24. The figure obviously shows a linear variation of viscosity with the molecular weight as expected in this low molecular weight regime. Two additional data points for two highly crystalline polyethylene waxes (4040/R7 and 4040/R9 of Marcus Oil & Chemical Corporation) are also included in the plot. This specific polyethylene wax is composed of highly linear molecules and its viscosity can be predicted by the extrapolation of the curve obtained for the n-paraffins. Although the figure shows a significant increase of viscosity with the molecular weight at a constant temperature, the melt layer viscosity only increases slightly due to the increase in the melt layer temperature. This important fact is presented in figure

7.25 which shows the reduced molecular weight dependence of the melt layer viscosity evaluated at the mean between melting and vaporization temperatures. Note that the viscosity values are normalized with respect to the n-pentane melt viscosity. However this temperature effect can only be realized for small molecular weights (i.e. paraffin waxes) since the temperature increase is trivial above a certain molecular weight.

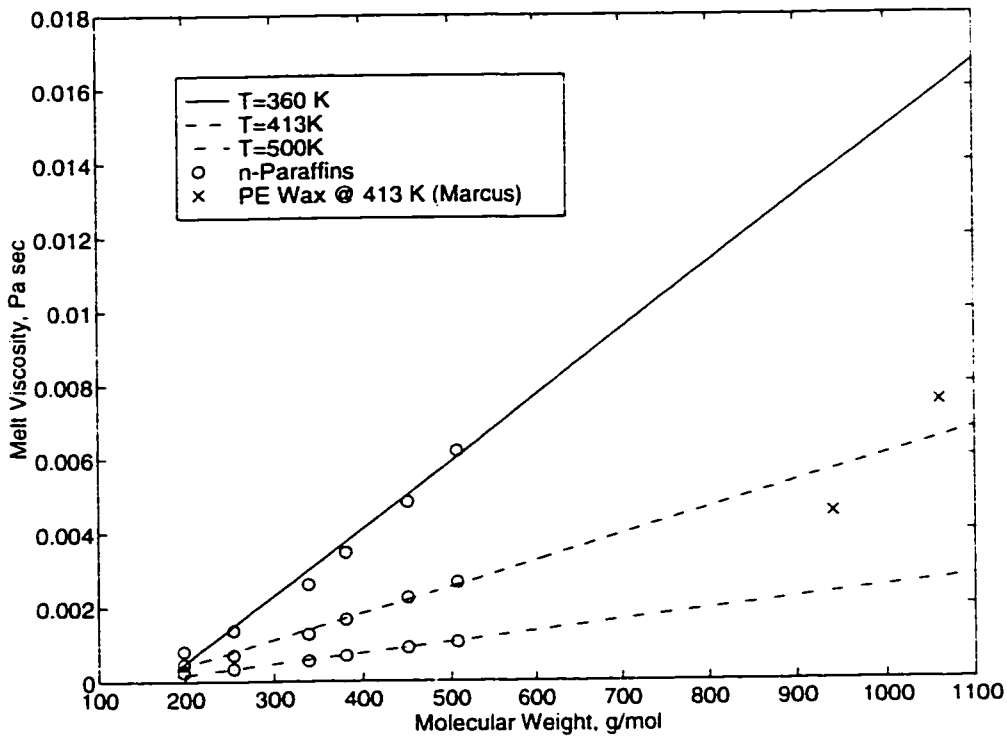

Figure 7.24. Viscosity as a function of the molecular weight for various n-parraffins and two highly crystalline polyethylene waxes.

Similar same arguments hold for the surface tension. Even though the surface tension of linear hydrocarbon series increases linearly with increasing molecular weight at a constant temperature, melt layer surface tension actually decreases with increasing molecular weight as shown in figure 7.25. This effect which can only be realized for relatively small molecular weights is also due to the increased melt layer surface temperatures with increasing molecular weight. These observations on the melt viscosity and surface tension indicates that moderate molecular weight hydrocarbons (i.e. paraffin waxes) could generate entrainment rates that are comparable to the entrainment rates of fast burning cryogenic materials such as n-pentane or acetone.

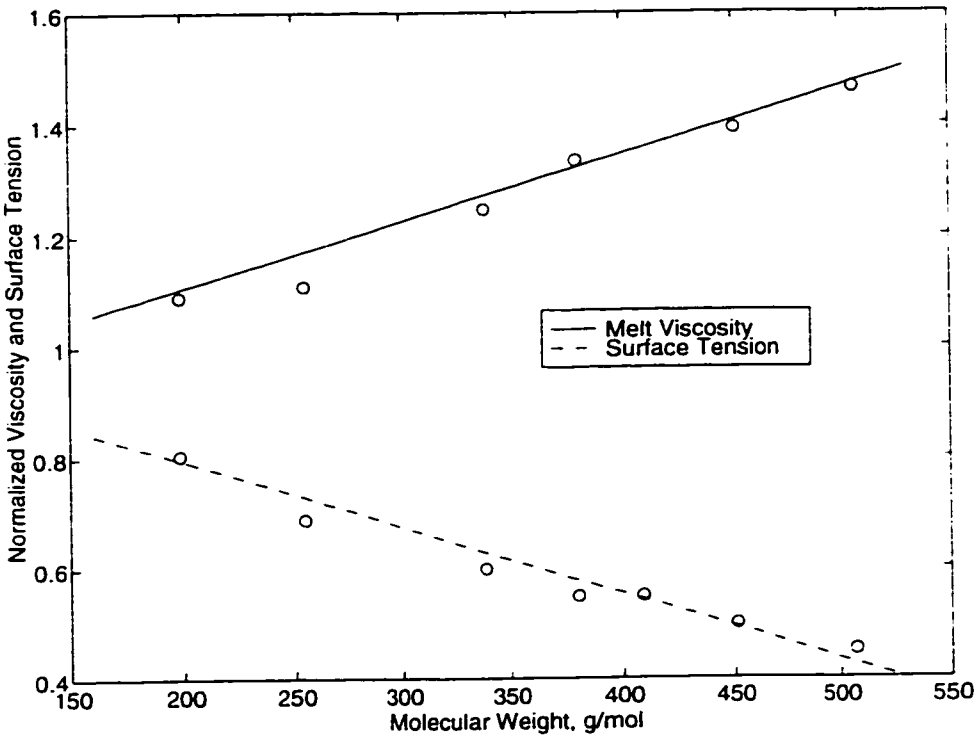

Figure 7.25. Viscosity and surface tension of the melt layer as a function of the molecular weight for various n-parraffins. The values of viscosity are evaluated at mean temperature between the melting and vaporization values and normalized with respect to the n-pentane viscosity. The surface tension values are evaluated at a temperature which is 80 % of the temperature difference between the melting and vaporization temperatures and normalized with respect to the pentane value.

It is interesting to note that high density polyethylene polymer is also a member of this linear molecule family in the very high molecular weight extreme (200,000 g/mole). The melt viscosity of the high density polyethylene is estimated at an average temperature between the melting point (135 °C) and the pyrolysis temperature (405 °C) with use of a technique presented in reference 86. Note that a simple extrapolation can not be used to determine the melt viscosity of these liquids with large molecules since above a critical value of the molecular weight the linear variation of viscosity with the molecular weight does not hold. The estimated viscosity value is 20 Pa sec which is 4 orders of magnitude larger than the melt viscosity of paraffin wax or the pentane liquid. This explains the low regression rates (no entrainment mass transfer) observed for melting polymeric propellants such as high density polyethylene.

We, now concentrate our investigations on a specific high melting point (67 °C) paraffin wax. The estimated material properties of such a wax (with an approximate average carbon number of 31) are also shown in table F.1 of appendix F. For these material properties it is found that wax forms a liquid layer with a comparable thickness

with the pentane film. The entrainment onset boundary for wax is determined to be below n-pentane's boundary which indicates that wax is likely to entrain droplets into the gas stream. Finally figure 7.26 shows the amount of entrainment calculated with use of Gater's empirical relation as a function of the mass flux for wax and pentane. It is clear that wax entrainment levels is even higher than the pentane entrainment mass transfer rates. All these results indicate that the paraffin wax will possibly burn several times faster than the conventional hybrid propellants.

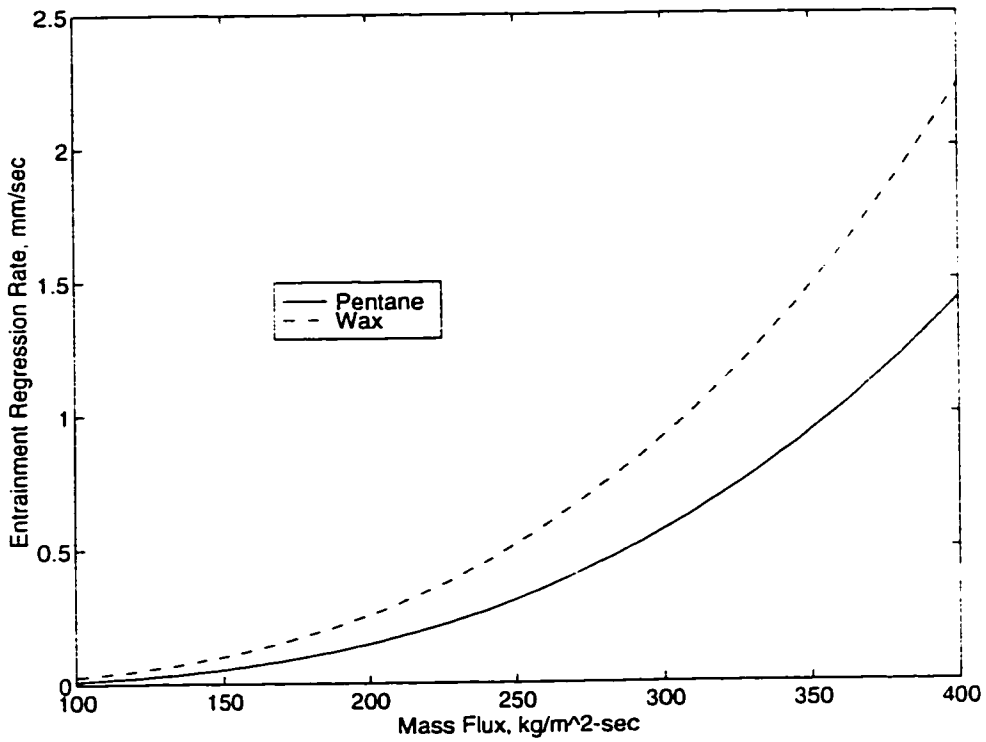

Figure 7.26. Entrainment regression rate as function port mass flux for paraffin wax and n-pentane.

It is essential to emphasize that some materials such as carbon black must be added to the paraffin waxes to improve the radiative absoptivity of the propellant. This is important since paraffin wax by itself may be heated in bulk by the penetration of radiation from the flame zone resulting in uncontrolled burning and possible sloughing of the propellant. It may also be desirable to mix the paraffin wax with polyethylene waxes (which typically have higher melting temperatures and also higher melt viscosities) at various concentrations to tailor the regression rate for a specific mission or to enhance the mechanical properties and the thermal stability of the propellant.

7.5 Conclusions for Liquid Layer Hybrid Combustion Theory

In this chapter the hybrid diffusion limited theory is generalized to hybrid fuels that burn by forming a liquid layer. In the first step of our development, we determined the conditions required to form a significant melt layer thickness on the fuel grain. It is shown that the melt layer thickness can be reasonably large for typical cryogenic hybrid operating conditions. Next we found that these thin films with strong blowing can be unstable under hybrid operating conditions. It is reported in the literature that the instabilities result in the entrainment of droplets into the gas stream. The extra mass transfer mechanism can potentially increase the regression rates an order of magnitude larger than the estimated rates from the classical theory. This is mainly due to the reduced "effective" heat of gasification, elevated gas mass flux in the chamber and decreased blocking factor in the hybrid boundary layer.

The cryogenic hybrid rocket tests performed in Edwards Airforce Base revealed regression rates 2-5 times larger than the expected rates estimated from the classical theory for low viscosity propellants such as pentane. The extended theory successfully predicts these very high regression rates observed in the cryogenic tests. The liquid layer theory can also predict the slow burning of the high viscosity propellants.

Eventually, the liquid layer hybrid combustion theory is applied to non-cryogenic materials which form a melt layer on their burning surface. The early findings indicate that paraffin wax which is a liquefying non-cryogenic material is a promising fast burning propellant. It is predicted that the WAX/LOX combination would play a significant role in the development of the next generation high performance hybrid propulsion systems.

Chapter 8

Summary and Conclusions

In this thesis two distinct aspects of hybrid rockets are studied. In chapters 3, 4, 5 and 6 the transients in hybrids are investigated and a dynamic model of the motor is developed. In chapter 7 the steady-state regression rate behavior of hybrid fuels that burn by forming a liquid layer is modeled. We will summarize the development and the important findings of each of these topics in the following paragraphs.

8.1. Transient Hybrid Model

Although the dynamic behavior of liquid and solid rocket systems have been studied extensively, the understanding of transient hybrid phenomena is not adequate. As a result, various transient phenomena occurring in the motor such as the low frequency instabilities remains unexplained. There have been some attempts to adopt the solid rocket instability concepts to hybrid rockets. However we strongly believe that this is not a reliable procedure, since the internal ballistics of the hybrid rocket is significantly different from that of other chemical systems. For that reason, in this study we investigated the dynamic phenomena occurring in hybrid rockets. We started with identifying and isolating the subsystems of the motor. This simplification is required due to the complex nature of the overall problem. We specifically focused on the thermal lags in the solid, hybrid boundary layer combustion and gasdynamics, since we think that these are the essential subsystems to capture the most fundamental aspects of hybrid rocket dynamics.

We started with the thermal lags in the solid which is relatively easy to handle. We considered the fuel as a slab in the planar geometry and assumed that the thermal thickness is much larger than the thickness of the reaction zone in the solid, but much smaller than the fuel web thickness. Our model uses the wall heat flux variation as the input and yields the time history of the regression rate. The problem is formulated mathematically as a nonlinear

moving boundary problem with no closed form solutions to our knowledge. Thus, we obtained perturbation solutions (and a linear transfer function) and also performed numerical simulations on the system. Various transients events are simulated by applying appropriate wall heat flux variations.

The throttling simulations are performed by increasing the wall heat flux from one value to another in a time period that determines the throttling rate. It is observed that the regression rate response first overshoots its target value in a rather short time and relaxes back to it asymptotically over the thermal relaxation time scale. This phenomenon suggested that there might be a secondary time scale for the thermal lag problem other than the well known thermal lag time. We claim that this time scale resembles the response of the thermal profile close to the surface and thus it is closely related to the surface phenomena modeled by the Arrhenius expression. It is determined that as the activation energy (which represents the sensitivity of the regression rate on the surface temperature) increases the surface time scale decreases and the overshooting becomes more dominant. In the extreme case of the infinite surface temperature (the constant wall temperature model) overshooting is most apparent. Whereas for very small activation energies the thermal lag model behaves as a first order system and the regression rate does not overshoot.

During a finite rate throttling the regression rate anticipates the heat loading over a large extent of the transient. However, we note that for every throttling rate there exists a finite time range right after the start of the transient for which the regression rate lags the heat input. We consider the thrust termination event as a special case of the throttling. Thus the anticipation of regression rate for the thrust termination case explains the well known phenomenon called $\dot{P}$ extinguishment in solid rocket motors.

The perturbation solutions and also the numerical simulations are used to determine the frequency response of the thermal lag system. It is found that there are phase lead and amplification domains for small frequencies in the frequency response of the regression rate. The increase in the activation energy increases the extent and strength of the amplification and the phase lead. Thus it is apparent that the phase lead and amplification are also related to the surface time scale. We note that the maximum value of the amplitude of the response is typically 30% higher than the quasi-steady value. Therefore, it can be stated that thermal lag system is stable and it does not possess any resonance behavior in the frequency domain. The phase lead generated by the thermal lag system is an essential component of the solid rocket L^* instability. However we claim that it is unlikely for an

hybrid system to possess an L^* type of an instability, since in hybrids the combustion and the chamber gasdynamics are not significantly coupled through the chamber pressure. Numerical simulations on the frequency response also showed some DC shift of the regression rate which is a phenomenon commonly observed in hybrids during unstable operation.

The transient gas phase problem that involves a turbulent boundary layer with combustion and strong blowing of the fuel from the surface is extremely complicated in nature. As a simplification, we first assumed quasi-steady gas phase response. Even in the quasi-steady gas phase case when the transients in the solid are considered, the classical diffusion limited theory can not be applied directly to obtain the law for the regression rate in terms of the mass flux in the port. The modification of the theory yields two distinct blowing parameters, the aerodynamic and the thermodynamic parameters. The final result for the analysis shows that during a transient the surface heat transfer explicitly depends on both the regression rate and also the local mass flux in the port. Note that the regression rate dependence originates from the blocking of the convective heat transfer by the normal injection of the fuel into the boundary layer flow.

It is expected that the relatively thick boundary layer developed on the fuel surface requires a significant time to adapt to the changes in the free stream conditions during a transient. For that reason, we investigated the literature on the dynamic response of the incompressible turbulent boundary layers with no blowing in the literature. We found that the scaling for the characteristic response time is proportional to the axial location from the starting point of the boundary layer and inversely proportional to the free stream velocity. We assumed that this scaling is also valid for the hydrodynamic and the thermal boundary layers developed in the hybrid rockets. We introduced two boundary layer delays: 1) the delay between the heat flux and the mass flux and 2) the delay between the wall heat flux and the regression rate.

The thermal lag model is coupled with the combustion model to obtain the TC coupled system. The dependence of the regression rate on the wall heat flux through the energy considerations in the thermal lag model and the dependence of the wall heat flux on the regression rate through the blocking effect in the combustion model are the core aspects of the TC coupling. The TC coupled system without the boundary layer delays is determined to be stable with no poles in the s plane. It is found that TC coupled system with delays between the wall heat flux and regression rate generates a row of unstable

poles. The frequency of the fundamental mode (the smallest frequency pole) is determined to fall in the region of the observed low frequency oscillations of hybrids. It is found that the delay between the wall heat flux and the mass flux does not affect the stability nature of the TC coupled system, since it only appears in the numerator of the transfer function.

The oscillation frequencies obtained from the TC coupled system with the boundary layer scaling, $\tau_{bl} = L/\bar{u}_e$, is compared with the test records of AMROC motors at various sizes. The estimated frequencies on the size effect are in reasonably good agreement with the measured frequencies. The model is also tested for the pressure and mass flux effect on the oscillation frequency by comparing the predictions with the JIRAD test results. The model is consistent with available tests in capturing the trend for pressure and mass flux effect and in predicting a band of frequencies not a single oscillation frequency.

The last subsystem investigated in this thesis is the chamber gasdynamics. The isothermal 2V-port model for the chamber gasdynamics which threats the port flow as a quasi 1D pipe and pre and post-combustion chambers as zero dimensional volume elements is developed. Both perturbation solutions and numerical simulations for the model are obtained. The simulations and perturbations solutions are proved to be in good agreement for the types of transient events considered.

The 2V-port model when it is coupled with the quasi-steady combustion dynamics and corrected for the isothermal assumption predicts the acoustic frequencies for the motor cavity within the observed range for the AMROC tests. The gasdynamic system with quasi-steady combustion is found to be stable, namely all the poles of the system have negative real components. It is also observed in the simulations that when the gasdynamic system is perturbed by some nonlinear disturbance, the acoustic modes of the chamber become activated. This ringing phenomenon is a plausible explanation for the coexistence of the acoustic modes with the low frequency oscillations commonly observed in hybrid tests.

Eventually, the TC coupled system is integrated with the gasdynamic model to obtain the overall system response (TCG coupled system). Each of the unstable poles of the TC coupled system are splitted by the gasdynamics in a small domain in the s plane. This reinforces the erratic behavior of the low frequency oscillations predicted by our model. In short, the overall system estimates the range and the scaling of the frequency of the oscillations with the size, pressure and mass flux reasonably well. However our linear

model predicts an indefinite growth of these pressure oscillations, contradicting the finite amplitude oscillations detected in the tests.

8.2. Liquid Layer Hybrid Combustion Model

In chapter 7, the classical diffusion limited theory is extended to the hybrid fuels that burn by forming a liquid layer. The most important application of this new theory is for the cryogenic hybrids which possess much larger regression rates than the rates predicted by the classical theory.

The development is performed in three stages. In the first stage the thickness of the melt layer that forms on the hybrid fuel surface during typical operating conditions is determined. It is found that for relatively transparent liquids, the radiative heat transfer significantly increases the thickness of the film.

In the second stage the stability of the liquid layer formed on the fuel surface under strong blowing and subject to large shear forces is investigated. An Orr-Sommerfeld equation for the linear stability of the liquid gas interface is derived and an exact solution is found for a linear base velocity profile. The exact solution for the liquid phase is coupled to the linearized gas phase response with appropriate boundary conditions at the interface to give an eigenvalue problem for the linear stability of the layer. The results for liquid layer Reynolds numbers of practical interest (50-300) show the existence of a range of unstable wave numbers. It is observed that both the most amplified wave number and the maximum amplification increases with the Reynolds number. The linear stability results and various empirical relations from the literature are used to determine a scaling law for the entrainment mass transfer from the liquid surface into the gas phase.

In the last stage the classical theory is adapted for the possibility of entrainment mass transfer from the surface. It is found that the existence of the entrainment transfer enhances the regression rates significantly. This is due to several factors: 1) reduced thermal energy requirement at the surface, 2) reduced blocking factor in the case of two phase flow, 3) increased convective heat transfer due to increased averaged mass flux in the port, 4) increased evaporation due to increased surface roughness. It can be stated that the agreement between the experimental regression rates and the theory predictions is reasonably good.

Finally the liquid hybrid combustion theory is applied to the liquefying non-cryogenic materials. The theory revealed that that paraffin wax blended with carbon black and polyethylene wax would be a controllable and fast burning hybrid fuel. We claim that the WAX/LOX combination would play a significant role in the development of next generation high performance hybrid propulsion systems.

8.3. Future Work

The model developed for the rocket dynamics yields a plausible mechanism for the generation of the low frequency instabilities. However it fails to explain the mechanism that limits their indefinite growth. In our opinion a nonlinear gasdynamic model that resolves the effect of the O/F shift in the motor is essential for a more realistic formulation. The O/F shift with other damping mechanisms would potentially limit the growth of the amplitude of pressure oscillations generated by the linear TCG coupled system.

Our delayed quasi-steady combustion model is a crude representation of the dynamics of the hybrid diffusion flame. This aspect of the theory needs the to be addressed more carefully. The major difficulties are, of course, the turbulent nature of the boundary layer and the existence of strong blowing and combustion in the transient flow field.

The theories developed in this thesis must be tested and improved by the guidance of direct experimental studies. Although there exists a set of experimental data on various size motors operating in a range of conditions, these test data, in general, are not specifically aimed to serve to improve the understanding of the transient operation of hybrids. In order to perform specific transient experiments, we started an experimental phase for our transient research. The design, fabrication and test firings of a 3 1/4 inch outer diameter lab scale hybrid motor is completed. However due to the lack of funding, the experimental phase of the program could not be completed. The details of the set up is discussed in appendix I. We conclude by stating that the experimental input is essential for direct verification and further development of the dynamic theory introduced in this thesis.

For the future development of cryogenic hybrids we think that an improved estimation procedure or direct measurement of the time dependent regression rate is beneficial. The application of the current theory for other fuel types is another aspect that requires further attention. The current state of the liquid layer hybrid theory is open for

further improvement in many respects. An important example is the determination of a more reliable scaling law for the entrainment mass transfer for the conditions present in hybrid applications. Finally it is desirable to perform some WAX/GOX tests and compare the observed regression rates with the liquid layer hybrid combustion theory predictions.

Appendix A

Momentum Integral Equation

In this appendix we will derive the momentum integral expression for the variation of the boundary layer thickness along the axial direction. The treatment is for a constant density boundary layer with self-similar velocity profiles. The latter condition requires that the similarity parameter, B does not change significantly along the axial direction. Note that for hybrid operating conditions this is a valid approximation.

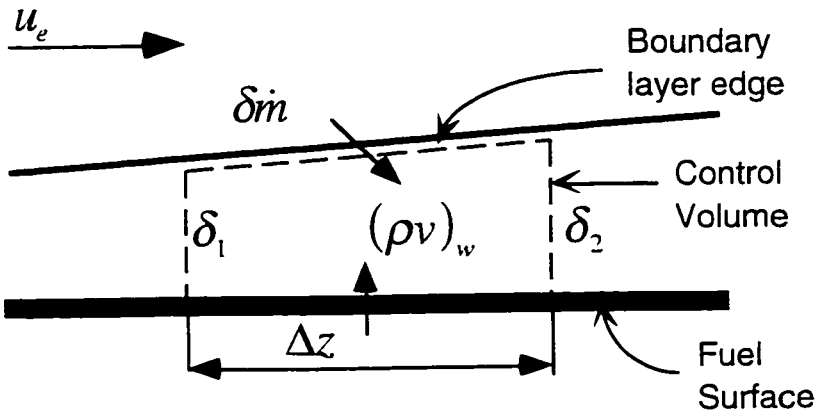

Figure A.1. Schematic of the control volume used in the momentum integral formulation.

The conservation of mass for a control volume shown in figure A.1 requires

$$\delta\dot{m} + \int_0^{\delta_1} \rho u_1 dy - \int_0^{\delta_2} \rho u_2 dy + (\rho v)_w \Delta z = 0.$$

This expression can be written in terms of nondimensional parameters as follows:

$$\frac{\delta\dot{m}}{\Delta z \rho u_e} = \frac{\delta_2 - \delta_1}{\Delta z}\int_0^1 \phi d\eta - B\frac{c_f}{2}. \qquad \text{(A.1)}$$

The conservation of momentum in the axial direction for the control volume is

$$u_e\delta\dot{m} + \int_0^{\delta_1} \rho u_1^2 dy - \int_0^{\delta_2} \rho u_2^2 dy + \tau_w \Delta z = 0.$$

Conservation of momentum in the nondimensional format reduces to

$$\frac{\delta\dot{m}}{\Delta z \rho u_e} = \frac{\delta_2 - \delta_1}{\Delta z}\int_0^1 \phi^2 d\eta + \frac{c_f}{2}. \qquad \text{(A.2)}$$

Equations A.1 and A.2 can be combined to give

$$\frac{\delta_2 - \delta_1}{\Delta z} = \frac{1 + B}{\int_0^1 \phi(1-\phi)d\eta}\frac{c_f}{2}.$$

In the limit of $\Delta z \to 0$ we obtain equation 2.33

$$\frac{d\delta}{dz} = \frac{1 + B}{I}\frac{c_f}{2} \qquad \text{where} \qquad I = \int_0^1 \phi(1-\phi)d\eta.$$

Appendix B

Reaction Layer Thickness

The thickness of the fuel layer in which the depolymerization reactions and the phase changes takes place will be estimated for the justification of the assumption used in our thermal lag model.

We assume a first order reaction mechanism for the surface phenomena.

$$P(s) \overset{k(T)}{\Rightarrow} M(g) \tag{B.1}$$

Here $P(s)$ is the solid phase polymer at ambient temperature. $M(g)$ is the gaseous phase depolymerization products at the surface temperature and $k(T)$ is the reaction rate for the surface phenomena. In our model we assumed an Arrhenius form for the gas generation rate.

$$k(T) = ae^{-E_a/RT} \tag{B.2}$$

We will use the Arrhenius expression and the steady-state temperature profile to make a rough estimate for the reaction thickness.

The slope of the rate at the surface can be written as

$$\left.\frac{dk}{dx}\right|_{\tau=0} = ae^{-E_a/RT_s}\frac{E_a}{RT_s^2}\left.\frac{dT}{dx}\right|_{\tau=0} = k|_{\tau=0}\frac{E_a}{RT_s^2}\left(-\frac{T_s - T_a}{\delta_T}\right) \tag{B.3}$$

Note that $dk/dx|_{\tau=0} \approx \Delta k/\delta_r$ where δ_r is the thickness of the reaction layer and is Δk a characteristic variation of k over δ_r. This expression can be combined with equation B.3 to yield

$$\left|\frac{\Delta k}{k|_{\tau=0}}\right| \approx \left|\frac{\Delta T}{T|_{\tau=0}}\right| \frac{E_a}{RT_s} \frac{\delta_r}{\delta_T}. \tag{B.4}$$

Assuming that both $\left|\Delta k/k|_{\tau=0}\right|$ and $\left|\Delta T/T|_{\tau=0}\right|$ are of order one. we obtain the following order of magnitude estimate for the reaction thickness.

$$\frac{\delta_r}{\delta_T} \approx \frac{1}{E_a/RT_s}. \tag{B.5}$$

For typical values of $E_a = 30$ kcal/mole and $T_s = 800$ K. one finds the reaction thickness approximately 5% of the thermal thickness. Thus for activation energies typically encountered in hybrid applications the reaction thickness is negligible compared to the thermal thickness in the solid.

Appendix C

Second Order Perturbation Solution for the Thermal Lag System

In this appendix we will discuss the derivation of the second order transfer function of the thermal lag system. The second order perturbation equations are already presented in section 4.2.3 of the main text. We start by taking the Laplace transforms of the second order equations 4.34, 4.35, 4.36 4.37 and 4.38 with respect to time. After simple rearrangements the transformed field equation can be written as follows:

$$s\theta_2 = \frac{d^2\theta_2}{dx^2} + \frac{d\theta_2}{dx} - \left(E_{E_1}\theta_2(s,0) + \beta f_3(s) - f_2(s)\right)e^{-x} + f_1(s)e^{-f_4(s)x}. \qquad (C.1)$$

Here θ_2 is the Laplace transform of the second temperature perturbation, $\bar{T}_2$ and the introduced functions of the transform variable are defined as

$$f_1(s) = F_1(s)Q_L^2(s) = -\frac{2E_{E_2}s\left(1+\sqrt{1+4s}\right)\left(s+E_{E_2}\right)Q_L^2(s)}{\left[\left(1+\sqrt{1+4s}\right)\left(s+E_{E_2}\right) - 2E_{E_2} + 2E_L E_{E_2}s\right]^2}$$

$$f_2(s) = F_2(s)Q_L^2(s) = \frac{4E_{E_2}^2 sQ_L^2(s)}{\left[\left(1+\sqrt{1+4s}\right)\left(s+E_{E_2}\right) - 2E_{E_2} + 2E_L E_{E_2}s\right]^2}$$

$$f_3(s) = F_3(s)Q_L^2(s) = \frac{4s^2Q_L^2(s)}{\left[\left(1+\sqrt{1+4s}\right)\left(s+E_{E_2}\right) - 2E_{E_2} + 2E_L E_{E_2}s\right]^2}$$

$$f_4(s) = \frac{1+\sqrt{1+4s}}{2}.$$

Note that the convolution theorem is used to determine the Laplace transforms of the cross terms $R_1 \partial \overline{T}_1/\partial x$ and $\overline{T}_1^2\big|_{\tau=0}$ that appear in the second order equations.

The homogeneous solution for the linear ordinary differential equation C.1 which satisfies the boundary condition 4.36 can simply be found as

$$\theta_{2h}(s,x) = Ce^{-f_4(s)x}$$

where C is the integration constant. We assume the following form for the particular solution:

$$\theta_{2p}(s,x) = De^{-\tau} + Fxe^{-f_4(s)x}.$$

The total solution can now be written as a sum of the homogeneous and particular solutions.

$$\theta_2(s,x) = \left[C - \frac{f_1(s)x}{1-2f_4(s)}\right]e^{-f_4(s)x} - \left[\frac{\left(\beta f_3(s) - f_2(s) + E_{E_1}C\right)\left(1-2f_4(s)\right)}{\left(1-2f_4(s)\right)\left(s+E_{E_1}\right)}\right]e^{-\tau} \qquad (C.2)$$

Note that the unknown constants D and F are determined upon substitution of the assumed form ($\theta_{2h} + \theta_{2p}$) in equation C.1.

The transform of the surface boundary condition, equation 4.35, takes the form

$$R_{2L}(s) = \frac{1}{E_L}\frac{\partial \theta_2}{\partial x}\bigg|_{\tau=0} \qquad (C.3)$$

where R_{2L} is the transform of the second order regression rate perturbation which can also be written as

$$R_{2L}(s) = E_{E_0}\theta_2(s,0) + \beta f_3(s). \qquad (C.4)$$

Equations C.2, C.3 and C.4 can be combined to obtain the remaining unknown coefficient, C.

$$C = \frac{\left(E_L E_{E_1} + 1\right)\left(\beta f_3(s) - f_2(s) + s f_1(s)\right)}{\left(E_L E_{E_1} - 2E_{E_1} + f_4(s)\right)\left(1 - 2f_4(s)\right)}$$

This expression with equations C.2 and C.3 yield the transfer function for the second order perturbation of the regression rate which assumes the first order perturbation of the wall heat flux as the input.

$$\frac{R_{2L}}{Q_L^2} = \frac{\left[\left(\beta F_3(s) - F_2(s)\right)\left(1 - 2f_4(s)\right) + sF_1(s)\right]\left(\left(E_L E_{E_1} - 2E_{E_1} + f_4(s)\right)\right)}{\left(E_L E_{E_1} - 2E_{E_1} + f_4(s)\right)\left(1 - 2f_4(s)\right)\left(s + E_{E_1}\right)} +$$

$$+ \frac{\left(E_L E_{E_1} + 1\right)\left(\beta F_3(s) - F_2(s) + sF_1(s)\right)\left[E_{E_2} - f_4(s)\left(s + E_{E_1}\right)\right]}{\left(E_L E_{E_1} - 2E_{E_1} + f_4(s)\right)\left(1 - 2f_4(s)\right)\left(s + E_{E_1}\right)} \qquad \text{(C.5)}$$

This transfer function is used to investigate the second order frequency response of the regression rate to the oscillations of wall heat flux. The result is plotted in figure C.1 for HTPB material at three different activation energy levels. The figure indicates that, as the oscillation frequency increases the second order perturbation of regression rate also increases. Note also that the second order perturbation is always positive, namely any wall heat flux oscillation generates a positive DC shift in the regression rate response. These observations are consistent with the simulation results which were discussed in the main text. The DC shift is more pronounced at high activation energies. It is interesting to note that the second order response asymptotes to a finite value at infinite frequency. Specifically, in the limit, $f \to \infty$, equation C.5 simplifies to

$$\frac{R_{2L}}{Q_L^2} = \frac{\left(E_L E_{E_2} + 1\right)E_{E_2}}{2E_L}.$$

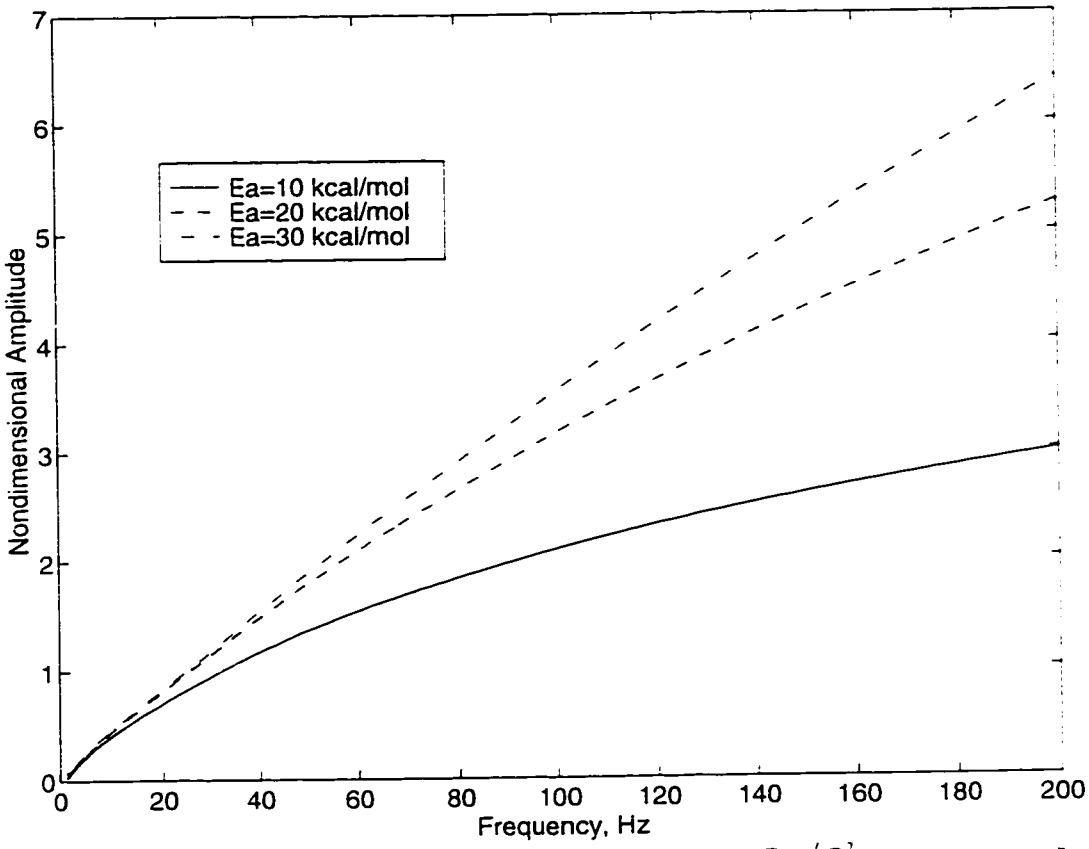

Figure C.1. The variation of the second order nondimensional response, R_{2L}/Q_L^2, with the heat flux oscillation frequency. The plots are for a HTPB system which is operating at conditions corresponding to a thermal lag time of 0.1186 seconds.

Appendix D

Inversion Integral

We are interested in determining the natural response of a system with a known transfer function which is not analytic in the s plane. In general, the time response of a system can be obtained by inverting its system transfer function back to the time domain with use of the Bramwich inversion integral [55, 57].

$$f(t) = \frac{1}{2\pi i} \int_{\gamma - i\infty}^{\gamma + i\infty} F(s) e^{st} ds \tag{D.1}$$

In this formula γ must be selected to keep all the poles of $F(s)$ on the left of the integration line.

The systems represented by a set of linear ordinary differential equations with constant coefficients have rational transfer functions that can be written as a ratio of two polynomials of s. In this case the inversion operation is simplified to the determination of the poles of the transfer function, which are the roots of the characteristic equation with use of the Residue Theorem. It is a well known result in control theory that the natural response of such a system can easily be expressed as a linear combination of the exponential functions of the poles multiplied by time [56]. However for systems that are formulated by linear partial differential equations or for systems represented by ordinary differential equations with some retarded dependent variables, the system transfer function, in general, can also possess fractional powers, elementary functions and even special functions of s. For that general case the poles of the system are still the roots of the denominator of the transfer function. But in general, those roots are not adequate to give the full natural behavior of the system. This is due to the possibility of an other type of singularities of the transfer function in the s plane, which are named as the branch points. In fact, the existence of the branch points may alter the nature of the response significantly. Those points are characterized with the fact that around any contour enclosing its branch point the complex

function will be multivalued. The most common type of functions with branch points are the ones possessing the fractional powers of s. Any complex function with a branch point will not be meromorphic and thus the Cauchy integral theorem can not be used over the entire domain even though the poles are isolated. A commonly used technique to deal with this difficulty is to make a mandatory branch cut in the s domain that makes the function single valued everywhere in the new domain.

We will now apply those arguments to our specific case. The linear TC coupled system has a transfer function given by equation 5.25. It can be shown that this transfer function has an infinite number of poles, all with the same real part, for non zero boundary layer delays. It is also essential to determine the order of those poles since, the expansion theorem gives different time responses for different orders. The order can be found by investigating the behavior of the characteristic equation by expanding it around a pole. Let's assume that s_o is a pole of the system, namely it solves the characteristic equation. We can define a local coordinate z in the neighborhood of that pole as $z = s - s_o$ where $z << s_o$. After performing the series expansions of the square root and the exponential functions and keeping only the second order terms, we can simplify the characteristic equation to the following quadratic expression

$$CE = a''z^2 + b''z + O(z^3)$$

where a'' and b'' are

$$a'' = \frac{2}{\sqrt{1+4s_o}} - 2E_{E_a}\sigma_1\bar{\tau}_{bl2}e^{-\bar{\tau}_{bl2}s_o}$$

$$b'' = 1 + \sqrt{1+4s_o} + \frac{2s_o}{\sqrt{1+4s_o}} + 2E_{E_a}\left[E_L + \sigma_1 e^{-\bar{\tau}_{bl2}s_o}(1 - s_o\bar{\tau}_{bl2})\right].$$

The roots of the expanded characteristic equation are $z_1 = s - s_o = 0$ and $z_2 = s_2 - s_o = -b''/a''$. Thus it is obvious that unless $b'' = 0$, s_o is a simple pole.

Due to the square root term, our transfer function has a branch point at $s = -1/4$. The inversion integral has to be evaluated with care. In order to generate a domain that our transfer function is meromorphic, we make a branch cut from $s = -1/4$ to minus infinity on

the real axis as indicated in figure D.1. We select the contour C as shown in figure D.1 which isolates the poles and also the branch point. In the domain enclosed by C, the transfer function is analytic since all the singularities are excluded and the Cauchy integral theorem can be applied, namely

$$\oint_C F(s)e^{st}ds = 0. \tag{D.2}$$

This contour integral can be divided into subsections as

$$\oint_C F(s)e^{st}ds = \int_{\gamma-i\infty}^{\gamma+i\infty} F(s)e^{st}ds - \sum_{n=1}^{N}\left[\oint_{C_n} F(s)e^{st}ds\right] + \oint_{BDE} F(s)e^{st}ds = 0. \tag{D.3}$$

Here N is the total number of poles (in our case $N \to \infty$). Note that in equation D.3 the contributions of the integrals along the paths AB and EF do not appear. This is due to Jordan's lemma which can be applied in our case since $\left|F\left(re^{i\theta}\right)\right|$ approaches to zero uniformly as $r \to \infty$ within the range of $-\pi/2 < \theta < \pi/2$ for $t > 0$. Unlike a pole cut, the function can be discontinuous across a branch cut and the cancellation of the two legs of the cut for the contour integral does not hold. For that reason a branch cut integral has to be performed over the entire path (i.e. in this case contour BDE). With use of the expansion theorem the second term, which is the sum of the contour integrals around the simple poles can be simplified to

$$\sum_{n=1}^{N}\left[\oint_{C_n} F(s)e^{st}ds\right] = 2\pi i\sum_{n=1}^{N}\frac{M(s_n)}{N'(s_n)}e^{s_n t} \tag{D.4}$$

Combining equations D.3 and D.4 with the definition of Bramwich integral yields the following time response for the system.

$$f(t) = \sum_{n=1}^{N}\frac{M(s_n)}{N'(s_n)}e^{s_n t} - \frac{1}{2\pi i}\oint_{BDE} F(s)e^{st}ds \tag{D.5}$$

This result states that the total natural response of the system is a combination of the well known response due to the poles of the system and a second term that reflects the

effect of the branch point. As expected for a linear system the response due to each singularity in the s plane is decoupled from the others.

A conclusion on the stability of the system can be drawn easily from that result (i.e. equation D.5). The sufficient condition for the system to be unstable is satisfied if the system has at least one of its poles in the positive right half plane. However the reverse statement is not valid, in general. For the system to be stable it is not sufficient to have all of its poles in the left halfplane, but also the contour integral has to be bounded as time asymptotes to infinity. In our case, it can be proved that the contour integral diminishes as t tends to infinity. The integration path is confined to the left halfplane and Real(s) is always negative. Thus the integrand tends to zero as $t \rightarrow \infty$ due to the exponential term (note that $F(s)$ is bounded along the integration path) and so does the integral.

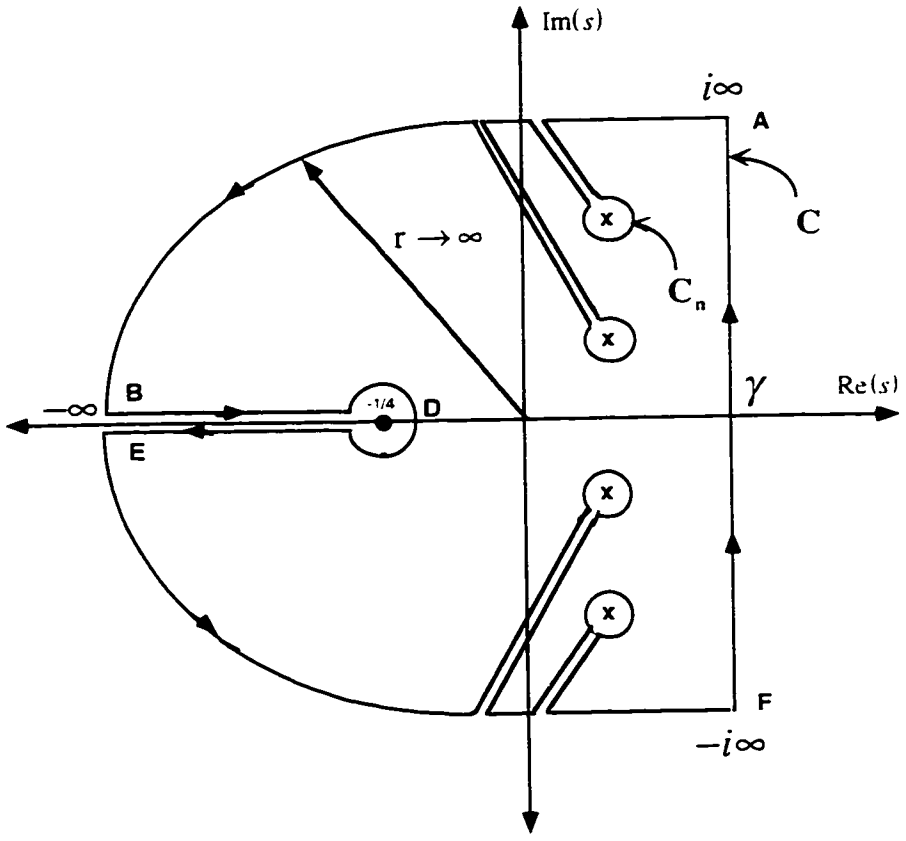

Figure D.1. Integration contour used to evaluate the inversion integral.

Appendix E

Numerical Simulations for Gasdynamic System

In this appendix we will present the numerical approach taken for the simulation of the gasdynamic system discussed in Chapter 6. The gasdynamic equations are first nondimensionalized with use of the steady-state reference operating point. $\{\overline{P}_1, \overline{P}_2, \overline{G}_a, \overline{G}_b, \overline{\rho}_a, \overline{\rho}_b\}$. For convenience the characteristic time is defined as

$$\tau_c = \frac{\overline{\rho}_a}{\rho_f} \frac{A_p/C}{a\overline{G}_a^n} \frac{1}{O/F}$$

where the motor O/F ratio is

$$\frac{O}{F} = \left(\frac{A_p}{CL}\right) \frac{1}{\rho_f a \overline{G}_a^{n-1}}.$$

The nondimensional variables are written as follows:

$$\tilde{t} = t/\tau_c \qquad \tilde{x} = x/L \qquad \tilde{\rho} = \rho/\overline{\rho}_a \qquad \tilde{G} = G/\overline{G}_a$$
$$\tilde{P}_1 = P_1/\overline{P}_1 \qquad \tilde{P}_2 = P_2/\overline{P}_1 \qquad \tilde{\dot{m}}_f = \dot{m}_f A_p/\rho_f a \overline{G}_a^n C.$$

The equations in the nondimensional form become:

$$\frac{d\tilde{P}_1}{d\tilde{t}} = a\left(\tilde{\dot{m}}_o - \tilde{G}_a\right) \tag{E.1}$$

$$\frac{d\tilde{P}_2}{d\tilde{t}} = -b_1\tilde{\rho}_b + b_2\tilde{G}_b \tag{E.2}$$

$$\frac{\partial \tilde{\rho}}{\partial \tilde{t}} = -\frac{\partial \tilde{G}}{\partial \tilde{x}} + \frac{\tilde{\dot{m}}_f}{O/F} \tag{E.3}$$

$$\frac{\partial \tilde{G}}{\partial \tilde{t}} = -\frac{\partial\left(\tilde{G}^2/\tilde{\rho}\right)}{\partial \tilde{x}} - \frac{1}{\gamma_1 \overline{M}_a^2}\frac{\partial \tilde{P}}{\partial \tilde{x}} - \left(\frac{\overline{C}_f}{2}\right)\frac{\tilde{G}^2}{\tilde{\rho}} \tag{E.4}$$

$$\tilde{P} = \tilde{\rho}\,\tilde{R}\tilde{T} \qquad \tilde{R}\tilde{T} = 1 + (R_{RT} - 1)\tilde{x}. \tag{E.5}$$

The coefficients are defined as

$$\overline{M}_a = \frac{\overline{G}_a/\overline{\rho}_a}{\sqrt{\gamma_1 (RT)_1}} \qquad \tilde{C}_f = \left(\frac{CL}{A_p}\right)C_f \qquad a = n_p \frac{L}{L_1}$$

$$b_1 = \sqrt{R_{RT}}\,\frac{L}{L_2}\frac{\theta\Gamma_c\sqrt{f_b}}{\sqrt{\gamma_1}\overline{M}_a} \qquad b_2 = R_{RT}\frac{L}{L_2}.$$

We use a finite difference technique for the solution of the nondimensional set of equations given by expressions E.1 to E.5 . Since the axial variations of the flow variables in the motor are expected to be uniform, a constant mesh spacing is selected. Specifically, for N+2 mesh points the mesh spacing becomes $\Delta\tilde{x} = 1/(N+1)$. A second order central finite difference scheme is used to reduce the conservation of mass (E.3) and conservation of momentum equations (E.4) to the following semi discrete form:

$$\frac{d\vec{\rho}}{d\tilde{t}} = F_\rho\left(\vec{G}, \vec{\rho}\right) + \tilde{\dot{m}}_a \vec{I} \tag{E.6}$$

$$\frac{d\vec{G}}{d\tilde{t}} = F_G\left(\vec{G}, \vec{\rho}\right). \tag{E.7}$$

Here the state vectors and the input vector are defined as

$$\vec{\rho} = \left[\rho_a \quad \rho_1 \quad \ldots \quad \rho_{N+1} \quad \rho_b\right]^T \qquad \vec{G} = \left[G_a \quad G_1 \quad \ldots \quad G_{N+1} \quad G_b\right]^T$$

$$\vec{I} = \left[a \quad 0 \quad \ldots \quad 0 \quad 0\right]^T.$$

The functions are given as

$$F_\rho\left(\vec{G},\vec{\rho}\right) = -\vec{\vec{A}}_G\,\vec{G} + \frac{1}{O/F}\vec{\dot{m}}_f - \vec{f}\tilde{\rho}_b \tag{E.8}$$

$$F_G\left(\vec{G},\vec{\rho}\right) = -\vec{\vec{D}}_C\,\vec{C} - \left(\frac{\tilde{C}_f}{2}\right)\vec{q} \tag{E.9}$$

where the vectors appear in these equations are defined as

$$\vec{C} = \begin{bmatrix} \tilde{G}_a^2/\tilde{\rho}_a + \tilde{P}_a/\gamma_1\overline{M}_a^2 \\ \tilde{G}_1^2/\tilde{\rho}_1 + \tilde{P}_1/\gamma_1\overline{M}_a^2 \\ \cdot \\ \cdot \\ \cdot \\ \tilde{G}_{N-1}^2/\tilde{\rho}_{N-1} + \tilde{P}_{N-1}/\gamma_1\overline{M}_a^2 \\ \tilde{G}_b^2/\tilde{\rho}_b + \tilde{P}_b/\gamma_1\overline{M}_a^2 \end{bmatrix} \qquad \vec{q} = \begin{bmatrix} \tilde{G}_a^2/\tilde{\rho}_a \\ \tilde{G}_1^2/\tilde{\rho}_1 \\ \cdot \\ \cdot \\ \cdot \\ \tilde{G}_{N-1}^2/\tilde{\rho}_{N-1} \\ \tilde{G}_b^2/\tilde{\rho}_b \end{bmatrix} \qquad \vec{f} = \begin{bmatrix} 0 \\ 0 \\ \cdot \\ \cdot \\ \cdot \\ 0 \\ b_1 \end{bmatrix}.$$

Note that $\vec{\vec{A}}_G$ and $\vec{\vec{D}}_C$ are tridiagonal matrices with size of $N+2$ which can be shown in the following short notation:

$$\vec{\vec{A}}_G = \frac{1}{2\Delta x}B_3\left(\vec{d}_{A1},\vec{d}_{A2},\vec{d}_{A3}\right) \qquad \vec{\vec{D}}_C = \frac{1}{2\Delta x}\vec{\vec{B}}_3\left(\vec{d}_{D1},\vec{d}_{D2},\vec{d}_{D3}\right)$$

where the diagonal vectors are

$$\vec{d}_{A1} = [-1 \quad -1 \quad . \quad . \quad . \quad -1 \quad 0] \qquad \vec{d}_{A2} = [2\Delta x a \quad 0 \quad . \quad . \quad . \quad 0 \quad -2\Delta x b_2]$$
$$\vec{d}_{A3} = [0 \quad 1 \quad . \quad . \quad . \quad 1 \quad 1] \qquad \vec{d}_{D1} = [-1 \quad -1 \quad . \quad . \quad . \quad -1 \quad -2]$$
$$\vec{d}_{D2} = [-2 \quad 0 \quad . \quad . \quad . \quad 0 \quad 2] \qquad \vec{d}_{D3} = [2 \quad 1 \quad . \quad . \quad . \quad 1 \quad 1].$$

Furthermore, note that $\vec{\dot{m}}_f$ is the nondimensional fuel mass generation vector which, in general, needs to be dynamically modeled with use of local boundary layer combustion arguments (i.e. TC coupled system). However, for the purposes of this study

we restrict the gasdynamic simulations to the quasi-steady combustion case for which the fuel mass generation reduces to the simple algebraic expression, $\bar{\dot{m}}_f = \bar{G}^n$.

In general, equations E.6 and E.7 form a set of $2(N+2)$ nonlinear ordinary differential equations that needs to be solved with the initial conditions $\bar{\rho} = \bar{\rho}(0)$, $\bar{G} = \bar{G}(0)$ and a specified oxidizer mass flow schedule in time. We developed a simulation code that use the RK4 explicit time marching scheme to integrate these equations.

We first checked validity of the gasdynamic code by running a steady-state simulation for a duration of time (global error). The pre-combustion chamber pressure level showed a finite but negligible drop during the course of the run. The consistency of the code is also tested by changing the special resolution and time step size for the same simulation case. Neither of those had a significant effect on the solution for the typical numerical parameters used in the calculations. Below a certain value of the CFL numbers we have encountered some numerical instabilities which are explained by a linear stability investigation performed on the semi-discrete system. For most of the calculations we found it adequate to use 100 mesh points and a (nondimensional) time step size of $0.3\ 10^{-4}$.

Appendix F

Properties of Various Solid Cryogenic Propellants

The thermophysical properties of various cryogenic propellant materials and a parffin wax are shown in table F.1.

Solid Propellant	Pentane C_5H_{12}	HFI	Acetone C_3H_6O	Isopropanol C_3H_8O	2,2,5 tmh C_9H_2O	Oxygen O_2	Wax
Molecular Weight (g/mol)	72.15	69.11	58.08	60.10	128.26	32.0	432.8
Surface Tension (mN/m)	14.3	15.6	19.2	16.4	11.3	13.2	7.1
Viscosity (mPa/sec)	0.46	2.5	0.51	5.0	0.42	0.33	0.65
Density-liquid phase (kg/m^3)	688.4	785.0	835.2	808.9	719.8	1226.9	654.4
Melting Temperature (K)	143.3	181	178.45	183.3	167.4	54.4	339.6
Boiling Temperature (K)	309.6	350	329.44	355.4	397.2	90.2	727.4
Heat of Fusion (kJ/kg)	116.7	96.3	98.0	89.4	48.3	13.7	167.2
Heat of Vaporization (kJ/kg)	357.8	540.2	513.0	663.4	261.8	190.58	163.5
Thermal Conduction liquid (W/mK)	0.14	0.137	0.17	0.14	0.12	0.17	0.12
Specific Heat liquid (kJ/kg-K)	2.06	2.03	2.07	2.28	2.00	1.67	2.92
Specific Heat-solid (kJ/kg-K)	1.10	1.09	1.33	1.10	-	0.83	2.03

Table F.1. Material properties of various liquefying propellants [81]. Paraffin wax properties are estimated for the following composition of n-paraffins: 5 %, C24, 15 %, C27, 30 %, C29, 30% C32, 20 %, C36.

The viscosity, density, thermal conductivity and specific heat of the liquid phase are evaluated at the average temperature between the melting and boiling temperatures of the material, whereas the surface tension is evaluated at the boiling temperature. The solid phase properties listed in the table are at an average temperature between the initial

propellant temperature and the boiling temperature. For hydrocarbons and oxygen, the initial temperatures are assumed to be 77 K (liquid nitrogen temperature) and 4 K (liquid helium temperature), respectively. Heats of fusion, evaporation and the melting, boiling temperatures are measured at one atmosphere pressure.

All the materials considered, except HFI are pure substances. Whereas, HFI is a mixture of hydrocarbon liquids (60% isopropanol, 30% hexanes, 10% tetrahydrofuran). The material properties of HFI are estimated by assuming an excess mixture energy ($\Delta U''/kT$) of 1. For example the viscosity of the mixture is calculated according to the following formula [85]:

$$\mu_m = \left[x\mu_1 + (1-x)\mu_2\right]\left[1 - x(1-x)\Delta U''/kT\right].$$

Here, x represents the molar fraction of isopropanol in the mixture, μ_1 is the viscosity of isopropanol and μ_2 is the viscosity of the ideal mixture of 30% hexane and 10% tetrahydrofuran.

Appendix G

Invariance of Navier-Stokes Equations

We will show that Navier-Stokes equations given by 7.21 a, b and c are invariant under the translational transformation

$$x' = x \qquad y' = y + \dot{r}t \qquad u' = u \qquad v' = v + \dot{r}$$

where $\dot{r}$ is constant.

The derivatives of the transformed variables that appear in equation 7.21a can be determined with use of the chain rule

$$\frac{\partial u}{\partial t} = \frac{\partial u'}{\partial t'}\frac{\partial t'}{\partial t} + \frac{\partial u'}{\partial x'}\frac{\partial x'}{\partial t} + \frac{\partial u'}{\partial y'}\frac{\partial y'}{\partial t} = \frac{\partial u'}{\partial t'} + \frac{\partial u'}{\partial y'}\dot{r}$$

$$u\frac{\partial u}{\partial x} = u'\frac{\partial u'}{\partial x'}$$

$$v\frac{\partial u}{\partial y} = (v' - \dot{r})\left(\frac{\partial u'}{\partial t'}\frac{\partial t'}{\partial y} + \frac{\partial u'}{\partial x'}\frac{\partial x'}{\partial y} + \frac{\partial u'}{\partial y'}\frac{\partial y'}{\partial y}\right) = (v' - \dot{r})\frac{\partial u'}{\partial y'}$$

$$\nabla^2 u = \nabla'^2 u' \qquad \text{and} \qquad \frac{\partial P}{\partial x} = \frac{\partial P}{\partial x'}.$$

Substitution of these terms in equation 7.21a yields

$$\frac{\partial u'}{\partial t'} + \dot{r}\frac{\partial u'}{\partial y'} + u'\frac{\partial u'}{\partial x'} + (v' - \dot{r})\frac{\partial u'}{\partial y'} = \frac{\mu}{\rho}\nabla'^2 u' - \frac{1}{\rho}\frac{\partial P}{\partial x'}$$

which simplifies to

$$\frac{\partial u'}{\partial t'} + u'\frac{\partial u'}{\partial x'} + v'\frac{\partial u'}{\partial y'} = \frac{\mu}{\rho}\nabla'^2 u' - \frac{1}{\rho}\frac{\partial P}{\partial x'}.$$

Note that equation 7.21a preserves its form in the transformed coordinates.

Similarly, the terms in equation 7.21b can be expressed as

$$\frac{\partial v}{\partial t} = \frac{\partial v'}{\partial t'} + \dot{r}\frac{\partial v'}{\partial y'}$$

$$u\frac{\partial v}{\partial x} = u'\frac{\partial v'}{\partial x'}$$

$$v\frac{\partial v}{\partial y} = v'\frac{\partial v'}{\partial v'}$$

$$\nabla^2 v = \nabla'^2 v' \qquad \text{and} \qquad \frac{\partial P}{\partial y} = \frac{\partial P}{\partial y'}.$$

Substitution of these in equation 7.21b keeps the form of the equation unchanged.

$$\frac{\partial v'}{\partial t'} + u'\frac{\partial v'}{\partial x'} + v'\frac{\partial v'}{\partial y'} = \frac{\mu}{\rho}\nabla'^2 v' - \frac{1}{\rho}\frac{\partial P}{\partial y'}$$

Finally the continuity equation can be simply transformed as follows:

$$\frac{\partial u}{\partial x} + \frac{\partial v}{\partial y} = \frac{\partial u'}{\partial x'} + \frac{\partial v'}{\partial y'}.$$

Thus, it is shown here that the Navier-Stokes equations are invariant under the translational transformation applied.

Appendix H

Derivatives of the Stream Function

The first three derivatives of the general solution of the Orr-Sommerfeld equation are used in the stability calculations, since they appear in the boundary conditions. For the sake of completeness we give the analytical expressions for these quantities.

The first derivatives of the four independent general solutions are given as follows:

$$\phi_1'(y) = \alpha e^{\alpha y}$$

$$\phi_2'(y) = -\alpha e^{-\alpha y}$$

$$\phi_3'(y) = \int_{y_0}^{y} \cosh\left[\alpha(y-\hat{y})\right] e^{-(B/2)z(\hat{y})} Ai\left[z(\hat{y}) + B^2/4\right] d\hat{y}$$

$$\phi_4'(y) = \int_{y_0}^{y} \cosh\left[\alpha(y-\hat{y})\right] e^{-(B/2)z(\hat{y})} Bi\left[z(\hat{y}) + B^2/4\right] d\hat{y}.$$

The second derivatives are

$$\phi_1''(y) = \alpha^2 e^{\alpha y}$$

$$\phi_2''(y) = \alpha^2 e^{-\alpha y}$$

$$\phi_3''(y) = \alpha \int_{y_0}^{y} \sinh\left[\alpha(y-\hat{y})\right] e^{-(B/2)z(\hat{y})} Ai\left[z(\hat{y}) + B^2/4\right] d\hat{y} + e^{-(B/2)z(y)} Ai\left[z(y) + B^2/4\right]$$

$$\phi_4''(y) = \alpha \int_{y_0}^{y} \sinh\left[\alpha(y-\hat{y})\right] e^{-(B/2)z(\hat{y})} Bi\left[z(\hat{y}) + B^2/4\right] d\hat{y} + e^{-(B/2)z(y)} Bi\left[z(y) + B^2/4\right].$$

Finally the third derivatives can be written as

$$\phi_1'''(y) = \alpha^3 e^{\alpha y}$$

$$\phi_2'''(y) = -\alpha^3 e^{-\alpha y}$$

$$\phi_3'''(y) = \alpha^2 \int_{y_0}^{y} \cosh\left[\alpha(y-\hat{y})\right] e^{-(B/2)z(\hat{y})} Ai\left[z(\hat{y}) + B^2/4\right] d\hat{y}$$
$$- i(\alpha \mathrm{Re})^{1/3} e^{-(B/2)z(y)} \left\{-(B/2) Ai'\left[z(y) + B^2/4\right] + Ai'\left[z(y) + B^2/4\right]\right\}$$

$$\phi_4'''(y) = \alpha^2 \int_{y_0}^{y} \cosh\left[\alpha(y-\hat{y})\right] e^{-(B/2)z(\hat{y})} Bi\left[z(\hat{y}) + B^2/4\right] d\hat{y}$$
$$- i(\alpha \mathrm{Re})^{1/3} e^{-(B/2)z(y)} \left\{-(B/2) Bi'\left[z(y) + B^2/4\right] + Bi'\left[z(y) + B^2/4\right]\right\}.$$

The first derivative of the Airy functions that appear in the last two equations can, however, be written in terms of the associated Bessel functions.

$$Ai'(x) = -\frac{x}{3}\left[I_{-2/3}\left(2x^{3/2}/3\right) - I_{2/3}\left(2x^{3/2}/3\right)\right]$$

$$Bi'(x) = -\frac{x}{\sqrt{3}}\left[I_{-2/3}\left(2x^{3/2}/3\right) + I_{2/3}\left(2x^{3/2}/3\right)\right]$$

Appendix I

Experimental Investigations

A concurrent experimental program is planned to guide the theoretical investigations and elucidate various aspects of combustion dynamics. Although Stanford University has a small hybrid rocket system available, a larger and more controllable tube burner has been designed and fabricated to be used in the transient experiments. Initial test firings are successfully performed with this apparatus. The progress in the experimental studies can be divided into two categories, 1) Small burner experiments, 2) Design, fabrication and testing of the large burner.

1) Small Burner Experiments:

The tube burner that is used in the preliminary experiments is a small system with an initial port diameter of 0.4 in. When it was operated at very low mass flow rates, the motor showed significant low frequency oscillations that matched the thermal lag times in the fuel grain reasonably well. This mode of unstable operation is well known in the literature and named chugging/chuffing. The small setup does not allow any quantitative measurement, however experience obtained is used to guide the design of the more advanced system.

2) Design and Fabrication of the 3 1/4 OD Motor:

The availability of quantitative data on the motor parameters such as the chamber pressure during the transients is extremely important in the verification and refinement of the analytical models developed in this work. For that reason we designed and fabricated a new hybrid test setup in the Fluid Mechanics Laboratories of the Aeronautical and Astronautical Department of Stanford University. Although this system is specifically designed for transient experiments it can also be used in testing the Wax liquefying propellants. The rocket has the following general specifications:

- System can operate with gaseous oxygen and various casted or machined polymeric fuels such as HTPB, PMMA, PE or non-cryogenic liquefying fuels such as paraffin wax.
- The port diameter can be varied from 0.5 to 2 inches.
- The length of the motor can be adjusted to 7 in, 12 in or 19 inches. Length adjustment is useful to investigate the effect of the O/F ratio on the operation at an approximately constant mass flux.
- The ignition of the motor is achieved by a methane-oxygen torch which itself is ignited by a spark plug.

Motor Components:

Major components of the motor are pre-combustion chamber, motor case, post combustion chamber, nozzle and insulators. Pre-combustion chamber is the fore-end of the motor which accommodates the oxidizer injection port, ignition torch port, auxiliary fuel injection (Methane) port and the pressure transducer port. Whereas the motor case which is the mid section of the motor holds the propellant grain. The case elements are modular and can be connected to each other with use of couplers to obtain the required length of the fuel grain. The aft-end of the motor is the post-combustion chamber which holds the nozzle and possesses the second pressure transducer port. These three main elements of the motor are tied together by four threaded rods and the whole system is bolted to an optic table with use of two support structures. The elements are sealed with viton O-rings and silicon grease. Low carbon steel is selected for the metal components due to its machinability capabilities. Temperature resistant metals are not considered since all internal surfaces of the motor which are exposed to oxygen or hot combustion products are insulated. The insulators of the pre-combustion chamber and post-combustion chamber and the nozzle are machined out of ATJ graphite. The use of ATJ graphite as the nozzle material limits the operation of the motor to small O/F ratios, but significantly reduces the costs over more advanced materials such as silica-pheonolic. Fabricated components are shown in figure I.2.

Feed System:

In a hybrid motor oxidizer mass flow rate is the main control variable and most of the transients are achieved by means of changing this variable. For that reason the design of the feed system that delivers the oxidizer to the motor must be capable of conducting the transient events of interest such as rapid throttling and simulated instability by oscillating

mass flow. We designed a feed system (see figure I.1) that can generate the transients of interest with use of solenoid valves. Solenoid valves are preferred due to their low costs. The feed system can flow up to 0.4 lbm/sec oxidizer mass flow rate at a maximum line pressure of 650 psi.

In order to uncouple the chamber pressure variations from the oxidizer mass flow rate, a sonic orifice is inserted in the oxidizer line. As soon as the orifice is choked, the measurement of the pressure and temperature upstream of the throat is adequate for the calculation of the mass flow rate from the mass flow equation of quasi one-dimensional gasdynamics. The standard NACA TM 952 design is selected for the sonic orifice. The discharge coefficient for this orifice is suggested to be 0.615. Note that for precise mass flow rate measurements the discharge coefficient must be determined by separate calibration experiments. The pressure measurement will be accomplished by a transducer (Kistler 601B1) inserted in the upstream section of the sonic orifice. The sonic orifice assembly is designed to accommodate the transducer and the replaceable orifice plate (see figure I.1). The orifice assembly and orifice plates with various hole sizes (to change the mass flow capacity) are fabricated out of steel.

The throttling event can be simulated by opening the throttling oxygen line solenoid valve and closing the main oxygen line which are at different regulator pressures. This instantaneous switching of the lines changes the sonic orifice upstream pressure and the oxidizer mass flow rate. The maximum throttling ratio which can be achieved by this procedure on our system is around 5. It is important to note that the throttling process is not instantaneous due to the opening/closing delay of the solenoid valves and the filling times of the tubing. In order to minimize the throttling times we used two Actomatic solenoid valves (3100 series) in parallel on each of the lines. These valves have the smallest possible opening/closing delays (15-20 msec.) for the required mass flow and maximum pressure ratings imposed, among all the other possible valves that was available in the market to our knowledge. We also assembled the feed system to keep the tubing volume as small as possible between the regulators and the motor injector.

Another small solenoid valve is inserted into the main oxidizer flow line in parallel to be used in the simulated stability experiments. This is also an Actomatic valve (S24C series) with a smaller mass flow rating but faster response time (8-12 msec). The valve will be opened and closed repetitively to generate a periodic oxidizer mass flow rate with an amplitude of approximately 10% of the mean and with a maximum frequency of around 70

Hz. We note that this small valve is the weakest component in the feed system which limits the pressure rating of the system to 650 psi. When this valve is removed from the system the pressure rating improves to 1000 psi. A photograph of the assembled feed system is shown in figure I.3. Note that this version of the feed system does not have the line pressure regulators required for throttling experiments. The regulator module of the feed system is built separately which can easily be assembled to execute throttling experiments.

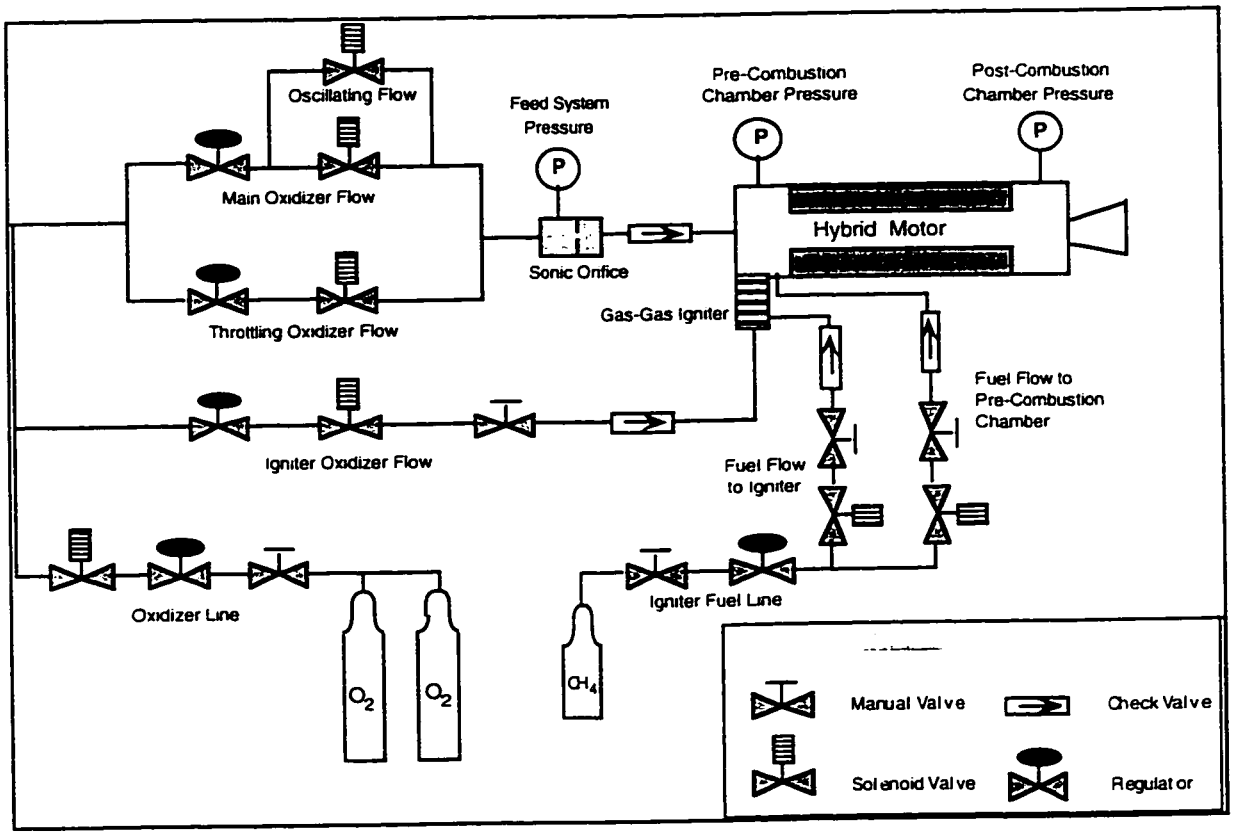

Figure I.1. Schematic of the experimental setup.

Ignition System:

The motor is ignited by the injection of the hot combustion products generated by a methane oxygen torch accompanied by the injection of the main oxidizer flow and some methane gas into the pre-combustion chamber. Since the transient experiments includes the investigation of the ignition phenomenon, the ignition system is designed to allow for the direct adjustment and quantitative measurement of the ignition parameters such as torch mass flow, torch stoichiometry and methane flow rate into the pre-combustion chamber. Igniter torch is fabricated from a hex steel bar which has ignition oxidizer, ignition fuel and

the spark plug ports. The combustion products flows through the exit port into the pre-combustion chamber. The stoichiometry and the total energy output of the torch can easily be controlled by adjusting the line pressures of the ignition oxidizer and the fuel and also by adjusting the flow coefficients of the metering valves inserted in the ignition lines.

Controls and Data Acquisition:

The transient property to be measured is primarily the combustion pressure. From a practical viewpoint, the pressure measurement is foremost because it is the property of concern in motor performance and stability and is relatively easy to measure with a high time response rate. The pressure-time curves of the transient events will be obtained by employing pressure transducers in the pre-combustion and post-combustion chambers. We selected the Kistler 601B1 piezoelectric transducers which have adjustable operating pressure ranges. These transducers possess excellent frequency response with a rise time of 2 microsec. and a natural frequency of 300 kHz. Kistler 5010B charge amplifier which allows for continuos adjustment for the signal gain and the time constant will be used to condition the transducer output signal for the readout equipment. It is also important to note that these piezoelectric transducers can be calibrated quasi-staticly due to the large time constant of the system. We believe that the simultaneous measurement of pressure at the fore-end and aft-end of the motor is critical in the simulated instability experiments.

For safety purposes, the experiments will be controlled remotely from a room next to the test chamber which is a separate room with steel reinforced walls. The controls and the data acquisition is achieved by a Macintosh computer (installed with a National Instruments data acquisition board NB-MIO-16X) devoted for this specific task. A Labview VI software is developed for the implementation of the required time line for any specific type of transient experiment and for data collection. During the experiments we plan to sample the pressures at three locations that are mentioned previously at a sampling rate that is adequate to resolve the 0.1 msec transients.

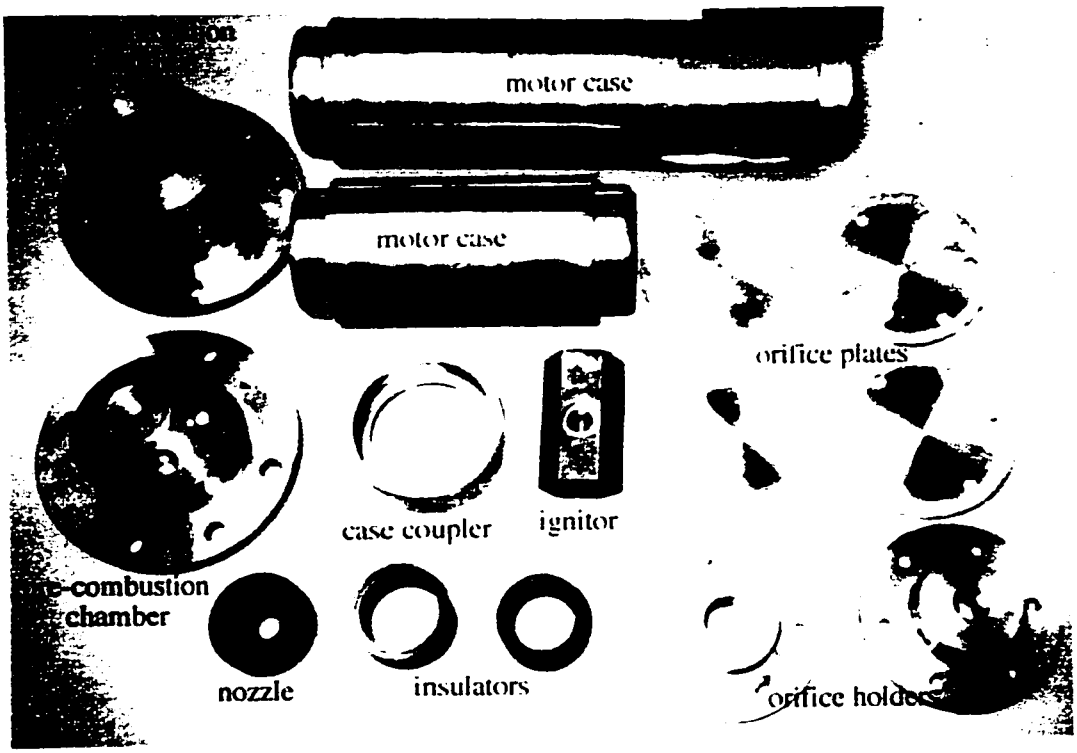

Figure I.2. Machined parts of the motor.

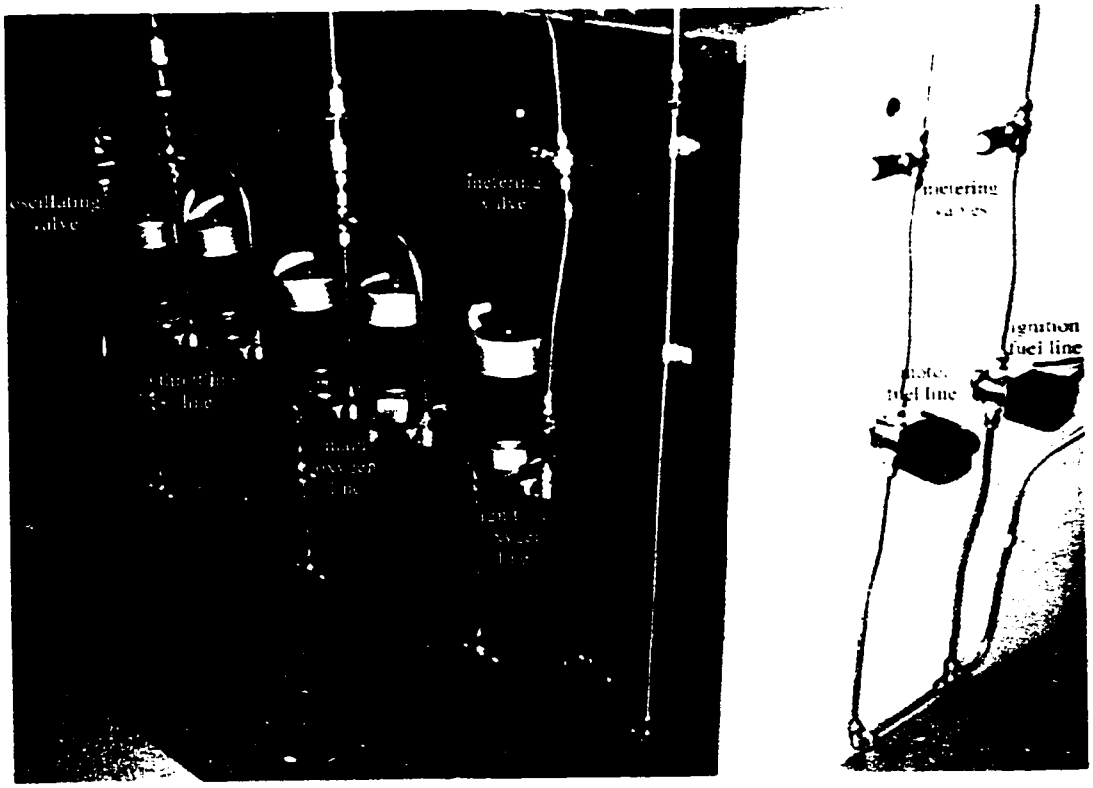

Figure I.3. Feed system of the motor. Left panel is for oxygen and the right panel is for fuel.

Design of the Test Motors:

In order to determine the motor operating conditions in terms of the propellant properties, geometrical parameters and oxidizer mass flow conditions, we developed a general on-design code for hybrid rockets. We used this code to calculate the required geometrical properties such as nozzle area, grain length, orifice area for given propellant combination and operating point selection and formed the test matrix shown in table I.1. The first two motors CP-1 and CP-2 which use Plexiglas are developed for overall system evaluation purposes. Whereas the motors LP-1, LP-2 and LP-3 will be used to investigate the performance of various Wax propellant formulations.

Motor Specifications	**CP-1**	**CP-2**	**LP-1**	**LP-2**	**LP-3**
Propellants	PMMA/GOX	PMMA/GOX	Wax/GOX	Wax/GOX	Wax/GOX
Chamber Pressure (psi)	40	60	55	90	200
Oxidizer Mass Flux (lbm/in^2-sec)	0.0846	0.166	0.06	0.108	0.10
Geometry					
Port Diameter (in)	0.50	0.50	1.0	1.0	1.5
Web Thickness (in)	0.9275	0.9275	0.678	0.678	0.428
Grain Length (in)	12	12	7	7	7
Nozzle Diameter (in)	0.37	0.37	0.5	0.5	0.5
Feed System Specs.					
Feed Pressure (psi)	175	335	430	390	650
Orifice Diameter (in)	0.1	0.1	0.1	0.155	0.155
Mass Flow Rates					
Oxidizer (lbm/sec)	0.017	0.0327	0.0472	0.0847	0.178
Fuel (lbm/sec)	0.0075	0.0113	0.0363	0.0798	0.109
Total (lbm/sec)	0.0242	0.44	0.0835	0.1645	0.287
Combustion Parameters					
Regression rate (in/sec)	0.010	0.015	0.05	0.11	0.1
O/F ratio	2.2	2.9	1.3	1.06	1.63
Equivalence Ratio	1.14	1.5	0.38	0.31	0.47
Combustion Temperature (K)	3426	3328	1951	1372	2693
Power Output (kW)	103	172	168	241	868
Performance Parameters					
Specific Impulse (sec)	126	147	129	119	162
Thrust (N)	13.5	28.8	48.1	87	207

Table I.1. Test matrix for the system evaluation and Wax performance experiments.

Table I.2 shows the HTPB motors that are planned to be used in the transient experiments. At present, the chamber pressure levels and mass flow rates are well below the capabilities of the designed system due to the current lack of an adequate exhaust system.

Motor Specifications	**M-H1a**	**M-H1b**	**M-H2**	**M-H3**
Propellants	HTPB/GOX	HTPB/GOX	HTPB/GOX	HTPB/GOX
Chamber Pressure (psi)	40	60	75	50
Oxidizer Mass Flux (lbm/in^2-sec)	0.151	0.151	0.164	0.075
Geometry				
Port Diameter (in)	1.00	1.00	0.70	1.30
Web Thickness (in)	0.687	0.687	0.837	0.537
Grain Length (in)	19	19	12	19
Nozzle Diameter (in)	0.98	0.80	0.50	0.80
Feed System Specs.				
Feed Pressure (psi)	200 (120)	200 (120)	225	180 (99)
Orifice Diameter (in)	0.228 (0.294)	0.228 (0.294)	0.155	0.228 (0.294)
Mass Flow Rates				
Oxidizer (lbm/sec)	0.120	0.120	0.063	0.10
Fuel (lbm/sec)	0.060	0.060	0.026	0.050
Total (lbm/sec)	0.180	0.180	0.089	0.15
Combustion Parameters				
Regression rate (in/sec)	0.030	0.030	0.030	0.019
O/F ratio	2.0	2.0	2.4	2.0
Equivalence Ratio	1.63	1.63	1.37	1.63
Combustion Temperature (K)	3403	3403	3566	3403
Power Output (kW)	765	765	426	637
Performance Parameters				
Specific Impulse (sec)	148	169	162	160
Thrust (N)	118	134	63	107
Transient Parameters				
Thermal lag time (sec)	0.169	0.169	0.169	0.380
Relative r variation* (%)	8.2	8.2	8.2	4.3

Table I.2. Test matrix for the transient experiments.

* This quantity is defined as the relative change in the regression rate due to the increase in the port area during a transient event with a duration of 1 second.

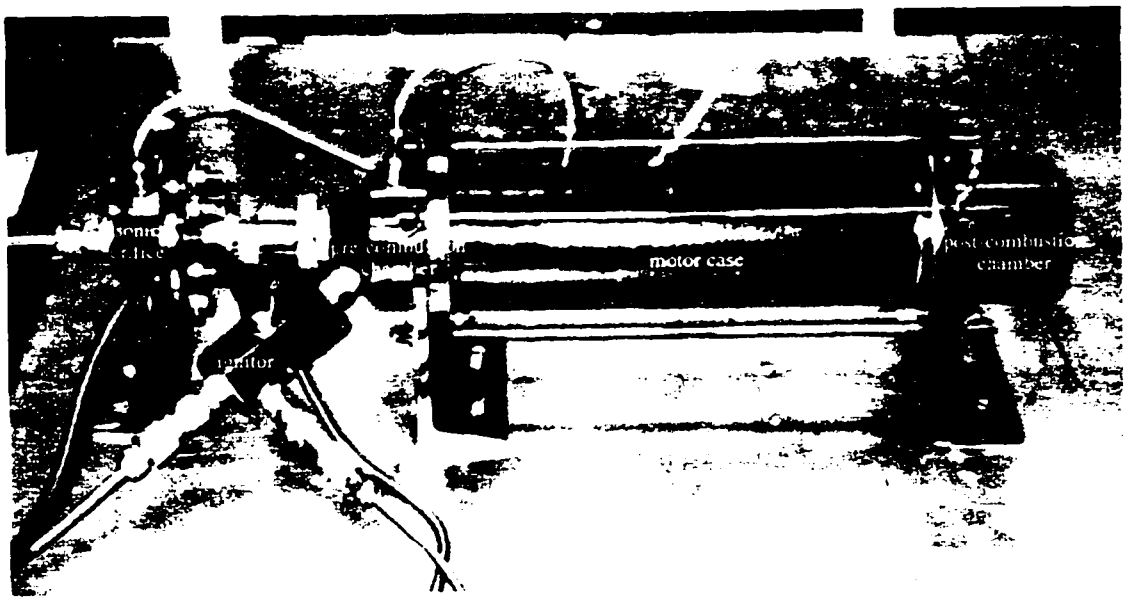

(a)

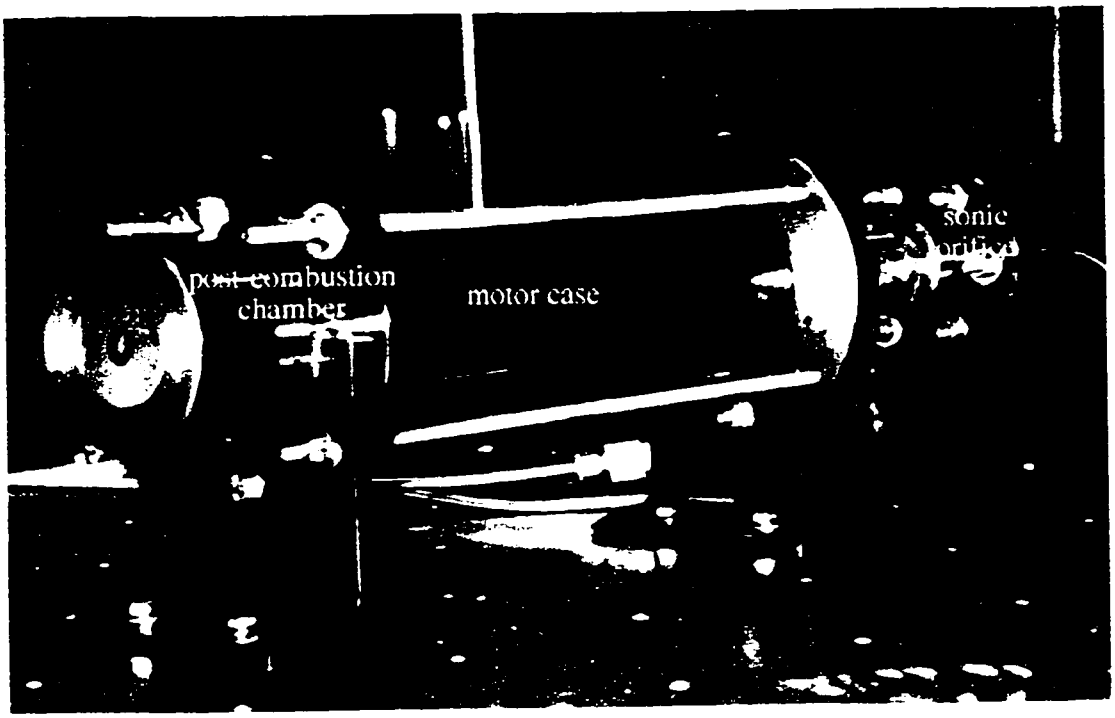

(b)

Figure I.4. Photographs of the assembled motor with 12 inch motor case. a) Side view. b) Aft view.

Test Firings:

The fabrication and the system tests of the 3 1/4 OD motor is completed. The photographs of the assembled motor taken from two different angles are shown in figure I.4. The test motor CP-1 is successfully fired several times. The timeline (in milliseconds) used for these tests is as follows:

t=0:	Start Labview program, start data acquisition
t=200:	Open main oxidizer and oxidizer ignition valves, start spark plug
t=250:	Open fuel ignition valve
t=600:	Close oxidizer and fuel ignition lines, stop spark plug
t=5200:	Close main oxidizer valve
t=5500:	Stop data acquisition, stop Labview program.

For these tests the ignition oxidizer mass flow rate was set to approximately 0.005 lbm/sec whereas the fuel mass flow rate was 0.0012 lbm/sec which gives a torch O/F ratio of 4.2 which is reasonably close to the stoichiometric value for methane/oxygen mixture. With these settings the ignition was smoothly and reliably achieved for all tests with no required use for the auxiliary fuel injection into the pre-combustion chamber. Figure I.5 shows the photograph of machined fuel grains (Plexiglas, polyethylene, and machinable wax) including the grain used in the CP-1 tests.

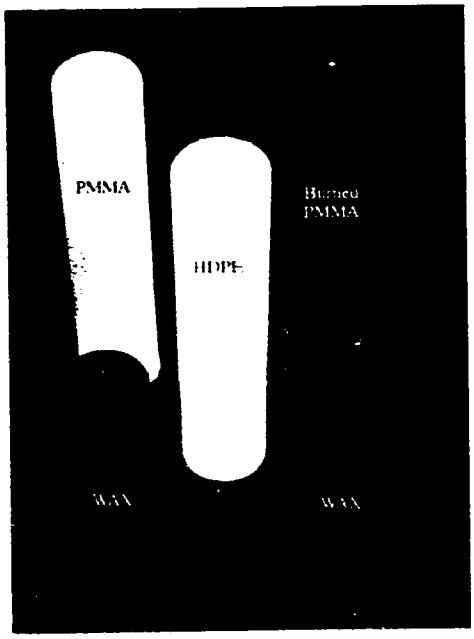

Figure I.5. Machined fuel rods. Short blue grains are made from machinable wax. A burned PMMA grain is also included in the photograph.

Bibliography

[1] D. Altman, " Hybrid Rocket Development History.", AIAA paper, No. 91-2515, 1991.

[2] Report of AIAA workshop on "Hybrid Rocket Propulsion", 1995.

[3] T. A. Boardman,T. M. Abel, S. E. Claflin and C. W. Shaeffer, "Design and Test Planning for a 250-klbf-Thrust Hybrid Rocket Motor Under the Hybrid Propulsion Development Program", AIAA paper No. 97-2804, AIAA/SAE/ASME/ASEE 33 rd Joint Propulsion Conference and Exhibit, July 1997.

[4] G. P. Sutton, "Rocket Propulsion Elements" Sixth Edition, 1992.

[5] National Research Council, Commitee on Earth-toOrbit Transportation Options, "From Earth to Orbit", National Academy Press, 1992

[6] G. A. Marxman, M. Gilbert, "Turbulent Boundary Layer Combustion in the Hybrid Rocket" , Ninth Symposium on Combustion, 1963 p 371.

[7] G. A. Marxman, "Combustion in the Turbulent Boundary Layer on a Vaporizing Surface", Tenth Symposium on Combustion, p 1337, 1965.

[8] G. A. Marxman, "Boundary layer Combustion in Propulsion", Eleventh Symposium on Combustion, 1967 p 269.

[9] C. W. Larson, K. L. Pfeil, M. E. DeRose and P. G. Carric, "High Pressure Combustion of Cryogenic Solid Fuels for Hybrid Rockets", AIAA paper No. 96-2594, AIAA/SAE/ASME/ASEE 32 nd Joint Propulsion Conference and Exhibit, July 1996.

[10] R. J. Muzzy. "Schelierin and Shadowgraph Studies of Hybrid Boundary Layer Combustion", AIAA Journal, vol 1, no. 9, pp. 2159-2160, 1963.

[11] D. Altman and R. Humble, Ch. 7 "Hybrid Rocket Propulsion Systems" in Space Propulsion Analysis and Design, McGraw Hill, 382, 1995.

[12] D. W. Netzer, "Hybrid Rocket Internal Ballistics", Chemical Propulsion Information Agency, 1972.

[13] P. Bradshaw, Course Notes on "Introduction to Turbulence", 1993.

[14] G. Lengelle, "Model Describing the Erosive Combustion and Velocity Response of Composite Propellants", AIAA Journal Vol 13 No. 3, p 315, 1975.

[15] H. Schlichting, "Boundary Layer Theory", McGraw Hill, 1955.

[16] L. Lees, "Convective Heat and Mass Transfer with Mass Addition and Chemical Reactions", Combustion and Propulsion, 3d AGARD Colloquium , Palermo, pp 451, Sicily, 1958.

[17] C. E. Wooldridge, "Internal Ballistic Considerations in Hybrid Rocket Design.", J. of Spacecraft, Vol. 4 No. 2, p225, 1967.

[18] C. E. Wooldrige and R. J. Muzzy, "Internal Ballistic Considerations in Hybrid Rocket Design", AIAA paper No. 66-1966, 1966.

[19] G. A. Marxman, C. E. Wooldridge and R.J. Muzzy, "Fundamentals of Hybrid Boundary Layer Combustion", Progress in Astronautics and Aeronautics, Vol.15, 1964 p 485.

[20] R. J. Muzzy, "Applied Hybrid Combustion Theory', AIAA paper, No. 72-1143, 1972.

[21] F. J. Kosdon and F. A. Williams, "Pressure Dependence of Nonmetalized Hybrid Fuel Regression Rates", AIAA Journal, vol 5, no 4, pp.774-778, 1966.

[22] L. D. Smoot, and C. F. Price, "Pressure Dependence of Hybrid Fuel Regression Rates", AIAA Journal, vol 5, no 1, pp.102-106, 1966.

[23] P. Estey, D. Altman and J. McFarlane, "An Evaluation of Scaling Effects for Hybrid Rocket Motors", AIAA paper, No. 91-2517, AIAA/SAE/ASME 27 th Joint Propulsion Conference and Exhibit, June 1991.

[24] D. D. Orhald and D. Altman , " Hybrid Propellant Combustion Characteristics and Engine Design", Third Symposium on Advanced Propulsion Concets, OSR/USAF, Oct. 1962.

[25] F. A. Williams, "Grain Design and Throttling of Hybrid Rocket Motors", Chemical Engineering Progress Series, No. 61, vol 62, pp. 86-91.

[26] D. M. Guthrie and R. S. Wolf, "Non-Acoustic Combustion Instability in Hybrid Rocket Motors", N 91-24250, 1991.

[27] T. A. Boardman, R. L. Carpenter and S. E. Claflin, "A Comperative study of the Effects of Liquid-Versus Gaseous-Oxygen Injection on Combustion Stability in 11-inch-Diameter Hybrid Motors", AIAA paper No97-2936, AIAA/SAE/ASME/ASEE 31 st Joint Propulsion Conference and Exhibit, July 1997.

[28] F. Dijkstra, P. Korting and R. van der Berg ,"Ultrasonic Regression Rate Measurement in Solid Fuel Ramjets" AIAA paper No. 90-1963, 1990.

[29] D. Altman, Private Communication 1997.

[30] T. A. Boardman, D. H. Brinton, R. L. Carpenter, T. F. Zolods, "An Experimental Investigation of Pressure Oscillations and Their Suppression in Subscale Hybrid Rocket Motors", AIAA paper 95-2689, 1995.

[31] T. A. Boardman, R. L. Carpenter, B. E. Goldberg, and C. W. Shaeffer, "Development and Testing of 11- and 24- Inch Hybrid Motors Under the Joint Government/Industry IR&D Program", AIAA Paper No. 93-2552, AIAA/SAE/ASME/ASEE 29 th Joint Propulsion Conference and Exhibit, June 1993.

[32]. B. Greiner and R. A. Frederick,Jr. "Hybrid Rocket Instability". AIAA paper. No. 93-2553. 1993.

[33] B. Greiner and R. A. Frederick,Jr. "Experimental investigation of Labscale Hybrid Instability". AIAA paper. No. 94-2878. 1994.

[34] R. M. Jenkins. J. R. Cook. "A Preliminary Analysis of Low Frequency Pressure Oscillations in Hybrid Rocket Motors". AIAA paper No. 95-2690. 1995.

[35] C. Wooldridge. G. A. Marxman and R. Kier. "Investigation of Combustion Instability in Hybrid Rockets". NASA CR-66812 Final Report. 1969.

[36] C. Wooldridge and G. A. Marxman. "Combustion Instability and the Role of Chemical Kinetics in Hybrid Combustion." AIAA Journal No. 68-498. 1968.

[37] R. S. Brown and R. J. Muzzy. "Linear and Nonlinear Pressure Coupled Instability of Solid Propellants". AIAA Journal. p 1492. 1970.

[38] M. W. Beckstead and E. W. Price. "Nonacoustic Combustion Instability". AIAA Journal Vol. 5. No. 11 p. 1989. 1967.

[39] E. W. Price. D. W. Rice and J. E. Crump. "Low-Frequency Combustion Instability of Solid Rocket Propellants". Technical Progress Report to U.S. Naval Ordanance Test Station. 1964.

[40] F A Williams. "Combustion Theory". Addison Wesley. 1965.

[41] L. Crocco and S. I. Cheng, " Theory of Combustion Instability in Liquid Propellant Rocket Motors". Agardograph No. 8. 1956.

[42] F. E. C. Culick and V. Yang, "Combustion Instabilities in Liquid Rockets". Progress in Astronautics and Aeronautics. Vol.169. pp 3-37. 1995.

[43] H. G. Landau, "Heat Conduction in a Melting Solid". Quarterly Journal of Applied Mathematics, Vol. 8. p 81, 1950.

[44] H. Lomax and T. Pulliam, "Finite Difference Methods for Fluid Dynamics", 1993.

[45] Yogesh Jaluria, Kenneth E. Torrance, "Computaional Heat Transfer", Hemisphere Publishing Coorparation, p. 128.

[46] Carslaw and Jeager, "Conduction of Heat in Solids", Oxford University Press, 1959.

[47] M. Van Dyke, "Perturbation Methods in Fluid Mechanics", Parabolic Press, 1975.

[48] E. Zauderer, "Partial Differential Equations of Applied Mathemathics", Wiley-Interscience, p. 287, 1989.

[49] Mark, Bikales, Overberger, Menges, "Encyclopedia of Polymer Science and Engineering", John Wiley and Sons, 1985.

[50] J. P. De Wilde, "Fuel Pyrolysis Effects on Hybrid Rocket and Solid Fuel Ramjet Combustion Performance.", Delft Univ. Press, 1991.

[51] D. R. Esker and M. Q. Brewster, "Laser Pyrolysis of Hydroxyl-Terminated Polybutadaine", Journal of Propulsion and Power, Vol. 12 No.2, 1996.

[52] G. C. Cheng, R. C. Farmer, H. S. Jones and J. S. McFarlane, "Numerical Simulation of the Internal Ballistics of a Hybrid Rocket Motor." AIAA Journal, No. 94-0554, 1994.

[53] W. Nachbar and F. A. Williams, "On the Analysis of Linear Pyrolysis Experiments", Ninth Symposium on Combustion, p 371, 1963.

[54] K. Ramohalli and D. B. Stickler, " Polymer-Degradation Theory of Pressure-Sensitive Hybrid Combustion.", Thirteenth Semposium on Combustion, 1970, p1059.

[55] Gyorgy Fodor, " Laplace Transformations in Engineering", 1965.

[56] R. H. Cannon, " Dynamics of Physical Systems", McGraw Hill, 1967.

[57] G. Arfken, "Mathematical Methods for Physicists", Academic Press Inc., 1985.

[58] M. D. Horton, P. S. Bruno and E. C. Graesser, "Depressurization Induced Extinction of Burning Solid Propellant", AIAA Journal, vol 6, no 2.

[59] Lu, "Pulsating Turbulent Water Flow in a Tube", Ph. D. thesis, Clarkson College of Technology, 1972.

[60] G. C. Kingstan, " Experimental and Theoretical Studies of Pulsating Turbulent Flow", Ph. D. thesis, Clarkson College of Technology, 1975.

[61] B. R. Ramaparian, " A Review of Experiments in Periodic Turbulent Pipe Flow", ASME FED-Vol 12, 1984.

[62] P. G. Parikh, R. Jayaraman, W. C. Reynolds and L. W. Carr, " Transient Response of a Turbulent Boundary Layer" ASME FED-Vol 12 1984.

[63] H. Daneshyar, "One-Dimensional Compressible Flow", Permagon press, 1976.

[64] H. Moriai, "Gasdynamic Transient Phenomena in Hybrid Rockets", Engineering Degree Thesis, Stanforrd University, 1996.

[65] D. G. Luenberger, "Introduction to Dynamic Systems", Wiley, 1979.

[66] C. W. Larson, M. E. DeRose, K. L. Pfeil, and P. G. Carric, "High Pressure Combustion of Cryogenic Hybrid Fuels in a Lab-Scale Burner", Proccedings of the 1996 JANNAF Joint Propulsion Conference, Albuquerque, NM, December 9-13, 1996, published by CPIA, John Hopkins University.

[67] M. E. DeRose, K. L. Pfeil, P. G. Carric C. and C. W. Larson, "Tube Burner Studies of Cryogenic Solid Combustion", AIAA paper No. 97-3076, AIAA/SAE/ASME/ASEE 33 rd Joint Propulsion Conference and Exhibit, July 1997.

[68] L. Lang, "Absorption Spectra in the Infrared Region", London Butterworths, 1974.

[69] F. F. Bentley, L. D. Smithson, A. L. Rozek, "Infrared Spectra and Characteristic Frequencies ~700-300 cm -1", Interscience Publishers, 1968.

[70] R. Seigel and J. R. Homel. "Thermal Radiation Heat Transfer". Hemisplane Publishing Coorporation. 1992.

[71] A. D. D. Craik. "Wind Generated Waves in Thin Liquid Films". J. of Fluid Mechanics. vol. 26. part 2. pp. 369-392. 1966.

[72] I-Dee Chang and P. E. Russel. "Stability of a Liquid Layer Adjacent to a High-Speed Gas Stream" The Physics of Fluids. vol. 8. no. 6. 1965.

[73] A. H. Nayfeh. W. S. Saric. 'Non-Linear Kelvin-Helmholtz Instability". J. of Fluid Mechanics. vol. 46. part 2. pp. 209-231. 1971.

[74] F. Gungor. "Diferansiyel Denklemler". Istanbul Teknik Universitesi/Turkey. 1995.

[75] T. B. Benjamin. "Shearing Flow over a Wavy Boundary". ". J. of Fluid Mechanics. vol. 6. pp. 161-205. 1959.

[76] R. A. Gater and M. R. L'Ecuyer. "A Fundamental Investigation of the Phenomena that Characterize Liquid Film Cooling". International Journal of Heat and Mass Transfer Vol. 13. pp 1925-1939. 1970.

[77] M. Ishii and M. A. Grolmes. "Inception Criteria for Droplet Entrainment in Two Phase Concurrent Film Flow". AICh Journal. vol. 21. no. 2. pp. 308-318. 1975.

[78] R. Nigmatulin. B. Nigmatulin. YA. Khodzaev and V. Kroshilin. "Entrainment and Deposition Rates in a Dispersed-Film Flow". International Journal of Multiphase Flow Vol. 22. pp. 19-30. 1996.

[79] Raznjevic. "Handbook of Thermodynamic Tables and Charts". Hemisphere Pub. Co.. 1976.

[80] W. C. Reynolds. " Thermodynamic Properties in SI". SUME. 1979.

[81] T. E. Dauber. R. T. Danner. "Physical and Thermodynamic Properties of Pure Chemicals. Data Compilation"..Taylor and Francis. 1997.

[82] J. S. McFarlane. R. J. Kniffen and L. Lichatowich. "Design and Testing of AMROC's 250.000 lbf Thrust Hybrid Motor". AIAA paper 93-2551. 1993.

[83] T. A. Boardman. R. L. Carpenter and S. L. Claflin. "A Comperative Study of the Effects of Liquid- Vesus Gaseous- Oxygen Injection on Combustion Stability in 11- Inch-Diameter Hybrid Motors". AIAA Paper No. 97-2936. 1997.

[84] B. I. Nigmatulin. L. A. Klebanonov. A. E. Kroshilin. "Heat transfer crisis for process steam-liquid dispersed annular flows under non-stationary conditions". High Temp. Thermal Phys. 18. 1242-1251. 1980.

[85] E. A. Moelwyn-Hughes. "Physical Chemistry". Permagon Press. 1961.

[86] Bicerano. J. "Prediction of Polymer Properties". Marcel Dekker Inc.. 1996.

[87] Altman. D.. Karabeyoglu. M. A.. Patent Pending. "High Regression Rate Rocket Fuels".

IMAGE EVALUATION
TEST TARGET (QA-3)

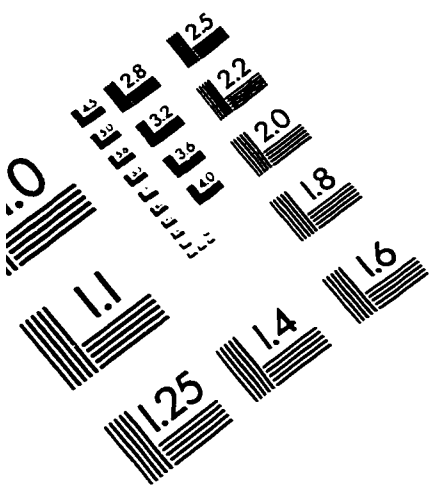

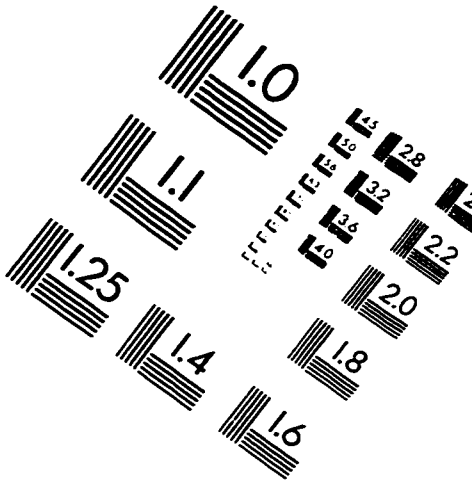

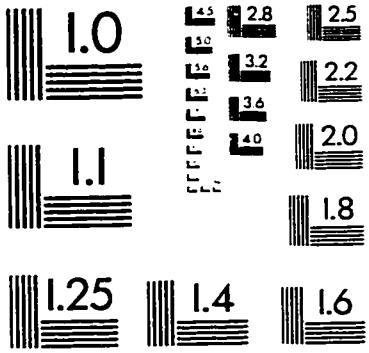

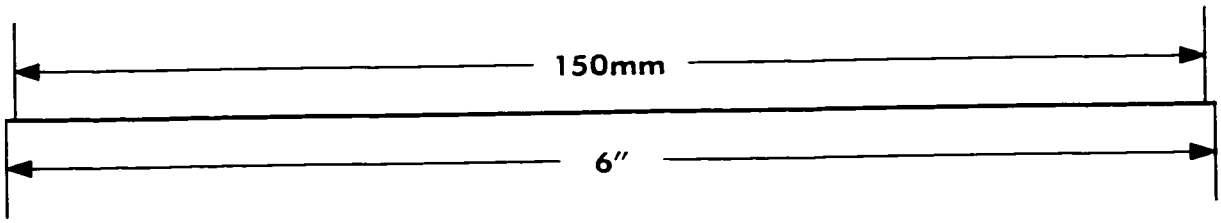

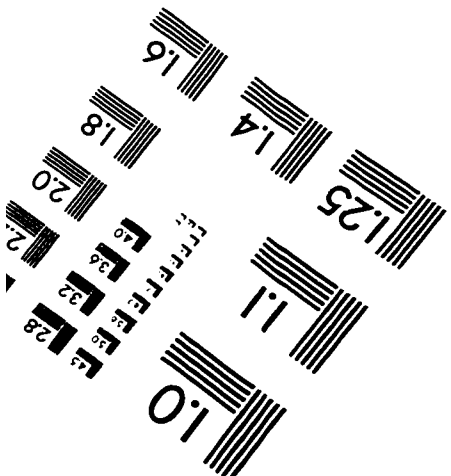

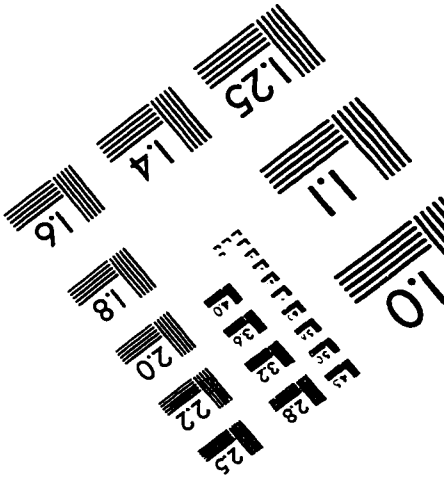

APPLIED IMAGE . Inc
1653 East Main Street
Rochester, NY 14609 USA
Phone: 716/482-0300
Fax: 716/288-5989